Development of Novel Functional and Degradable Materials for Use in Microstereolithography

by

Edward J. Cant MChem (Hons)

A thesis submitted in partial fulfilment of the requirements for the degree of:

Doctor of Philosophy in Engineering

2017

Written in loving memory of

Francis Henry Cant

Acknowledgements

First of all, I would like to thank both my supervisors, Professor Andrew Dove and Dr Simon Leigh, for giving me the opportunity to work within their groups. Their continued guidance and expertise has proven invaluable and without which, I would not be standing where I am today. I would also like to acknowledge the EPSRC (Engineering and Physical Sciences Research Council) for their funding.

Massive thanks go to all past and present members from both the O'Doveilly and DMTL (Digital Materials Technology Laboratory) groups. Thanks to Dr Craig Bell, Dr Chris Purssell and Dr Vinh Truong for everything you've done whether it be helping me in the lab, encouraging me to get out of the lab or even making sure I've got a constant supply of packing chips. Thanks to James, Ruairi, Ant, Guillaume, "The Angels" (Annette, Chiara and Laura), Alice, Anne and Emma without whom the last four years would not have been half as much fun! Special thanks to Netty (a.k.a. Team Twin) for making the lab a far more enjoyable place to be. Additional thanks go to those who helped proof read this thesis (Guillaume, Josh, Chiara, Vinh, Chris and Cai).

Thanks to my parents, Chris and Debbie, my sister, Sam and the rest of my family for believing in me throughout. I will be forever grateful for the endless support, encouragement and advice you have given me over the years. Thanks to my best friends Hanson, Nesbitt and Jason for reminding me there's a world outside the lab and indeed Warwick. Caroline, thanks for getting me out of the lab at weekends and for being there for me throughout what has undoubtedly been one of the hardest, yet also by far one of the best years of my life. I've loved every minute and can't wait to see what the future holds for us. Finally, thank you Grandad Frank, although he wasn't here to see it completed, it was in his memory that this thesis was written.

Declaration of Authorship

This thesis is presented in accordance with the regulations for the degree of Doctor of Philosophy. Unless otherwise stated the experimental work within this thesis is original and carried out solely by the author within the School of Engineering or the Department of Chemistry at the University of Warwick between September 2013 and August 2017. No material within this thesis has been submitted for any other degree, or at any other institution.

Experimental work and analysis conducted by other authors are detailed as followed: Scanning electron microscopy (Chapter 2) was carried out with the help of Annette Christie, Atomic force microscopy (Chapter 2) was carried out by Gordon Herwig, Differential scanning calorimetry and thermal gravitational analysis (Chapter 2) was conducted by Panagiotis Bexis, Elemental analysis (Chapters 3 and 4) was conducted by Warwick Analytical Services and biocompatibility assays were conducted by Dr Chiara Arno.

Signed: _____ Date: _____

Edward Cant

List of abbreviations

µSL	Microstereolithography
2D	Two dimensional
3D	Three dimensional
4D	Four dimensional
AFM	Atomic force microscopy
AlMa	Allyl malate
AM	Additive manufacturing
BHT	Butylated hydroxytoluene
BMP	Bone morphogenetic protein
BnMa	Benzyl malate
BSA	Bovine serum albumin
BuMa	Butyl malate
CAD	Computer aided design
CLIP	Continuous liquid interface production
CQ	Camphorquinone
CT	Computed tomography
DD	Drug Delivery
DBS	Dibutenyl sussinate
DCM	Dichloromethane
DDT	Dodecanethiol
DEF	Diethyl fumarate
DEF-HA	Diethyl fumarate - Hyaluronic acid
DIC	Diisopropylcarbodiimide

DLP	Digital light projection
DLW	Direct laser writing
$Đ_m$	Polydispersity
DMAP	Dimethylaminopyridine
DMD	Digital micromirror device
DMF	Dimethylformamide
DMTL	Digital materials technologies laboratory
DP	Degree of polymerisation
DPPHA	Dipentaerythritol penta-/hexa-acrylate
DPTS	4-(dimethylamino)pyridinium 4-toluene-sulfonate
DSC	Differential scanning calorimetry
EDC	N′-ethylcarbodiimide hydrochloride
EDG	Electron donating group
EDMAB	Ethyl 4-(dimethylamino)benzoate
EPSCR	Engineering and physical sciences research council
EtMa	Ethyl malate
EWG	Electron withdrawing group
FAME	Fumaric acid monoethylester
FDM	Fused deposition modelling
FT-IR	Fourier-transform infrared spectroscopy
HA	Hyaluronic acid
HDDA	Hexanediol diacrylate
HEMA	2-hydroxyethyl methacrylate
IPA	Isopropanol
IR	Infrared

LCD	Liquid crystal display
LH	Lighthammer
LMW	Low molecular weight
MA	Malic acid
MEM	Minimum essential medium
M_n	Number averaged molecular weight
MRI	Magnetic resonance imaging
M_w	Weight averaged molecular weight
NBnMa	Nitrobenzyl malate
NMR	Nuclear magnetic resonance
NVP	N-vinyl-2-pyrrolidone
*o*NB	*ortho*-Nitrobenzyl
PCL	Poly(caprolactone)
PDLLA	Poly(DL-Lactic acid)
PDMMA	Poly(dimethylmethacrylate)
PDMS	Polydimethylsiloxane
PEG	Poly(ethylene glycol)
PEGDA	Poly(ethylene glycol) diacrylate
PEG-*o*NB	Poly(ethylene glycol) *ortho*-nitrobenzyl ester
PI	Photoinitiator
PLA	Poly(lactic acid)
PLGA	Poly(lactic-*co*-glycolic acid)
PLLA	Poly(L-lactic acid)
PMA	Poly(malic acid)
PMMA	Poly(methyl methacrylate)

PPF	Poly(propylene fumarate)
ppm	Parts per million
PT3M	Pentaerythritol tetrakis(3-mercaptopropionate)
PTMC	Poly(trimethylene carbonate)
*p*TSA	*para*-Toluene sulfonic acid
RGD	Arginylglycylaspartic acid
RI	Refractive index
ROP	Ring opening polymerisation
ROS	Radical oxygen species
SEC	Size exclusion chromatography
SEM	Scanning electron microscopy
SL	Stereolithography
SLM	Spatial light modulator
STL	Standard tessellation language
TE	Tissue Engineering
TES	Tissue Engineering Scaffold
TEM	Transmission electron microscopy
TFAA	Trifluoroacetic anhydride
TGA	Thermal gravimetric analysis
THF	Tetrahydrofuran
UTS	Ultimate tensile strength
UV	Ultraviolet
UV-Vis	Ultraviolet-Visible
VSI	Verticle scanning interferometry

Table of contents

Acknowledgements i

Declaration of Authorship ii

List of abbreviations iii

Table of contents vii

List of figures xii

List of tables xxiii

List of schemes xxv

Abstract xxvii

1. Introduction 1

1.1. Additive Manufacturing 2

1.2. StereoLithography (SL) and MicroStereoLithography (µSL) 4

1.2.1. Direct Laser Writing 6

1.2.2. Digital Light Projection (DLP) 7

1.2.3. Constrained and Free Surface Variations in µSL 8

1.2.4. Continuous Liquid Interface Production (CLIP) 3D printing 11

1.2.5. The µSL Process 12

1.2.6. Resin Components 14

1.2.7. Chemistry of Components 21

1.2.8. Combining Resin Components in the Curing Process 23

1.3. Materials Used in µSL and Their Applications 24

1.3.1. Commercially available resins 24

1.3.2. Non-commercially available resins 26

1.4. Conclusions 36

1.5. References 37

2 Development of a 4D photodegradable material for use in μSL 49

2.1 Introduction 50

2.2 Results and Discussion 57

2.2.1 Synthesis of photodegradable linker 57

2.2.2 Resin composition optimisation 61

2.2.3 Degradation 72

2.3 Conclusion and future work 84

2.4 References 86

3. Synthesis and characterisation of poly(malates) via direct polycondensation and their potential as candidates for use in μSL 92

3.1. Introduction 93

3.2. Results and discussion 99

3.2.1. Monomer synthesis 99

3.2.2. Homopolymer synthesis 102

3.2.3. Tuning and controlling hydrophobicity 118

3.2.4. Copolymer synthesis 121

3.3. Conclusions and future work 131

3.4. References 133

4. Development of surface erodible materials for use in drug eluting implants made by μSL 139

4.1. Introduction 140

4.2. Results and Discussion 146

4.2.1. Resin composition optimisation 146

4.2.2. Exposure time optimisation 152

4.2.3. Initial accelerated degradation study 153

4.2.4. Controlled small molecule release 156

4.2.5. Resin composition alteration for tuning degradation and release 158

4.2.6. Mechanical properties of the cured materials 161

4.2.7. 3D printing 164

4.2.8. Tuneable degradation and release 169

4.2.9. Non-accelerated in vitro degradation study 172

4.2.10. Biocompatibility 174

4.2.11. Towards temporal release 175

4.3. Conclusions and Future work 181

4.4. References 182

5. Conclusions & Future Work 188

Conclusions 189

Future Work 191

6. Experimental 194

6.1. Materials 195

6.2. Instrumental Methods 195

6.2.1. NMR Spectroscopy and Size Exclusion Chromatography (SEC) 195

6.2.2. UltraViolet-Visible Light (UV-Vis), InfraRed (IR) and Raman Spectroscopy 196

6.2.3. Optical Microscopy and Scanning Electron Microscopy (SEM) 196

6.2.4. Interferometry 197

6.2.5. Atomic Force Microscopy (AFM) 197

6.2.6. Thermal Analysis 197

6.2.7. Drop Shape Analysis 198

6.2.8. Rheology 198

6.2.9. Microstereolithography 198

6.2.10. Degradation and Release 199

6.2.11. Tensile Analysis 199

6.2.12. Micro X-ray Computed Tomography (MicroCT) 199

6.3. Experimental procedures for Chapter 2 200

6.3.1. Procedure for the synthesis of ethyl 4-(4-acetyl-2-methoxyphenoxy) butanoate, 3: 200

6.3.2. Procedure for the synthesis of ethyl 4-(4-acetyl-2-methoxy-5-nitrophenoxy)butanoate, 4: 201

6.3.3. Procedure for the synthesis of 4-[4-(1-hydroxyethyl)-2-methoxy-5-nitrophenoxy]butanoic acid, 5: 201

6.3.4. Procedure for the synthesis of 4-[4-(1-(Acryloyloxy)ethyl)-2-methoxy-5-nitrophenoxy] butanoic acid, 7: 202

6.3.5. Procedure for the synthesis of PEG-oNB, 8: 203

6.4. Experimental Procedures for Chapter 3 204

6.4.1. Procedure for the synthesis of Benzyl malate, BnMa: 204

6.4.2. Procedure for the synthesis of NitroBenzyl Malate, NBnMa: 205

6.4.3. Procedure for the synthesis of Ethyl Malate, EtMa: 205

6.4.4. Procedure for the synthesis of Butenyl Malate, BuMa: 206

6.4.5. General procedure for high temperature homopolymerisations of malate monomers: 207

6.4.6. Procedure for ambient temperature homopolymerisation of BnMa: .208

6.4.7. General procedure for copolymerisations of BnMa, NBnMa and EtMa with BuMa: 208

6.4.8. Typical procedure for NMR scale study assessing alkene reactivity of the copolymers towards dodecanethiol: 209

6.5. Experimental Procedures for Chapter 4: 209

6.5.1. General procedure for the large-scale synthesis of P(EtMa-co-BuMa): 209

6.5.2. Procedure for the synthesis of Dibutenyl Succinate: 210

6.5.3. Procedure for biocompatibility assay: 210

6.6. References 211

List of figures

Figure 1.1. Diagram outlining the key steps in the SL process from design to manufacture.....5

Figure 1.2. Diagram illustrating the method of direct laser writing (DLW) in traditional stereolithography (SL) to cure photosensitive resins and the inherent problems associated with laser focussing 6

Figure 1.3. Diagram illustrating the method of digital light projection (DLP) as a technique in more modern µSL apparatus displaying its ability to cure different parts of the resin in a parallel manner.....8

Figure 1.4. Diagram illustrating the key components within the 'free surface' (top down) µSL configuration. 9

Figure 1.5. Diagram illustrating the key components within the 'constrained surface' (bottom up) µSL configuration. 10

Figure 1.6. Diagram illustrating the oxygen permeable membrane leading to the "dead zone" that allows for speedy, continuous printing in the CLIP process 12

Figure 1.7. Diagram depicting the µSL apparatus and process 13

Figure 1.8. Chemical structures of a selection of more commonly used photoinitiators for both UV and visible light based systems.....20

Figure 1.10. Diagram illustrating the various components found in most µSL resins and how they come together to form a cross-linked material 23

Figure 1.11. Chemical structures of degradable polymers utilised in µSL.....30

Figure 1.12. Images of a tissue engineering device made from PDLLA (A) and a microneedle array made from PPF (B)[48, 82].....33

Figure 1.13. Images of the piezoelectric devices produced by Woodward et al. (A) and the tissue engineering scaffold made by Ronca et al. (B) 34

Figure 1.14. Image demonstrating the swelling ability of a hydrogel scaffold made by µSL.....35
Figure 2.1. Image depicting the self-folding of a six-sided box from the thermally induced shape memory behaviour of the printed ink that make up the hinges of the box[10].....51
Figure 2.2. Image demonstrating the independent blooming of petals in a flower at various temperatures as a result of printing multiple shape memory materials with various activating temperatures[12].....52
Figure 2.3. Images depicting the ability of cross-linked gels containing oNB to undergo photodegradation as a result of exposure to a) mask-based photolithography and b) focussed multiphoton laser[33].....55
Figure 2.4. Schematic displaying the ability to build 3D objects from the synthesised resin (1) using a visible wavelength of light (λ^1) in the µSL process (2) and then the ability to selectively degrade away regions of the object (3) with a second wavelength of light (λ^2).....56
Figure 2.5. ^{1}H NMR spectrum of PEG-oNB (400MHz, * = $CHCl_3$, ** = DCM).....60
Figure 2.6. Size exclusion chromatograms of non-functionalised PEG (M_n = 650, M_w = 800, and $Đ_m$ = 1.19) PEG-oNB (M_n = 1400, M_w = 3000, and $Đ_m$ = 2.19). Using poly(styrene) standards with $CHCl_3$ as eluent.....61
Figure 2.7. UV-Vis spectra of PEGDA/DPPHA resin compositions both with and without photoinitiator (PI) (A) and with increasing amounts of PEG-oNB doping (B, 5 wt % and C, 10 wt%). (dashed red line refers to transmission maxima of blue LED light source used).....62
Figure 2.8. UV-Vis absorbance spectra of various different visible light photoinitiators 64

Figure 2.9. Image of cross-linked solid materials formed upon stirring resins both with (A) and without (B) PEGDA.....66
Figure 2.10. Picture of ill-defined rectangle of cured material with residual uncured materials surrounding it on glass slide with mask illustrating the rectangle of light exposed onto the pool of resin 68
Figure 2.11. Picture of well-defined cured rectangle of cross-linked resin after post-processing with mask illustrating the rectangle of light exposed onto the pool of resin 70
Figure 2.12. Emission spectra of the visible light sources from both the 'custom msl' and 'custom mini' 3D printers illustrating the broader region of visible light emitted by the 'custom mini' printer.....70
Figure 2.13. Layer thickness of cured resin as a function of exposure time. Pictures are of the respective rectangles cured for each exposure time.....71
Figure 2.14. UV-Vis absorbance spectra of PEG-oNB at increasing doses of UV light exposure 73
Figure 2.15. Normalised SEC traces of coupled PEG-oNB in DMF SEC eluent exposed to increasing durations of UV-Light from the metalight chamber and table illustrating the decrease in number average molecular weight after increasing exposures (using PMMA as standards with DMF as eluent).....74
Figure 2.16. FT-IR spectra of cross-linked PEG-oNB before and after varying degree of exposure to UV light from the metalight chamber indicating the occurance of photolysis 76
Figure 2.17 FT-IR spectra of cross-linked PEG-oNB before and after 16 passes of UV light from the Light Hammer, indicating the increased occurance of photolysis from a more powerful light source 77

Figure 2.18. Optical microscopy images (Left) and Scanning Electron Microscopy (SEM) (Right) images of the thin film exposed to UV light through the square holes of a TEM grid.....78

Figure 2.19. VSI 3D profile of the surface of the thin film exposed to 16 passes of the light hammer 79

Figure 2.20. Surface topography of cross-section of selectively photodegraded thin film sample acquired by AFM and processed using Gwyddion software 81

Figure 2.21. DSC (left) and TGA (right) thermal analysis data of PEG-oNB showing no observable melting points until thermal degradation onset at 130 °C 82

Figure 2.22. Optical microscopy images of the TEM grid used as a photomask depicting the more transparent strut centres (orange/red) as compared with the opaque edges of the grid (dark black).....83

Figure 3.1. Figure showing the various malate α-ester monomers including Allyl malate (AlMa), Benzyl malate (BnMa), Ethyl malate (EtMa) and Nitrobenzylmalate (NBnMa). 96

Figure 3.2. Schematic representing the concept of utilising a hydrophobic (red) photoresponsive monomer in the copolymer that, upon exposure to one wavelength of light could undergo cross-linking in the μSL process. The subsequent photolysis of the cross-linked material would yield the hydrophilic (blue) poly(malic acid) making it more hydrophilic and susceptible to water ingress leading to hydrolytic degradation on the surface. 97

Figure 3.3. ^{1}H NMR spectrum of Benzyl malate (BnMa) after purification by acidic work up ($CDCl_3$, 400 MHz, 293 K, * = $CHCl_3$) 99

Figure 3.4. ^{1}H NMR spectrum of nitrobenzyl malate (NBnMa) after purification by acidic work up ($CDCl_3$, 400 MHz, 293 K, * = Acetone).....100

Figure 3.5. ^{1}H NMR spectrum of butenyl malate (BuMa) after removal of excess 3 buten-1-ol by high vacuum distillation at 35 °C ($CDCl_3$, 400 MHz, 293 K, * = $CHCl_3$) 101

Figure 3.6. ^{1}H NMR spectrum of ethyl malate (EtMa) after purification by recrystallisation ($CDCl_3$, 400 MHz, 293 K, * = Acetone).....101

Figure 3.7. (A) Assigned ^{1}H NMR spectrum (top) and (B) zoomed in spectra illustrating the decrease in signal intensity corresponding to the proton next to the secondary alcohol of the monomer (*) compared to the increase in signal intensity corresponding to the same proton in the polymer as conversion increases. ($(CD_3)_2CO$, 400 MHz, 293K ** = Acetone).....103

Figure 3.8. Plot of conversion against time for the homopolymerisation of BnMa carried out at temperatures between 110 and 140 °C in the absence of catalyst. 106

Figure 3.9. SEC chromatograms of P(BnMa) synthesised by polymerising BnMa at varying reaction temperatures between 110 and 140 °C. Samples measured against PMMA standards using DMF as eluent.....107

Figure 3.10. ^{1}H-NMR spectrum depicting the increasing formation of fumarate based by-products caused by intramolecular dehydration at increasing temperatures 108

Figure 3.11. SEC chromatogram of P(NBnMa) and P(BnMa) produced at 130 °C depicting the higher intensity of lower molecular weight species formed as a consequence of fumarate formation. Samples measured against PMMA standards using DMF as eluent 109

Figure 3.12. ^{1}H NMR spectra of P(NBnMa) and P(BnMa) produced after 7 days illustrating the increased presence of fumarate formation for the NBnMa containing polymer ($(CD_3)_2CO$, 400MHz (PNBnMa) and ($CDCl_3$, 400MHz P(BnMa)) 110

Figure 3.13. SEC chromatograms of P(BuMa) at varying extents of polymerisation depicting the increased intensity of low molecular weight species formed. Samples measured against PMMA standards using DMF as eluent 114
Figure 3.14. Chemical structures of the carbodiimide (N,N'diisopropylcarbodiimide) (DIC) and respective catalyst (4-(dimethylamino)pyridinium 4-toluene-sulfonate) (DPTS) used in the low temperature polymerisation of BnMa.....116
Figure 3.15. SEC chromatogram of P(BnMa) synthesised by low temperature methods with corresponding Mn, $Mw$and Đm values of 2600 g mol^{-1}, 3700 g mol^{-1} and 1.41 respectively. Sample measured against PMMA standards using DMF as eluent....117
Figure 3.16. ^{1}H NMR spectrum of P(BnMa) made by low temperature polymerisation also illustrating the difficulty in removing impurities.....118
Figure 3.17. Drop shape analysis of distilled water on thin films of the NBnMa, BnMa & EtMa homopolymers demonstrating the difference in hydrophobicity. 118
Figure 3.18. UV-Vis absorbance spectra of P(NBnMa) at different lengths of exposure to UV light demonstrating the loss of the absorbance corresponding to the nitrobenzyl ester and increase in the absorbance corresponding to the nitrobenzyl aldehyde photolysis product. 120
Figure 3.19. Drop shape analysis of P(NBnMa) thin films before and after a 30 minute exposure to UV light demonstrating the ability to alter the surface wettability upon exposure to an external stimulus.....121
Figure 3.20. SEC chromatograms of copolymers of BnMa, NBnMa and EtMa with BuMa illustrating the lower moleculer weight species observed for the more EW P(NBnMa-co-BuMa) copolymer. Samples measured against PMMA standards using DMF as eluent. 123

Figure 3.21. ^{1}H NMR spectra of copolymers of; A, P(BnMa-co-BuMa), B, P(NBnMa-co-BuMa) and C, P(EtMa-co-BuMa). (** = residual monomer * = acetone) (400MHz, $(CD_3)_2CO$) R' = Bn, NBn, Et or Bu. 125

Figure 3.22. ^{1}H-NMR spectroscopy of the small molecule study carried out both before and after exposure to blue light (465 nm) for 1 h illustrating a 67 % reduction in the signals corresponding to the alkene functionality in addition to the appearance of peaks corresponding to the thioether functionality (ca. 1.8 ppm) (($CD_3)_2CO$), 400 MHz) 128

Figure 3.23. ^{1}H NMR spectra before (A & C) and after (B & D) exposure to blue light for 1 h illustrating the non-reactivity and reactivity of BuMa towards dodecanethiol in the presence of NBnMa (A & B) and BnMa (C & D), respectively (($CD_3)_2CO$), 400 MHz) 129

Figure 3.24. UV-Vis absorbance spectra of the various copolymers with respect to the camphorquinone photoinitiator used demonstrating that, at the same concentration, there should be no inhibition of the photoinitiator by the copolymers 130

Figure 4.1. Schematic illustration of the surface and bulk eroding mechanisms undertaken by hydrolysable, biodegradable polymers[31] 142

Figure 4.2. Gravimetric analysis of PCl-based (A) and PPF-based (B) materials printed from stereolithographic resins exemplifying their near linear surface eroding degradation profiles[28, 29] 143

Figure 4.3. Schematic illustrating the potential temporal control over release from a multimaterial spherical device 145

Figure 4.4. SEC chromatogram of P(EtMa-co-BuMa) produced on a large scale (> 50g). Samples measured against PMMA standards using DMF as eluent 146

Figure 4.5. ^{1}H-NMR spectra of P(EtMa-co-BuMa) both before and after reaction with dodecanethiol illustrating the complete loss of signals corresponding to the olefinic protons after UV exposure (400MHz, * = acetone, ** = residual monomer).....147
Figure 4.6. Viscosity vs. temperature graph illustrating the reduced viscosity of P(EtMa-co-BuMA) containing 10 wt% propylene carbonate as non-reactive diluent at higher temperatures.....148
Figure 4.7. Synthesis scheme and assigned ^{1}H-NMR spectrum for Dibutenyl Succinate (DBS) (400MHz, * = $CHCl_3$).....149
Figure 4.8. ^{1}H-NMR spectra of Dibutenyl Succinate (DBS) both before and after reaction with dodecanethiol illustrating the complete loss of signals corresponding to the olefinic protons after UV exposure (400MHz, * = Chloroform).....150
Figure 4.9. Resin composition comparison (A) for varying weight percentages of DBS with respect to Poly(EtMa-co-BuMa) and the respective viscosities (B) of these compositions as determined by rheology (sheer rate = 5 s^{-1}).....151
Figure 4.10. Rendered CAD drawing of curing time optimisation part (A) with side on view of the part illustrating the different height of the bars and the respective slice taken (dashed red line) (B) to produce the respective images masks (C). 152
Figure 4.11. Images illustrating the ability of the material to print 5 layer walls at exposures greater than 15 seconds for a layer height of 50 µm (A) and greater than 25 seconds for a layer height of 100 µm (B).....153
Figure 4.12. Gravimetric analysis of degradation pucks fabricated using the P(EtMa-co-BuMa) containing resin as compared with pucks fabricated using a commercially available resin (EnvisionTec R11) under accelerated conditions (1M NaOH) and physiological temperature (37 °C) 154

Figure 4.13. Dimensions and surface areas of the base and lateral surfaces of the designed puck (A). Images of an exemplar puck at various time points during degradation to illustrate the surface eroding nature of the material (B) and the data corresponding to the percentage decrease in both height and diameter during the course of degradation (C).....155

Figure 4.14. Pictures illustrating the printed hemispheres (A) and an assembled sphere (B). 157

Figure 4.15. Gravimetric analysis of fluorescein loaded spheres fabricated using the P(EtMa-co-BuMa) containing resin (A) and the respective release profile (B) under accelerated degradation conditions (0.1M NaOH) and physiological temperatures (37 °C).....158

Figure 4.16. Graph illustrating the viscosity of resins containing between 30 and 60 wt% P(EtMa-co-BuMa) whilst maintaining constant quantities of reactive diluent and cross-linker.....159

Figure 4.17. Drop shape analysis of distilled water on thin films of cured resin compositions containing 0, 30 and 50 wt% P(EtMa-co-BuMa), respectively.....160

Figure 4.18. Plot of stress (MPa) vs. strain (%) for photocured resins containing 0, 30 and 50 wt% P(EtMa-co-BuMa) respectively.....162

Figure 4.19. Raman spectra of the three resin compositions (0,30 and 50 wt% P(EtMa-co-BuMa) both in the liquid resin and the solidified material after the curing process 163

Figure 4.20. Varying views from a CAD render of the '(10, 3)-a' crystal structure generated by George Hart exemplifying the intricacy and complex nature of the design 165

Figure 4.21. Photograph taken of the (10, 3)-a gyroid structures printed using the 0, 30 and 50 wt% P(EtMa-co-BuMa) containing resins 166
Figure 4.22. Images produced from microCT reconstructions illustrating the ability of 0, 30 and 50 wt% P(EtMa-co-BuMa) containing resins to print complex 3D structures in addition to representing the internal features and porous architectures of the printed hartcubes 167
Figure 4.23. Gravimetric analysis of fluorescein loaded spheres fabricated using 30 wt% P(EtMa-co-BuMa) containing resin (A) and the respective release profile (B) under accelerated degradation conditions (0.1M NaOH) and physiological temperatures (37 °C) 169
Figure 4.24. Gravimetric analysis of fluorescein loaded spheres fabricated using 0 wt% P(EtMa-co-BuMa) containing resin (A) and the respective release profile (B) under accelerated degradation conditions (0.1M NaOH) and physiological temperatures (37 °C) 171
Figure 4.25. Gravimetric analysis of 0, 30 and 50 wt% P(EtMa-co-BuMa) containing degradation pucks under non-accelerated conditions (MEM) and physiological temperature (37 °C).....172
Figure 4.26. Cell counts from a cell viability assay carried out on cured 0, 30 and 50 wt% P(EtMa-co-BuMa) containing resins as compared with one carried out on a PLLA control sample 174
Figure 4.27. CAD design of 1 mm^2 multimaterial cube and its cross-sectional view (A), separate CAD designs and their cross sectional views for non-encapsulated (B) and encapsulated (C) parts and the respective masks generated, placed in order and colour coded to distinguish between the different layers and whether encapsulated (red) or non-encapsulated resin should be used (D).....176

Figure 4.28. Images of the partially printed array next to a rule for scale (A) and a close up (B) to exhibit the lack of distinction between encapsulated and non-encapsulated material. 177
Figure 4.29. Process for fabrication of multimaterial spheres 177
Figure 4.30. Photographs of exemplar parts made during the fabrication process (A), an aerial view of the filled hemisphere (B), two bound hemispheres in solution (C) and a microCT image of a cross-section of the fabricated part (D). 179
Figure 4.31. Gravimetric analysis of multimaterial almost spherical devices fabricated using 50 wt% P(EtMa-co-BuMa) containing resin (A), the respective release profile (B) under accelerated degradation conditions (0.1M NaOH) and physiological temperatures (37 °C), and photos of the degradation medium taken at each time point illustrating the ‘off-on’ release profile visually (C) 180

List of tables

Table 1.1. Table illustrating the seven AM categories, the respective technologies associated with them, the types of compatible materials in addition to a selection of known applications and the state of the material required for processing. 3

Table 1.2. Table illustrating the chemical structures of various reactive components used in µSL resins and their respective advantages 22

Table 1.3. Table presenting a selection of the various types of commercially available materials, their developers, the resin composition, the ultimate tensile strength of the printed material, the viscosity of the resin and their intended application.....25

Table 1.4. Table listing some of the materials found in the literature alongside their intended application(s) 28

Table 2.1. Incrementally decreasing the pH of the resin using either benzoic or lactic acid in order to prevent premature cross-linking 68

Table 2.2. Effect of non-reactive diluent (propylene carbonate) on film formation..69

Table 3.1. Extent of reaction and SEC data for the direct polycondensation of BnMa to P(BnMa) at various temperatures 105

Table 3.2. Extent of reaction and SEC data for the direct polycondensation of NBnMa, EtMa and BuMa to their respective homopolymers carried out at 130 °C[1] and/or 110 °C[2] 113

Table 3.3. Extent of reaction and SEC data for the direct polycondensation of NBnMa, EtMa and BnMa with BuMa to form their respective copolymers carried out at 110 °C for 72h. 123

Table 3.4. Conversion, degree of polymerisation (DP), Number avergae molecular weight (Mn), degree of alkene functionality as a percentage and average number of

alkene units per polymer chain based on the assumption that all polymer chains are terminated by fumarate formation (all determined by ^{1}H NMR spectroscopy 126

List of schemes

Scheme 2.1. Synthetic scheme for the 5 steps involved in the synthesis of the photodegradable oNB molecule 58

Scheme 2.2. Functionalisation of PEG with oNB using EDC.HCl and DMAP in DCM 59

Scheme 2.3. Resin composition used by Leigh et al. to produce cross-linked networks of complex 3D architectures by μSL[41] 61

Scheme 2.4. Mechanism of thiol hydrogen abstraction by peroxy radicals[45] 65

Scheme 2.5. Mechanisms for base catalysed, nucleophile initiated and free radical thiol-ene reactions (Nu = nucleophile, PI = Photoinitiator, R & R' = alkyl chains).. 67

Scheme 2.6. Degradation products formed by photodegradation of PEG-oNB in solution after exposure to UV light 72

Scheme 3.1. Schematic illustrating the numerous steps involved in producing monomers for ring opening polymerisation into the respective poly(malate) esters and subsequent deprotection steps to afford PMA. 95

Scheme 3.2. Schematic demonstrating the direct polycondensation of malic acid into the respective poly(α, β-malic acid) 96

Scheme 3.3. Synthesis of benzyl malate via initial ring closing of malic acid using TFAA followed by subsequent ring opening of MAA by benzyl alcohol 99

Scheme 3.4. Synthesis of nitrobenzyl malate via initial ring closing of malic acid using TFAA followed by subsequent ring opening of MAA by nitrobenzyl alcohol in DCM 100

Scheme 3.5. Synthesis of butenyl malate via initial ring closing of malic acid using TFAA followed by subsequent ring opening of MAA by 3 buten-1-ol 101

Scheme 3.6. Synthesis of ethyl malate via initial ring closing of malic acid using TFAA followed by subsequent ring opening of MAA by ethanol 101
Scheme 3.7. Synthesis of P(BnMa) via direct polycondensation of BnMa at elevated temperatures under reduced pressure 102
Scheme 3.8. Formation of fumarate end-capped polymer chains caused by the competitive intramolecular dehydration side reaction 107
Scheme 3.9. Scheme illustrating the dehydration of the secondary alcohol at the poly(malate) propagating chain end via the E1 elimination mechanism 110
Scheme 3.10. Scheme illustrating the dehydration of the secondary alcohol at the poly(malate) propagating chain end via the $E1_{CB}$ elimination mechanism 111
Scheme 3.11. Scheme depicting the homopolymerisation of the various different malates produced at 110 °C 113
Scheme 3.12. Schematic depicting the low temperature step-growth polymerisation of BnMa and the reaction conditions used 116
Scheme 3.13. Molecular structure of products formed as a consequence of photolysis of P(NBnMa).....120
Scheme 3.14. Schematic representation of the copolymerisation of BuMa with either of NBnMa, EtMa or BnMa 121
Scheme 3.15. Small molecule study used to determine the reactivity of the various copolymers (R = Bn, NBn or Et) towards dodecanethiol in the presence of camphorquinone and its coinitiator (EDMAB).....127

Abstract

The research carried out in this thesis focusses on the development of novel functional and degradable materials for use in Microstereolithography (µSL), a type of additive manufacturing (AM) technology. Chapter 1 provides a background into the µSL technology with regards to key developments and the current state-of -the-art for the µSL apparatus itself in addition to providing an overview of the various types of commercially or non-commercially available materials currently developed for µSL.

Chapter 2 describes the current state-of-the-art in terms of four-dimensional (4D) printing materials used within the µSL technology and subsequently focusses on expanding the limited scope of materials currently developed. The previously described poly(ethylene glycol) di-*ortho*-nitrobenzyl (PEG-*o*NB) ester molecule is successfully synthesised. Upon optimisation of a PEG-*o*NB containing resin, the material was found to be capable of solidifying to a defined two dimensional (2D) shape utilising one wavelength of light in the µSL apparatus and subsequently able to undergo photodegradation upon controlled exposure by a secondary wavelength of light thereby exemplifying a fourth dimension.

In chapter 3, a library of previously described and novel malate based monomers with various functionality are synthesised and subsequently polymerised by step-growth polymerisation either in bulk or in solution to form short chain homopolymers. Copolymerisations carried out in bulk are shown to form polymers with the desired alkene bearing functionality required for cross-linking *via* radical thiol-ene coupling and the Poly(EtMa-*co*-BuMa) copolymer is successfully functionalised using dodecanethiol demonstrating its potential for use as a material within µSL.

Chapter 4 describes the successful application of Poly(EtMa-*co*-BuMa), as synthesised in chapter 3, within a novel resin composition, containing dibutenyl succinate (DBS) as reactive diluent, that is capable of printing complex 3D architectures within the μSL process. The materials produced demonstrate exemplar degradation *via* the surface erosion mechanism and consequently exhibit near-zero order release kinetics upon encapsulation of a model small molecule. Furthermore, small alterations of the resin composition allowed for the rate of degradation and release to be tuned whilst applying multiple materials within the same device allows for controlled, temporal release.

Chapter 5 concludes the most significant findings of Chapters 2-4 whilst Chapter 6 lists all the experimental protocols and methods used in this thesis.

1. Introduction

1.1. Additive Manufacturing

Additive Manufacturing (AM) was first developed in the 1980s. Unlike subtractive manufacturing processes that fabricate three dimensional (3D) objects by successively removing material from a solid block of material, AM produces 3D objects by consecutively joining material together, usually in a layer by layer fashion.[1] Such layer by layer processing (often referred to as 3D printing) allows for complex objects to be produced directly from 3D Computer Aided Design (CAD) models that would ordinarily be impossible to produce *via* conventional subtractive techniques.[2-3] While AM technologies have shown limited use in the mass production of functional, end-user parts they have demonstrated an ability to reduce lead times and be more cost-effective for producing one-off parts or small batches.[4-5] Furthermore, there is also significantly less material wastage in AM when compared to conventional subtractive processes, thereby making it more favourable from an economical and environmental perspective.[6]

Until recently, AM processes have mostly been applied to rapid prototyping applications, because of their inability to mass produce parts, the lack of readily available, functional materials and the poor surface finish characteristic of some AM processes.[4, 7] However, with the ongoing development of AM technologies and the respective materials used, AM processes have or are beginning to find purpose in producing parts for a much broader scope of applications including tooling, aerospace, biomedical and construction fields to name a few.[8-16] Therefore, the number of AM parts that are being produced as finished items rather than models or prototypes is rapidly increasing and so it is unsurprising that forecasters envision AM to have an

economic impact of $550 billion per annum by 2025 (nearly 8 times the current machine-tool market at $70 billion).[17]

Table 1.1. Table illustrating the seven AM categories, the respective technologies associated with them, the types of compatible materials in addition to a selection of known applications and the state of the material required for processing.

Category	Technology	Material	Application	State of material
Vat photopolymerisation	- Stereolithography - Digital light processing - Continuous digital light processing	- Polymer - Polymer composites - Hydrogels	- Microdevices - Biomedical - Prototyping	Liquid
Material extrusion	- Fused deposition modelling	- Polymer - Polymer composites	- Hobbyist - Prototyping - Tooling	Solid
Material jetting	- Material jetting - Nanoparticle jetting - Drop on demand	- Polymer - Metal - Wax	- Prototypes - Casting	Liquid
Powder bed fusion	- Selective laser sintering - Multi jet fusion - Selective laser melting - Electron beam melting	- Polymer - Metal - Composites	- Prototypes - Tools - One-off parts (post processing necessary)	Powder
Binder jetting	- 3D printing - Ink-jetting	- Metal - Polymer - Ceramic	- Prototypes - Tools/Molds	Liquid/ Powder
Sheet lamination	- Laminated object manufacturing	- Paper - Composites	- Visual/Aesthetic models	Solid
Direct energy deposition	- Laser engineering net shape - Electron beam additive manufacturing	- Metal - Plastic	- Repair of structural parts - Coatings - One-off parts	Liquid/ Solid

There have been numerous types of AM technologies developed over the past few decades that can be sorted into 7 categories including; material extrusion, vat photopolymerisation, material jetting, powder bed fusion, binder jetting, sheet lamination and direct energy deposition (**Table 1.1**).[4] These technologies differ most by the state of the starting material being employed - including solids, liquids or powders. Whilst they all have their respective advantages and disadvantages, the decision to choose one type of AM technology over another often culminates from several factors. These factors include cost (both initial instrument cost and continuing running costs), printing times, process compatible materials, build envelope, accuracy

compared to the original design and intended application for the part being manufactured.

Of the seven categories mentioned, vat photopolymerisation, or more specifically StereoLithography (SL), was the first AM technology to be made commercially available by 3D Systems Corporation in 1988 after its invention by Kodama in 1981 and subsequent patenting by Charles Hull (founder of 3D Systems Corporation) in 1984.[18-19] By exploiting photosensitive resins, Kodama demonstrated the ability to build 3D objects by sequentially curing or solidifying layers of material using an UltraViolet (UV) light source. Since the pioneering work of Kodama and Hull there have been numerous developments in both the technology used in the SL apparatus and the properties of the materials used during printing (detailed later in this chapter). Because of these advances, SL and its derivatives have found a niche in the production of accurate, high resolution 3D parts for use in a number of applications including dentistry, production of hearing aids, Micro Electro-Mechanical Systems (MEMS), microfluidics and biomedical devices.[20-26] Despite ongoing advances, the lack of readily available resins with enhanced properties and functionality beyond maintaining the ability to be processed by SL is still considered one of the key drawbacks to the technique.[27-28] The research carried out in this thesis aims to address this issue by developing novel SL capable materials with novel properties that have not been reported before.

1.2. StereoLithography (SL) and MicroStereoLithography (μSL)

SL works by converting a 3D CAD model (**Figure 1.1**, A) to a Standard Tessellation Language (.STL) file (**Figure 1.1**, B) and subsequently using specialist software to slice it into layers of equal thickness (**Figure 1.1**, C). The slices generated are 2D representations of the XY-cross-section of the model at increasing Z-heights of the

part and are ultimately used to either draw or project the cross-sectional pattern with UV or visible light into a photosensitive resin one on top of the other until the part has been fabricated (**Figure 1.1**, D). MicroStereoLithography (µSL) works in much the same way as SL with the only difference being the resolution of the process and hence, the minimum feature size of the part being produced. Whilst there used to be a substantial difference between the capabilities of different SL apparatus to produce parts with either macro or micro-scale resolution, the majority of modern commercially available SL apparatus are capable of printing parts with sub-millimetre resolution and thus the distinction has become less relevant. This section covers some of the different variations in technology and processes used to achieve µSL over the past few decades in addition to outlining some of the key advancements and the current state-of-the-art.

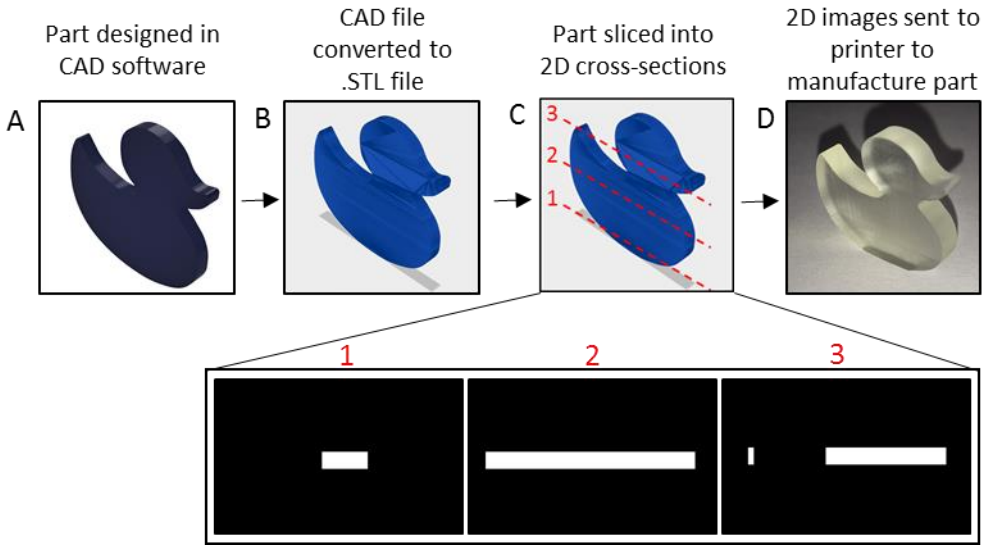

Figure 1.1. Diagram outlining the key steps in the SL process from design to manufacture

1.2.1. Direct Laser Writing

Traditional μSL techniques involve selective curing of a photosensitive resin *via* a single wavelength process using a focused laser and a pair of mirrors that are positioned using galvanometers (**Figure 1.2**).[29] The moveable mirrors reflect the laser spot and effectively 'write' the cross section of one slice of the 3D object across the surface of the resin. This method is known as direct laser writing (DLW) and whilst it has been demonstrated to produce 3D objects with micro-scale features, it has some inherent drawbacks. For instance, although the laser spot remains focused when writing directly above/below it, as the laser spot is positioned toward the extremities of the build volume, the laser spot becomes de-focused and so producing large or multiple parts can result in the fabrication of less accurate parts (**Figure 1.2**). One method of overcoming this problem was to constrain the movement of the laser and move the vat of resin, however, this hampers the speed of fabrication because of the slow movements required to avoid the resin moving about too much. Moreover, the serial nature of the direct laser writing technique also restricts the rate at which parts can be printed, thereby not lending itself to large-scale production in terms of batch size.

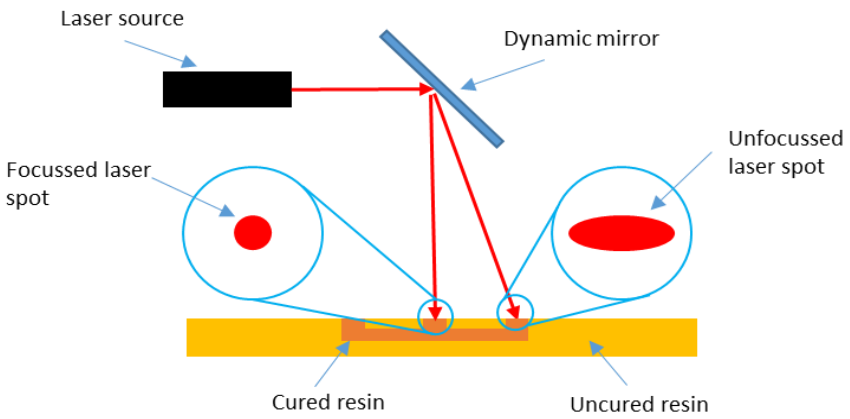

Figure 1.2. Diagram illustrating the method of direct laser writing (DLW) in traditional stereolithography (SL) to cure photosensitive resins and the inherent problems associated with laser focussing

1.2.2. Digital Light Projection (DLP)

The use of a mask projected onto the surface of the resin rather than direct writing with a laser allows for simultaneous fabrication of parts in a parallel manner thereby meaning that an entire layer can be exposed at once (**Figure 1.3**).[30-31] This in turn, is particularly desirable when fabricating multiple parts in the same build since it requires no extra time. To print layers on the order of tens of microns in thickness, the number of masks required for individual layers can be in the hundreds or thousands depending on the height of the part. In order to achieve this process, a method of dynamically exposing individual masks representative of consecutive layers of the part is required. The first example of using a dynamic mask system for production of parts by μSL was developed by Bertsch *et al.* who used a Liquid Crystal Display (LCD) Spatial Light Modulator (SLM) as their dynamic mask generator.[32] Whilst their approach proved to significantly reduce manufacturing times, the use of an LCD as the dynamic mask also came with several limitations.[31] Firstly, LCDs tend to absorb UV light as a consequence of not being fabricated from quartz glass, therefore restricting its compatibility with UV sensitive resins. Additionally, the low switching speed and the low optical density of the refractive elements during the 'off' mode not only hinders the contrast of the pattern generated but can also lead to premature curing of the resin if not used in combination with a light shutter.

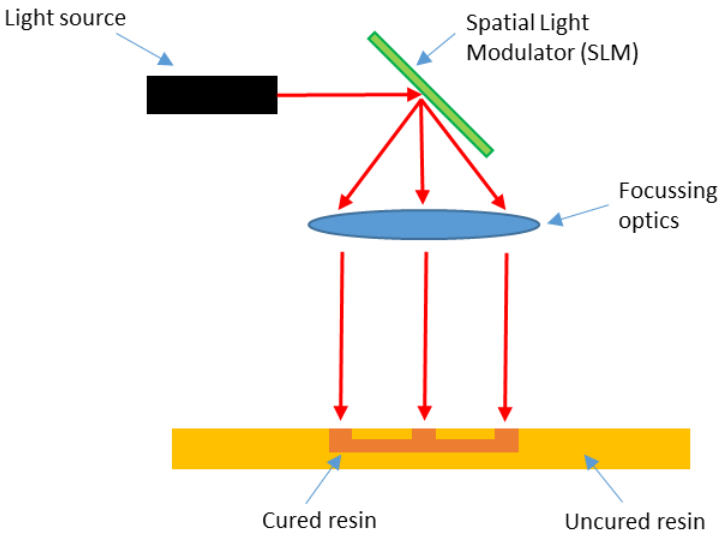

Figure 1.3. Diagram illustrating the method of digital light projection (DLP) as a technique in more modern µSL apparatus displaying its ability to cure different parts of the resin in a parallel manner

The development of another type of SLM device, namely the Digital Micromirror Device (DMD), invented by Texas instruments, was demonstrated to be far superior to LCD SLMs and is now found in most projectors.[33] Not only is the DMD more compatible with UV light, it is also capable of achieving a higher resolution (smaller pixel size) with a shorter switching time. Sun *et al*. demonstrated its ability as a dynamic mask generator and showed that it was capable of high resolution µSL, producing parts with minimum feature sizes on the order of tens of microns.[31] The dynamic mask projection technology utilising a DMD equipped projector, is now given the term Digital Light Projection (DLP) and is currently the technology of choice for most µSL apparatus manufacturers.

1.2.3. Constrained and Free Surface Variations in µSL

Both DLW and DLP can be further classified into two further sub-categories depending on the configuration of the µSL apparatus.[34] The first and more traditional being the 'free surface' configuration whereby the surface of the resin that is being irradiated by the light source is open to the air (**Figure 1.4**).

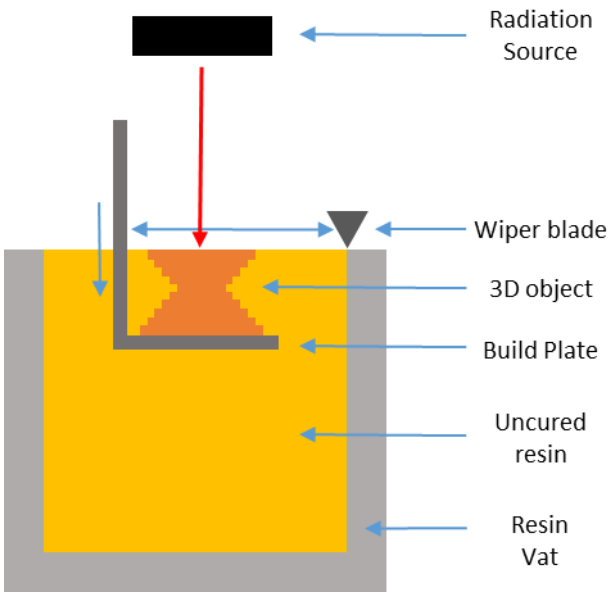

Figure 1.4. Diagram illustrating the key components within the 'free surface' (top down) µSL configuration.

In this configuration, as each layer is consecutively cured, the build plate moves down into the resin vat by a distance equal to one layer thickness of the part being manufactured. A wiper blade then recoats the surface of the part with surrounding resin ready for the next layer to be cured. Whilst this configuration has shown to be effective at producing accurate parts, there are several limitations.[35] Firstly, the size of the part to be produced is restricted by the size of the resin vat used which means much more resin is required to fill such large vats. Secondly, achieving control over layer thickness utilising the free surface method can be difficult because of the convex shape in which the top layer is held, as a consequence of surface tension. Furthermore, a longer waiting time between layers is required for the movement of resin to reach equilibrium after re-coating with the wiper blade. This configuration is often referred to as 'top down' since the radiation source irradiated from the top of the part is directed downwards.

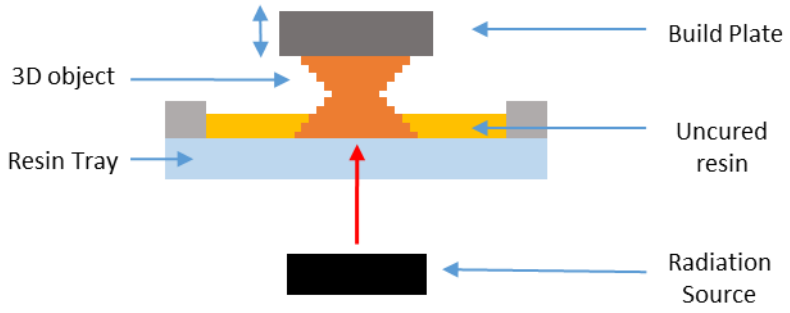

Figure 1.5. Diagram illustrating the key components within the 'constrained surface' (bottom up) µSL configuration.

The second configuration is known as 'constrained surface' as the surface of the uncured resin is at a constrained interface between resin tray and the 3D object (**Figure 1.5**). In this configuration, 3D objects are built upside down and as each layer is cured, the build plate moves up by a distance equal to one layer thickness. The resin then flows beneath the part being built and a subsequent layer of resin is cured.[34] This configuration is often referred to as 'bottom up' since the resin is illuminated from beneath through an optically clear resin tray. Whilst this configuration overcomes some of the limitations of the 'free surface' configuration such as; requiring less resin within a tray rather than a vat, more control over layer thickness and decreased wait times between resin reflowing, it is known to have one inherent drawback.[36] As a consequence of curing the resin between two interfaces, it is essential that the material adheres preferentially to the build plate rather than the resin tray so as to avoid failed prints. There have been several directions taken to avoid the part preferentially adhering to the tray rather than the build plate such as the use of non-adhering materials (e.g. PDMS) on the surface of the resin tray in combination with a peel/sliding mechanism that reduces the adhesion forces across the entire surface area of the part.[37-38] More recently, Tumblestone *et al.* developed Continuous Liquid Interface Production (CLIP) 3D printing, an analogue of µSL, that avoids any adhesion

between cured material and the resin tray whilst still using the 'constrained surface' configuration and is described in more detail in the next section.[39]

1.2.4. Continuous Liquid Interface Production (CLIP) 3D printing

CLIP 3D printing was initially developed to decrease the undesirable substantial build times associated with µSL because of the traditional stepwise, layer-by-layer approach. By using an oxygen permeable resin tray, Tumblestone *et al.* were able to use the normally disadvantageous oxygen inhibition process to their advantage in creating a very thin layer (described as a "dead zone") above the resin tray within which no curing of material can occur (**Figure 1.6**).[39] This "dead zone" was found to be approximately tens of microns thick and still enabled the resin above it to cure and adhere to the build plate/layer of cured material above. In creating this "dead zone" they removed the requirement for any form of peel mechanism between layers, thereby demonstrating the ability to remove any undesirable resin tray adhesion. Furthermore, by removing any mechanical limitations to the printing process, the only factors remaining that limit the CLIP process are resin viscosity and cure rates. Because of this, the CLIP technology, in combination with DLP based µSL, has demonstrated an ability to build 3D objects by continuously projecting a continuous sequence of UV images in a non-stop process with print times on the order of minutes rather than hours. They were also able to demonstrate improved surface finish since the continuous nature of the process produced parts with more discrete step-marks at z-height resolutions equal to traditional techniques that display distinct step-marks characteristic of a step-by-step process.

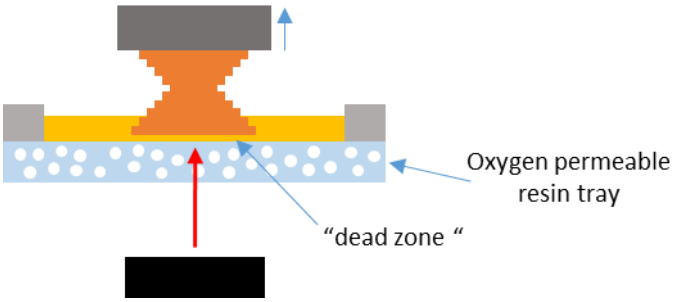

Figure 1.6. Diagram illustrating the oxygen permeable membrane leading to the “dead zone” that allows for speedy, continuous printing in the CLIP process

Unfortunately, the CLIP process is currently only compatible with Carbon 3Ds M1 & M2 3D printers that are only available through an annual subscription. This subscription is immensely costly ($40,000/yr for M1 and $50,000/yr for M2), can only be taken out for a minimum of 3 years and doesn’t include maintenance and upkeep costs. Whilst other companies such as Autodesk and Gizmo3D printers claim that their printers are capable of fast printing at similar speeds to the M1 and M2, the former requires certain adaptations to be made to the printer in order to achieve it, whilst the latter is based on top down configurations and thus suffers from some of the same drawbacks as mentioned in Section 1.2.3. Furthermore, the CLIP process is only compatible with acrylate-based resins that are inhibited by the presence of oxygen therefore restricting the range of materials that can be used.

1.2.5. The µSL Process

The µSL configuration utilised in this thesis was based on a ‘constrained surface’ configuration utilising DLP as the method of curing photosensitive resins. A ‘constrained surface’ configuration was chosen for a number of reasons: not only does it require less complex apparatus (*i.e.* there is no requirement for a wiper blade since layer thickness is controlled by the gap between build plate and resin tray) but it also only requires the use of minimal amounts of resin to achieve small (< 1 cm^3) builds. Utilising minimal resin quantities is ideal when developing new materials because in

the early stages of a materials development, production may only be on a small-scale (on the order of grams), thus filling up a vat for use in the free surface approach is near impossible. Furthermore, whilst optimising the resin, being able to use small quantities for initial printing tests significantly reduces waste, until a final resin composition is decided upon.

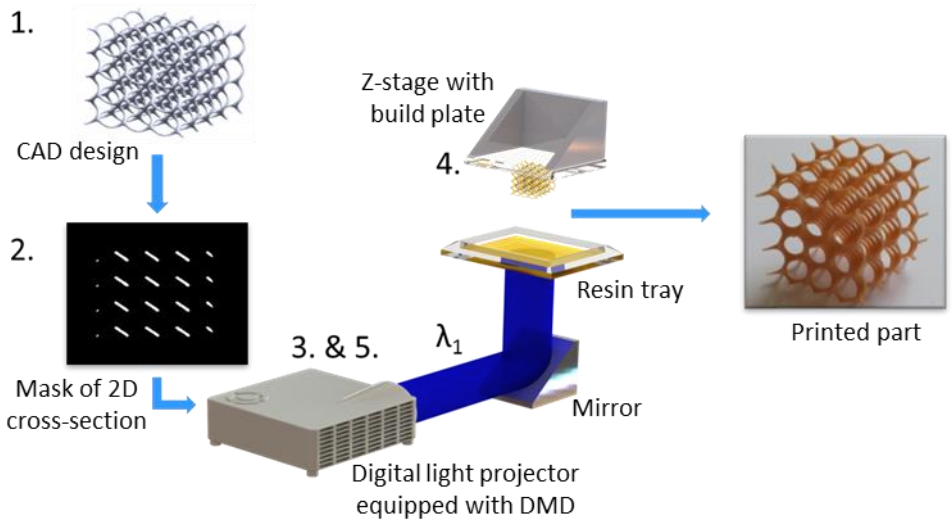

Figure 1.7. Diagram depicting the µSL apparatus and process

The apparatus and process for µSL utilising a 'constrained surface' configuration in combination with a DMD equipped DLP light source are illustrated in **Figure 1.7**. This was the final setup used throughout this thesis and full details of the equipment can be found in chapter 6. The process by which a design is converted to a completed 3D object is outlined below:

1. The 3D model is designed in CAD software and saved as an .STL file
2. The object is digitally sliced into a number of horizontal, cross-sectional 2D images using specialised slicing software. The number of images created is dependent on the desired Z-resolution (*i.e.* number of layers in the z-axis).
3. The images are reproduced *via* a dynamic light projection in order to generate a precise pattern of light (λ_1) on the surface of the photosensitive resin.

4. Once the first layer of resin has been cured with the desired geometry and adhered to the build plate, the build platform is moved upwards by a precise distance (dependent on the layer height chosen) and the process is paused to allow for resin to reflow under the previous layer.
5. Another 2D image is projected and a consecutive layer of resin is cured to the layer above.

Steps 3 to 5 are repeated until the desired 3D object has taken shape and the build is complete. After printing, residual uncured resin will remain on the part. This excess resin is usually removed by a post-print wash in a suitable solvent (usually isopropanol) that does not cause any damage (*e.g.* softening or distortion) to the cured material.[26] Despite the resin being cured sufficiently for the 3D object to have been printed, the resin will not have been completely cured (often referred to the printed part's 'green state') and so a secondary exposure, post-printing, is necessary to make sure the part has been completely cured.[40] The incomplete curing during the printing process is deliberate as to leave behind reactive functionalities in the previous layer for the subsequent layer to react with.

1.2.6. Resin Components

Within the photosensitive resin there are a number of different components that each have their own roles to play, either in the curing process itself or by providing the final printed material with specific properties. These components include, but are not limited to; the functional monomer/oligomer, cross-linker, diluent and photoinitiator. These are explained in more detail in their respective sections below.

Functional monomer/oligomer

The functional monomer/oligomer usually makes up the majority of the resin as this tends to be the component that provides the desired properties within the printed part. For example, choosing aliphatic oligomers will yield more soft and flexible printed components whilst choosing oligomers containing rigid functionalities such as aromatic groups will cause the printed material to be hard and brittle.[41] For example, Hegde *et al.* have recently demonstrated the ability to print all-aromatic polyimides (pyromellitic dianhydride and 4,4′-oxydianiline) producing parts with excellent thermal stability and outstanding mechanical properties.[42] In contrast, Harri *et al.* have studied the use of aliphatic polyurethanes to produce parts with exceptional elasticity.[43] Monomers/oligomers are inherently utilised rather than polymers because of their lower molecular weight thereby exhibiting characteristically low viscosity.[44] The requirement for resins to have inherently low viscosities is highlighted later in this section under the 'Diluents' heading.

Cross-linker

The cross-linker is a low molecular weight monomer with multiple reactive functionalities (examples of functionalities used are covered in the following section) that is capable of reacting with the monomer/oligomer chosen or indeed, itself, to form a solid network. Without the cross-linker, the monomer would undergo a photoinitiated polymerisation, whilst an oligomer would undergo a photoinitiated chain growth reaction; neither of which is capable of forming a cross-linked network as required by µSL. Whilst there are some exceptions where the oligomers used may be capable of reacting at multiple sites and acting as a cross-linker itself, the use of a separate, lower molecular weight cross-linker is often advantageous in enhancing mechanical properties of the printed material.[45] Leigh *et al.* utilised dipentaerythritol

penta-/hexa-acrylate (DPPHA) as an acrylate based multifunctional cross-linker in their poly(ethylene glycol) diacrylate (PEGDA) based system whereas Barker *et al.* exploited pentaerythritol tetrakis(3-mercaptopropionate) (PT3M) as a four arm thiol based cross-linker in their poly(trimethylene carbonate) (PTMC) based resin.[46-47] Both resins were found to exhibit suitable mechanical properties for use within tissue engineering applications.

Diluent

In µSL, the viscosity of the resin produced is a critical parameter and one that can determinte the difference between the success or failure of a print. Not only are more viscous materials less able to flow they are also slower to cure.[48] Whilst the former significantly slows down the µSL process, the latter can cause inaccuracies in the parts produced. After a layer is cured, the z-stage firstly moves the build plate up from the resin tray to a set distance so that resin can re-flow back underneath the previous layer thus providing material for the next layer to be projected into. If the viscosity of the resin is too high, then the re-flow of the resin will take longer meaning that the wait time between layers needs to be increased leading to lengthier build times.

High viscosity resins will be slower to cure since the movement of oligomers or growing polymer chains will be restricted, which decreases the number of interactions between reactive functionalities. This would require an increased exposure time which would not only increase overall build times but may also cause issues with the accuracy of the print. For instance, although the exposure time required to cure a single layer sufficiently so that it adheres to the layer above may be increased, this increased exposure can also cause over-curing in the x-y plane. If the extent of over-cure is quantified, adjustments can be made in the scaling of the design to account for over-cure.[49]

From the literature, there is a broad range of suitable resin viscosities described for use in µSL, varying from 250 cP for monomeric based resins to 5000 cP for some ceramic-containing resins.[49] There have even been reports of some polymeric-based resins with viscosities as high as 10,000 cP, so although the viscosity of a resin is important, there are also numerous other variables to consider.[50] Some materials, such as polymers, are indeed inherently highly viscous and therefore they must be combined with viscosity modifiers to reduce their viscosity to render them compatible with the µSL process. These viscosity modifiers can be separated into either reactive or non-reactive diluents and whilst both are effective in reducing viscosity, they both have their own associated advantages and disadvantages.

Using too high quantities of a non-reactive diluent can lead to the production of significantly swollen networks thereby creating weaknesses within parts.[51] Although the non-reactive diluent can be removed after printing this can often be quite a laborious process depending on the nature of the diluent chosen. For example, in a recent study by Bochove *et al.* high contents (50 wt%) of propylene carbonate were utilised that took more than 7 days to remove.[52] Furthermore, removal of this non-reactive diluent will also lead to shrinkage of the part produced, meaning that the degree of shrinkage needs to be known in order to design parts (*i.e.* scale up the design of parts) that will ultimately have the desired geometry.[53] The main advantage of using a non-reactive diluent is that it does not react with the oligomer/monomer component and so, providing it can be used in sufficiently low quantities and can be easily removed after printing, it should not interfere with the properties that the oligomer/monomer was chosen for.

A reactive diluent, as the name suggests, reacts with the monomer/oligomer and cross-linker components of the resin and can therefore significantly alter the properties of

the material. Sometimes this can have a desirable outcome, however in the case of degradable materials, using too much of a reactive diluent can impede the degradability of the material as it will incorporate significant amounts of non-degradable component.[49] Additionally, reactive diluents can also be used in combination with oligomer species that contain less-reactive end groups such as the alkene functionalities found in fumarate containing oligomers (*e.g.* polypropylene fumarate or fumarate functionalised PLLA) so as to increase reaction rates making the resin more suitable for processing by µSL.[54-55] For instance, Grijpma *et al.* published a paper describing the photo-crosslinking of various polymers end-capped with the fumarate functionality that took 3 h to photocure under flood illumination.[56] The same authors then applied these materials to µSL however, found that incorporation of N-vinyl-2-pyrrolidone (NVP) as a reactive diluent was required to speed up the photo-crosslinking reaction enough to cure films of resin in the short timescales required by µSL.[55] Therefore, choosing between non-reactive or reactive diluents is a trade-off between how much diluent is necessary to reduce the viscosity of the resin enough to be compatible with µSL and the desired properties of the final part.

Photoinitiator

In order to cross-link the components mentioned above during µSL, the cross-linking reaction must be initiated by an external source of radiation (light in this instance).[41] For this to happen, an initiating species, referred to as a photoinitiator, that can start off this chain reaction when exposed to light is required. Once sufficient energy from a light source is provided to the photoinitiator, it decays to form reactive species that can initiate the curing process. The energy required to do so is governed by the difference in energy between ground and excited states for the photoinitiator in question, and is achieved through absorption of photons.[40] This light absorption (*A*)

can be determined by equation 1.1. whereby ε is the extinction coefficient or molar absorptivity, β is the concentration of the photoinitiator and L is the path length that the light travels before interacting with the photoinitiator containing resin.

$$A = \varepsilon\beta L \qquad (1.1.)$$

Depending on the type of photoinitiator used, the reactive species formed can either be ionic or free radical and so choosing a suitable photoinitiator is very important. If the resin composition in question has reactive functionalities that cross-link *via* a cationic process, then an ionic photoinitiator is required; whereas a radical-generating photoinitiator would be used for a resin system using a free radical mechanism.[41] The wavelength at which maximum absorption occurs for various photoinitiators is of great importance. For instance, utilising a photoinitiator with a peak absorbance in the UV region of the UV-Vis spectrum and no further absorbance peaks in visible range would be ineffective if the light source in the projector only emits visible light. In addition to producing the correct reactive species and having a suitable absorption for the wavelength of the light utilised, the photoinitiator should also possess other qualities. These qualities are; a high solubility within the resin components, a high initiation efficiency, an ability to be stored and not to produce undesirable or toxic products after photoinitiated decay.[40]

The materials developed in this thesis rely solely on the free radical process for forming cross-linked polymer networks and therefore only photoinitiators that form radicals upon excitation were considered for use. Amongst these, there are both photoinitiators that absorb in the UV range of the UV-Vis spectrum and the visible range. Some examples of more commonly used photoinitiators for both are given in **Figure 1.8**.

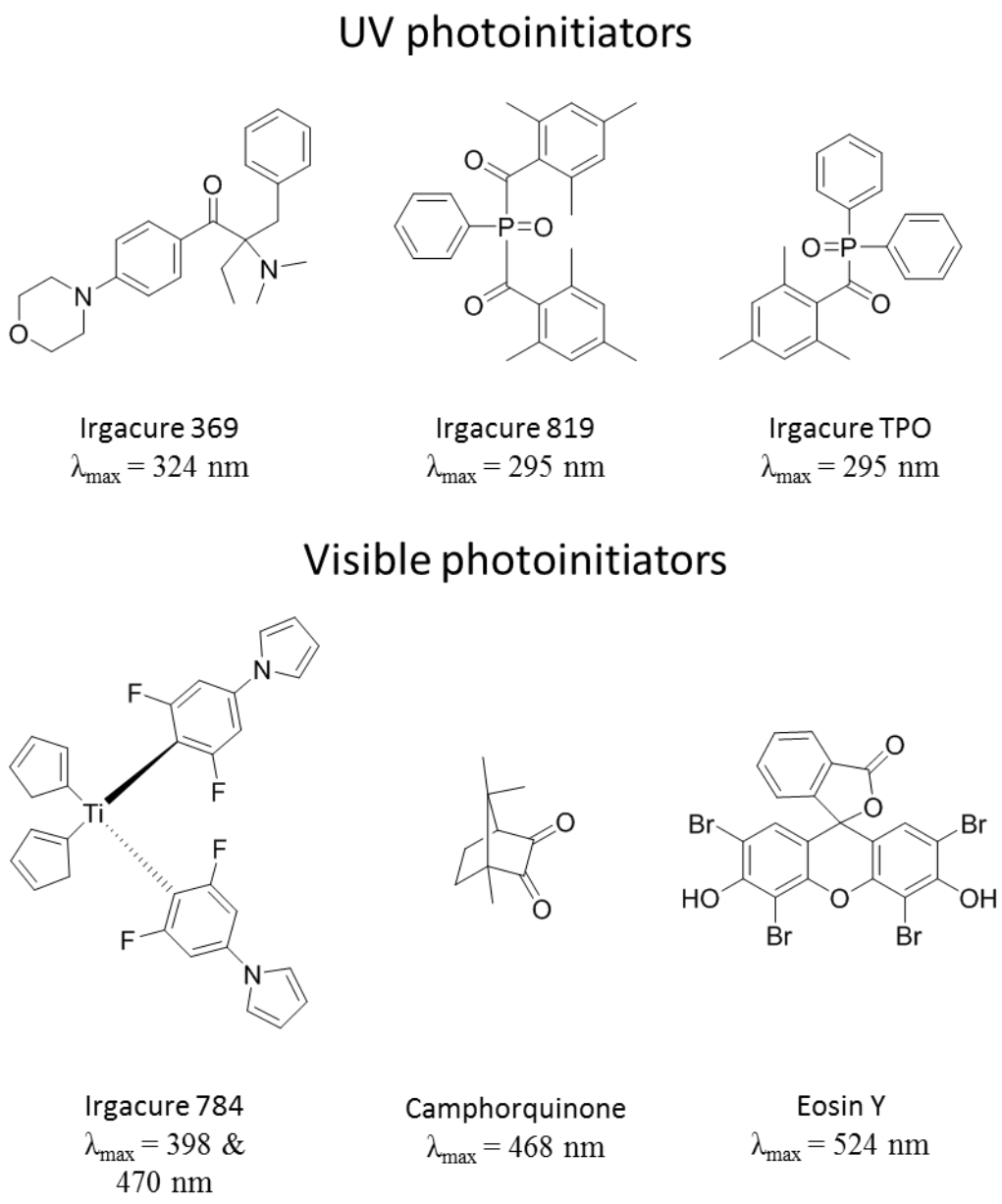

Figure 1.8. Chemical structures of a selection of more commonly used photoinitiators for both UV and visible light based systems

Photoinhibitor

The inclusion of a photoinhibitor may seem counterintuitive after the previous section, however, this is still an important component within µSL resins as they help limit the unfavourable effects of ambient light as well as reduce the degree of overcure caused by uncontrolled diffusion of light through the resin by the projector.[46] Although light travels through the depth of the resin (Z-direction) as is necessary to achieve layer-to-layer adhesion, it is also capable of diffusing out in the horizontal (XY-direction) as a

result of internal reflections in the solidifying resin. This can lead to unwanted overcure of the part in the XY plane which, in some cases can be so severe that adapting the initial design to account for this has little effect. Therefore, photoinhibitors, such as dyes, tend to be used to absorb some of the light that gets reflected, in doing so reducing the amount of overcure and increasing the accuracy of the part. The choice of photoinhibitor can be as difficult as choosing a suitable photoinitiator because they often have similar limitations. For instance, the photoinhibitor is also required to be soluble in the rest of the resin composition and have an absorption maxima close to the wavelength of the light being used. As an example, Paprika extract, a naturally occurring red dye taken from various types of red peppers, has been used as a photoinhibitor in μSL systems that utilise visible, blue light (465 nm), whereas orasol orange, a synthetically made orange dye, is commonly used in UV-based systems.[47, 50]

1.2.7. Chemistry of Components

As mentioned in section 1.2.6., there are two major types of cross-linking chemistries that either rely on ionic or free-radical species to initiate and propagate the cross-linking reaction. Until recently, the majority of photopolymerisable resins used in μSL have contained components with either (meth)acrylate or epoxy functionalities (**Table 1.2**) that rely on free-radical or cationic mechanisms respectively.[26, 55] Whilst the former displays excellent cure rates and is inexpensive, the latter suffers from slow cure rates, is more costly and requires cationic photoinitiators that can be difficult to find for UV based systems.[40] However, unlike (meth)acrylate based resin compositions, epoxy resins are well known to cause less shrinkage in the part produced and be inherently stronger than acrylate counterparts.[57] Guess *et al*. demonstrated that after one irradiation of the same intensity light source on an epoxy and acrylate based

resin, respectively, the former shrunk by 1.4 % whereas the latter shrunk by 1.0 %. However, upon further dosages of the irradiation source the acrylate based resin continued to shrink and improve mechanical properties further whilst the epoxy resin showed negligible differences.[57] The increased mechanical properties are partly because of the nature of epoxy based resins to undergo dark curing whereby the cationic cross-linking reaction continues after irradiation by the light source which is considered negligible in (meth)acrylate systems.[58] Despite these advantages associated with epoxy based materials, the majority of resins developed for µSL are still based on (meth)acrylate chemistry.

Table 1.2. Table illustrating the chemical structures of various reactive components used in µSL resins and their respective advantages

Meth(acrylates)	Epoxides	Thiol-ene
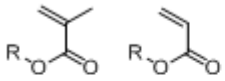		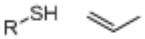
- Rapid curing rates	- Low Shrinkage	- Rapid curing rates
- Inexpensive	- Good mechanical properties	- Biocompatibility
		- Low shrinkage

Barker *et al.* recently demonstrated that thiol-ene based resins (**Table 1.2**) were also capable of being utilised in the µSL process *via* a free radical mechanism.[47] Whilst thiol-ene chemistry relies on different components within the resin having either the thiol or alkene functionality in order to achieve cross-linking, the curing rate and cross-linking efficiency are both excellent. For biomedical purposes, thiol-ene chemistry may also be preferred because unreacted (meth)acrylates are found to be toxic *in vivo*.[46] Thiol-ene chemistry may also be utilised and unlike (meth)acrylates, is not inhibited by the presence of oxygen but at the same time can take advantage of using the same radical generating photoinitiators as (meth)acrylate chemistry that are more readily available.

1.2.8. Combining Resin Components in the Curing Process

Combining each of the various resin components outlined above, in a manner that provides an optimised resin with suitable qualities for printing, in addition to maintaining the desired chemical and physical properties in the final 3D object, can be a difficult process. The ratios in which they are combined are usually governed by numerous factors including desired cure rate, viscosity, cross-linking density and efficiency, mechanical properties and the intended application for the material in question. Taking these factors into consideration, as well as the numerous types of chemical functionalities capable of being used in the cross-linking reaction, it is apparent that there are countless possibilities. Thus, attempting to set some defined rules as to determine what the final resin composition should be would be impractical. There are, however, some exceptions, especially in the case of resins whereby each of the reactive components have different yet mutually reactive functionalities. For example, thiol-ene chemistry relies on there being a stoichiometric equivalence between thiol and alkene functionalities to attain a high cross-linking efficiency. Thus, it is important that the ratio in which components with the alkene functionality are combined with components that contain the thiol functionality is kept to 1:1.

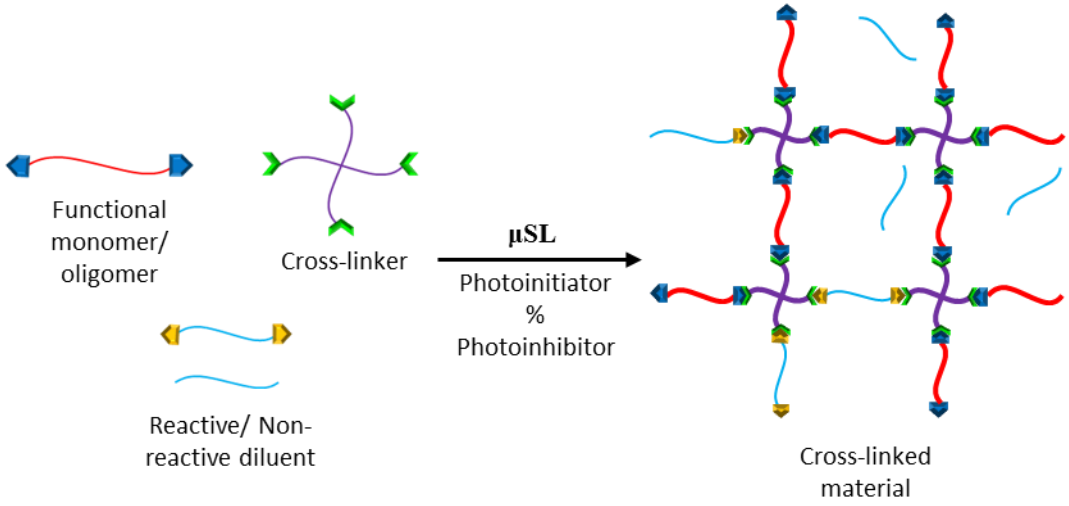

Figure 1.9. Diagram illustrating the various components found in most µSL resins and how they come together to form a cross-linked material

Despite the number of variations in resin composition, once a resin is optimised and ready to be processed by μSL, they all undergo a similar curing process (**Figure 1.9**). Upon application of energy to the photoinitiator within the resin by the light source, reactive species are generated that initiate the cross-linking reaction. Initially, the viscosity of the resin increases until it can no longer flow; at which point two phases coexist; a gel phase and a sol phase.[40] The sol phase remains soluble whilst the gel phase is cross-linked and remains insoluble in non-degrading solvents. Upon further cross-linking, the gel phase becomes more prominent and the viscosity increases significantly until the gel point is reached. This overall increase in viscosity reduces the mobility of the growing chains and cross-linked material, thereby causing the photoreaction to convert from being kinetically controlled at a low degree of cross-linking to being diffusion controlled at a high degree of cross-linking.

1.3. Materials Used in μSL and Their Applications

1.3.1. Commercially available resins

In a similar manner to other additive manufacturing technologies, the majority of commercially available materials developed for use in μSL have been focused on prototyping applications. The nature of μSL to be mainly suited to rapid prototyping was originally because of the brittle nature of cross-linked materials causing the fabricated parts to have relatively poor mechanical properties causing them to be unsuitable for making functional, end-user products.[26] Despite these materials being brittle and lacking functionality, they have found application in several fields including the production of orthodontic, artistic and surgical models. More recently, some of the key μSL companies have developed their scope of materials to encompass a broader range of properties that make the technology far more suitable for producing functional, end-user parts. For instance, the likes of 3D Systems, envisionTEC and

Formlabs have all introduced resins to the market capable of incorporating elasticity, high temperature resistance and casting abilities into their range of materials, thereby expanding the number and type of applications µSL can be exploited for. Some of these materials are listed in **Table 1.3**.

Table 1.3. Table presenting a selection of the various types of commercially available materials, their developers, the resin composition, the ultimate tensile strength of the printed material, the viscosity of the resin and their intended application.

Company	Resin	Resin components	Material UTS (Mpa) / Resin Viscosity(cP)	Applications
envisionTEC	R11 (std prototyping)	HDDA, acrylates	50 / NA	Consumer goods, education, manufacturing
envisionTEC	E-model flex (flexible)	unknown	55-60 / NA	Aerospace, automotive, consumer goods, medical devices
envisionTEC	EPIC (casting)	unknown	NA / NA	Investment casting
envisionTEC	Photosilver (high temp)	HDDA, Isobornyl acrylate, acrylates, TiO_2	NA / NA	Production of vulcanized rubber moulds
3Dsystems	Accura 55 (std prototyping)	unknown	63-68 / 155-185	Functional assemblies, shortrun production parts
3Dsystems	Accura Xtreme (high temp)	unknown	45-50 / 650-750	Snap fits & assemblies, master patterns for vacuum casting
3Dsystems	Accura 25 (flexible)	unknown	55-58 / 250	Snap fits & assemblies, master patterns for vacuum casting, durable & functional prototypes
3Dsystems	Visijet M3 procast (casting)	unknown	32 / NA	Investment casting
Formlabs	Standard resin (std prototyping)	Methacrylated monomers/oligomers	65 / NA	Rapid prototyping & product developement
Formlabs	High temperature	(Meth)acrylated monomers/oligomers	51.1 / NA	Mold prototyping, heat resistant fixings, hot air & fluid flow, environmental testing
Formlabs	Flexible resin	Multifunctional acrylated oligomers, acrylated monomers	7.7-8.5 / NA	Handles, grips & overmolds, cushioning & dampening, wearables, prototyping, packaging stamps
Formlabs	Durable resin	(meth)acrylated oligomers & monomers	31.8 / NA	Prototyping, impact resistant casings, low friction & low-wear moving parts, snap fits & ball joints
Photocentric	Hard resin	Bisphenol a ethoxylate dimethacrylate, acrylates	42 / 230	Not stated
Photocentric	Flexible resin	2-[[(butylamino)carbonyl]oxy]ethyl acrylate, acrylates	4.9 / 200	Not stated

Unfortunately, some companies such as 3D Systems and envisionTEC work within a closed ecosystem whereby they only allow for their own branded resins to be used on their own machines. By doing so, the target market for such companies is often restricted to the industrial sector since the likes of hobbyists cannot afford such expensive equipment and materials. Moreover, researchers endeavouring to develop new materials are not able to test how successfully they can be processed by µSL using these commercially available machines. There are, however, a few companies that aim to make the µSL technology not only more accessible but also more affordable. For instance, Formlabs, a company created in 2011, sell a DLW based µSL printer at a more affordable price (< £4000) in addition to allowing users the use of third party resins or indeed to develop their own resins rather than Formlabs own brand. More recently, Photocentric 3D (a photopolymer company that entered the µSL field in 2013), aimed to develop affordable machines based on DLP and even more affordable resins for use not only in their own printers but others that permit the use of third-party resins. The resins developed by Formlabs and Photocentric are nearly half and one-fifth of the price of resins sold by envisionTEC, respectively. Considering that the inherent properties and functionalities of the materials produced by Formlabs and Photocentric are not all that different to their more expensive counterparts, it is of no surprise that µSL is becoming more accessible. So much so that µSL-capable machines are now found on desktops in both workspaces and homes and are becoming part of day-to-day life for designers, engineers, jewellers and hobbyists.

1.3.2. Non-commercially available resins

Despite numerous attempts by industry to develop materials with a broader range of properties and functionalities, there are still only four key functions that have been accommodated for. These include standard hard materials for prototyping, high

temperature materials capable of being utilised in molding processes and high temperature environments, flexible materials that have shown promise in some biomedical applications and finally, materials for investment casting. To expand upon this limited scope of materials, researchers have continued to add their findings to a wealth of literature encompassing a plethora of innovative and functional materials for which their compatibility with the µSL process has been demonstrated. These materials can be split into three categories; polymer, composites and hydrogels all of which have their own properties and have found their own niche in several important applications such as the production of tissue engineering scaffolds and piezoelectric devices. The following sections aim to give a brief overview of the current state-of-the-art in each of these categories in addition to describing the potential scope of applications that each material is intended for. **Table 1.4** lists some of the materials developed and published by members of the research community with their respective intended applications.

Table 1.4. Table listing some of the materials found in the literature alongside their intended application(s)

Category	Resin components	Authors	Applications	Ref
Polymer	PPF/DEF	Cooke *et al*	TE – Initial fabrication of simple constructs	64
Polymer	PPF/DEF	Lee *et al*	TES – effect of formulation & pore size investigation	53
Polymer	PPF/DEF	Walker *et al*	TES – Effect of porosity on *in vitro* degradation	67
Polymer	PPF/DEF + PLGA microspheres	J.W.Lee *et al*	TES + DD – sustained release of growth factors from microspheres to promote bone regrowth	75
Composite	PPF/DEF-HA	J.W.Lee *et al*	TES – Increased bioactivity with HA powder providing nano/microscale topology	86
Polymer	PCL + PTMC	Matsuda *et al*	DD – microneedles and other constructs coated with anti-inflammatory drugs	78
Polymer	P(depsipeptide-*co*-CL)	Elomaa *et al*	TES – incorporation of depsipeptide increases hydrophilicity + accelerates degradation	68
Composite	PCL + Bioactive glass	Elomaa *et al*	TES – presence of bioactive glass increases bioactivity	81
Polymer	PEGDA/DPPHA	Leigh *et al*	TES – cellular constructs for regenerative medicine	45
Composite	PEGDA + Magnetic nanospheres	Santis *et al*	TES – capable of absorbing magnetic material from surrounding solution	85
Composite	PEGDA + $AgNO_3$	Fantino *et al*	Electircal conductivity – study of resistance and conductivity at varying temperatures	87
Hydrogel	PEG/acrylic-PEG collagen	Chan *et al*	Functional microdevices – fabrication of Actuators and Cantilevers	93
Hydrogel	PEG/PDLLA	Seck *et al*	TES + DD + Cell-transplantation – fabricated porous structures with excellent biocompatiblity.	91
Polymer	PDDLA/NVP	Jansen *et al*	TES – Avoids potentially toxic acrylate functionality	54
Polymer	PDMMA/PMMA	Stampfl *et al*	Fabrication of water soluble moulds	83
Hydrogel/ Composite	PTMC/PEG + laponite nanoclay	Sharifi *et al*	TE – incorporation of nanoclay to hydrogels to increase mechanical properties	92
Polymer	PTMC	Barker *et al*	TES – first resin to utilise more biocompatible thio-ene cross-linking chemistry	46
Polymer	PTMC	Schu¨ller-Ravoo *et al*	TES – production of exceptionally flexible structures	49

Polymers

Over the past two decades there have been several advances in the use of polymers within stereolithographic resins. Initially, higher molecular weight macromers and

oligomers were introduced to impart more desirable mechanical properties over previous resin formulations that contained low molecular weight, multifunctional monomers and produced materials that were primarily rigid and glassy by nature.[50] Because of this improvement in mechanical properties towards more elastomeric materials, the number of applications for parts made by µSL has increased, with most polymeric based resins finding use within applications in the biomedical field. For instance, when used in combination with clinical imaging techniques such as MRI or CT scanning, µSL can be used to produce patient specific surgical models for surgeons to study, thereby speeding up procedures, in addition to helping create one-off patient specific implants.[59-61]

One application that has received much attention in the literature is the production of scaffolds in the field of tissue engineering.[61] Such scaffolds are utilised in order to form a temporary structure or template throughout which, cells can be seeded and hence tissues regenerated either *in vivo* or *in vitro*. A key requirement for *in vivo* scaffolds is that they should be entirely resorbable by the human body either after the regeneration of tissue or, more ideally, at a rate that matches the growth of new tissue.[62] To achieve this, the scaffolds must be made from materials that contain hydrolytically and enzymatically degradable carbonate or ester bonds that degrade into non-toxic degradation products in addition to avoiding causing any sort of inflammatory response.[63] The first biodegradable polymer for use in µSL was that of poly(ε-caprolactone-*co*-trimethylene carbonate) developed by Matsuda *et al*. in 2000.[64] Since then, there have been a number of other biodegradable resins developed based on different ester or carbonate based polymers including poly(DL-lactide) PDLLA, poly(propylene fumarate) (PPF) and other variations of poly(ε-caprolactone)

(PCL) and poly(trimethylene carbonate) (PTMC).[49-50, 53, 55, 65-71] The structures of these polymers are shown in **Figure 1.10**.

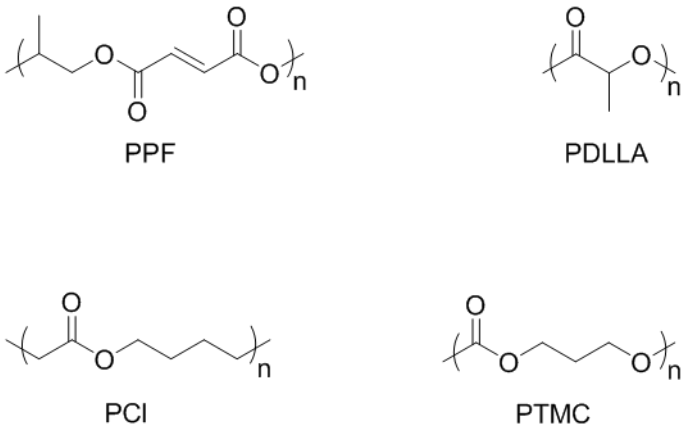

Figure 1.10. Chemical structures of degradable polymers utilised in µSL

Due to its rigidity, strength and inherent biodegradability PDLLA has been widely exploited in bone tissue engineering applications.[72-74] The work carried out by Melchels *et al.* utilised methacrylate end-functionalised PDLLA oligomers in combination with ethyl lactate as a non-reactive diluent.[49] A dynamic mask-based µSL system was employed in order to generate porous, gyroid structures with high resolution and the material was found to readily adhere and proliferate mouse pre-osteoblasts. In similar research carried out by Jansen *et al*. fumaric acid monoethyl ester (FAME) end-functionalised PDLLA oligomers are photo-cross-linked by a digital mask-based projection system in order to fabricate precise, gyroid tissue engineering scaffolds.[55] FAME was incorporated since its degradation product, fumaric acid, is naturally found in the body. As previously mentioned in section 1.2.6, NVP was utilised as a reactive diluent and the ratio of which could be altered in order to tune both the mechanical and water uptake properties.

PPF is an unsaturated linear polyester and is susceptible to degradation *via* hydrolysis of the ester bonds into the respective non-toxic degradation by-products, fumaric acid and propylene glycol.[75] Lee *et al.* have pioneered the majority of the research utilising

PPF in the fabrication of tissue engineering scaffolds.[76] Their research includes optimising control over pore architecture within the scaffold as well as producing scaffolds capable of delivering growth factors in the form of a suspension of microspheres and PPF/DEF macromers where the microspheres are poly(DL-lactic-*co*-glycolic acid) (PLGA) loaded with bone morphogenetic protein-2 (BMP-2).[75-76] The geometries of the scaffolds produced were restricted to simple shapes due to difficulties in the 3D fabrication of interconnecting channels. These difficulties were a consequence of the defocussing problem faced by DLW μSL. Although some synthetic polymers such as PPF exhibit biocompatibility, they tend to be hydrophobic and therefore not bioactive.[27] By coating fabricated PPF scaffolds with biologically recognised amino acid sequences such as Arg-Gly-Asp (RGD), cyclo RGD and a mixture of RGD-KRSR (lysine-arginine-serine-arginine), Shin *et al.* were able to achieve surface modification leading to enhanced cell adhesion, differentiation and proliferation providing improved bioactivity.[77]

Scaffolds made from PTMC based resins tend to exhibit more mechanical flexibility when compared with their PPF counterparts, making them less suitable for skeletal tissue engineering but more suitable for soft tissue applications. As well as the work utilising PTMC and PCL, Matsuda *et al.* have also polymerised methacrylate end-capped PTMC onto low molecular weight poly(ethylene glycol) or trimethylolpropane (TMP) in order to create a photo-polymerisable liquid resin.[78] The material using TMP displayed a high degree of cell adhesion and proliferation. Lee *et al*. also used a combination of PTMC and TMP alongside a DLW μSL system in order to generate 3D scaffolds with controllable reproducible inner architecture.[79] This work demonstrated the significance of using staggered lattice type scaffolds, instead of previously reported simple rectangular pore shapes, in order to achieve greater cell

adhesion and viability. More recently, Ravoo *et al*. have optimized the use of PTMC in combination with a DLP-based µSL system in order to fabricate both porous and non-porous complex 3D structures. Elevated temperatures, >60 °C, and propylene carbonate, as a non-reactive diluent, were employed to tune the viscosity of the resin to be compatible with the µSL process. They were able to produce high resolution, highly complex gyroid pore 3D architectures with mechanical properties suitable for tissue engineering applications (elongations at break >900%).[50] In a later paper, Ravoo *et al*. studied the biocompatibility of the same materials and found that complete coverage of the scaffolds with bovine chondrocytes was achieved after 6 weeks.[71] In addition, they also discovered that the compression moduli of fully coated structures increased by 50 %.

PCl is a highly biocompatible and elastic polymer that has been identified as having tuneable degradation kinetics as well as adjustable physical and mechanical properties.[80] Aside from the pioneering work of Matsuda *et al.*, Elomaa *et al*. are the only group developing PCl-based material scaffolds for µSL applications.[69-70, 81] In their work, methacrylic anhydride end-functionalised, three-armed PCL oligomers with varying molecular weights were photo-cross-linked by µSL forming cylindrical structures with a gyroid pore network as well as cuboidal structures with a diamond pore network.[70] The application of heat to the resin to obtain a suitable viscosity meant no solvent diluent was used leading to minimal shrinkage after extraction and drying. As a result, the dimensions and geometry of the structures formed closely matched the modelled structures produced by CAD. More recently, Elomaa *et al*. have utilised the same resin system in combination with a bioactive glass which is known to promote interactions of cells on polymeric tissue engineering scaffolds.[81] The bioactive glass was homogeneously incorporated throughout the 3D structures by mixing the PCl

macromer with varying weight percentages of bioactive glass powder. The bioactive glass inclusions resulted in improved bioactivity and enhancement in the attachment and proliferation of human fibroblasts.

Whilst the majority of research in this area has focussed on the generation of devices for tissue engineering (**Figure 1.11**, **A**) there has been some mention of biodegradable materials being utilised in other biomedical applications such as the fabrication of microneedles (**Figure 1.11**, **B**) and other drug administering devices.[82] Additionally there are a few examples of resins produced for non-biomedical devices such as the poly(methylmethacrylate) PMMA based resin developed by Stampfl *et al.*to fabricate water soluble moulds for rapid prototyping applications.[83]

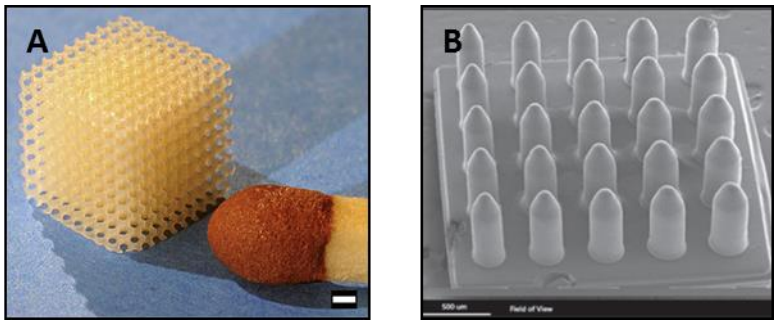

Figure 1.11. Images of a tissue engineering device made from PDLLA (A) and a microneedle array made from PPF (B)[48, 82]

Composites

Polymer/multifunctional monomer-ceramic composite resins have been developed in order to produce parts with enhanced properties such as increasing their mechanical strength and stiffness, improving a materials' biocompatibility by generating nano/microscale topology and even imparting electrical conductivity or magnetism.[81, 84-87] Whilst using ceramic composites can bestow such desirable properties within a part, adding ceramic particles to a stereolithographic resin can lead to difficulties in processing, such as increasing the viscosity of the resin and causing increased light scattering and absorption therefore restricting the layer height.[84] Despite these

difficulties, there have been a number of examples in the literature of parts fabricated with high ceramic particle loadings of greater than 80% and some have even been sintered to remove the surrounding polymer matrix to leave behind an all-ceramic device.[22, 84]

Devices made from polymer-ceramic composites have found application in the likes of tissue engineering scaffolds (especially for hard tissues such as bone) and piezo electrics.[51, 88-89] For instance, Woodward *et al.* demonstrated the ability to produce piezoelectric devices capable of emitting ultrasound in the MHz range utilising a HDDA/DPPHA based resin containing high incorporations of piezoelectric materials (**Figure 1.12**, **A**).[89] Other research carried out by Ronca *et al.* examined the use of hydroxyapatite (HA)-loaded PDLLA-based resins to better mimic the hard, calcium phosphate-containing biological tissues in doing so they not only increased the bioactivity but also the strength of the structures produced compared with solely PDLLA based materials (**Figure 1.12**, **B**).[51]

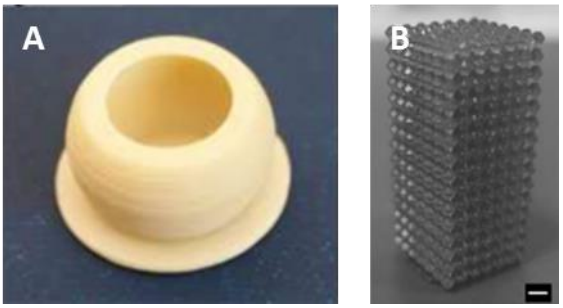

Figure 1.12. Images of the piezoelectric devices produced by Woodward *et al*. (A) and the tissue engineering scaffold made by Ronca *et al*. (B)

Hydrogels

Hydrogels are hydrophilic, polymer networks that are water insoluble and yet capable of absorbing thousands of times their dry weight in water (**Figure 1.13**).[90] This high-water content makes them relatively non-viscous rendering them suitable for processing by µSL in addition to making them more akin to the native Extra Cellular

Matrix (ECM) thereby enhancing their suitability within biomedical applications. It is therefore unsurprising that there are several examples of 3D printed hydrogel structures made using the µSL technique in the literature with the majority being applied in the biomedical field.[91-93] To date, the majority of resins developed to produce hydrogel structures contain PEG because of its hydrophilicity and subsequent biocompatibility. In fact, the biocompatibility of these structures was proven to be so good that even live cells could be encapsulated during the printing process.[93]

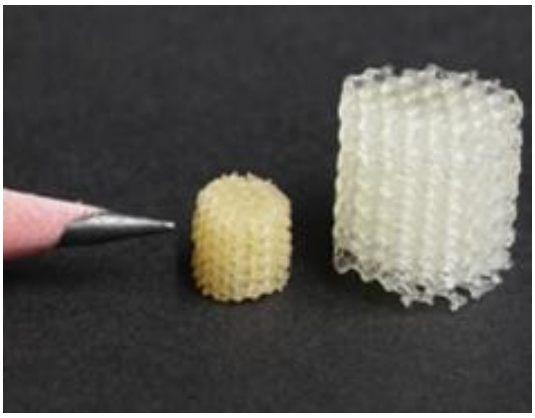

Figure 1.13. Image demonstrating the swelling ability of a hydrogel scaffold made by µSL

Unfortunately, solely PEG based hydrogels are non-degradable and so Seck *et al.* and Sharifi *et al.* have copolymerised it with degradable PDLLA or PTMC blocks, respectively, to make it more suitable for use in biomedical applications such as tissue engineering where biodegradability is desirable.[91-92] However, the incorporation of such hydrophobic polymers can cause decreased hydrophilicity and thus Seck *et al.* were forced to create initial structures utilising a combination of both organic and aqueous solutions.[91] Additionally, the relatively low mechanical strength of such hydrogel materials caused by their high-water contents makes them more suitable for the likes of soft tissue engineering applications and studying cell-cell interactions.

1.4. Conclusions

In conclusion, the prior and ongoing technological developments in the field of μSL have made it more accessible than ever before with some printers being so affordable that they are beginning to appear in the homes of the everyday hobbyist. Whilst commercially available materials provided by the likes of Formlabs and envisionTEC more than suit the needs of hobbyists and the majority of the current market, there still lie a few sectors that it does not cater for. For instance, the only sectors covered within the biomedical field are those of dentistry, hearing aid manufacture and the production of surgical models that aid surgeons prior to carrying out procedures, thereby ignoring the requirement for implantable materials.

The development of degradable materials for use within μSL is clearly overlooked within industry but has, to a certain extent, been an area of key interest in the research community for the development of tissue engineering constructs in the first instance but also in the development of some drug administering devices. The versatility of the technique towards these different materials has allowed structures with varying mechanical properties and functionality to be produced, however, despite the efforts of numerous research groups, the overall lack of readily available biodegradable materials is still considered one of the key drawbacks to the technique. Furthermore, the majority of the current state-of-the-art only consists of materials that have pre-determined mechanical properties and functionalities. Although there have been some examples of 4D materials (covered in chapter 2) capable of undergoing changes in functionality and properties after the printing process, this exciting new avenue for material development is still in its infancy and thus, requires more attention from industry and researchers alike.

1.5. References

1. Kruth, J. P.; Leu, M. C.; Nakagawa, T., Progress in Additive Manufacturing and Rapid Prototyping. *CIRP Annals - Manufacturing Technology* **1998,** *47* (2), 525-540.

2. Conner, B. P.; Manogharan, G. P.; Martof, A. N.; Rodomsky, L. M.; Rodomsky, C. M.; Jordan, D. C.; Limperos, J. W., Making sense of 3-D printing: Creating a map of additive manufacturing products and services. *Additive Manufacturing* **2014,** *1–4*, 64-76.

3. Sachs, E.; Cima, M.; Cornie, J., Three-Dimensional Printing: Rapid Tooling and Prototypes Directly from a CAD Model. *CIRP Annals - Manufacturing Technology* **1990,** *39* (1), 201-204.

4. Huang, Y.; Leu, M. C.; Mazumder, J.; Donmez, A., Additive Manufacturing: Current State, Future Potential, Gaps and Needs, and Recommendations. *J. Manuf. Sci. Eng.* **2015,** *137* (1), 014001-014010.

5. Calignano, F.; Manfredi, D.; Ambrosio, E. P.; Biamino, S.; Lombardi, M.; Atzeni, E.; Salmi, A.; Minetola, P.; Iuliano, L.; Fino, P., Overview on Additive Manufacturing Technologies. *Proceedings of the IEEE* **2017,** *105* (4), 593-612.

6. Drizo, A.; Pegna, J., Environmental impacts of rapid prototyping: an overview of research to date. *Rapid Prototyping Journal* **2006,** *12* (2), 64-71.

7. Petrovic, V.; Vicente Haro Gonzalez, J.; Jordá Ferrando, O.; Delgado Gordillo, J.; Ramón Blasco Puchades, J.; Portolés Griñan, L., Additive layered manufacturing: sectors of industrial application shown through case studies. *Int. J. Prod. Res.* **2011,** *49* (4), 1061-1079.

8. Levy, G. N.; Schindel, R.; Kruth, J. P., Rapid manufacturing and rapid tooling with layer manufacturing (LM) technologies, state of the art and future perspectives. *CIRP Ann-Manuf. Technol.* **2003,** *52* (2), 589-609.

9. Ding, D.; Pan, Z.; Cuiuri, D.; Li, H., Wire-feed additive manufacturing of metal components: technologies, developments and future interests. *Int. J. Adv. Manuf. Tech.* **2015,** *81* (1), 465-481.

10. Lim, C. W. J.; Le, K. Q.; Lu, Q.; Wong, C. H., An Overview of 3-D Printing in Manufacturing, Aerospace, and Automotive Industries. *IEEE Potentials* **2016,** *35* (4), 18-22.

11. Schiller, G. J. In *Additive manufacturing for Aerospace*, 2015 IEEE Aerospace Conference, 7-14 March 2015; 2015; pp 1-8.

12. Saripalle, S.; Maker, H.; Bush, A.; Lundman, N. In *3D printing for disaster preparedness: Making life-saving supplies on-site, on-demand, on-time*, 2016 IEEE Global Humanitarian Technology Conference (GHTC), 13-16 Oct. 2016; 2016; pp 205-208.

13. Lim, S.; Buswell, R. A.; Le, T. T.; Austin, S. A.; Gibb, A. G. F.; Thorpe, T., Developments in construction-scale additive manufacturing processes. *Automation in Construction* **2012,** *21*, 262-268.

14. Dippenaar, D. J.; Schreve, K., 3D printed tooling for vacuum-assisted resin transfer moulding. *Int. J. Adv. Manuf. Tech.* **2013,** *64* (5), 755-767.

15. Murphy, S. V.; Atala, A., 3D bioprinting of tissues and organs. *Nat. Biotech.* **2014,** *32* (8), 773-785.

16. Mota, C.; Puppi, D.; Chiellini, F.; Chiellini, E., Additive manufacturing techniques for the production of tissue engineering constructs. *J. Tissue. Eng. Regen. Med.* **2015,** *9* (3), 174-190.

17. A printed smile. https://www.economist.com/news/science-and-technology/21697802-3d-printing-coming-age-manufacturing-technique-printed-smile (accessed 14/07/2017).

18. Kodama, H., Automatic method for fabricating a three-dimensional plastic model with photo-hardening polymer. *Review of Scientific Instruments* **1981,** *52* (11), 1770-1773.

19. Hull, C. W. Apparatus for production of three-dimensional objects by stereolithography. 4575330, 11th March, 1986.

20. Nayar, S.; Bhuminathan, S.; Bhat, W. M., Rapid prototyping and stereolithography in dentistry. *J. Pharm. Bioallied. Sci.* **2015,** *7* (1), 216-219.

21. Reeves, P.; Tuck, C.; Hague, R., Additive Manufacturing for Mass Customization. In *Mass Customization: Engineering and Managing Global Operations*, Fogliatto, F. S.; da Silveira, G. J. C., Eds. Springer London: London, 2011; pp 275-289.

22. Zhang, X.; Jiang, X. N.; Sun, C., Micro-stereolithography of polymeric and ceramic microstructures. *Sensors and Actuators A: Physical* **1999,** *77* (2), 149-156.

23. Bertsch, A.; Heimgartner, S.; Cousseau, P.; Renaud, P., Static micromixers based on large-scale industrial mixer geometry. *Lab on a Chip* **2001,** *1* (1), 56-60.

24. Lee, W.; Kwon, D.; Choi, W.; Jung, G. Y.; Au, A. K.; Folch, A.; Jeon, S., 3D-Printed Microfluidic Device for the Detection of Pathogenic Bacteria Using Size-based Separation in Helical Channel with Trapezoid Cross-Section. *Sci. Rep.* **2015,** *5* (7717), 1-6.

25. van Lith, R.; Baker, E.; Ware, H.; Yang, J.; Farsheed, A. C.; Sun, C.; Ameer, G., 3D-Printing Strong High-Resolution Antioxidant Bioresorbable Vascular Stents. *Adv. Mat. Tech.* **2016,** *1* (9), 1600138.

26. Melchels, F. P.; Feijen, J.; Grijpma, D. W., A review on stereolithography and its applications in biomedical engineering. *Biomaterials* **2010,** *31* (24), 6121-6130.

27. Pereira, R. F.; Bártolo, P. J., Photocrosslinkable Materials for the Fabrication of Tissue-Engineered Constructs by Stereolithography. In *Tissue Engineering: Computer Modeling, Biofabrication and Cell Behavior*, Fernandes, P. R.; Bartolo, P. J., Eds. Springer Netherlands: Dordrecht, 2014; pp 149-178.

28. Stampfl, J.; Baudis, S.; Heller, C.; Liska, R.; Neumeister, A.; Kling, R.; Ostendorf, A.; Spitzbart, M., Photopolymers with tunable mechanical properties processed by laser-based high-resolution stereolithography. *J. Micromech. Microeng.* **2008,** *18* (12), 1-9.

29. Ikuta, K.; Maruo, S.; Kojima, S. In *New micro stereo lithography for freely movable 3D micro structure-super IH process with submicron resolution*, Proceedings MEMS 98. IEEE. Eleventh Annual International Workshop on Micro Electro Mechanical Systems. An Investigation of Micro Structures, Sensors, Actuators, Machines and Systems 25-29 Jan 1998; 1998; pp 290-295.

30. Takagi, T.; Nakajima, N. In *Photoforming applied to fine machining*, Proceedings IEEE Micro Electro Mechanical Systems, 7-10 Feb 1993; pp 173-178.

31. Sun, C.; Fang, N.; Wu, D. M.; Zhang, X., Projection micro-stereolithography using digital micro-mirror dynamic mask. *Sensors and Actuators A: Physical* **2005,** *121* (1), 113-120.

32. Bertsch, A.; Jézéquel, J. Y.; André, J. C., Study of the spatial resolution of a new 3D microfabrication process: the microstereophotolithography using a dynamic mask-generator technique. *J. Photochem. Photobiol. Chem. A* **1997,** *107* (1–3), 275-281.

33. Hadipoespito, G.; Yang, Y.; Choi, H.; Ning, G.; Li, X. In *Digital Micromirror device based microstereolithography for micro structures of transparent photopolymer and nanocomposites*, Solid Freeform Fabrication Symposium, Austin, TX, 2003; pp 13-24.

34. Ikuta, K.; Hirowatari, K. In *Real three dimensional micro fabrication using stereo lithography and metal molding*, Proceedings IEEE Micro Electro Mechanical Systems, 7-10 Feb 1993; pp 42-47.

35. Bertsch, A.; Jiguet, S.; Bernhard, P.; Renaud, P., Microstereolithography: a Review. *MRS Proceedings* **2011,** *758*.

36. Pan, Y.; Pan, Y.; He, H.; He, H.; Xu, J.; Xu, J.; Feinerman, A.; Feinerman, A., Study of separation force in constrained surface projection stereolithography. *Rapid Prototyping Journal* **2017,** *23* (2), 353-361.

37. Liravi, F.; Das, S.; Zhou, C., Separation force analysis and prediction based on cohesive element model for constrained-surface Stereolithography processes. *Computer-Aided Design* **2015,** *69*, 134-142.

38. Pan, Y.; Zhou, C.; Chen, Y., A Fast Mask Projection Stereolithography Process for Fabricating Digital Models in Minutes. *J. Manuf. Sci. Eng.* **2012,** *134* (5), 051011-051019.

39. Tumbleston, J. R.; Shirvanyants, D.; Ermoshkin, N.; Janusziewicz, R.; Johnson, A. R.; Kelly, D.; Chen, K.; Pinschmidt, R.; Rolland, J. P.; Ermoshkin, A.; Samulski, E. T.; DeSimone, J. M., Continuous liquid interface production of 3D objects. *Science* **2015,** *347* (6228), 1349-1352.

40. Bártolo, P. J., Stereolithographic processes. In *Stereolithography*, Springer: 2011; pp 1-36.

41. Decker, C., Photoinitiated crosslinking polymerisation. *Prog. Polym. Sci.* **1996,** *21* (4), 593-650.

42. Hegde, M.; Meenakshisundaram, V.; Chartrain, N.; Sekhar, S.; Tafti, D.; Williams, C. B.; Long, T. E., 3D Printing All-Aromatic Polyimides using Mask-Projection Stereolithography: Processing the Nonprocessable. *Advanced Materials*, 1701240.

43. Harri, K.; Marjo, L.; Minna, M.; Luong, N. D.; Jürgen, W.; Torsten, W.; Matthias, S.; Jukka, S., Novel photo-curable polyurethane resin for stereolithography. *RSC Advances* **2016,** *6* (56), 50706-50709.

44. Davis, F. J.; Mitchell, G. R., Polymeric Materials for Rapid Manufacturing. In *Stereolithography: Materials, Processes and Applications*, Bártolo, P. J., Ed. Springer US: Boston, MA, 2011; pp 113-139.

45. Stampfl, J.; Baudis, S.; Heller, C.; Liska, R.; Neumeister, A.; Kling, R.; Ostendorf, A.; Spitzbart, M., Photopolymers with tunable mechanical properties processed by laser-based high-resolution stereolithography. *J. Micromech. Microeng.* **2008,** *18* (12), 125014.

46. Leigh, S. J.; Gilbert, H. T.; Barker, I. A.; Becker, J. M.; Richardson, S. M.; Hoyland, J. A.; Covington, J. A.; Dove, A. P., Fabrication of 3-dimensional cellular constructs via microstereolithography using a simple, three-component, poly(ethylene glycol) acrylate-based system. *Biomacromolecules* **2013,** *14* (1), 186-192.

47. Barker, I. A.; Ablett, M. P.; Gilbert, H. T. J.; Leigh, S. J.; Covington, J. A.; Hoyland, J. A.; Richardson, S. M.; Dove, A. P., A microstereolithography resin based on thiol-ene chemistry: towards biocompatible 3D extracellular constructs for tissue engineering. *Biomater. Sci.* **2014,** *2* (4), 472-475.

48. Decker, C.; Elzaouk, B.; Decker, D., Kinetic Study of Ultrafast Photopolymerization Reactions. *J. Macromol. Sci. A.* **1996,** *33* (2), 173-190.

49. Melchels, F. P.; Feijen, J.; Grijpma, D. W., A poly(D,L-lactide) resin for the preparation of tissue engineering scaffolds by stereolithography. *Biomaterials* **2009,** *30* (23-24), 3801-3809.

50. Schuller-Ravoo, S.; Feijen, J.; Grijpma, D. W., Preparation of flexible and elastic poly(trimethylene carbonate) structures by stereolithography. *Macromol. Biosci.* **2011,** *11* (12), 1662-1671.

51. Ronca, A.; Ambrosio, L.; Grijpma, D. W., Preparation of designed poly(D,L-lactide)/nanosized hydroxyapatite composite structures by stereolithography. *Acta Biomater.* **2013,** *9* (4), 5989-5996.

52. van Bochove, B.; Hannink, G.; Buma, P.; Grijpma, D. W., Preparation of Designed Poly(trimethylene carbonate) Meniscus Implants by Stereolithography: Challenges in Stereolithography. *Macromol. Biosci.* **2016,** *16* (12), 1853-1863.

53. Melchels, F. P.; Bertoldi, K.; Gabbrielli, R.; Velders, A. H.; Feijen, J.; Grijpma, D. W., Mathematically defined tissue engineering scaffold architectures prepared by stereolithography. *Biomaterials* **2010,** *31* (27), 6909-6916.

54. Lee, K. W.; Wang, S. F.; Fox, B. C.; Ritman, E. L.; Yaszemski, M. J.; Lu, L. C., Poly(propylene fumarate) bone tissue engineering scaffold fabrication using stereolithography: Effects of resin formulations and laser parameters. *Biomacromolecules* **2007,** *8* (4), 1077-1084.

55. Jansen, J.; Melchels, F. P. W.; Grijpma, D. W.; Feijen, J., Fumaric Acid Monoethyl Ester-Functionalized Poly(d,l-lactide)/N-vinyl-2-pyrrolidone Resins for the Preparation of Tissue Engineering Scaffolds by Stereolithography. *Biomacromolecules* **2009,** *10* (2), 214-220.

56. Grijpma, D. W.; Hou, Q.; Feijen, J., Preparation of biodegradable networks by photo-crosslinking lactide, epsilon-caprolactone and trimethylene carbonate-based oligomers functionalized with fumaric acid monoethyl ester. *Biomaterials* **2005,** *26* (16), 2795-2802.

57. Guess, T.; Chambers, R.; Hinnerichs, T.; McCarty, G.; Shagam, R. *Epoxy and acrylate stereolithography resins: In-situ measurements of cure shrinkage and stress relaxation*; Sandia National Labs., Albuquerque, NM (United States): Dayton, OH 4-6 Jun 1995.

58. Esposito Corcione, C.; Greco, A.; Maffezzoli, A., Photopolymerization kinetics of an epoxy-based resin for stereolithography. *J. Appl. Polym. Sci.* **2004,** *92* (6), 3484-3491.

59. Sinn, D. P.; Cillo, J. E. J.; Miles, B. A., Stereolithography for Craniofacial Surgery. *J. Cranio. Surg.* **2006,** *17* (5), 869-875.

60. Melissinaki, V.; Gill, A. A.; Ortega, I.; Vamvakaki, M.; Ranella, A.; Haycock, J. W.; Fotakis, C.; Farsari, M.; Claeyssens, F., Direct laser writing of 3D scaffolds for neural tissue engineering applications. *Biofabrication* **2011,** *3* (4), 1-12.

61. Skoog, S. A.; Goering, P. L.; Narayan, R. J., Stereolithography in tissue engineering. *J. Mater. Sci. Mater. Med.* **2014,** *25* (3), 845-856.

62. Hollister, S. J., Porous scaffold design for tissue engineering. *Nat. Mater.* **2005,** *4* (7), 518-524.

63. O'Brien, F. J., Biomaterials & scaffolds for tissue engineering. *Mater. Today* **2011,** *14* (3), 88-95.

64. Matsuda, T.; Mizutani, M.; Arnold, S. C., Molecular Design of Photocurable Liquid Biodegradable Copolymers. 1. Synthesis and Photocuring Characteristics. *Macromolecules* **2000,** *33* (3), 795-800.

65. Cooke, M. N.; Fisher, J. P.; Dean, D.; Rimnac, C.; Mikos, A. G., Use of stereolithography to manufacture critical-sized 3D biodegradable scaffolds for bone ingrowth. *J. Biomed. Mater. Res. B Appl. Biomater.* **2003,** *64* (2), 65-69.

66. Choi, J. W.; Wicker, R.; Lee, S. H.; Choi, K. H.; Ha, C. S.; Chung, I., Fabrication of 3D biocompatible/biodegradable micro-scaffolds using dynamic mask projection microstereolithography. *J. Mater. Process. Technol.* **2009,** *209* (15-16), 5494-5503.

67. Luo, Y.; Dolder, C. K.; Walker, J. M.; Mishra, R.; Dean, D.; Becker, M. L., Synthesis and Biological Evaluation of Well-Defined Poly(propylene fumarate) Oligomers and Their Use in 3D Printed Scaffolds. *Biomacromolecules* **2016,** *17* (2), 690-697.

68. Walker, J. M.; Bodamer, E.; Krebs, O.; Luo, Y.; Kleinfehn, A.; Becker, M. L.; Dean, D., Effect of Chemical and Physical Properties on the In Vitro Degradation of 3D Printed High Resolution Poly(propylene fumarate) Scaffolds. *Biomacromolecules* **2017,** *18* (4), 1419-1425.

69. Elomaa, L.; Kang, Y.; Seppälä, J. V.; Yang, Y., Biodegradable photocrosslinkable poly(depsipeptide-co-ε-caprolactone) for tissue engineering: Synthesis, characterization, andIn vitroevaluation. *J. Polym. Sci. A Polym. Chem.* **2014,** *52* (23), 3307-3315.

70. Elomaa, L.; Teixeira, S.; Hakala, R.; Korhonen, H.; Grijpma, D. W.; Seppala, J. V., Preparation of poly(epsilon-caprolactone)-based tissue engineering scaffolds by stereolithography. *Acta Biomater.* **2011,** *7* (11), 3850-3856.

71. Schuller-Ravoo, S.; Teixeira, S. M.; Feijen, J.; Grijpma, D. W.; Poot, A. A., Flexible and elastic scaffolds for cartilage tissue engineering prepared by

stereolithography using poly(trimethylene carbonate)-based resins. *Macromol. Biosci.* **2013,** *13* (12), 1711-1719.

72. Liu, X.; Ma, P. X., Polymeric scaffolds for bone tissue engineering. *Ann. Biomed. Eng.* **2004,** *32* (3), 477-486.

73. Wu, L.; Ding, J., In vitro degradation of three-dimensional porous poly (D, L-lactide-co-glycolide) scaffolds for tissue engineering. *Biomaterials* **2004,** *25* (27), 5821-5830.

74. Roether, J.; Gough, J.; Boccaccini, A. R.; Hench, L.; Maquet, V.; Jérôme, R., Novel bioresorbable and bioactive composites based on bioactive glass and polylactide foams for bone tissue engineering. *J. Mater. Sci. Mater. Med.* **2002,** *13* (12), 1207-1214.

75. Lee, J. W.; Lan, P. X.; Kim, B.; Lim, G.; Cho, D. W., Fabrication and characteristic analysis of a poly(propylene fumarate) scaffold using micro-stereolithography technology. *J. Biomed. Mater. Res. B Appl. Biomater.* **2008,** *87* (1), 1-9.

76. Lee, J. W.; Kang, K. S.; Lee, S. H.; Kim, J. Y.; Lee, B. K.; Cho, D. W., Bone regeneration using a microstereolithography-produced customized poly(propylene fumarate)/diethyl fumarate photopolymer 3D scaffold incorporating BMP-2 loaded PLGA microspheres. *Biomaterials* **2011,** *32* (3), 744-752.

77. Shin, J. H.; Lee, J. W.; Jung, J. H.; Cho, D.-W.; Lim, G., Evaluation of cell proliferation and differentiation on a poly(propylene fumarate) 3D scaffold treated with functional peptides. *J. Mater. Sci.* **2011,** *46* (15), 5282-5287.

78. Kwon, I. K.; Matsuda, T., Photo-polymerized microarchitectural constructs prepared by microstereolithography (muSL) using liquid acrylate-end-capped trimethylene carbonate-based prepolymers. *Biomaterials* **2005,** *26* (14), 1675-1684.

79. Lee, S. J.; Kang, H. W.; Park, J. K.; Rhie, J. W.; Hahn, S. K.; Cho, D. W., Application of microstereolithography in the development of three-dimensional cartilage regeneration scaffolds. *Biomed Microdevices* **2008,** *10* (2), 233-241.

80. Puppi, D.; Chiellini, F.; Piras, A. M.; Chiellini, E., Polymeric materials for bone and cartilage repair. *Prog. Polym. Sci.* **2010,** *35* (4), 403-440.

81. Elomaa, L.; Kokkari, A.; Närhi, T.; Seppälä, J. V., Porous 3D modeled scaffolds of bioactive glass and photocrosslinkable poly(ε-caprolactone) by stereolithography. *Compos. Sci. Technol.* **2013,** *74*, 99-106.

82. Lu, Y.; Mantha, S. N.; Crowder, D. C.; Chinchilla, S.; Shah, K. N.; Yun, Y. H.; Wicker, R. B.; Choi, J.-W., Microstereolithography and characterization of poly (propylene fumarate)-based drug-loaded microneedle arrays. *Biofabrication* **2015,** *7* (4), 045001.

83. Stampfl, J.; Wöß, A.; Seidler, S.; Fouad, H.; Pisaipan, A.; Schwager, F.; Liska, R., Water Soluble, Photocurable Resins for Rapid Prototyping Applications. *Macromol. Symp.* **2004,** *217* (1), 99-108.

84. Arnaud, B.; Sébastien, J.; Philippe, R., Microfabrication of ceramic components by microstereolithography. *J. Micromech. Microeng.* **2004,** *14* (2), 197.

85. De Santis, R.; D'Amora, U.; Russo, T.; Ronca, A.; Gloria, A.; Ambrosio, L., 3D fibre deposition and stereolithography techniques for the design of multifunctional nanocomposite magnetic scaffolds. *J. Mater. Sci. Mater. Med.* **2015,** *26* (10), 250.

86. Lee, J. W.; Ahn, G.; Kim, D. S.; Cho, D.-W., Development of nano- and microscale composite 3D scaffolds using PPF/DEF-HA and micro-stereolithography. *Microelectron. Eng.* **2009,** *86* (4-6), 1465-1467.

87. Gonzalez, G.; Chiappone, A.; Roppolo, I.; Fantino, E.; Bertana, V.; Perrucci, F.; Scaltrito, L.; Pirri, F.; Sangermano, M., Development of 3D printable formulations containing CNT with enhanced electrical properties. *Polymer* **2017,** *109*, 246-253.

88. Kim, K.; Zhu, W.; Qu, X.; Aaronson, C.; McCall, W. R.; Chen, S.; Sirbuly, D. J., 3D Optical Printing of Piezoelectric Nanoparticle–Polymer Composite Materials. *ACS Nano* **2014,** *8* (10), 9799-9806.

89. Woodward, D. I.; Purssell, C. P.; Billson, D. R.; Hutchins, D. A.; Leigh, S. J., Additively-manufactured piezoelectric devices. *Physica Status Solidi (a)* **2015,** *212* (10), 2107-2113.

90. Hoffman, A. S., Hydrogels for biomedical applications. *Advanced Drug Delivery Reviews* **2012,** *64*, 18-23.

91. Seck, T. M.; Melchels, F. P.; Feijen, J.; Grijpma, D. W., Designed biodegradable hydrogel structures prepared by stereolithography using poly(ethylene glycol)/poly(D,L-lactide)-based resins. *J. Control Release* **2010,** *148* (1), 34-41.

92. Sharifi, S.; Blanquer, S. B.; van Kooten, T. G.; Grijpma, D. W., Biodegradable nanocomposite hydrogel structures with enhanced mechanical properties prepared by photo-crosslinking solutions of poly(trimethylene carbonate)-poly(ethylene glycol)-poly(trimethylene carbonate) macromonomers and nanoclay particles. *Acta Biomater.* **2012,** *8* (12), 4233-4243.

93. Chan, V.; Zorlutuna, P.; Jeong, J. H.; Kong, H.; Bashir, R., Three-dimensional photopatterning of hydrogels using stereolithography for long-term cell encapsulation. *Lab on a Chip* **2010,** *10* (16), 2062-2070.

2 Development of a 4D photodegradable material for use in μSL

2.1 Introduction

To date, the majority of polymer-based resins developed for μSL have been formulated for rapid prototyping-based applications. As is the nature of rapid prototyping, multiple attempts at producing the desired part will be carried out before a final design is decided upon. Such prototyping is expensive not only in terms of the cost associated with the resin utilised, but also in terms of manufacturing times required to produce each part. Despite the recent development of continuous liquid interface production (CLIP) technology by Carbon3D that has demonstrated substantial reductions in build time (> 100 times faster), the costs involved in running and maintaining a Carbon3D instrument are considerably high (> $45000/year) and are only available on a subscription basis. Whilst there are other, more affordable instruments, capable of manufacturing parts in similarly short timescales the necessity to reprint or manually modify a part using post processing techniques upon the realisation of faults or imperfections remains. Therefore, it was hypothesised that the development of a material capable of undergoing a secondary, non-interfering, high resolution, subtractive manufacturing process either after or during the printing process (on-line) to remove defects or gradually refine a part (i.e. remove layer artefacts leading to smoother finishes) would reduce manufacturing timescales and remove the necessity to re-manufacture very expensive prints.

For this secondary, subtractive process to be capable of being carried out and therefore achieve digital tuning of the part being manufactured, it needs to be non-interfering in the sense that no physical interaction can take place between the part being printed and the method of subtractive manufacture. This is because physical interaction with the part could potentially cause the print to detach from the build plate leading to a failed print. Consequently, the application of conventional subtractive manufacturing

techniques such as milling or sanding can be instantly ruled out therefore necessitating that removal of material be carried out using alternative methods.

One potential route to achieving a non-interfering subtractive process would be to develop a material that is initially capable of being processed by the µSL technique but then has an intrinsic functionality embedded, allowing for the reverse of the cross-linking process to occur as a response to some sort of external stimulus. Such stimuli responsive materials are often referred to as 'smart' materials, which, when applied to 3D printed components allows them to alter their properties post processing, thereby adding a fourth dimension to the material itself.[1-2] This concept has recently been given the term '4D printing' and is currently receiving increased attention in the literature.

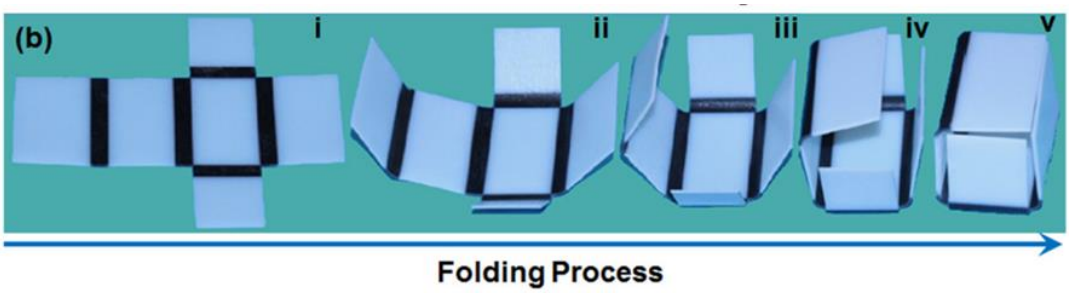

Figure 2.1. Image depicting the self-folding of a six-sided box from the thermally induced shape memory behaviour of the printed ink that make up the hinges of the box[10]

Recently Ge *et al.* have pioneered the concept of 4D printing in their research on 3D printed shape memory materials. In their initial work, shape memory fibres were incorporated into a polymer ink capable of producing thin laminates that upon thermal triggering can take on complex 3D configurations which can later be reverted to their original lamina form by heating the material once again.[3] They also demonstrated the use of their shape memory material as hinges in an active device that integrates 6 stiff plastic plates which upon cooling can assemble into a closed box structure (**Figure 2.1**). Zarek *et al.* reported the ability to produce shape memory components from a poly(caprolactone) (PCL) based resin for use in µSL.[4] These components were found

to be rigid below the melting point of the PCL used, and malleable above their melting point. Any shape initially created by heating up the material could then be fixated by allowing the component to cool back down before undergoing the reverse process regenerating the original conformation. Ge *et al.* later took this concept of printing shape memory polymers that exhibit a response to temperature as an external stimulus one step further.[5] They were able to combine materials with varying activating temperatures within a top-down multimaterial μSL process, allowing for the production of an open flower which upon closure to a flower bud is then capable of opening the outer ring of petals at one temperature and then sequentially opening the inner ring of petals at another slightly raised temperature thereby recovering its original shape (**Figure 2.2**).

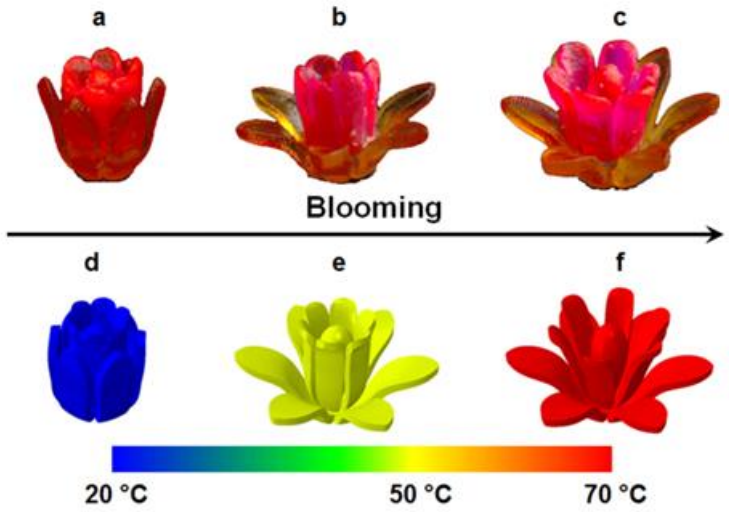

Figure 2.2. Image demonstrating the independent blooming of petals in a flower at various temperatures as a result of printing multiple shape memory materials with various activating temperatures[12]

Whilst the majority of research carried out in this field thus far has continued to focus on shape memory or self-assembling materials, there has been no evidence of exploiting smart materials in order to achieve an online or post printing subtractive process. Although the external stimulus of temperature has proven to be an effective means of inducing shape change in shape memory 4D printed materials, it would be

inconvenient for use in selectively removing defects or small unwanted features, since inducing thermal degradation of the polymers used would require elevated temperatures. Elevated temperatures are not only likely to induce premature cross-linking of resin if not localised to the printed part but the necessary temperatures required to thermally degrade such cross-linked materials may cause further defects by melting parts of the print that are required to remain unchanged.

Other than the use of temperature to induce shape change, there is little evidence of other stimuli responsive materials being used in combination with AM technologies and in particular μSL. Despite this, there is a wealth of literature describing environmentally sensitive macromolecules that have been developed into novel smart materials that have yet to be applied to 3D printing.[6-12] pH and light are two examples of the stimuli that such materials are responsive to and whilst the former would be of little use in achieving the application considered here, the latter may have more potential. As a consequence of the requirement that the subtractive process has to be selective over areas that are desired to be left untouched, the type of stimulus must have the potential of being applied in a site-specific manner. Whilst pH responsive materials rely on being in solution in order to respond to changes in the pH of the solution surrounding them, light responsive materials lend themselves much more to site specificity, since there is the potential for directing certain wavelengths using lasers or masks.[13] Thus, light was selected as an appropriate stimulus.

Azobenzenes are one class of materials that are recognized as being photoresponsive and when exposed to either UV or visible light they undergo a reversible molecular switch causing them to be either hydrophilic or hydrophobic respectively.[14-17] This reversible switching has allowed them to be used in controlling surface wettability on a number of substrates. Spyropyrans are a similarly photosensitive class of chemical

compounds that have also been shown to be able to influence surface wettability.[18] Unfortunately, despite both of the above undergoing transformations at the molecular level, neither of them undergo the necessary type of chemical bond scission required for degradation in a cross-linked material. Fortunately, there is a well-known class of chemical compounds that are capable of inducing photodegradation, namely that of the *ortho*-nitrobenzyl (*o*NB) functionality.[19] It was envisaged that the well-studied *o*NB functionality would allow a material to be printed *via* the μSL process using one wavelength of light, but could also undergo the reverse degradation process upon exposure to another wavelength of light, either during or after the print, would be possible.

Owing to its successful incorporation within in cross-linked material networks, the photodegradable *ortho*-nitrobenzyl ether (*o*NB) moiety, 4-(4-(1-(acryloyloxy)ethyl)-2-methoxy-5-nitrophenoxy)butanoic acid, was selected as a suitable starting point for developing a novel 4D printing material for use in μSL.[20-25] In the past *o*NB, or derivatives thereof, have been used in a number of polymer based materials to accomplish a variety of functions.[19, 26-29] For instance, Anseth *et al.* and Kasko *et al.* both used *o*NB functionalised PEG in combination with varying cross-linking chemistries in order to produce hydrogels capable of having channels etched into them (**Figure 2.3**) in order to follow the migration of cells or in some cases to control the release of drugs.[26, 30] Zhao *et al.* were able to demonstrate the use of *o*-NB in copolymers to form micelles that upon irradiation were capable of releasing small molecules making them suitable for drug delivery whereas other groups have demonstrated *o*-NBs ability to be used as thin film positive-type photoresists.[31-33] Whilst not all of the examples mentioned above have been used in materials containing cross-linked networks, they are good examples of *o*NBs ability to undergo photolysis

either in solution (hydrogels/micelles) or in bulk (photoresists). Although there are many reports of *o*NB being utilised in order to disrupt and therefore degrade cross-linked networks, none of these networks have been shown to be capable of initially being cross-linked *via* an alternative wavelength of light to that used to induce photolysis.

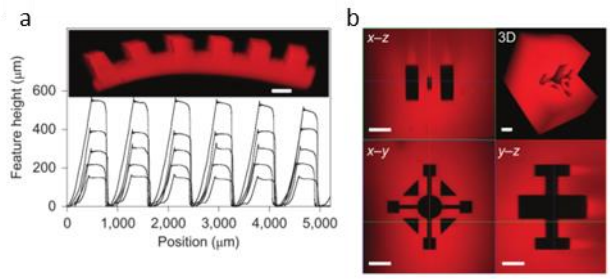

Figure 2.3. Images depicting the ability of cross-linked gels containing *o*NB to undergo photodegradation as a result of exposure to a) mask-based photolithography and b) focussed multiphoton laser[33]

This chapter encompasses the initial development of a μSL compatible resin from synthesis through optimisation of the resin composition, cross-linking of thin films using visible light and ultimately demonstrating degradability under UV light (**Figure 2.4**). More specifically, low molecular weight PEG was functionalised with *o*NB in an attempt to maintain the low viscosity required for 3D printing. This photodegradable diacrylate was then combined with a suitable cross-linker, viscosity modifier and visible light photoinitiator to allow for printing using a custom made visible light μSL apparatus. Thin films created by photo cross-linking were then subjected to various UV light sources, either by flood irradiating the bulk material as a whole or selective exposure using photomasks, and finally analysed to determine the degree of degradation achieved.

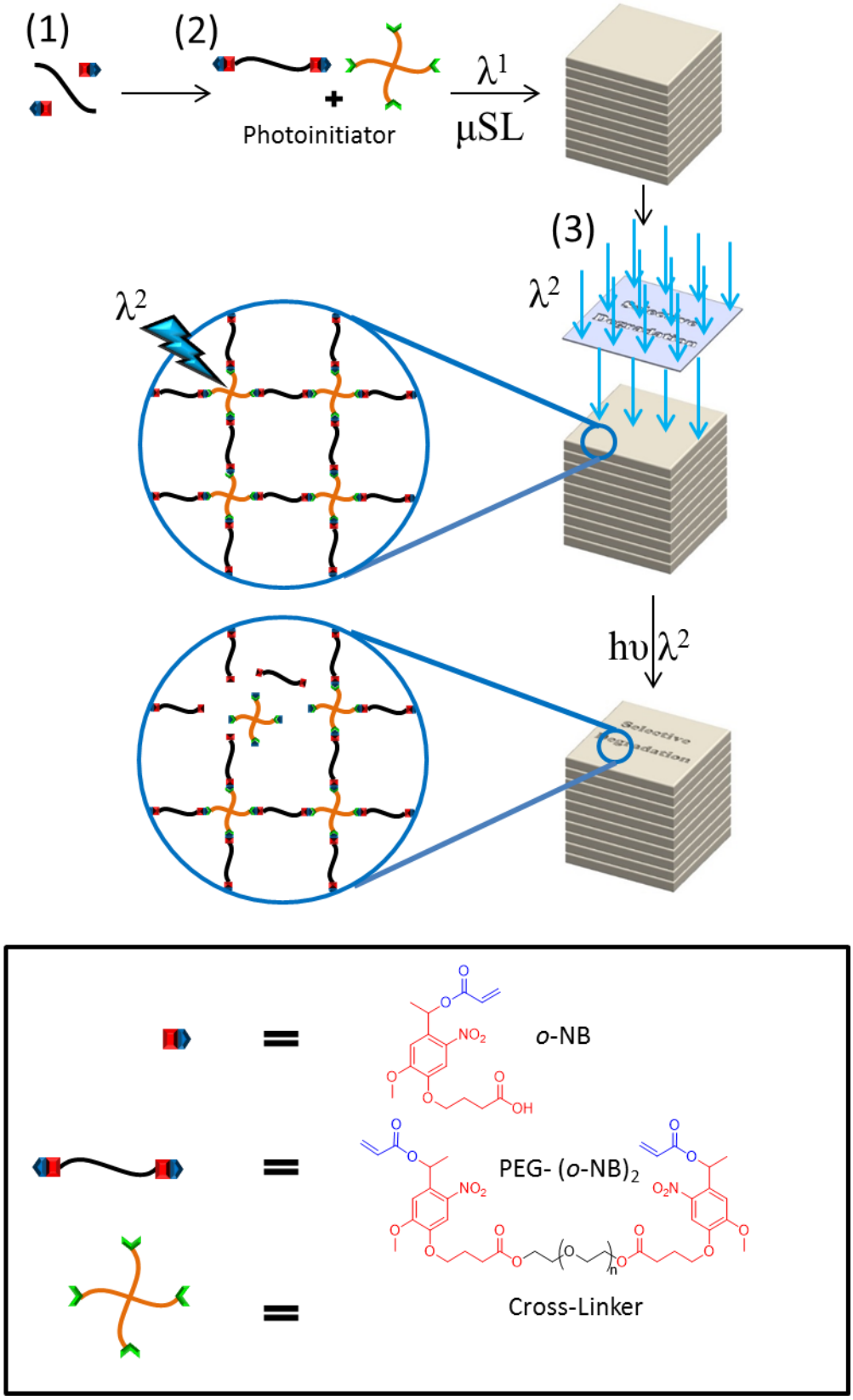

Figure 2.4. Schematic displaying the ability to build 3D objects from the synthesised resin (1) using a visible wavelength of light (λ^1) in the μSL process (2) and then the ability to selectively degrade away regions of the object (3) with a second wavelength of light (λ^2)

2.2 Results and Discussion

2.2.1 Synthesis of photodegradable linker

PEG-*o*NB was chosen as a suitable linker due to its successful application in the production of photodegradable hydrogels, furthermore, it is also very similar to non-photodegradable PEG-diacrylate, which has previously demonstrated great potential as a key component in μSL resins capable of producing highly accurate 3D architectures.[34] The synthesis of the photodegradable linker was carried out using modified techniques from several previously reported procedures.[35-36] There was a total of 4 synthesis steps required to produce the photodegradable molecule, 4-(4-(1-(acryloyloxy)ethyl)-2-methoxy-5-nitrophenoxy)butanoic acid (*o*NB), which was then coupled with poly(ethylene glycol) (PEG) in an additional step to form the photodegradable linker, PEG-*o*NB.

The first step in the synthesis of *o*NB was a nucleophilic substitution (S_N2) of ethyl-4-bromobutyrate, **2**, by the alkoxide anion of acetovanillone, **1**, to produce the ether, ethyl 4-(4-acetyl-2-methoxyphenoxy) butanoate, **3**. This is followed by nitration at the *ortho* position with respect to the already substituted ketone of **3** using nitric acid and acetic anhydride to afford ethyl 4-(4-acetyl-2-methoxy-5-nitrophenoxy)butanoate, **4**. This step was performed on a smaller scale (*ca*. 20g) in order to maximise the efficiency of cooling the solution as to make sure the nitration only occurs at the *ortho* position. Tandem hydrolysis of the ester functionality into the corresponding carboxylic acid using concentrated HCl in acetic acid and subsequent sodium borohydride reduction of the ketone into a secondary alcohol afforded 4-[4-(1-hydroxyethyl)-2-methoxy-5-nitrophenoxy]butanoic acid, **5**. The final step in synthesising *o*NB is the formation of the ester *via* nucleophilic substitution of acryloyl

chloride, **6**, by the secondary alcohol of **5** in the presence of TEA to yield 4-[4-(1-(Acryloyloxy)ethyl)-2-methoxy-5-nitrophenoxy] butanoic acid, **7**, (**Scheme 2.1**).

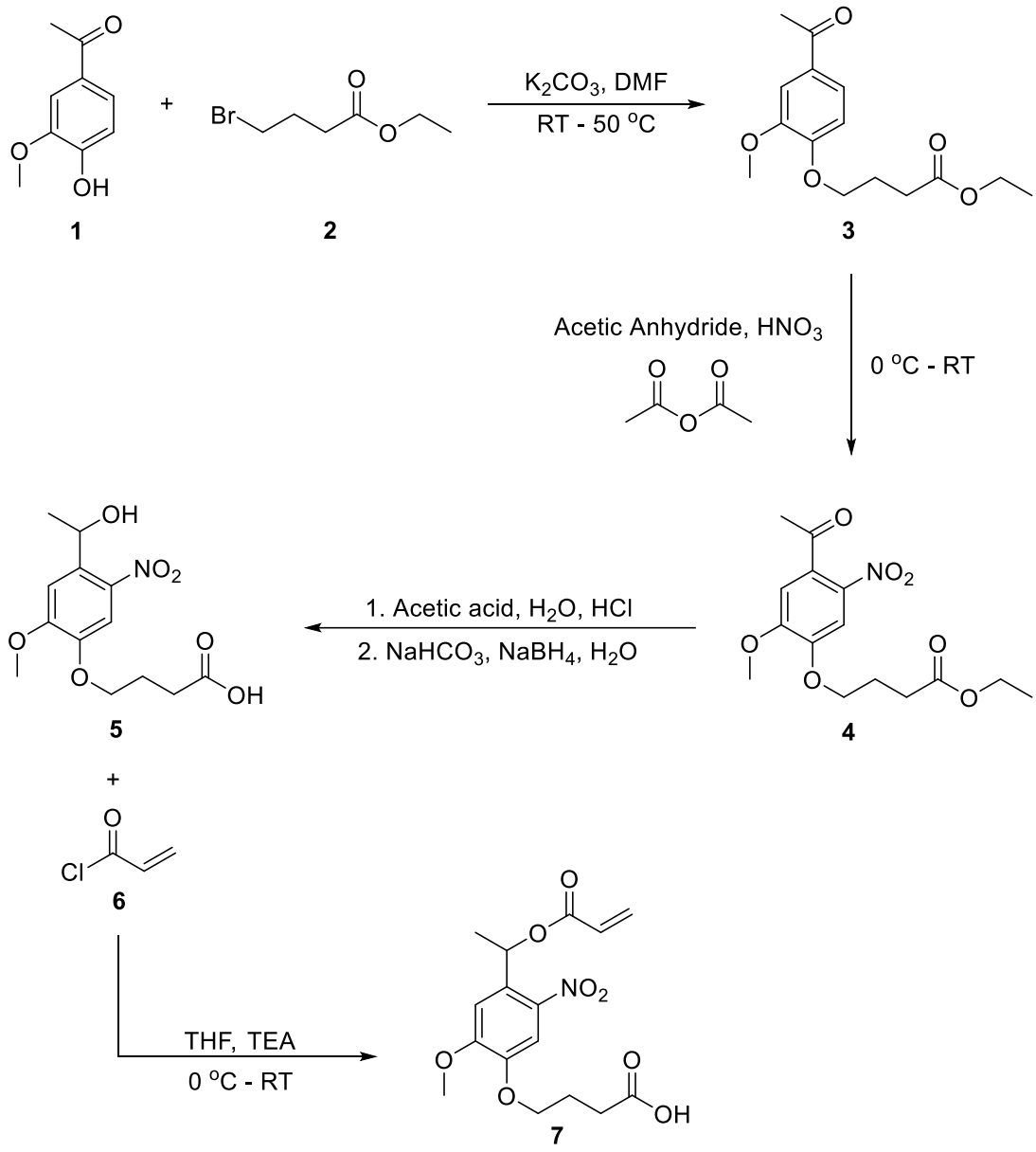

Scheme 2.1. Synthetic scheme for the 5 steps involved in the synthesis of the photodegradable *o*NB molecule

As polymers with low viscosity are desirable when formulating a printable resin, low molecular weight PEG (M_n 400), a non-viscous liquid at room temperature before functionalisation, was chosen as the diol to be functionalised. Initial attempts at functionalising PEG with *o*NB were carried out using traditional Fischer esterification techniques whereby *o*NB was used in excess in non-polar solvents (benzene/toluene)

with acid catalysts under dean-stark conditions. These attempts produced PEG-*o*NB with a high degree of functionalisation (>99%), however, upon using both sulphuric acid and p-toluenesulfonic acid it was found that the high temperatures required to remove the water as an azeotrope, caused charring of the functionalised polymer that could not be removed by typical purification techniques. Whilst the ^{1}H NMR spectrum of these materials was as expected, and with little to no degradation observed by UV-Vis, the black colour was regarded as a possible hinderence to the penetration of visible light in the µSL process. As such, low temperature methods for functionalisation were exploited instead.

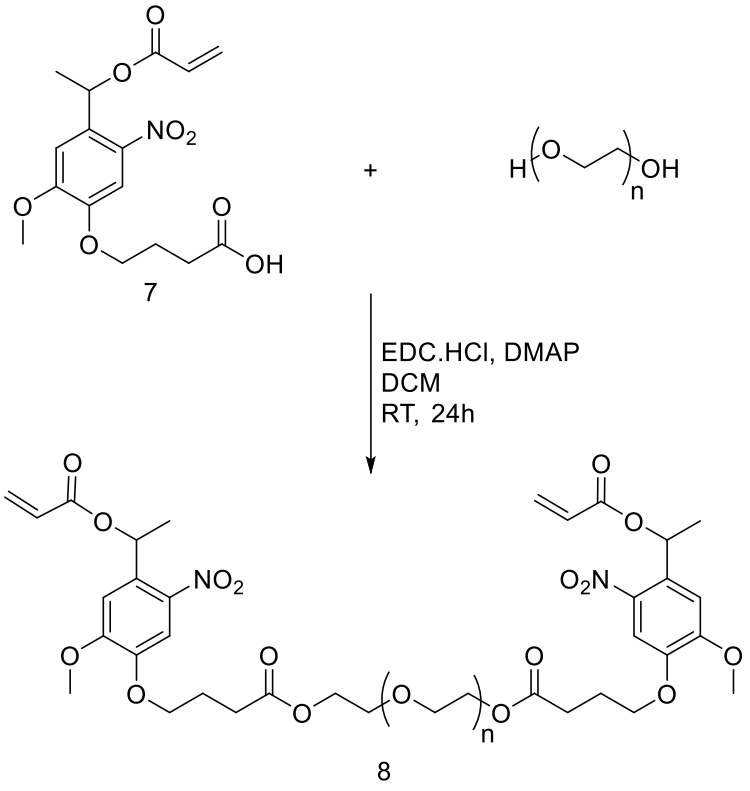

Scheme 2.2. Functionalisation of PEG with *o*NB using EDC.HCl and DMAP in DCM

Carbodiimide coupling using 1-Ethyl-3-(3-dimethylaminopropyl)carbodiimide hydrochloride (EDC.HCl) alongside the acyl transfer reagent 4-dimethylaminopyridine (DMAP) as required in order to reduce side reactions and therefore increase yields was exploited (**Scheme 2.2**). The reaction was carried out in

DCM for 24 h at room temperature and upon work up yielded PEG-*o*NB as a yellowy brown viscous liquid. ^{1}H NMR spectroscopy was then used to determine the degree of functionalisation of the *o*NB attached to PEG by comparison of the integral for the PEG chain end methylene resonance δ = 4.26 ppm with the resonance for the polymer backbone methylene resonances δ = 3.66 ppm. This degree of functionalisation was determined to be greater than 90% which was deemed high enough to achieve a cross-linked material in the printing process (**Figure 2.5**).

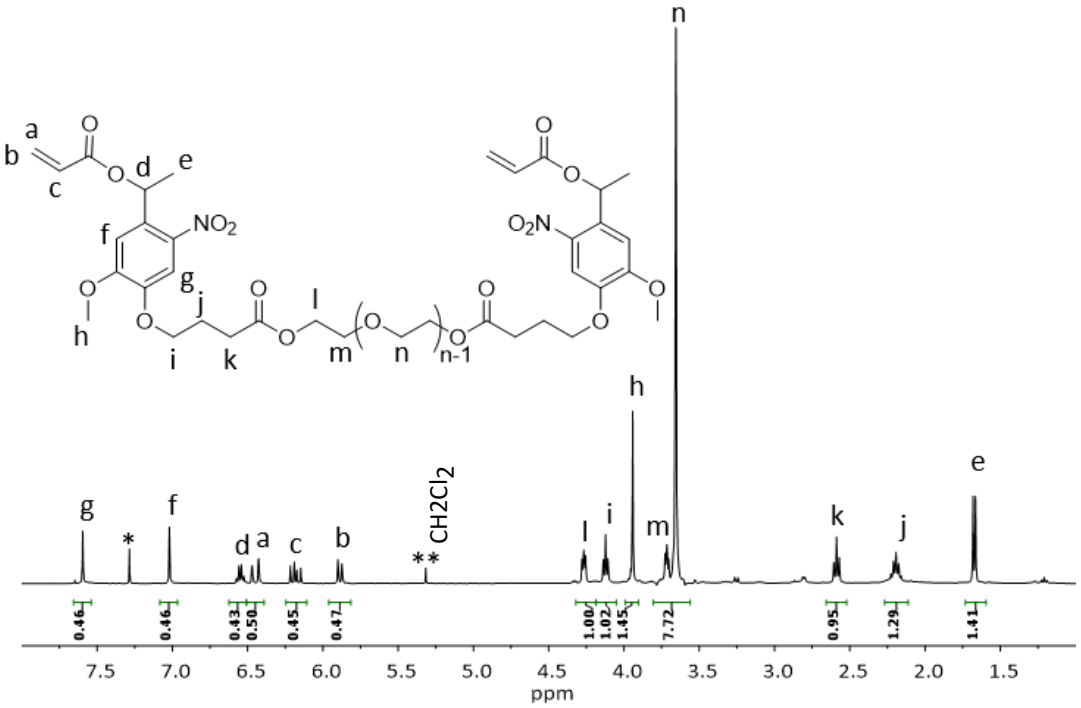

Figure 2.5. ^{1}H NMR spectrum of PEG-*o*NB (400MHz, * = $CHCl_3$, ** = DCM)

Size exclusion chromatography (SEC) of the functionalised polymer (**Figure 2.6**) shows low molecular weight impurities arising from both non-functionalised PEG and some low molecular weight impurities already present in the PEG starting materials. As a consequence of the low molecular weight nature of the PEG-*o*NB produced, all attempts to purify it proved unsuccessful including precipitation into diethyl ether, dialysis and silica gel plugs. Despite the small amount of impurities, the PEG-*o*NB was found to be capable of producing solid materials upon cross-linking.

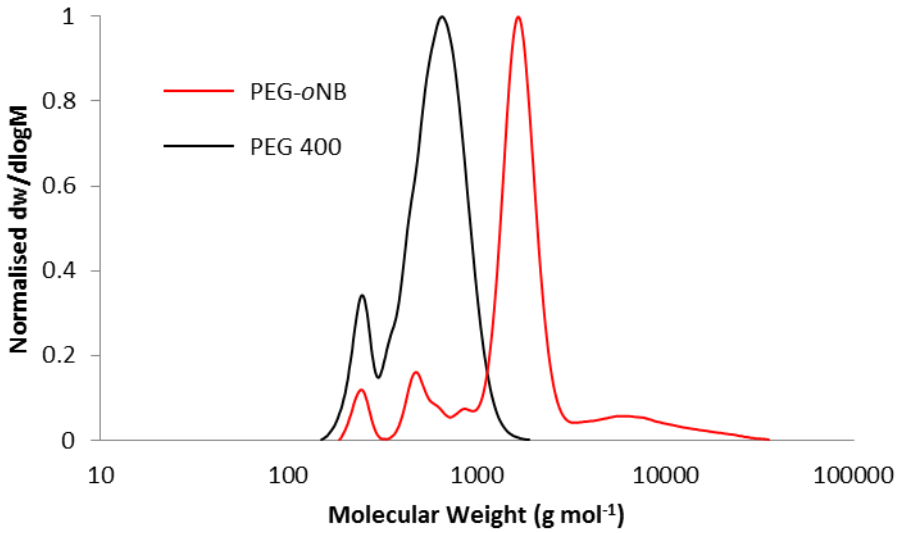

Figure 2.6. Size exclusion chromatograms of non-functionalised PEG (M_n = 650, M_w = 800, and $Đ_m$ = 1.19) PEG-*o*NB (M_n = 1400, M_w = 3000, and $Đ_m$ = 2.19). Using poly(styrene) standards with $CHCl_3$ as eluent

2.2.2 Resin composition optimisation

Following the success of Leigh *et al.* in producing tissue engineering scaffolds using low molecular weight PEG-diacrylate (PEGDA) with dipentaerythritol penta-/hexa-acrylate (DPPHA) as cross-linker in combination with Irgacure 784 as a visible light PI (**Scheme 2.3**.), a similar system was chosen in this research as a suitable starting point owing to the similarity between PEGDA and PEG-*o*NB.[34]

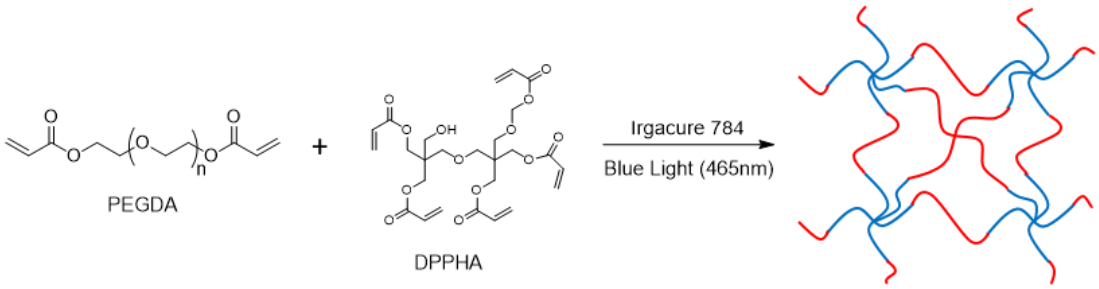

Scheme 2.3. Resin composition used by Leigh *et al.* to produce cross-linked networks of complex 3D architectures by μSL[41]

The PEGDA in this composition was simply replaced by PEG-*o*NB and mixed with DPPHA maintaining the 4:1 ratio of the diacrylate to the cross-linker by volume. Upon addition of 1.8 wt% Irgacure 784 and 10 wt% propylene carbonate (used to reduce viscosity of the resin) the mixture was deposited on a glass slide and exposed to

rectangular projections of blue light (465 nm) using a custom made µSL 3D printer (referred to as 'custom µSL') to test curing ability. After exposure to the rectangular projection and washing with isopropanol to remove non-crosslinked resin, no cured material remained on the glass substrate even after long exposures (> 60 s). Since the previously reported PEGDA system was capable of curing defined shapes with suitable layer heights for printing within 10 s it was postulated that PEG-*o*NB was inhibiting the curing process.[34] Consequently, a UV-Vis spectroscopy investigation was carried out in order to determine whether or not the optical properties of PEG-*o*NB were having an effect on the materials' ability to cross-link. More specifically, UV-Vis spectra of PEG-*o*NB doped PEGDA based resins were acquired for resins containing 0, 5 and 10 wt% PEG-*o*NB, both with and without photoinitiator (PI) (**Figure 2.7**).

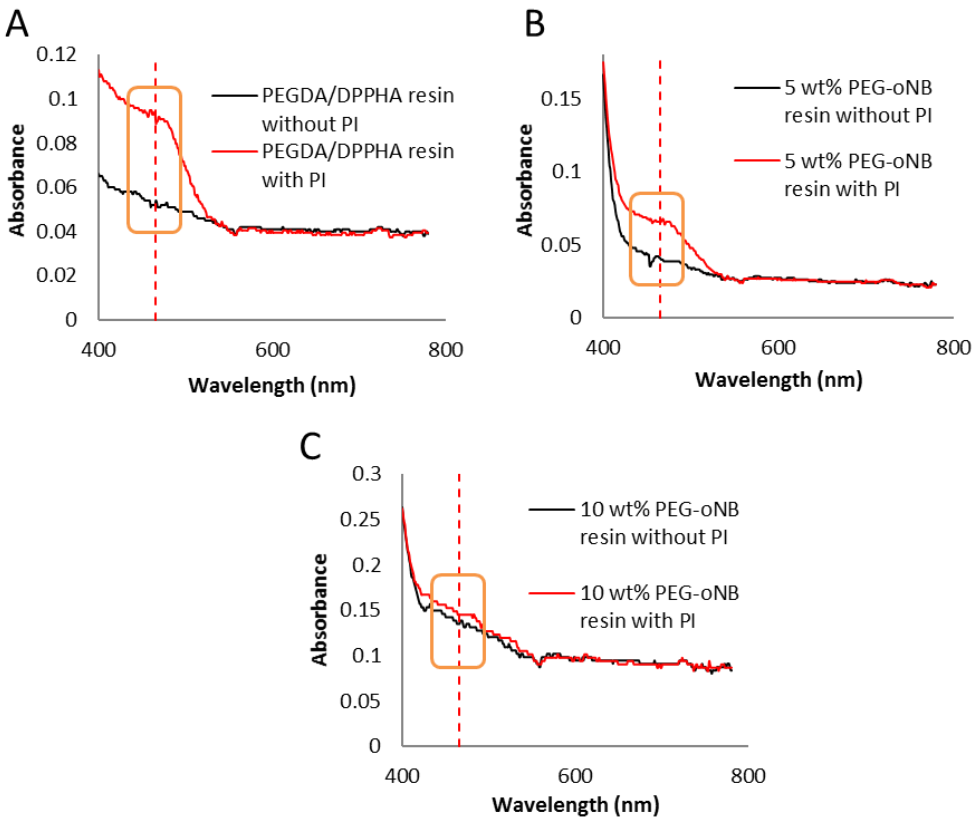

Figure 2.7. UV-Vis spectra of PEGDA/DPPHA resin compositions both with and without photoinitiator (PI) (A) and with increasing amounts of PEG-*o*NB doping (B, 5 wt % and C, 10 wt%). (dashed red line refers to transmission maxima of blue LED light source used).

For the resin containing no PEG-*o*NB (**Figure 2.7 A**) there is a significant difference between the absorptions of the resin with PI compared with the resin without PI in the wavelength region corresponding to the light source used (465 nm). This allows for the initiator to absorb radiation, thereby generating the necessary radicals for acrylates to cross-link. Indeed, this particular resin composition with PI does cure upon irradiation with visible light. Introducing 5 wt% of PEG-*o*NB (**Figure 2.7 B**) causes the difference in absorption between the resins with and without PI to decrease when compared to the resin containing no PEG-*o*NB. This behaviour explains the long exposure time required to produce only a very thin film, since the PEG-*o*NB is also absorbing the incident light required by the PI. Increasing the amount of PEG-*o*NB to 10 wt% (**Figure 2.7 C**) further decreases the difference in absorption between the resins with and without PI to the point where they almost overlap. Therefore, it is unsurprising that this particular resin showed no signs of curing even after irradiation for one minute. Using different concentrations of the same PI did not improve the curing process and so investigations into using other potential PIs were carried out. It was hypothesised that by using a PI with an absorbance maxima at a longer wavelength than the absorbance of the polymer, the PI may receive enough excitation energy in order to generate the radicals necessary for the cross-linking reaction to occur.

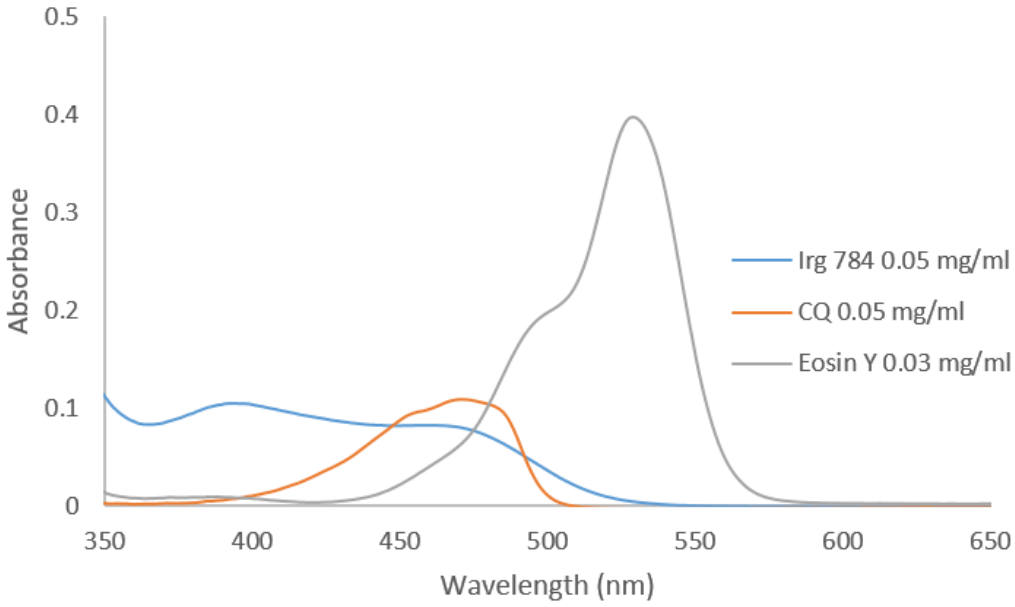

Figure 2.8. UV-Vis absorbance spectra of various different visible light photoinitiators

Firstly, camphorquinone was tested. This photoinitiator was able to cure films of PEGDA/DPPHA, but it was ineffective at curing resins containing low weight percentages of PEG-*o*NB likely because of its absorbance maxima (475nm) being at the same wavelength to that for Irgacure 784 (475nm) and still not be far enough away from the absorbance of the *o*NB containing polymer (**Figure 2.8**). Another photoinitiator, Eosin Y, which absorbs further into the visible region (524nm) therefore moving to longer wavelengths of light, where the nitrobenzyl chromophore does not absorb. Despite using a PI with a maximum absorbance at a longer wavelength, there was still no curing observed for resins containing small amounts of PEG-*o*NB. This suggests the absorbance of the nitrobenzyl chromophore is not the only parameter inhibiting the cross-linking reaction.

Since the curing of PEG-*o*NB/DPPHA based resins have been demonstrated to show inhibition of curing as a consequence of the nitrobenzyl chromophore absorbing in the same region as visible photoinitiators in addition to inhibition of acrylate cross-linking

by the presence of oxygen as described in chapter 1, a new direction was taken in order to minimise the latter of these. Whereas free radical polymerisation of (meth)acrylates is well known to be inhibited by the formation of radical oxygen species (ROS) in the presence of oxygen, the free radical step-growth polymerisation between thiols and alkenes can in fact be propagated by ROS and subsequently consume them.[37-38] More specifically, in a thiol-ene system whereby the 'ene' part is an acrylate, oxygen will react with initiator, acrylic and thiyl radicals to form peroxy radicals. Whilst these peroxy radicals aren't active towards subsequent addition reactions in acrylic systems they are reactive towards hydrogen abstraction and so aid propagation in the thiol-ene click reaction (**Scheme 2.4**). Therefore, changing the cross-linking chemistry from acrylate based to thiol-ene click chemistry was considered a promising alternative. Consequently pentaerythritol tetrakis(3-mercaptopropionate) (PT3M) was chosen as a suitable thiol functionalised cross-linker because as it was exploited by Barker *et al*. in the first ever μSL resin based on thiol-ene chemistry.[38-39]

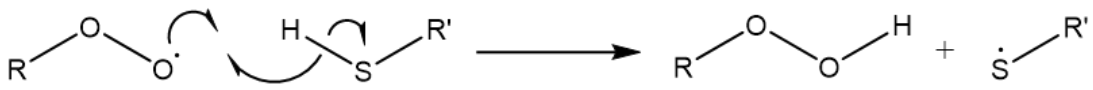

Scheme 2.4. Mechanism of thiol hydrogen abstraction by peroxy radicals[45]

Initially PT3M was used in a resin comprising of both PEGDA and PEG-*o*NB which was found to cross-link upon stirring and form a solid mass **(Figure 2.9**, **A**). Since this was a mixed system it was impossible to tell whether both PEGDA and PEG-*o*NB were reacting with PT3M and so a separate resin containing only PEG-*o*NB and PT3M was formulated. Again, upon stirring, it was found that the resin cross-linked in the vessel forming a solid (**Figure 2.9**, **B**).

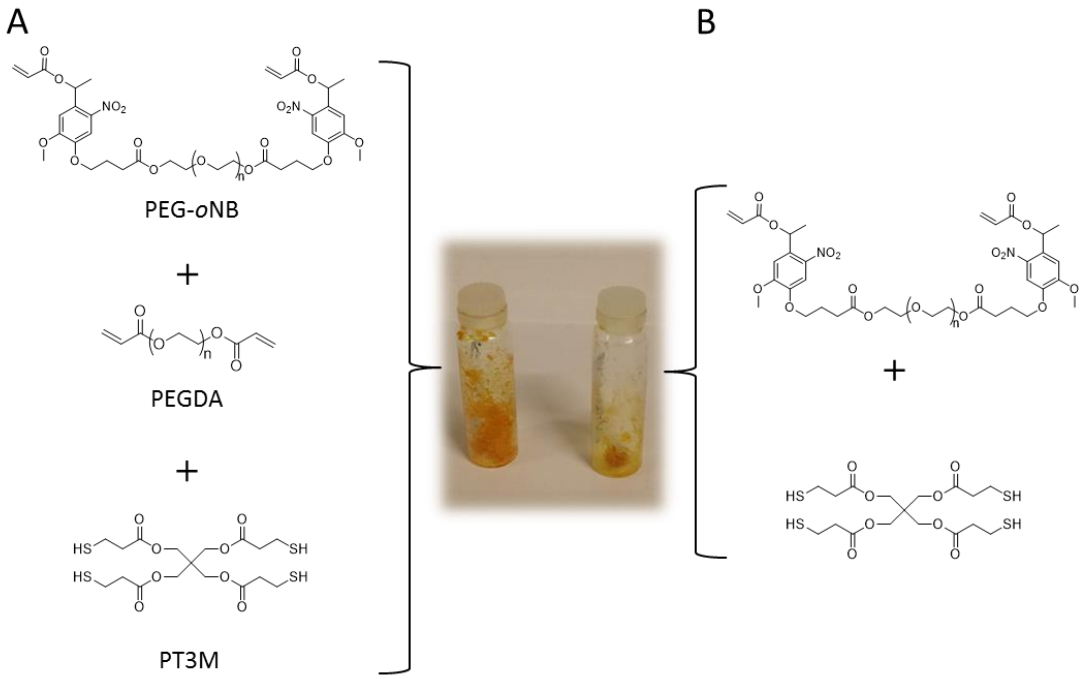

Figure 2.9. Image of cross-linked solid materials formed upon stirring resins both with (A) and without (B) PEGDA

Since cross-linking had occurred before any addition of a PI, it was postulated that the acrylates of PEG-*o*NB and the thiols from the cross-linker were, in fact, undergoing thiol-ene michael addition by either a base-catalysed or nucleophile-initiated mechanism (**Scheme 2.5**). Although the premature cross-linking displayed by this system was initially considered to be a promising sign, it was still undesirable because of the necessity for curing to occur during the printing process as a consequence of the free radical mechanism (**Scheme 2.5**). Considering that both the base catalysed and nucleophile initiated pathways can be inhibited by acidic protons, the use of an acid to remove any premature cross-linking was investigated. Initially, benzoic acid was tested and although it appeared to hinder premature cross-linking, the resin mixture still began to solidify after 5 minutes (**Table 2.1**). This was likely due to the inhomogeneous mixing of the solid benzoic acid in the liquid resin. In an attempt to achieve homogenous mixing lactic acid, an organic acid produced in the muscles of humans and animals, was chosen as a suitable alternative.[40] Small quantities of lactic

acid (*c.a.* 1.5 wt%) were found to completely inhibit the photoinitiator-free cross-linking reaction (**Table 2.1**).

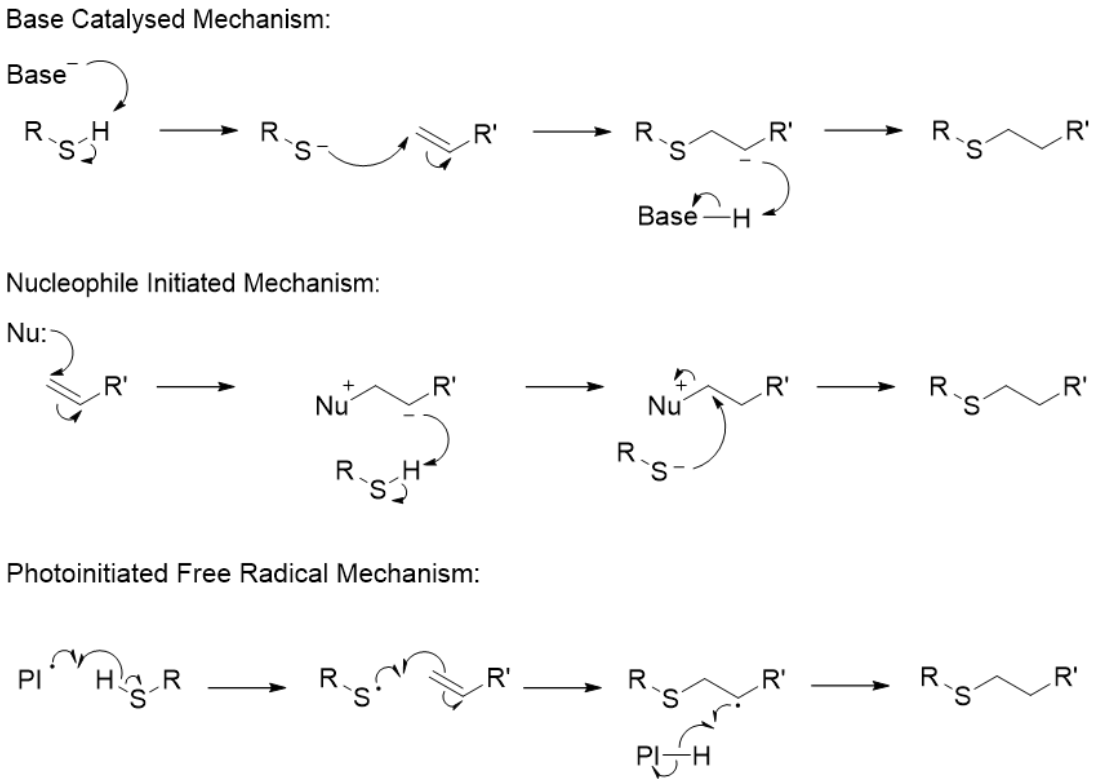

Scheme 2.5. Mechanisms for base catalysed, nucleophile initiated and free radical thiol-ene reactions (Nu = nucleophile, PI = Photoinitiator, R & R' = alkyl chains)

To ensure that the inhibition of undesirable premature cross-linking didn't also inhibit the photoinitiated free radical reaction, a small quantity of Irgacure 784 as photoinitiator (*ca.* 2 wt%) was added to the inhibited reaction vessels and the subsequent PI containing resins were exposed to rectangles of blue light (465nm) for 1 minute on the custom μSL 3D printer. After exposure and subsequent post processing using isopropanol (IPA) to wash off any residual unreacted resin a very thin layer of cured material remained on the glass substrate for the three resins containing increased amounts of lactic acid.

Table 2.1. Incrementally decreasing the pH of the resin using either benzoic or lactic acid in order to prevent premature cross-linking

Resin	Benzoic Acid	Lactic Acid	pH	Cross-linking upon mixing?	Cross-linking after addition of Irgacure 784 and exposure?
A	~15 mg	0 mg	5/6	Yes (~5mins)	-
B	0 mg	23 mg	5	No	Yes
C	0 mg	69 mg	4	No	Yes
D	0 mg	138 mg	2/3	No	Yes
E (control)	0 mg	0 mg	7/8	Yes (instant)	-

Despite a thin layer of material being cured, the rectangle of cross-linked material was not particularly well-defined and even after soaking in IPA for 10 minutes residual uncured resin remained on the glass substrate surrounding the cured rectangle (**Figure 2.10**). This suggested that the starting resin was too viscous and so the potential for using a non-reactive diluent to modify the resin viscosity was investigated. Propylene carbonate was selected to achieve this for several reasons, first of all, it is a very non-viscous high boiling point solvent which would not evaporate prior to the μSL process. It has also been previously exploited in μSL based resins that have been capable of producing highly accurate 3D parts.[41-42]

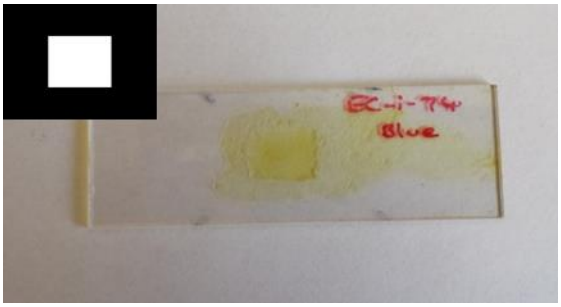

Figure 2.10. Picture of ill-defined rectangle of cured material with residual uncured materials surrounding it on glass slide with mask illustrating the rectangle of light exposed onto the pool of resin

Resins of PEG-*o*NB and PT3M were formulated maintaining the thiol-alkene ratio of 1:1 making sure that a minimal amount of lactic acid was incorporated into one of the two components prior to mixing. Varying amounts of propylene carbonate, ranging from 10 to 40 wt%, were introduced to different resins alongside Irgacure 784 as PI

before being exposed to rectangles of blue light. The results showed that 10 wt% of propylene carbonate was an optimal amount, since it reduced the viscosity enough to produce a well-defined cross-linked rectangle and allowed for residual resin to be removed after curing. Increasing the amount of diluent further yielded non-rectangular films that were too fragile to be removed from the glass substrate without breaking them (**Table 2.2**). This result was to be expected, since increasing the amount of non-reactive diluent would essentially reduce the concentration of reactive end groups. Although this may improve chain movement at low incorporations and therefore allow more interactions between thiol and alkene moieties, at higher incorporations it causes the functional groups to be so far apart they cannot react with each other as readily.

Table 2.2. Effect of non-reactive diluent (propylene carbonate) on film formation

Resin	**PEG-oNB (mg)**	PT3M **(mg)**	**Lactic Acid (mg)**	**Propylene Carbonate (mg)**	**Irgacure 784 (mg)**	**Result after 1 minute exposure**
A	268	61	23	39 (10 wt%)	2wt%	Very defined rectangular thin film
B	268	61	23	88 (20 wt%)	2wt%	Thin film with undefined shape
C	268	61	23	151 (30 wt%)	2wt%	Same as B
D	268	61	23	235 (40 wt%)	2wt%	Same as B

In an attempt to reduce exposure time and ultimately reduce build times the now optimised resin was tried out on a different μSL system. This system was again custom made and is referred to as 'Custom mini'. In this case, a different projector equipped with a more powerful visible light LED source (that covered a broader spectrum of visible light (red, green and blue)) was used. The resin was exposed to a rectangle of white light from the 'Custom mini' for one minute before being post processed. After washing with IPA and post exposure in a custom made visible light post exposure box it was found that the custom mini was capable of curing a much thicker layer of resin

than the custom µSL over the same period of time and with much more defined features (**Figure 2.11**). A custom-made post exposure box had to be utilised since commercially available ones usually supplied with µSL 3D printers tend to be equipped with UV light sources which would potentially degrade the photosensitive PEG-*o*NB.

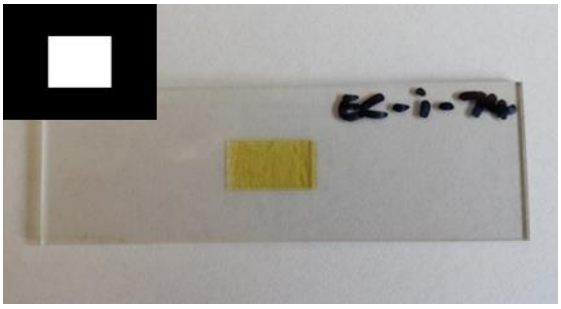

Figure 2.11. Picture of well-defined cured rectangle of cross-linked resin after post-processing with mask illustrating the rectangle of light exposed onto the pool of resin

The improved definition and cure depth of the cross-linked rectangle was attributed to not only the higher power light source but also the broader spectrum of wavelengths used. Whilst the former overcomes light attenuation through the resin allowing for thicker cure depths, the latter will excite the PI over a broader range of its absorption spectrum thereby increasing its efficiency (**Figure 2.12**). To gain an approximation of exposure time required to achieve a 3D print of the material, the exposure time was varied between 15 and 60 seconds and the resulting thickness of the cured material was measured (**Figure 2.13**).

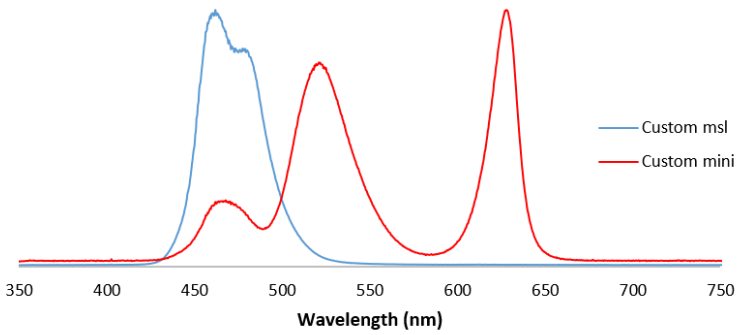

Figure 2.12. Emission spectra of the visible light sources from both the 'custom msl' and 'custom mini' 3D printers illustrating the broader region of visible light emitted by the 'custom mini' printer

It is clear from the data in **Figure 2.13** that by using the white light from the 'Custom mini', curing times for the PEG-*o*NB based resin could be reduced by almost half to acquire rectangles with sharply defined corners. From this experiment, it can be deduced that exposure times of at least 30 s would be required for printing parts with a z-resolution of 50 μm since exposing the material for less time (15 and 20 seconds) did not yield rectangles with a defined shape after post-processing. The data also suggests that parts with 100 μm z-resolution can be achieved with an exposure time of at least 60 s. Before attempting to print multiple layers using the exposure times above as a starting point, a logical progression was to assess the degradability of the material produced.

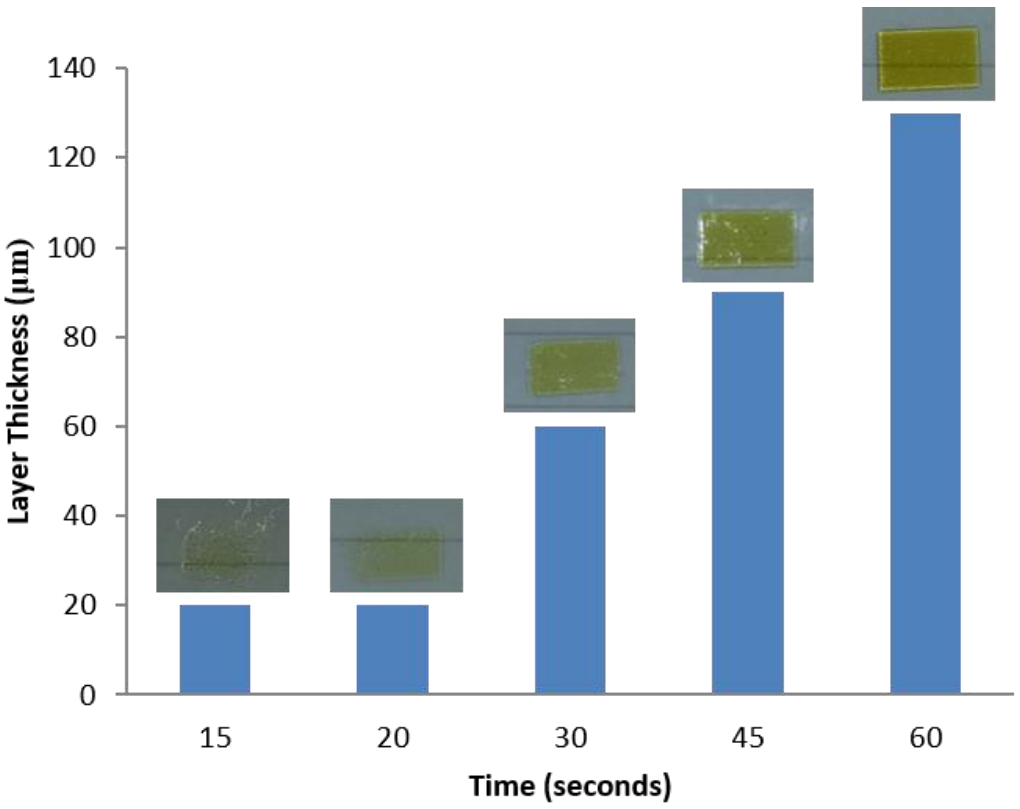

Figure 2.13. Layer thickness of cured resin as a function of exposure time. Pictures are of the respective rectangles cured for each exposure time

2.2.3 Degradation

Before trying to achieve bulk degradation of the thin films produced in the previous section, the degradation of PEG-*o*NB was investigated following previously reported procedures.[35] The *ortho*-nitrobenzyl ether moiety is well known to cleave *via* a radical mechanism when exposed to cytocompatible, low intensity (20-40 mW/cm^2), wavelengths (365-420 nm) of single photon flood irradiation.[43-44] Upon exposure to UV light it cleaves to form the ketone and respective carboxylic acid (**Scheme 2.6**) causing a shift in UV absorbance due to the change from the nitro ($-NO_2$) substituent on the benzene ring to the nitroso (-NO) substituent (**Figure 2.14**).

The maximum absorbance corresponding to the unexposed nitro-functionalised moiety is observed at a wavelength of 340 nm. After 5 minutes of exposure to UV light the maximum absorbance shifts from λ = 340 nm to λ = 377 nm. Increasing the duration of exposure to UV light causes the absorbance at λ = 340 nm to decrease further as expected from further photolysis of PEG-*o*NB, together with the absorbance at λ = 377 nm increasing as a consequence of there being increased amounts of nitroso-functionalised product formed. However, this behaviour was not observed and in fact the peak at λ = 377 nm also began to decrease at longer exposures. This drop in absorption was ascribed to the nitroso product precipitating out of solution as observed by the appearance of sediment in the cuvette used to carry out the experiment.

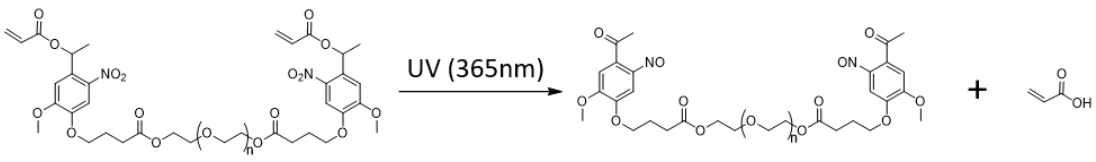

Scheme 2.6. Degradation products formed by photodegradation of PEG-*o*NB in solution after exposure to UV light

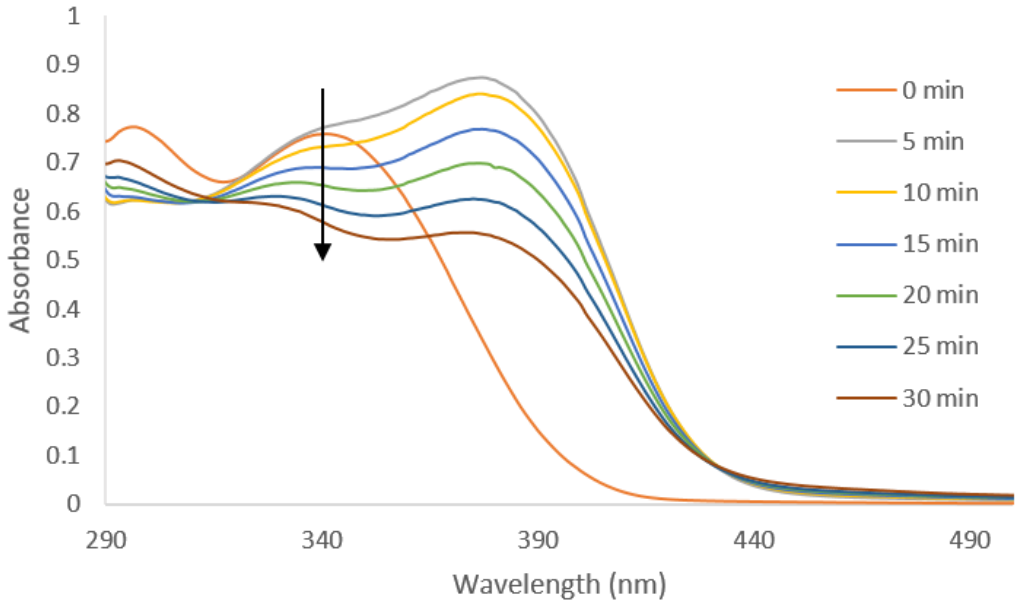

Figure 2.14. UV-Vis absorbance spectra of PEG-*o*NB at increasing doses of UV light exposure

The photolysis of PEG-*o*NB was further investigated using SEC. Since the overall molecular weight and therefore hydrodynamic volume should decrease as a consequence of cleavage of acrylic acid, a small shift in the SEC trace towards a lower molecular weight and therefore greater retention time should be observed. Because of the difference in molecular weight between cleaved PEG-*o*NB and non-cleaved PEG-*o*NB, initial experiments showed only very minimal differences between SEC traces that were close to the lower limit of the SEC calibration. In order to investigate this further, a small amount of PEG-*o*NB was allowed to undergo chain growth *via* acrylate addition so that higher molecular weight coupled PEG-*o*NB chains were observable in the SEC trace. Upon photolysis the coupled PEG chains formed should cleave from one another thereby demonstrating a shift in retention time within the molecular weight limits of the SEC calibration. The respective mixture of coupled and uncoupled PEG-*o*NB was dissolved in SEC eluent (dimethylformamide in this instance) and irradiated with UV light for varying durations of time before being analysed (**Figure 2.15**).

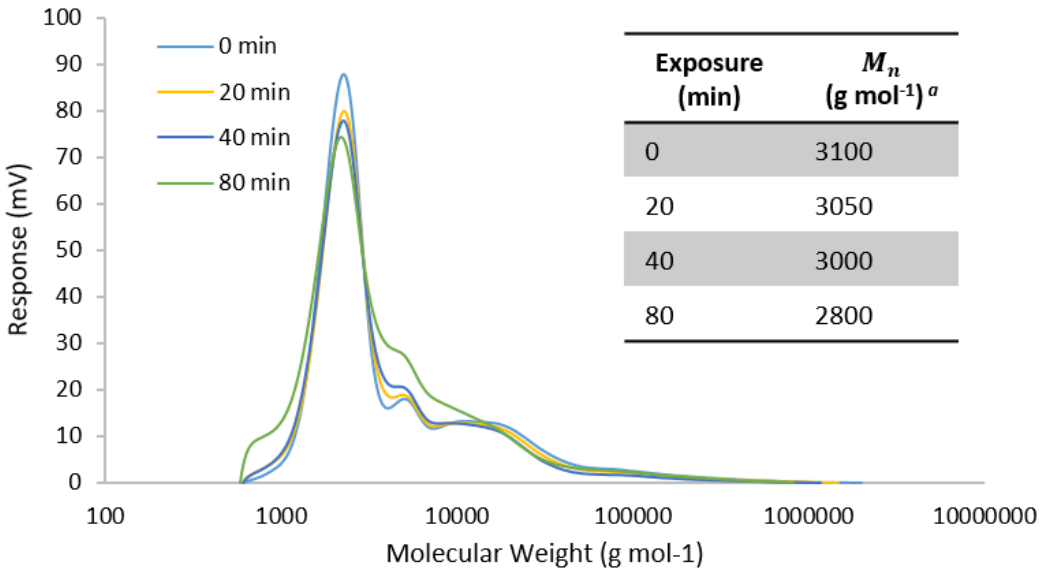

Exposure (min)	M_n (g mol^{-1}) [a]
0	3100
20	3050
40	3000
80	2800

Figure 2.15. Normalised SEC traces of coupled PEG-*o*NB in DMF SEC eluent exposed to increasing durations of UV-Light from the metalight chamber and table illustrating the decrease in number average molecular weight after increasing exposures (using PMMA as standards with DMF as eluent)

Whilst the main peak at M_n = 3100 g mol^{-1} in **Figure 2.15** corresponds to one PEG-*o*NB molecule, the higher molecular weight shoulders are attributed to the addition across acrylate functionalities between polymer chains. Although this side reaction isn't ideal for the creation of a uniformly cross-linked network, the photolysis reaction should still take place and helps exemplify degradability of the material. It was found that the amount of lower molecular weight species increases with increasing UV exposure times. This trend is less clear for the first 40 minutes of exposure, however after 80 minutes there is an obvious shift of the SEC traces to lower molecular weights with a low molecular weight shoulder appearing at *ca*. 1000 g mol^{-1}.

After demonstrating the previously reported ability of PEG-*o*NB to undergo cleavage of the nitrobenzyl ester bond by photolysis in solution, the next step was to establish if the bulk cross-linked material was also capable of undergoing degradation upon exposure to UV light. Initial experiments involved flood irradiating thin films similar to those produced in Section 2.2.2. using the same UV light source utilised to degrade PEG-*o*NB in solution. As a consequence of the thin films being in the solid state in

addition to the inability of the cross-linked materials to be solubilised in solvents, alternative methods of analysing the materials for signs of photolysis had to be employed. Because the photolysis reaction causes several changes to the various different functional groups within PEG-*o*NB, it was postulated that infrared (IR) spectroscopy could be exploited to monitor the changes in vibrational frequencies of these respective functional groups. For example, during the photolysis reaction vibrational frequencies corresponding to the symmetrical and asymmetrical stretching of N-O bonds in the nitro ($-NO_2$) functionality are expected to decrease since they get converted to the nitroso (-NO) functionality during UV exposure.

To confirm degradation *via* IR spectroscopy, the thin films prior to and after both 15 and 30 minutes of exposure to UV light were analysed by IR spectroscopy. The IR spectra (**Figure 2.16**) demonstrate that a reduction in the strength of the vibration corresponding to the $-NO_2$ functionality appears at about 1520 cm^{-1} and a slight increase in the strength corresponding to the stretching frequency of the -NO functionality appears at 1580 cm^{-1}. There is also a slight reduction in the strength of the vibration at 1730 cm^{-1} corresponding the carbonyl absorption found in esters as well as an increase in strength of the vibration corresponding to stretching frequency of the carbonyl functionality in ketones at 1705 cm^{-1}. This is also indicative of photolysis, since it is known to cause cleavage of the nitrobenzyl ester moiety into the respective ketone and carboxylic acid (**Scheme 2.6**). After 30 minutes of exposure to the relatively low powered flood source of UV light no more change in strength of IR absorptions were observed. This was ascribed to the inability of the light source to penetrate the surface of the bulk material. No data in terms of film thickness after irradiation could be collected as a consequence of the necessity to compress the sample

onto the IR diamond which may in turn cause very small alterations to the thickness of the film used.

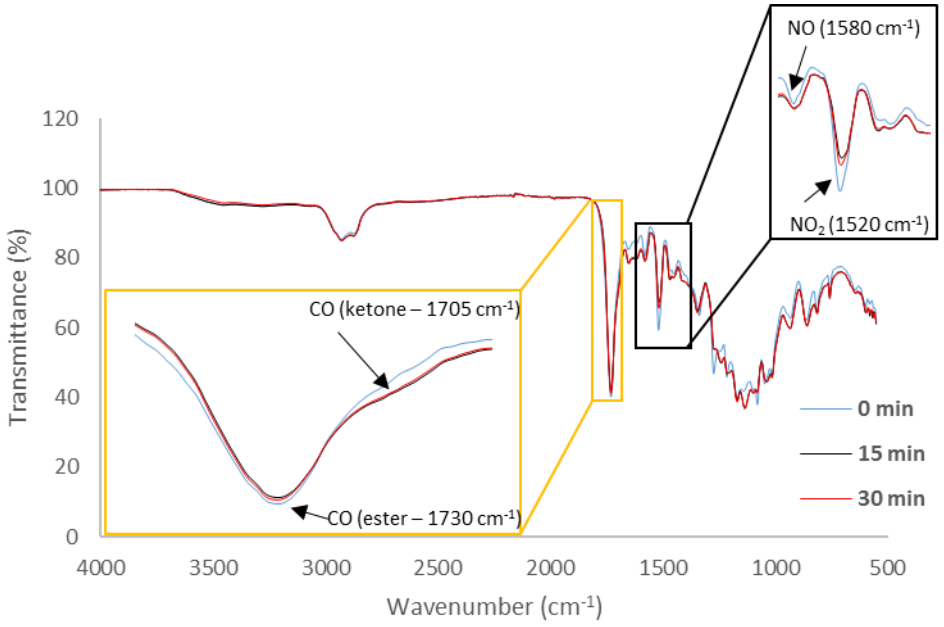

Figure 2.16. FT-IR spectra of cross-linked PEG-*o*NB before and after varying degree of exposure to UV light from the metalight chamber indicating the occurance of photolysis

Despite the IR data suggesting only very minimal degradation on the surface of the sample, this was still considered a promising result since the metalight chamber UV light source used in this experiment was relatively low in power (6 mW cm^{-2}). Previously reported successful attempts at degrading PEG-*o*NB containing hydrogels used irradiation sources with power in the range of 20-40 mW cm^{-2} in order to induce cleavage of the ester bond and achieve visible signs of degradation.[26]

In order to try and improve on this low degree of degradation observed, a far more powerful UV light source was used. The light source used was that of a Fusion UV Inc. Light Hammer (LH) 6 capable of producing 200 Wcm^{-2}, roughly thirty thousand times more powerful than the metalight chamber previously used. Thin films of cross-linked PEG-*o*NB were exposed to varying dosages of UV light from the LH. As a

consequence of the high temperatures generated by the LH, during exposure samples have to be traversed at constant speed by a conveyer belt and therefore, instead of subjecting the samples to different time intervals of UV light, they are subjected to a number of passes of the LH. Thin films (*c.a.* 130 μm) were subjected to 2, 4, 6 and 16 passes of UV light from the LH respectively. **Figure 2.17** shows a much more significant difference between the IR spectra of unexposed films and a film that has been subjected to 16 passes when compared with the previous results (**Figure 2.16**). The peaks corresponding to the -NO_2 functionality and the CO ester group have been reduced more drastically whilst the respective -NO and CO from the ketone are far more apparent, suggesting a greater degree of degradation has occurred. Furthermore, a change in intensity was observed for the broad band around 3200 – 2500 cm^{-1}, signifying an increase in the amount of -OH functionality from the carboxylic acid that is formed during photolysis.

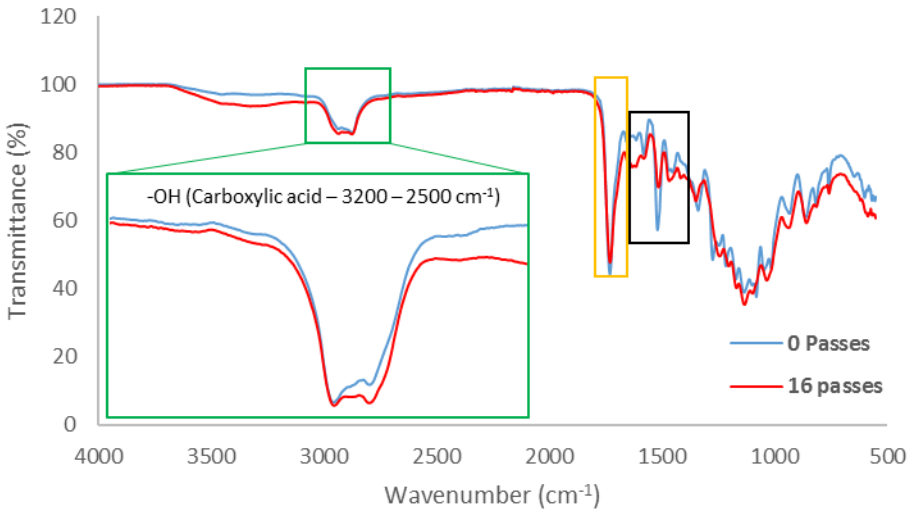

Figure 2.17 FT-IR spectra of cross-linked PEG-*o*NB before and after 16 passes of UV light from the Light Hammer, indicating the increased occurance of photolysis from a more powerful light source

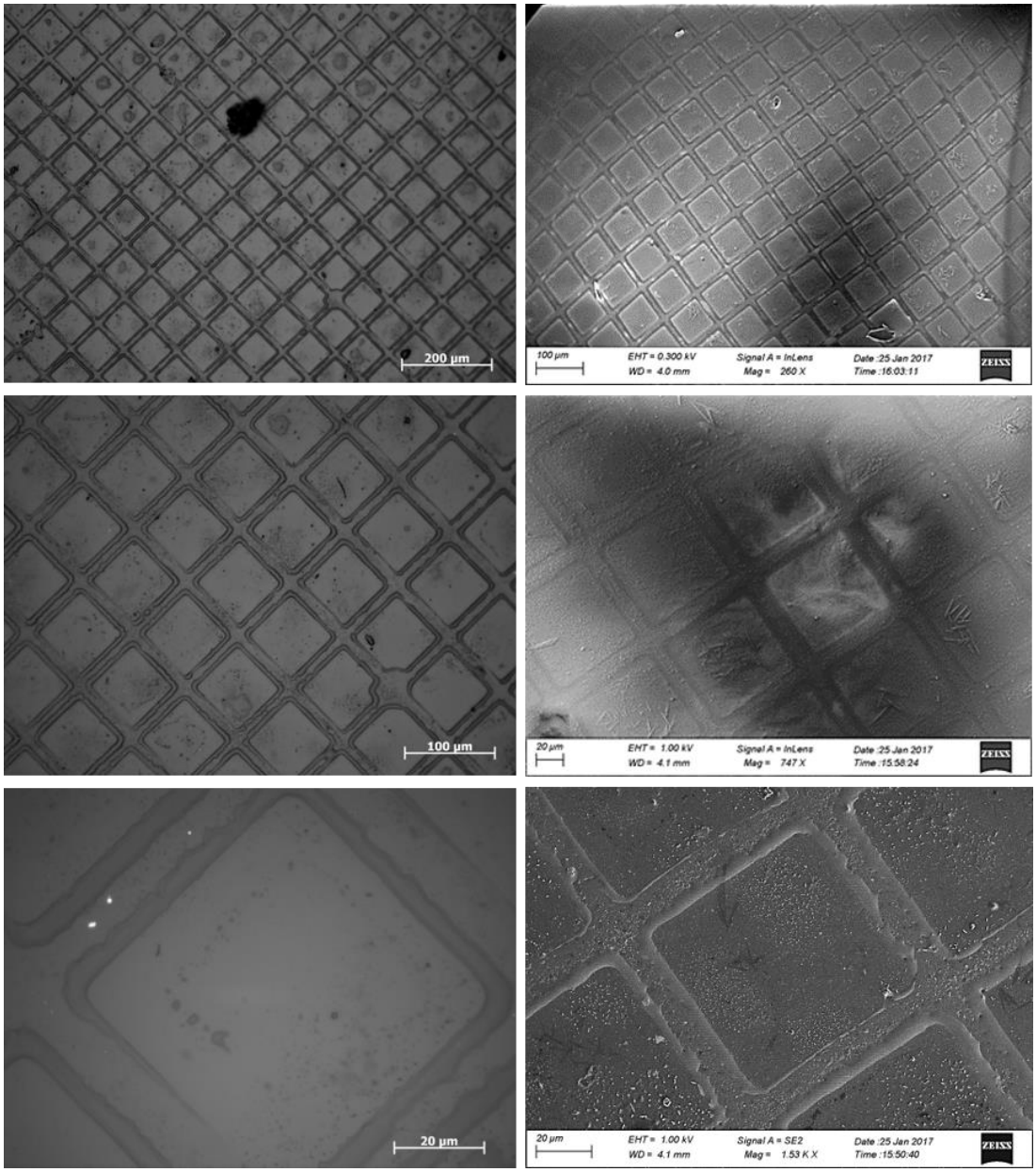

Figure 2.18. Optical microscopy images (Left) and Scanning Electron Microscopy (SEM) (Right) images of the thin film exposed to UV light through the square holes of a TEM grid

To demonstrate selective degradability, a transmission electron microscopy (TEM) grid was used as a photomask. The grid was placed directly on top of the thin films before they were exposed to 2, 4, 6 and 16 passes of the LH as before. Upon removal of the TEM grid the thin films appeared darker in areas where they had been exposed and lighter in unexposed areas suggesting that photolysis was occurring selectively. Upon further examination using optical and scanning electron microscopy (SEM), there appeared to be very little to no difference for the films subjected to 2, 4 and 6

passes. However, for the film subjected to 16 passes there was quite a clear difference between exposed and unexposed areas (**Figure 2.18**). The optical and SEM images show that the areas exposed (squares) look like they are inset from the unexposed areas (lines) that the TEM grid covers. Whilst these images cannot prove that selective etching of the material was achieved, they represent a promising sign and enough evidence to warrant investigation into the 3D profile of the grid.

Vertical scanning interferometry (VSI) was used to analyse the surface of the thin film exposed to 16 passes of the LH (**Figure 2.19**). From the topography of the samples' surface it is clear to see where photolysis has occurred, corresponding to the areas where sample has been etched away. The square shaped recesses that are more red in colour are where the UV light from the LH would have been able to irradiate, whilst the green peaks represent the areas where the sample was covered by the TEM grid.

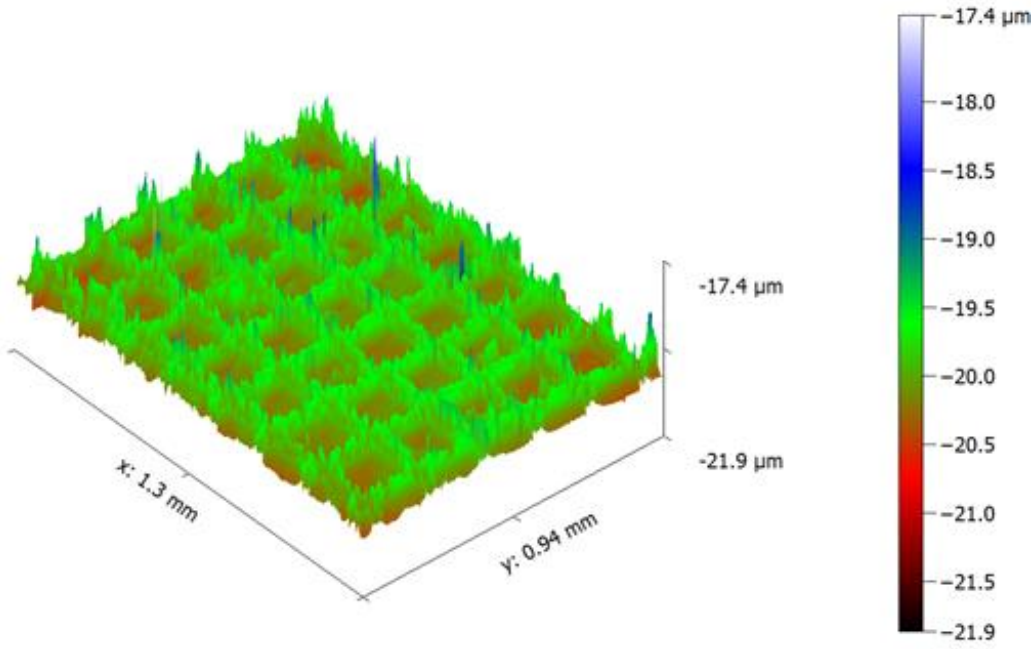

Figure 2.19. VSI 3D profile of the surface of the thin film exposed to 16 passes of the light hammer

By subtracting the height of these peaks (roughly -19 to -19.5 µm) with height from the recesses (roughly -20 to -20.5 µm) an estimate of the degree of degradation into the bulk material can be determined. Although the degree of etching is on the order of

0.5 to 1 µm which was considered negligible considering the layer height for 3D printed part is usually between 50 and 100 times higher it has to be taken into consideration that whilst interferometry is a useful tool in determining surface roughness of materials and in differences in elevation where there is more of a slope between topographic transitions, it isn't particularly accurate where the topographic transition is nearly vertical. The ability of the interferometer to map the surface of a material relies on wavelengths of light undergoing constructive interference on the surface of the material which are reflected back into the instrument and read by a detector. Where a slope on the surface is quite shallow some of the light will be scattered in other directions than back up into the detector, whereas for nearly vertical slopes the majority of light will be scattered therefore leaving voids in data. The fact that the areas exposed are a slightly darker colour to those unexposed will also mean that the light from the interferometer will be reflected back slightly differently. This may also cause inaccuracies in determining the degree of degradation and so alternative options were investigated.

Atomic force microscopy (AFM) was chosen because of its ability to mechanically probe the surface of materials at a much higher resolution (fractions of a nanometer) since it has no diffraction limit. By scanning the position of the sample as compared with the height of the tip of the probe, the surface topography over a small section (90 μm^2) of the sample can be imaged. AFM was carried out on a small section of the thin film exposed to UV from the LH through the TEM grid as a photomask and the result is displayed in **Figure 2.20**.

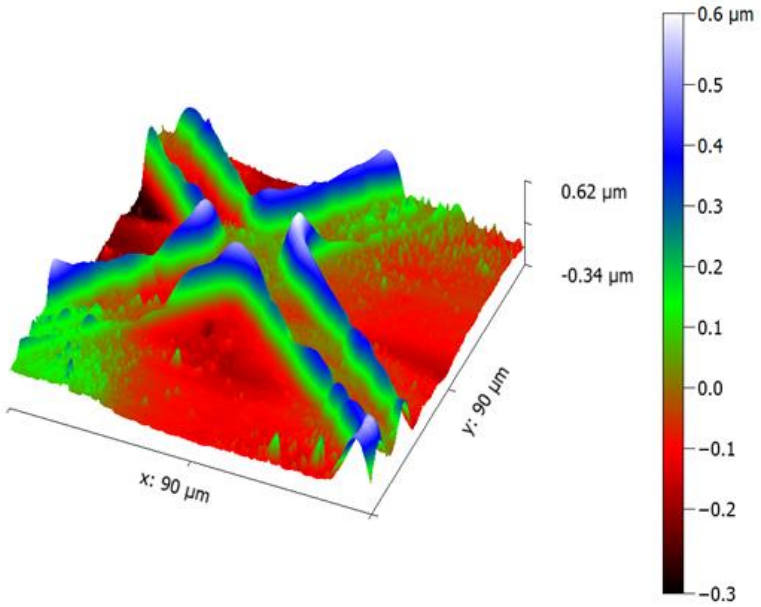

Figure 2.20. Surface topography of cross-section of selectively photodegraded thin film sample acquired by AFM and processed using Gwyddion software

The AFM image (**Figure 2.20**) shows that there is quite a clear difference between exposed areas and unexposed areas. The difference in height between these regions is also in good agreement with the interferometry profile, suggesting that the degree of photodegradation of the material is on the order of 0.5 – 1 µm. The AFM also showed a slight discrepancy in that the centre of the areas that are supposedly meant to be left unexposed have also been etched away to a similar but slightly lesser degree to that observed in the entirely exposed square regions. At first, this undesired etching in the centre of struts was thought to be a consequence of the material melting sooner than undergoing photolysis. However, upon further investigation using thermal analysis techniques by DSC and TGA (**Figure 2.21**) it was found that the cross-linked material had no observable melting points and didn't undergo decomposition until reaching temperatures of greater than 130 °C. Considering that the films exposed to light from the LH wouldn't have experienced such high temperatures it was unlikely for the material to undergo decomposition. Closer inspection of the TEM grid used as a photomask revealed that whilst the edges of the grid were in fact opaque to visible light, the centres of the struts in the grid were slightly transparent making it possible for the LH to etch away some of the material under the grid (**Figure 2.22**).

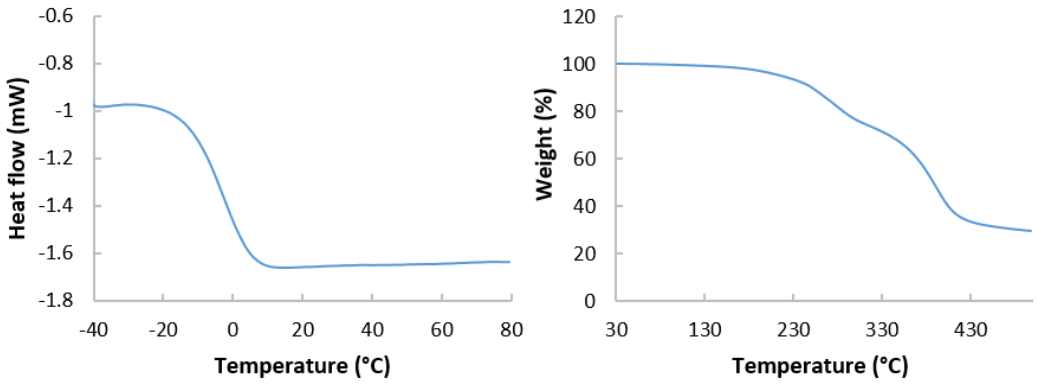

Figure 2.21. DSC (left) and TGA (right) thermal analysis data of PEG-*o*NB showing no observable melting points until thermal degradation onset at 130 °C

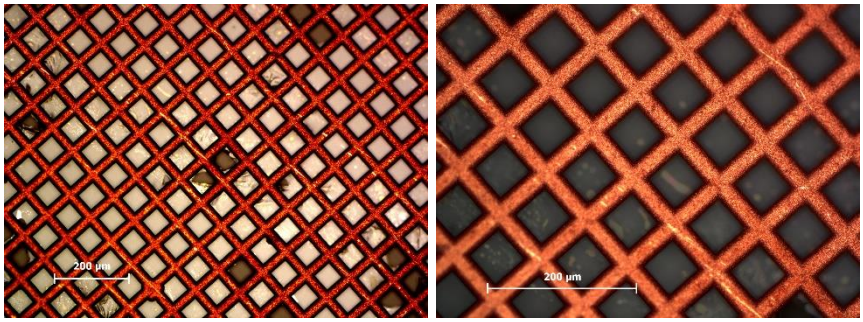

Figure 2.22. Optical microscopy images of the TEM grid used as a photomask depicting the more transparent strut centres (orange/red) as compared with the opaque edges of the grid (dark black)

2.3 Conclusion and future work

The formation of a 4D material with the ability to be photo-cross-linked under one wavelength of light and subsequently etched/degraded away under a secondary wavelength of light has been described. The resin produced was found to be capable of curing defined single layer films with thicknesses and exposure times suitable for use in the µSL process. Whilst the material was shown to be capable of undergoing photolysis and hence selective etching/photodegradability under a secondary wavelength of light, the lengthy exposures and significant amount of power required to achieve less than 1 µm was considered too great and therefore limited the materials applicability in an on-line subtractive process. However, having to utilise such high intensity UV light also means that the material will not undergo degradation under ambient light conditions and so any secondary subtractive process carried out on the part would be deliberate in a second processing step as was intended. Consequently, it may be possible to gradually refine selected regions of the part utilising a UV laser attached to a robotic system to expose these regions and subsequently wash away etched material between exposures. Future work should focus on scaling up the synthesis of the material to make it more suited to being able to 3D print with it and consequently generate parts that can be tested for their ability to be refined in a secondary subtractive process.

The material may also find use as a potential support material that can be removed using flood irradiation sooner than being mechanically removed (as is the case with currently used support structures), thereby negating any possibility of defects forming as a consequence of tool damage. The resin can also be considered a combination of a negative and positive type photoresist. Whilst negative and positive type photoresists have been previously developed they haven't displayed an ability to be processed by

µSL since their initial cross-linking has been slow (40 minutes) and has been carried out by flood irradiating solvent cast films in a non-controlled manner.[45] Such slow curing times would result in prints that take days to weeks rather than hours and so the PEG-*o*NB based resin developed herein with exposure times of less than a minute is a significant improvement and one that lends the material to be compatible with the µSL process. Furthermore, to the best of the authors knowledge, it is the first example of a PEG-*o*NB based system capable of being cross-linked under one wavelength of light and subsequently degraded under a second.

As a consequence of having to maintain low viscosity in the initial resin, short PEG chains have to be employed which would involve using relatively large amounts of the laboriously synthesised *o*NB. One potential route for not only increasing the scale at which the material can be produced at, but also providing 3D printed objects with a greater degree of photodegradability would be to utilise longer PEG chains in an aqueous system and therefore print hydrogels. Considering the wealth of literature describing photodegradable hydrogels using *o*NB based materials it is surprising that none have endeavoured to initially attempt to 3D print them. Perhaps some of the problems associated with photo-cross-linking *o*NB detailed within this chapter has hindered previous research and therefore by exploiting our newly developed system new doors may be opened to realising truly 4D printed hydrogel materials.

2.4 References

1. Leist, S. K.; Zhou, J., Current status of 4D printing technology and the potential of light-reactive smart materials as 4D printable materials. *Virtual and Physical Prototyping* **2016,** *11* (4), 249-262.

2. Tibbits, S., 4D Printing: Multi-Material Shape Change. *Architectural Design* **2014,** *84* (1), 116-121.

3. Ge, Q.; Qi, H. J.; Dunn, M. L., Active materials by four-dimension printing. *Applied Physics Letters* **2013,** *103* (13), 131901.

4. Zarek, M.; Layani, M.; Cooperstein, I.; Sachyani, E.; Cohn, D.; Magdassi, S., 3D Printing of Shape Memory Polymers for Flexible Electronic Devices. *Adv. Mater.* **2016,** *28* (22), 4449-4454.

5. Ge, Q.; Sakhaei, A. H.; Lee, H.; Dunn, C. K.; Fang, N. X.; Dunn, M. L., Multimaterial 4D Printing with Tailorable Shape Memory Polymers. *Sci. Rep.* **2016,** *6*, 1-11.

6. de Las Heras Alarcon, C.; Pennadam, S.; Alexander, C., Stimuli responsive polymers for biomedical applications. *Chem. Soc. Rev.* **2005,** *34* (3), 276-285.

7. Roy, D.; Cambre, J. N.; Sumerlin, B. S., Future perspectives and recent advances in stimuli-responsive materials. *Prog. Polym. Sci.* **2010,** *35* (1-2), 278-301.

8. Stuart, M. A.; Huck, W. T.; Genzer, J.; Muller, M.; Ober, C.; Stamm, M.; Sukhorukov, G. B.; Szleifer, I.; Tsukruk, V. V.; Urban, M.; Winnik, F.; Zauscher, S.; Luzinov, I.; Minko, S., Emerging applications of stimuli-responsive polymer materials. *Nat. Mater.* **2010,** *9* (2), 101-113.

9. Mano, J. F., Stimuli-Responsive Polymeric Systems for Biomedical Applications. *Advanced Engineering Materials* **2008,** *10* (6), 515-527.

10. Hoffman, A. S., Stimuli-responsive polymers: biomedical applications and challenges for clinical translation. *Adv. Drug. Deliv. Rev.* **2013,** *65* (1), 10-16.

11. Katz, J. S.; Burdick, J. A., Light-responsive biomaterials: development and applications. *Macromol. Biosci.* **2010,** *10* (4), 339-348.

12. Meng, H.; Hu, J., A Brief Review of Stimulus-active Polymers Responsive to Thermal, Light, Magnetic, Electric, and Water/Solvent Stimuli. *J. Intell. Material Syst. Struct.* **2010,** *21* (9), 859-885.

13. Bertrand, O.; Gohy, J.-F., Photo-responsive polymers: synthesis and applications. *Polym. Chem.* **2017,** *8* (1), 52-73.

14. Katsonis, N.; Lubomska, M.; Pollard, M.; Feringa, B.; Rudolf, P., Synthetic light-activated molecular switches and motors on surfaces. *Prog. Surf. Sci.* **2007,** *82* (7-8), 407-434.

15. Feng, C. L.; Zhang, Y. J.; Jin, J.; Song, Y. L.; Xie, L. Y.; Qu, G. R.; Jiang, L.; Zhu, D. B., Reversible Wettability of Photoresponsive Fluorine-Containing Azobenzene Polymer in Langmuir−Blodgett Films. *Langmuir* **2001,** *17* (15), 4593-4597.

16. Lim, H. S.; Han, J. T.; Kwak, D.; Jin, M.; Cho, K., Photoreversibly Switchable Superhydrophobic Surface with Erasable and Rewritable Pattern. *J. Am. Chem. Soc.* **2006,** *128* (45), 14458-14459.

17. Delorme, N.; Bardeau, J. F.; Bulou, A.; Poncin-Epaillard, F., Azobenzene-Containing Monolayer with Photoswitchable Wettability. *Langmuir* **2005,** *21* (26), 12278-12282.

18. Rosario, R.; Gust, D.; Hayes, M.; Jahnke, F.; Springer, J.; Garcia, A. A., Photon-Modulated Wettability Changes on Spiropyran-Coated Surfaces. *Langmuir* **2002,** *18* (21), 8062-8069.

19. Zhao, H.; Sterner, E. S.; Coughlin, E. B.; Theato, P., o-Nitrobenzyl Alcohol Derivatives: Opportunities in Polymer and Materials Science. *Macromolecules* **2012,** *45* (4), 1723-1736.

20. Luo, Y.; Shoichet, M. S., A photolabile hydrogel for guided three-dimensional cell growth and migration. *Nat. Mater.* **2004,** *3* (4), 249-253.

21. Wosnick, J. H.; Shoichet, M. S., Three-dimensional chemical patterning of transparent hydrogels. *Chem. Mater.* **2008,** *20*, 55-60.

22. Kloxin, A. M.; Kasko, A. M.; Salinas, C. N.; Anseth, K. S., Photodegradable hydrogels for dynamic tuning of physical and chemical properties. *Science* **2009,** *324* (5923), 59-63.

23. Wong, D. Y.; Griffin, D. R.; Reed, J.; Kasko, A. M., Photodegradable Hydrogels to Generate Positive and Negative Features over Multiple Length Scales. *Macromolecules* **2010,** *43* (6), 2824-2831.

24. Johnson, J. A.; Finn, M. G.; Koberstein, J. T.; Turro, N. J., Synthesis of photocleavable linear macromonomers by ATRP and star macromonomers by a tandem ATRP-click reaction: Precursors to photodegradable model networks. *Macromolecules* **2007,** *40*, 3589-3598.

25. Peng, K.; Tomatsu, I.; van den Broek, B.; Cui, C.; Korobko, A. V.; van Noort, J.; Meijer, A. H.; Spaink, H. P.; Kros, A., Dextran based photodegradable hydrogels formed via a Michael addition. *Soft Matter* **2011,** *7* (10), 4881-4887.

26. DeForest, C. A.; Anseth, K. S., Cytocompatible click-based hydrogels with dynamically tunable properties through orthogonal photoconjugation and photocleavage reactions. *Nat. Adv. Mater. Chem.* **2011,** *3* (12), 925-931.

27. DeForest, C. A.; Anseth, K. S., Photoreversible patterning of biomolecules within click-based hydrogels. *Angew. Chem. Int. Ed. Engl.* **2012,** *51* (8), 1816-1819.

28. Zhao, Y., Photocontrollable block copolymer micelles: what can we control? *J. Mater. Chem.* **2009,** *19* (28), 4887-4895.

29. Truong, V. X.; Tsang, K. M.; Simon, G. P.; Boyd, R. L.; Evans, R. A.; Thissen, H.; Forsythe, J. S., Photodegradable Gelatin-Based Hydrogels Prepared by Bioorthogonal Click Chemistry for Cell Encapsulation and Release. *Biomacromolecules* **2015,** *16* (7), 2246-2253.

30. Griffin, D. R.; Schlosser, J. L.; Lam, S. F.; Nguyen, T. H.; Maynard, H. D.; Kasko, A. M., Synthesis of photodegradable macromers for conjugation and release of bioactive molecules. *Biomacromolecules* **2013,** *14* (4), 1199-1207.

31. Micelles, L.-d. B. C.; Jiang, J.; Tong, X.; Morris, D.; Zhao, Y., Toward Photocontrolled Release Using. *Synthesis* **2006**, 4633-4640.

32. Li, L.; Deng, X.-X.; Li, Z.-L.; Du, F.-S.; Li, Z.-C., Multifunctional Photodegradable Polymers for Reactive Micropatterns. *Macromolecules* **2014,** *47* (14), 4660-4667.

33. Radl, S.; Kreimer, M.; Manhart, J.; Griesser, T.; Moser, A.; Pinter, G.; Kalinka, G.; Kern, W.; Schlögl, S., Photocleavable epoxy based materials. *Polymer* **2015,** *69*, 159-168.

34. Leigh, S. J.; Gilbert, H. T.; Barker, I. A.; Becker, J. M.; Richardson, S. M.; Hoyland, J. A.; Covington, J. A.; Dove, A. P., Fabrication of 3-dimensional cellular constructs via microstereolithography using a simple, three-component, poly(ethylene glycol) acrylate-based system. *Biomacromolecules* **2013,** *14* (1), 186-192.

35. Kloxin, A. M.; Tibbitt, M. W.; Anseth, K. S., Synthesis of photodegradable hydrogels as dynamically tunable cell culture platforms. *Nat. Protoc.* **2010,** *5* (12), 1867-1887.

36. Holmes, C. P., Model Studies for New o-Nitrobenzyl Photolabile Linkers: Substituent Effects on the Rates of Photochemical Cleavage. *J. Org. Chem.* **1997,** *62*, 2370-2380.

37. Roberts, J. J.; Bryant, S. J., Comparison of photopolymerizable thiol-ene PEG and acrylate-based PEG hydrogels for cartilage development. *Biomaterials* **2013,** *34* (38), 9969-9979.

38. O'Brien, A. K.; Cramer, N. B.; Bowman, C. N., Oxygen inhibition in thiol–acrylate photopolymerizations. *J. Polym. Sci. A Polym. Chem.* **2006,** *44* (6), 2007-2014.

39. Barker, I. A.; Ablett, M. P.; Gilbert, H. T. J.; Leigh, S. J.; Covington, J. A.; Hoyland, J. A.; Richardson, S. M.; Dove, A. P., A microstereolithography resin based on thiol-ene chemistry: towards biocompatible 3D extracellular constructs for tissue engineering. *Biomater. Sci.* **2014,** *2* (4), 472-475.

40. Kulkarni, R. K.; Moore, E. G.; Hegyeli, A. F.; Leonard, F., Biodegradable poly(lactic acid) polymers. *J. Biomed. Mater. Res.* **1971,** *5* (3), 169-181.

41. Schuller-Ravoo, S.; Feijen, J.; Grijpma, D. W., Preparation of flexible and elastic poly(trimethylene carbonate) structures by stereolithography. *Macromol. Biosci.* **2011,** *11* (12), 1662-1671.

42. Schuller-Ravoo, S.; Teixeira, S. M.; Feijen, J.; Grijpma, D. W.; Poot, A. A., Flexible and elastic scaffolds for cartilage tissue engineering prepared by stereolithography using poly(trimethylene carbonate)-based resins. *Macromol. Biosci.* **2013,** *13* (12), 1711-1719.

43. Il'ichev, Y. V.; Schwörer, M. A.; Wirz, J., Photochemical Reaction Mechanisms of 2-Nitrobenzyl Compounds: Methyl Ethers and Caged ATP. *J. Am. Chem. Soc.* **2004,** *126* (14), 4581-4595.

44. Pelliccioli, A. P.; Wirz, J., Photoremovable protecting groups: reaction mechanisms and applications. *Photochem. Photobiol. Sci.* **2002,** *1* (7), 441-458.

45. Wei, J.; Hoogen, N.; Lippert, T.; Hahn, C.; Nuyken, O.; Wokaun, A., Characterisation of combined positive-negative photoresists by excimer laser ablation. *Applied Physics A: Materials Science and Processing* **1999,** *69*, 849-853.

3. Synthesis and characterisation of poly(malates) *via* direct polycondensation and their potential as candidates for use in μSL

3.1. Introduction

Owing to the continuing depletion of petrochemical-based polymers as a consequence of finite oil supplies, the demand for developing new materials from renewable feedstocks is ever-growing.[1] Currently, the only renewable biomass derived material demonstrated to be compatible with the microstereolithography (μSL) process is that of PDLLA.[2-4] Whilst poly(DL-lactide) (PDLLA) has proven to be successfully exploited in several biomedical applications, its hydrophobic nature causes degradation in *vivo* to be inherently slow, thereby limiting its applicability.[5-7] For instance, in the field of μSL, PDLLA has only been considered for tissue engineering applications because it has mechanical properties that approach that of bone.[4, 8-9] To advance the μSL technology further, a broader range of material properties and functionalities are required and so an alternative biomass derived renewable material with alternate traits and enhanced degradability was sought.

Poly(malic acid) (PMA) is a poly(carboxylic acid) derived from renewable resources and is well known for its ability to undergo bulk degradation leading to non-toxic, water soluble oligomers and small malic acid molecules *via* hydrolysis.[10] This degradability is a consequence of the hydrophilic nature of the material therefore introduction of functionalies into the poly(malic acid) backbone with hydrophobic molecules can tune the degradability.[11] The ability to tune degradation in biomedical applications is desirable for several reasons. For example, in the case of tissue engineering scaffolds, not all tissues within the body heal at the same rate and so being able to match the degradation rate with the rate of healing of a certain tissue is highly desirable.[12] Furthermore, in the case of small molecule/drug release, knowing the rate at which the material containing the drug degrades can be advantageous in determining the rate of release. In addition to allowing hydrophobicity tuneability, functionalising

the backbone of PMA with reactive groups, such as alkenes or alkynes, provides cross-linking junctions as required to be processed by µSL.

As well as the necessity for polymers used in µSL to have cross-linkable functionalities, polymers are also required to have a low viscosity.[13] The low viscosity is usually achieved by various methods, including the use of viscosity modifiers (*e.g.* reactive/non-reactive diluents) or a heated resin vat.[14-16] Moreover, if the molecular weight of the polymer used is low enough, the amount of modification required to reduce the viscosity can be lessened. In doing so, more of the properties exhibited by the chosen polymer will be maintained in the printed material and the part created should also be of higher accuracy since the use of viscosity modifiers is well known to induce shrinkage in the part.[3] Avoiding elevated temperatures to reduce the viscosity also allows for more flexibility in choosing the crosslinking chemistry. For example, whilst potentially toxic, acrylate chemistry can tolerate slightly raised temperatures before premature cross-linking occurs, the more temperature sensitive thiol-ene based chemistry cannot.[15, 17] Therefore, suitable methods for producing low molecular weight (LMW) polymers/oligomers on a large scale, whilst abiding to as many green chemistry principles as possible, were investigated herein.

In the past, PMA has been synthesised using ring-opening polymerisation (ROP) or condensation based techniques.[18] The use of ROP has been studied intensively because of its ability to produce high molecular weight polymers, in relatively short time scales under milder conditions.[19] Monomers produced for ROP of malic acid are usually either based on four membered or six-membered rings produced by cyclization through the alcohol and β-carboxylic acid or by dimerization of the alcohol and α-carboxylic acid, respectively (**Scheme 3.1**).[20-22] Because protic species may deactivate or prematurely initiate commonly used catalysts, the free carboxylic group of MA

based ROP monomers is normally protected with benzyl protecting groups.[23] Such protecting groups would normally be removed post-polymerisation to afford PMA (**Scheme 3.1**), however, by selecting protecting groups that can be functionalised post-polymerization, the desired functionality of the final polymer can be acquired. For example, Leboucher-Durand *et al.* replaced the benzyl protecting group of benzyl *β*-malactonate with alkene containing substituents which were later epoxidized post-polymerisation.[24] Although such elegant strategies for producing functionalised PMA are very successful, the requirements associated with ROP makes it not possible for production of large quantities of material in an industrial environment. In particular, not only are numerous steps required to synthesise and purify the initial monomers, the ROP process usually requires inert conditions and that the monomers must be exhaustively dried from moisture to eliminate side reactions from occurring, making it unsuitable for scale-up.

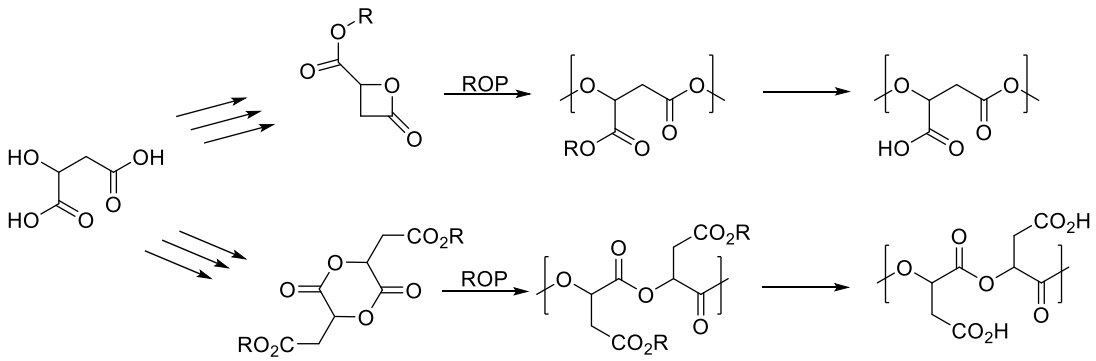

Scheme 3.1. Schematic illustrating the numerous steps involved in producing monomers for ring opening polymerisation into the respective poly(malate) esters and subsequent deprotection steps to afford PMA.

Polycondensation of malic acid is a more straightforward alternative and there have been several examples of researchers using complex strategies to produce high molecular weight polymers *via* this method. For example, early work carried out by Ohtani *et al.* and Kajiyama *et al.* has shown to be more than suitable for producing short chain polymers/oligomers directly from MA in a one-step process (**Scheme 3.2**).[25-34] Ohtani *et al*. were able to utilize direct thermal polycondensation to produce

poly(α, β–malic acid) with a number average molecular weight (M_n) of 2000 g mol^{-1} (by SEC). Kajiyama *et al.* later improved upon this using tin based catalysts to produce polymers of a higher molecular weight (M_n = 2800 g mol^{-1}). Whilst both authors eluded to the possibility of using the prepared PMA in biomedical applications, no follow-up reports on their subsequent application were found in the literature. This lack of follow-up work was likely as a consequence of the relative LMW of the polymers thereby limiting the resulting materials properties. One avenue for investigation that has been overlooked was the possibility of using similarly LMW polymers in cross-linked networks thereby enhancing mechanical properties and making them more suitable for a wider scope of biomedical applications.

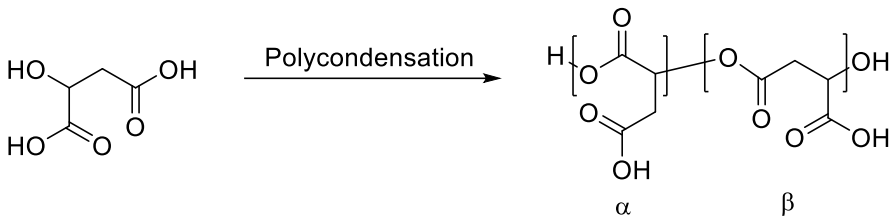

Scheme 3.2. Schematic demonstrating the direct polycondensation of malic acid into the respective poly(α, β-malic acid)

Bin *et al.* used the thermal polycondensation techniques to produce PMA (M_n = 1400 g mol^{-1}) that was subsequently chain-end functionalised with 2-hydroxyethyl methacrylate (HEMA) and employed the polymer in the preparation of photo-polymerised, cross-linked biodegradable hydrogels, demonstrating the applicability of LMW PMA in biomedical based applications.[35] However, the use of PMA derivatives in preparing bulk cross-linked networks, specifically within the field of µSL, has been overlooked.

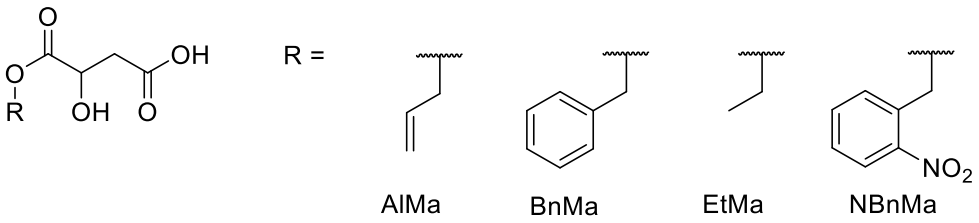

Figure 3.1. Figure showing the various malate α-ester monomers including Allyl malate (AlMa), Benzyl malate (BnMa), Ethyl malate (EtMa) and Nitrobenzylmalate (NBnMa).

Since MA contains two carboxylic acids and one secondary alcohol per molecule, it can form polyesters either through α or β linkages. Thus, it was envisioned that esterifying one of the carboxylic acids would allow for incorporation of the desired functionality while maintaining the molecules ability to polymerise through the remaining carboxylic acid. This concept was previously investigated in a study carried out by Ohtani *et al.*, who demonstrated the ability to copolymerise β-ethyl malate with malic acid utilising the thermal polycondensation technique.[34] Therefore, several monomers (**Figure 3.1**) were initially chosen to provide a wide scope of potential functionality, in addition to increasing the chances of finding a material compatible with the µSL process.

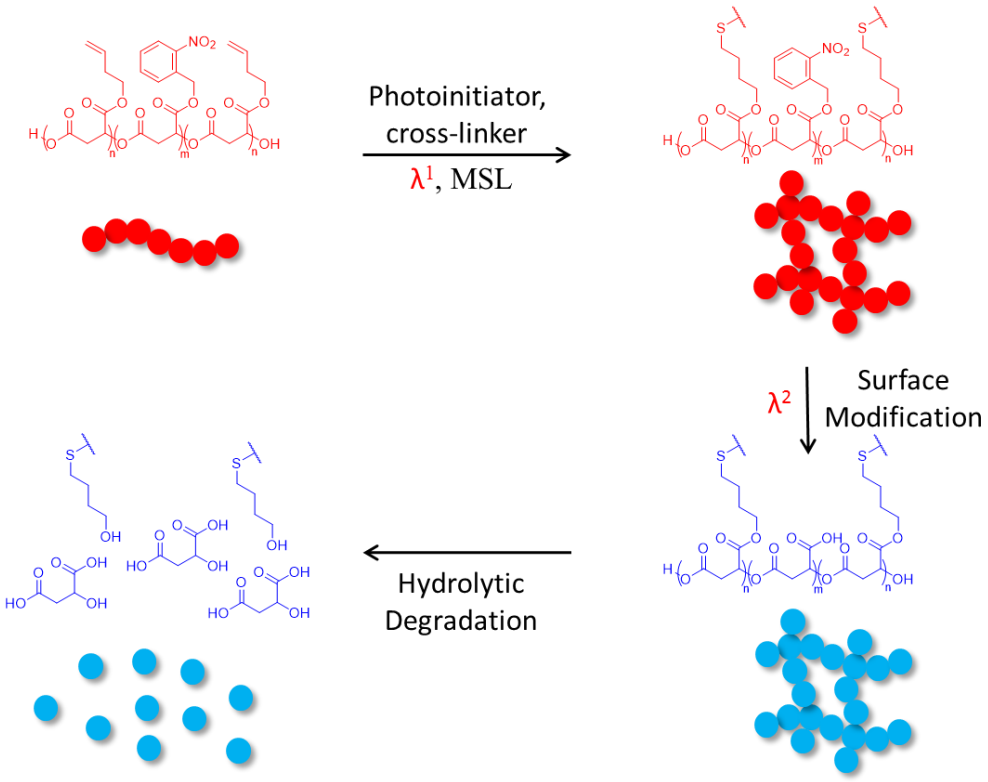

Figure 3.2. Schematic representing the concept of utilising a hydrophobic (red) photoresponsive monomer in the copolymer that, upon exposure to one wavelength of light could undergo cross-linking in the µSL process. The subsequent photolysis of the cross-linked material would yield the hydrophilic (blue) poly(malic acid) making it more hydrophilic and susceptible to water ingress leading to hydrolytic degradation on the surface.

Allyl malate (AlMa) was first chosen to provide the necessary functionality for cross-linking of the material *via* radical thiol-ene chemistry.[36] Copolymerisation of AlMa

with one of benzyl malate (BnMa) and ethyl malate (EtMa) was anticipated to demonstrate the difference between the hydrophobicity of aromatic and aliphatic alkyl based substituents. Finally, the use of nitrobenzyl malate (NBnMa) was expected to produce a material whose surface wettability could be controlled *via* UV light as an external stimulus, thereby potentially creating another 4D printing material (**Figure 3.2**).

This chapter focusses on the synthesis of monomers outlined above and the subsequent homopolymerisation of these monomers with a model study being carried out on BnMa to determine the optimum polymerisation conditions. Drop shape analysis was used to verify that the different homopolymers behave as expected as well as to demonstrate that p(NBnMa) could have its hydrophobicity controlled by UV light. In addition, BnMa, EtMa and NBnMa were copolymerised with an alkene functional monomer to investigate their compatibility with the µSL process. A small molecule study with dodecanethiol was also undertaken to determine whether cross-linking would be achievable.

3.2. Results and discussion

3.2.1. Monomer synthesis

To synthesise the various malic acid esters (malates) required for polycondensation, a procedure originally described by Miller *et al.* was adopted with some modifications in the case of malates not previously reported.[37] Ring closing of *DL*-malic acid was initially carried out using TFAA yielding the trifluoroacetate of malic acid anhydride. Subsequent ring opening with the respective alcohol then occurred predominantly at the more electropositive carboxy group *α* to the hydroxyl group as a consequence of the electron withdrawing effect of the trifluoroacetate functionality.

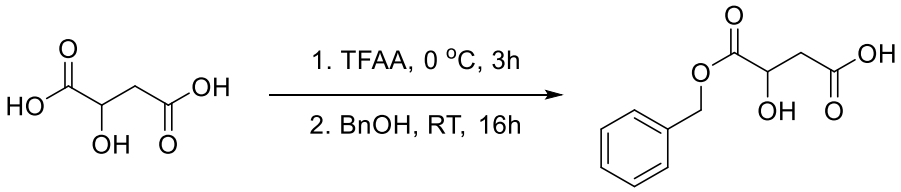

Scheme 3.3. Synthesis of benzyl malate via initial ring closing of malic acid using TFAA followed by subsequent ring opening of MAA by benzyl alcohol

Benzyl malate (BnMa) was first synthesized (**Scheme 3.3**) with a final yield of 77%. and the structure of the pure product was confirmed by ^{1}H NMR spectroscopy (**Figure 3.3**). Similarly, the nitrobenzyl derivative was synthesized from nitrobenzyl alcohol starting material (**Scheme 3.4**) with a yield of 72% (**Figure 3.4**).

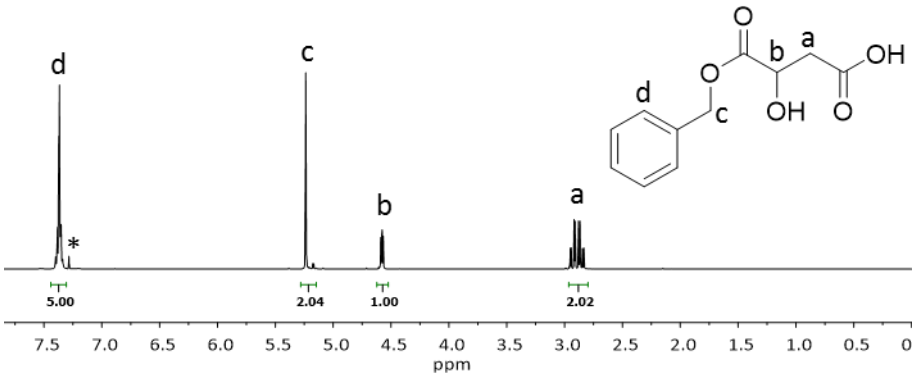

Figure 3.3. ^{1}H NMR spectrum of Benzyl malate (BnMa) after purification by acidic work up ($CDCl_3$, 400 MHz, 293 K, * = $CHCl_3$)

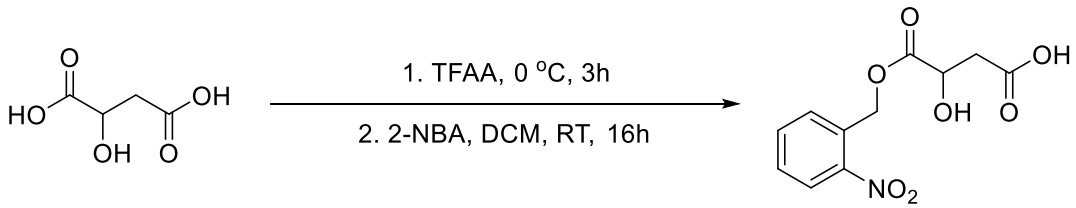

Scheme 3.4. Synthesis of nitrobenzyl malate *via* initial ring closing of malic acid using TFAA followed by subsequent ring opening of MAA by nitrobenzyl alcohol in DCM

Both butenyl malate (BuMa) (**Scheme 3.5**) and ethyl malate (EtMa) (**Scheme 3.6**) were synthesised in a comparable manner to BnMa, however, as a consequence of the respective alcohols having much lower boiling points and therefore being more volatile, any excess 3 buten-1-ol or ethanol was removed by vacuum distillation at slightly raised temperatures (35-40 °C). BuMa was found to require no further purification after removal of excess 3-buten-1-ol and could be produced with high yield (*ca.* 95%) (**Figure 3.5**). EtMa could then be further purified by recrystallization from ethyl acetate and hexane to afford the product in 54% yield (**Figure 3.6**). BuMa was used instead of AlMa since AlMa was found to be unstable under subsequent polymerisation conditions likely as a consequence of the more reactive allyl functionality and also couldn't be stored for more than a few weeks.

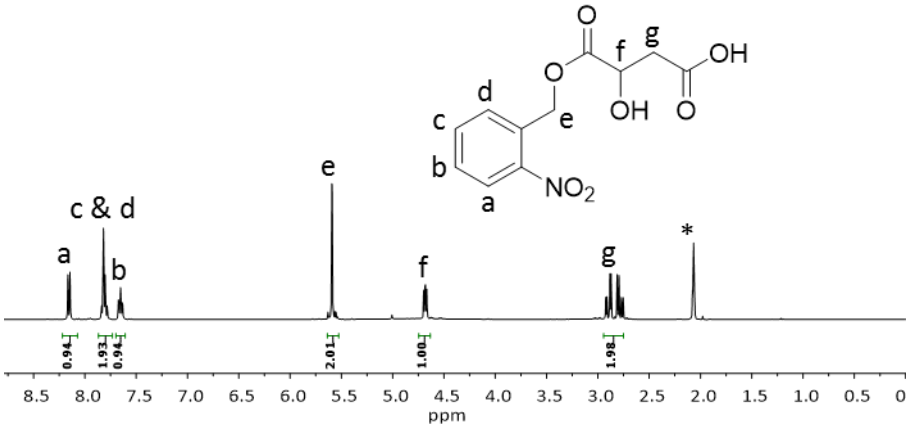

Figure 3.4. ^{1}H NMR spectrum of nitrobenzyl malate (NBnMa) after purification by acidic work up ($CDCl_3$, 400 MHz, 293 K, * = Acetone)

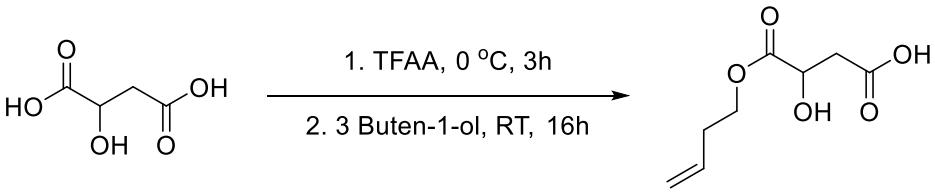

Scheme 3.5. Synthesis of butenyl malate *via* initial ring closing of malic acid using TFAA followed by subsequent ring opening of MAA by 3 buten-1-ol

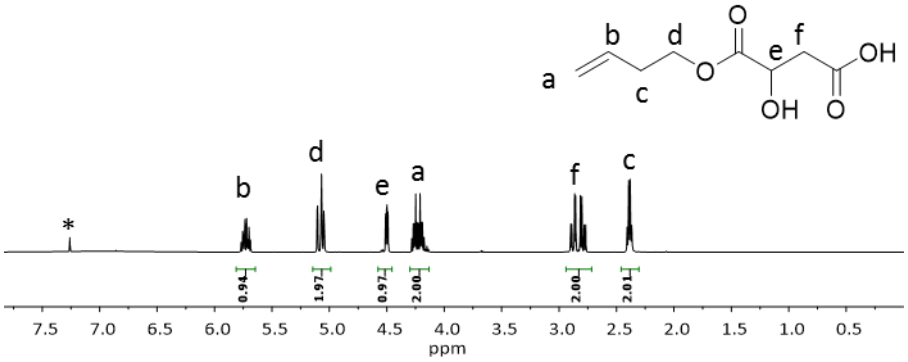

Figure 3.5. ^{1}H NMR spectrum of butenyl malate (BuMa) after removal of excess 3 buten-1-ol by high vacuum distillation at 35 °C ($CDCl_3$, 400 MHz, 293 K, * = $CHCl_3$)

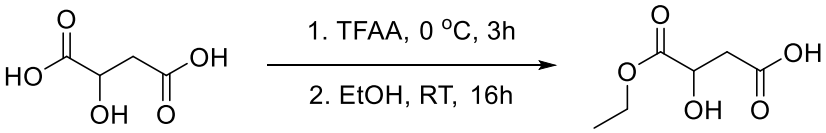

Scheme 3.6. Synthesis of ethyl malate *via* initial ring closing of malic acid using TFAA followed by subsequent ring opening of MAA by ethanol

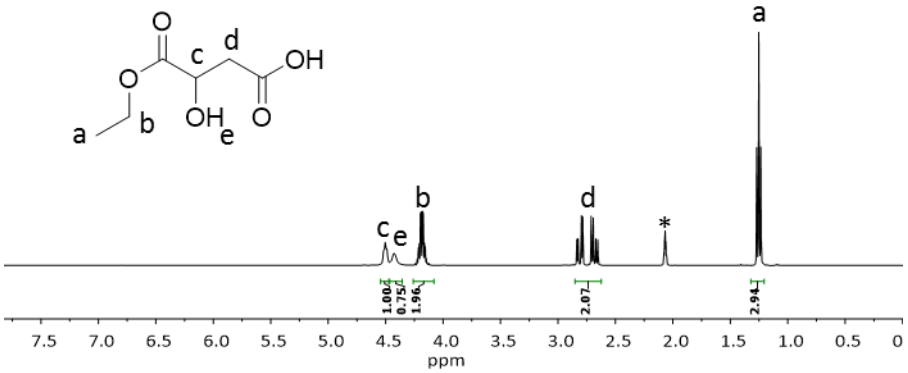

Figure 3.6. ^{1}H NMR spectrum of ethyl malate (EtMa) after purification by recrystallisation ($CDCl_3$, 400 MHz, 293 K, * = Acetone)

3.2.2. Homopolymer synthesis

3.2.2.1. Bulk polycondensation

Preliminary studies into the ability of the prepared monomers to undergo polymerisations under elevated temperatures were initially assessed using BnMa. To adhere to green chemistry principles, the use of organic solvents was avoided. Thus, all high temperature polymerisations of BnMa were carried out in bulk and under high vacuum (*ca.* 11 mmHg) to remove water produced during condensation. Using a similar approach to that reported by Kajiyama *et al.*,[32-33] BnMa was heated at temperatures between 110 °C and 140 °C for several days (**Scheme 3.7**). Whilst Kajiyama *et al.* exploited the use of tin-based catalysts in their work to speed up reaction times it was considered more favourable to endure long reaction times rather than risk possible contamination of toxic metal in the resultant polymer products. Monomer conversion for all BnMa polymerisations were monitored by following the change in chemical shift of the proton next to the secondary alcohol in the monomer compared to proton next to the ester group in the polymer (δ at 4.55 ppm and 5.52 ppm respectively) (**Figure 3.7**).

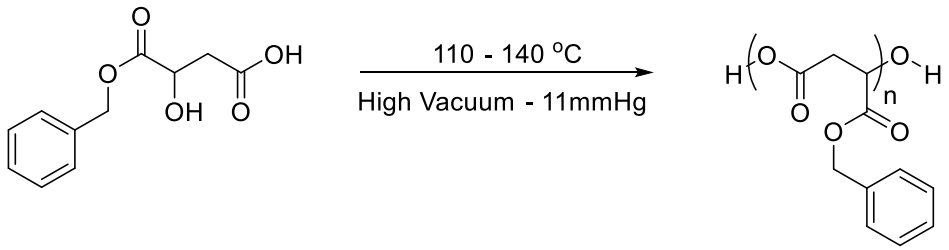

Scheme 3.7. Synthesis of P(BnMa) *via* direct polycondensation of BnMa at elevated temperatures under reduced pressure

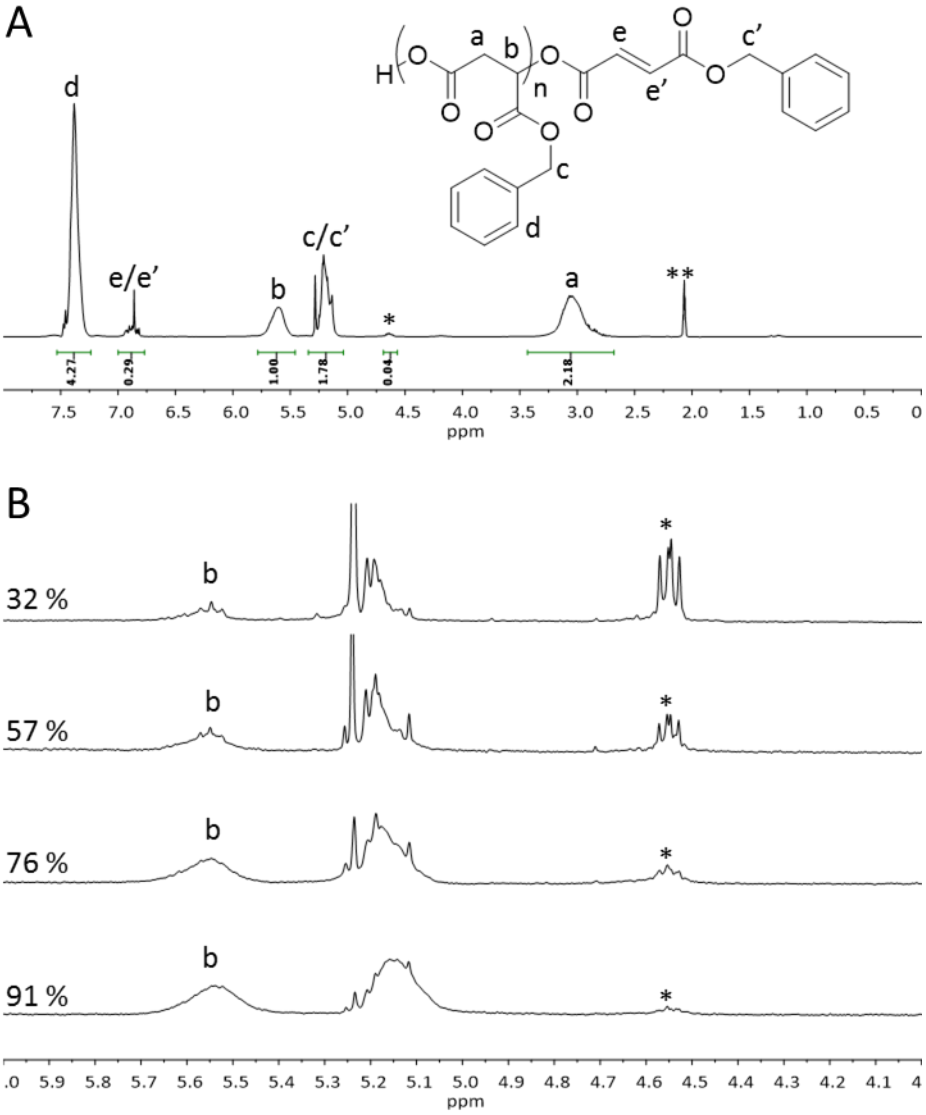

Figure 3.7. (A) Assigned ^{1}H NMR spectrum (top) and (B) zoomed in spectra illustrating the decrease in signal intensity corresponding to the proton next to the secondary alcohol of the monomer (*) compared to the increase in signal intensity corresponding to the same proton in the polymer as conversion increases. ($(CD_3)_2CO$, 400 MHz, 293K ** = Acetone)

The polymerisation of BnMa follows step-growth polymerisation mechanism in which, providing the monomer is pure, there is an exact stoichiometric equivalence of the two reacting groups (carboxylic acid and alcohol). Because of this stoichiometric equivalence the Carothers equation (1.1.) can be used to determine the number average degree of polymerisation (DP), $\overline{x}_n$, where p is the extent of the reaction or conversion as determined by ^{1}H NMR spectroscopic analysis.

$$\overline{x}_n = \frac{1}{1-p} \tag{3.1}$$

Using p, the determination of the number average molar mass, M_n, using the following equation (3.2), can be achieved.

$$M_n = M_0 \overline{x}_n \tag{3.2}$$

Where M_0 is the mean molar mass of a single monomer unit. However, because of the side reaction leading to formation of fumarate groups *via* dehydration of the secondary alcohol (detailed later on in this chapter and described in **Figure 3.7**) the actual number average molar mass, M_n, determined by SEC analysis may be different from the calculated value.

To determine the optimum temperature for producing high molecular weight polymers the M_n, M_w (weight averaged molecular weight), dispersity ($Đ_m$) and conversion were recorded for homopolymerisations of BnMa carried out at 110, 120, 130 and 140 °C (**Table 3.1**). The dispersities of the resultant polymers at all temperatures approached 2 with increasing degrees of conversion, which is expected for step-growth polymerisation. The highest molecular weights were achieved for polymerisations carried out at the temperatures of 110 and 120 °C for 242 and 160 h respectively. The polymerisation carried out at 110 °C produced P(BnMa) with M_n and M_w values of 2500 and 4800 g mol^{-1} respectively, whilst the polymerisation carried out at 120 °C produced P(BnMa) with M_n and M_w values of 2500 and 4900 g mol^{-1} respectively. These values are comparable to those reported by Kajiyama *et al*., however, in this work no catalyst was used leading to longer reaction times. In addition to there being an absence of catalyst, the longer reaction times required to drive the polymerisation to completion were also a result of the steric hindrance of the bulky benzyl substituent in the monomer structure.

Table 3.1. Extent of reaction and SEC data for the direct polycondensation of BnMa to P(BnMa) at various temperatures

Temperature (°C)	Time (hours)	Conversion (%)[a]	SEC M_w[b]	SEC M_n[b]	$Đ_m$[b]
110	96	70	1800	1300	1.32
110	120	76	2500	1600	1.6
110	144	84	3300	2000	1.67
110	168	91	3700	2100	1.75
110	192	93	4500	2400	1.85
110	218	95	4700	2400	1.92
110	242	95	4800	2500	1.92
110	262	99	5000	2400	2.05
120	72	75	2700	1600	1.66
120	94	93	3800	2200	1.73
120	118	93	4400	2300	1.89
120	136	95	4700	2300	2.03
120	160	95	4900	2500	1.94
130	45	91	3800	1900	1.98
130	69	88	3700	2000	1.86
130	89	95	3800	2100	1.77
130	113	97	3900	2100	1.88
140	21	76	2100	1100	1.81
140	26	83	2800	1700	1.7
140	33	91	2500	1300	1.98
140	49	94	2400	1200	1.99

[a] obtained by ^{1}H NMR spectroscopic analysis ($(CD3)_2CO$, 400 MHz) [b] obtained by SEC in DMF as eluent using PMMA standards

Increasing the temperature of the polymerisation to 130 and 140 °C decreased the polymerisation time significantly compared to the polymerisation carried out at 110 °C, (*ca.* 50 and 75% faster, respectively, see **Figure 3.8**). While the polymerisation carried out at 130 °C took 5 days to reach 97% conversion, only 2 days were required to reach 94% at 140 °C. This increase in the polymerisation rate is a consequence of

the faster rate of water removal at elevated temperatures. However, compared to those carried out at lower temperatures, the molecular weights of the polymers produced at high temperature were significantly lower. Indeed, the molecular weight of P(BnMa) produced at 130 °C after 89 h had the same conversion (95 %) as the polymerisation carried out at 110 °C after 242 h and resulted in the M_n and M_w values of 2100 and 3800 g mol^{-1} respectively compared to 2500 and 4800 g mol^{-1} respectively. This is further exemplified by the polymerisation carried out at 140 °C whereby at 91% conversion it had the M_n and M_w values of 1300 and 2500 g mol^{-1} respectively whereas the polymerisation carried out at 110 °C, upon reaching the same conversion of 91%, had an M_n and M_w of 2100 and 3700 g mol^{-1} respectively.

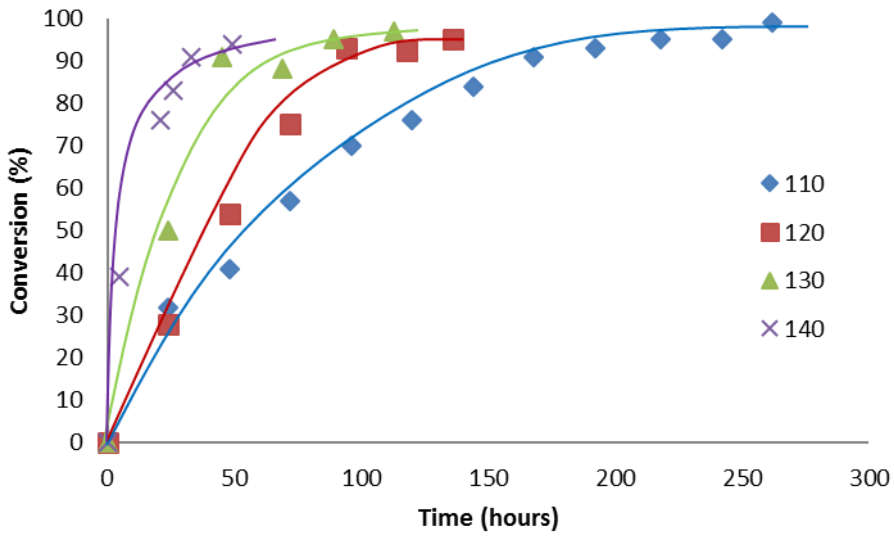

Figure 3.8. Plot of conversion against time for the homopolymerisation of BnMa carried out at temperatures between 110 and 140 °C in the absence of catalyst.

This decrease in polymer molecular weight observed for higher temperatures at similarly high conversions can be attributed to side reactions becoming more dominant. At lower temperatures intermolecular dehydration between growing chains is still the dominant reaction whereas at higher temperatures intramolecular dehydration becomes more competitive and forms fumarate end-capped chains (**Scheme 3.8**). Under these conditions, the alkoxy functionality is removed hence

changing the stoichiometry of the system thereby terminating the propagation of polymer chain ends leading to polymers with a lower molecular weight.

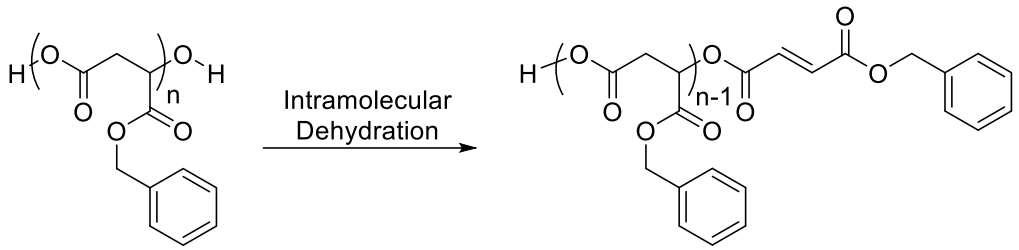

Scheme 3.8. Formation of fumarate end-capped polymer chains caused by the competitive intramolecular dehydration side reaction

This phenomenon can also be observed in the SEC traces (**Figure 3.9**) that demonstrate that, for all polymerisations taken to their highest conversion, there is significant differences in the overall molecular weight depending on the temperature used. Whilst polymerisations carried out at 110 and 120 °C nearly overlap, those carried out at 130 and 140 °C have traces shifted to lower molecular weights and in the case of the 140 °C experiment, multiple peaks at molecular weights between 100 and 1000 g mol^{-1} can be observed. These peaks were attributed to the increased fumarate formation in both monomer and poly/oligomer species in doing so halting polymerisation in addition to depolymerisation caused by transesterification. Such depolymerisation can also be seen in the SEC data in **Table 3.1** whereby the molecular

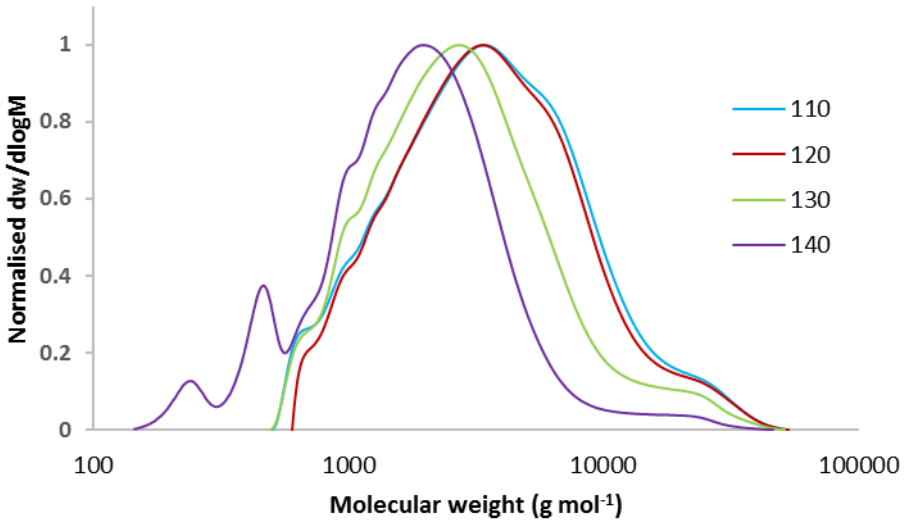

Figure 3.9. SEC chromatograms of P(BnMa) synthesised by polymerising BnMa at varying reaction temperatures between 110 and 140 °C. Samples measured against PMMA standards using DMF as eluent

weight for the polymerisation carried out at 140 °C decreases from M_n and M_w values of 1700 and 2800 at 83 % conversion down to 1200 and 2400 g mol^{-1} respectively at 94 % conversion.

The increase in the amount of fumarate formation can also be observed in the ^{1}H NMR spectra of the polymers prepared at different temperatures (**Figure 3.10**). There is a clear increase in the signal corresponding to olefinic protons at δ = 6.9 ppm as the temperature is increased. This is in agreement with previous reports in which the fumaric acid was formed in purely malic acid based polymerisations in bulk and at elevated temperatures.[32-33, 38]

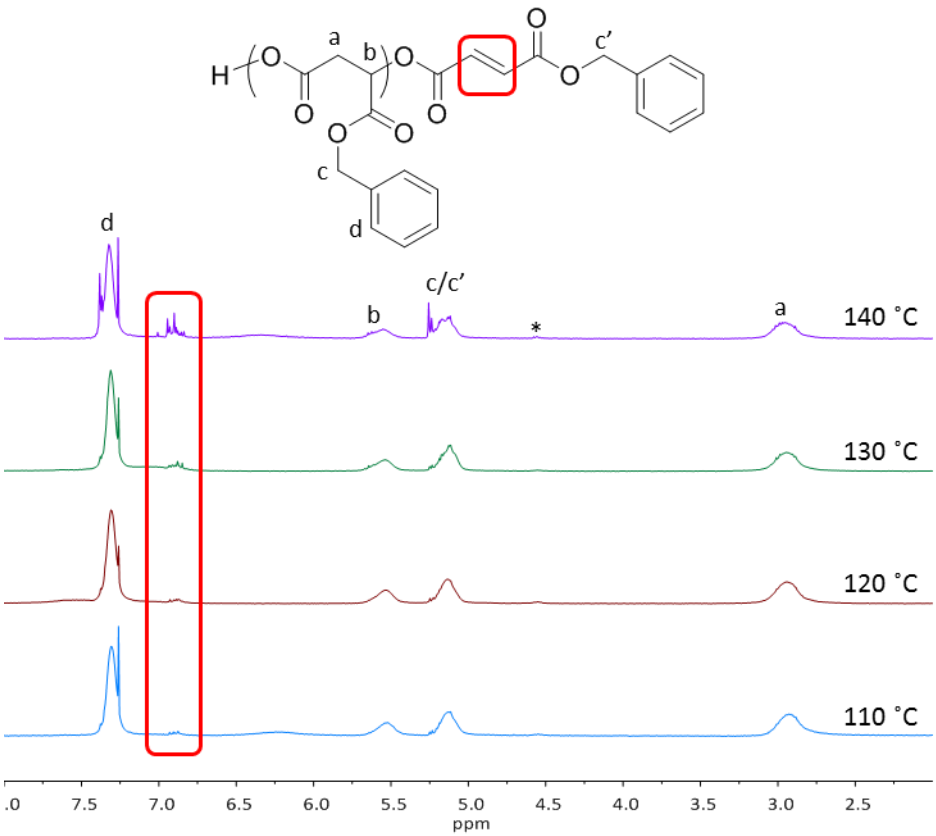

Figure 3.10. ^{1}H-NMR spectrum depicting the increasing formation of fumarate based by-products caused by intramolecular dehydration at increasing temperatures

Since the polymers produced herein are to be used in µSL, a small amount of fumarate terminated chains was considered to be a favourable and, to a certain extent, a beneficial side reaction. Not only does it produce an additional cross-linking junction for the thiol-ene crosslinking, it also helps with the low molecular weight necessary to

maintain a low resin viscosity. Therefore 130 °C was chosen as the suitable temperature to carry out subsequent polymerisations.

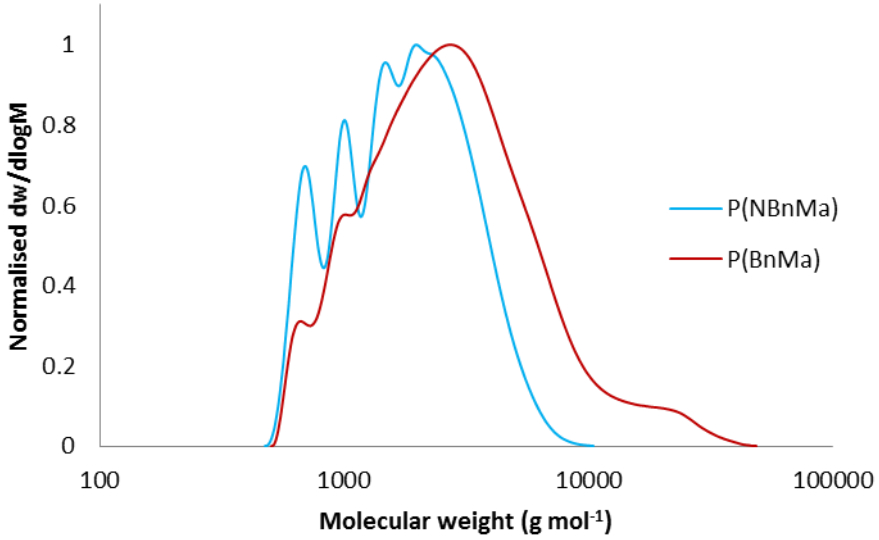

Figure 3.11. SEC chromatogram of P(NBnMa) and P(BnMa) produced at 130 °C depicting the higher intensity of lower molecular weight species formed as a consequence of fumarate formation. Samples measured against PMMA standards using DMF as eluent

With the polymerisation temperature optimised, the homopolymerisation of NBnMa was carried out under the same conditions and whilst achieving similarly high conversions in a shorter period of time, a decrease in molecular weight was observed (**Table 3.2**). BnMa was found to produce higher molecular weight polymers (M_n = 2000 and M_w = 3700 g mol^{-1}) after a similar amount of time being polymerised at 130 °C as compared with NBnMa (M_n = 1500 and M_w = 2100 g mol^{-1}) despite NBnMa having gone to a higher conversion (94 %) than BnMa (88 %). SEC analysis (**Figure 3.11**) shows there are an increased amount of low molecular weight peaks for P(NBnMa) compared with P(BnMa) therefore suggesting that there is more chain termination occurring as a consequence of fumarate formation. Even at the lower temperature of 110 °C the presence of the olefin protons resulting from this side reaction, was shown to be much greater for P(NBnMa) as compared with P(BnMa) as confirmed by ^{1}H NMR spectroscopic analysis (**Figure 3.12**). This increased amount

of fumarate formation for P(NBnMa) was attributed to the more electron withdrawing nature of the nitrobenzyl group.

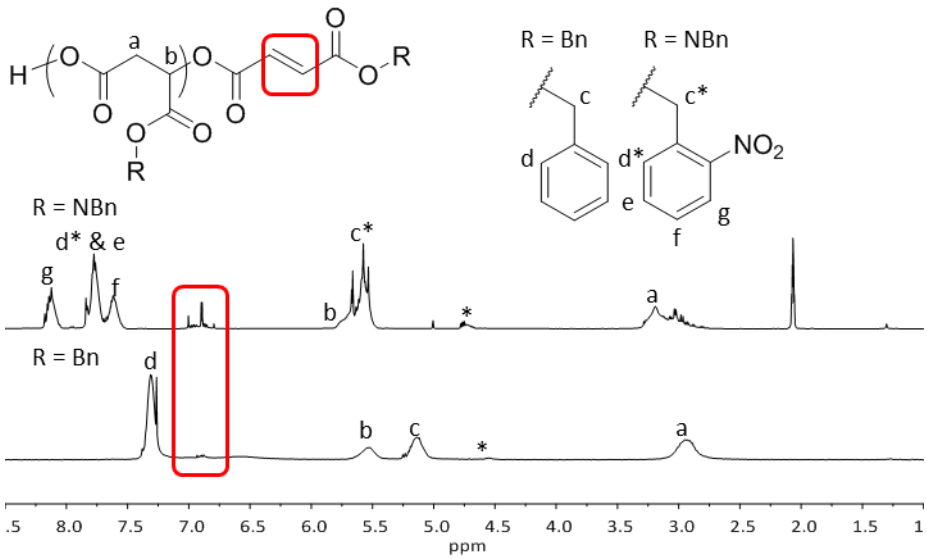

Figure 3.12. ^{1}H NMR spectra of P(NBnMa) and P(BnMa) produced after 7 days illustrating the increased presence of fumarate formation for the NBnMa containing polymer ($(CD_3)_2CO$, 400MHz (PNBnMa) and ($CDCl_3$, 400MHz P(BnMa))

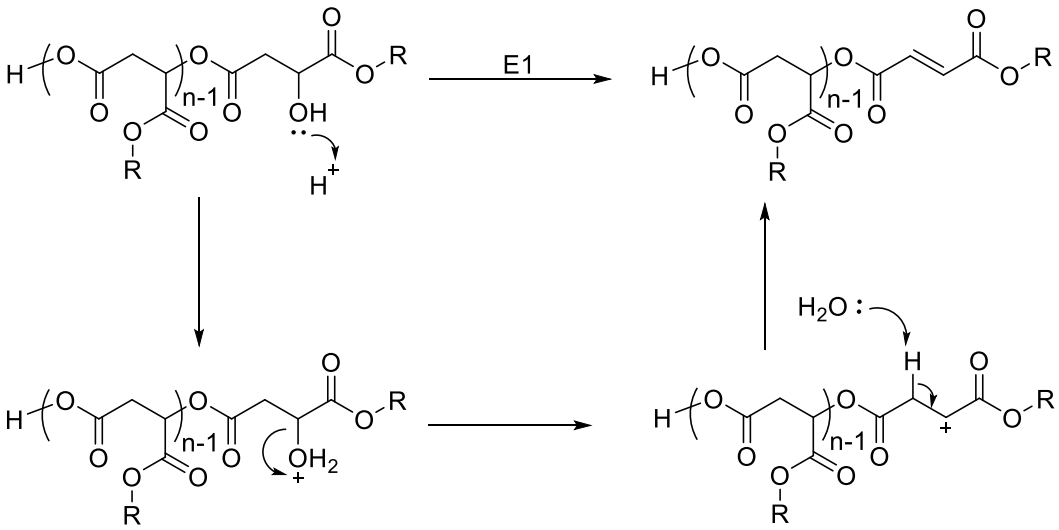

Scheme 3.9. Scheme illustrating the dehydration of the secondary alcohol at the poly(malate) propagating chain end *via* the E1 elimination mechanism

If the dehydration of the secondary alcohol were to undergo a unimolecular rate determining elimination (E1) mechanism (**Scheme 3.9**), a carbocation at the chiral carbon of the malate molecule/propagating chain end would form. However, this is less likely since the carbocation would be unstable next to the carbonyl group. Thus,

it is more likely that the dehydration occurs *via* an $E1_{CB}$ mechanism (**Scheme 3.10**) whereby proton abstraction is followed by elimination of the -OH leaving group. If a more electron withdrawing group (EWG) is used such as the nitrobenzyl ester, the carbonyl group adjacent to the ester will be less delocalised making the carbanion destabilised thereby promoting the elimination reaction and causing more fumarate formation. With a more electron donating group (EDG) such as the benzyl ester, the formation of the carbanion is less likely as it would be more stabilised.

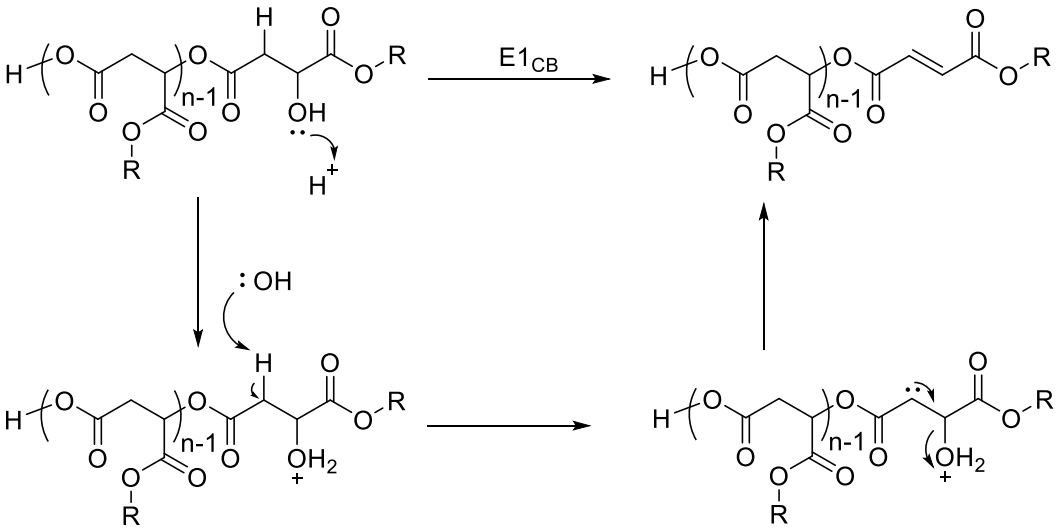

Scheme 3.10. Scheme illustrating the dehydration of the secondary alcohol at the poly(malate) propagating chain end *via* the $E1_{CB}$ elimination mechanism

In order to decrease the amount of fumarate formation, the temperature of the NBnMa polymerisation was reduced to 110 °C. Both Ethyl malate (EtMa) and Butenyl Malate (BuMa) were also polymerised at this temperature for direct comparison (**Scheme 3.11**). The respective monomer conversion and molecular weights of these homopolymerisations were followed by ^{1}H NMR spectroscopy and SEC analyses respectively (**Table 3.2**). After one week of reacting under vacuum at 110 °C P(NBnMa) and P(EtMa) both achieved similar molecular weights despite P(NBnMa) having gone to a significantly higher conversion (P(NBnMa) = 96 %, P(EtMa) = 90 %). P(NBnMa) had M_n and M_w values of 1900 and 2800 g mol^{-1} respectively whereas P(EtMa) had lower M_n and M_w values of *ca.* 1800 and 2200 g mol^{-1} respectively. The

similarity in molecular weight was attributed to the ethyl ester being more electron donating compared with the nitrobenzyl ester, leading to lower degree of chain termination by fumarate formation.

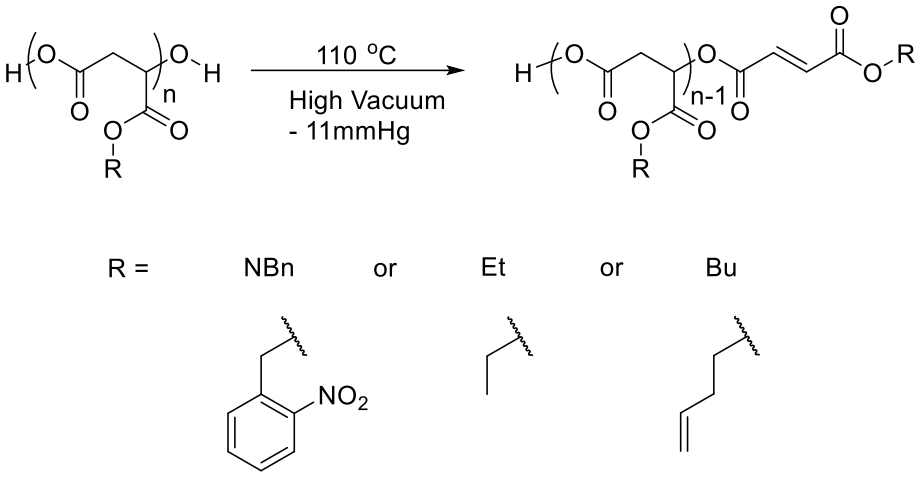

Scheme 3.11. Scheme depicting the homopolymerisation of the various different malates produced at 110 °C

Table 3.2. Extent of reaction and SEC data for the direct polycondensation of NBnMa, EtMa and BuMa to their respective homopolymers carried out at 130 °C[1] and/or 110 °C[2]

Homopolymer	Time (hours)	Conversion (%) [a]	SEC M_w [b]	SEC M_n [b]	$Đ_m$ [b]
P(NBnMa)[1]	72	94	2100	1500	1.40
P(NBnMA) [2]	48	79	1900	1400	1.33
P(NBnMA) [2]	94	89	2400	1700	1.40
P(NBnMA) [2]	120	92	2600	1800	1.46
P(NBnMA)[2]	142	95	2700	1800	1.47
P(NBnMA) [2]	168	96	2800	1900	1.46
P(EtMa) [2]	72	71	1800	1600	1.16
P(EtMa) [2]	96	80	2000	1700	1.21
P(EtMa) [2]	122	86	2100	1800	1.20
P(EtMa) [2]	168	90	2200	1800	1.23
P(BuMa) [2]	72	82	2100	1500	1.39
P(BuMa) [2]	96	84	2100	1500	1.44
P(BuMa) [2]	122	84	2200	1500	1.44
P(BuMa) [2]	168	83	2200	1400	1.54

[a] obtained by ^{1}H NMR spectroscopic analysis ($(CD3)_2CO$, 400 MHz) [b] obtained by SEC in DMF as eluent using PMMA standards

Considering that BuMa contains the more electron withdrawing butenyl group it was unsurprising that it produced lower molecular weight P(BuMa) polymers (M_n = 1400 and M_w = 2200 g mol^{-1}) as compared with the other homopolymers. Whilst following the polymerisation of BuMa by SEC analysis, the low molecular weight peak at *ca.* 1000 g mol^{-1} was found to increase significantly after 3 days (**Figure 3.13**). This suggested that the intramolecular dehydration side reaction was becoming more dominant. It was also observed that the P(BuMa) was becoming highly viscous and, to a certain extent, not dissolving in SEC eluent or deuterated solvent required for characterisation. This suggests that cross-linking was occurring because of the presence of reactive functionalities under such harsh conditions. The crosslinked fractions may not pass through the SEC filter thereby only lower molecular weight fractions were observed in the SEC chromatograms. Therefore, the polymerisation of BuMa was stopped at 80% conversion to avoid unwanted crosslinking reaction.

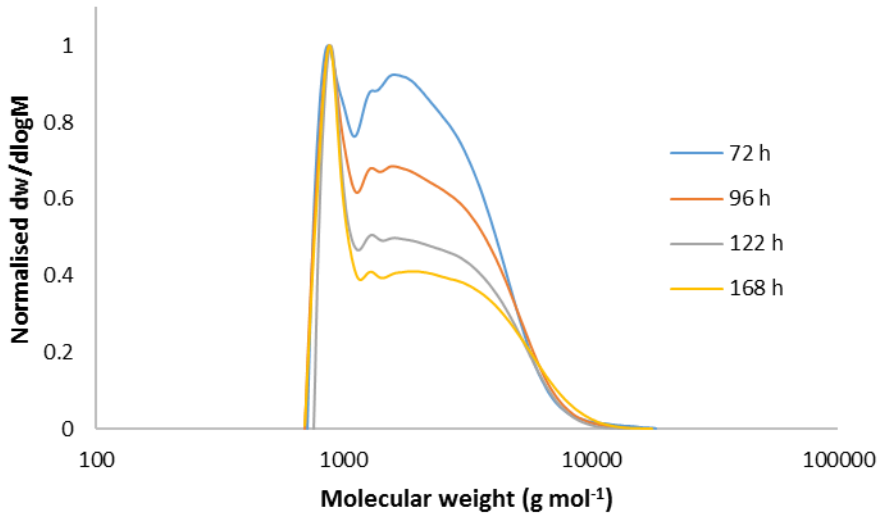

Figure 3.13. SEC chromatograms of P(BuMa) at varying extents of polymerisation depicting the increased intensity of low molecular weight species formed. Samples measured against PMMA standards using DMF as eluent

3.2.2.2. Low temperature step-growth polymerisation

Because polymerisation of the malate hydroxy acid monomers under high temperatures and low pressures led to an undesirable degree of formation of side product, especially in the case of monomers with more electron withdrawing esters attached, an alternative method for polymerising the monomers under milder conditions was investigated. Since step-growth polymerisations are, in most cases, considered to be continuous expansions of coupling reactions from simple organic chemistry in order to form polymer chains, efforts were focussed on methods in which the alcohol and carboxylic acid functionalities can be coupled.

As a consequence of the requirement to carry out the polymerisation at low temperatures in addition to the fact that the monomers used are relatively inactive (unlike their amine counterparts) the use of activated esters was necessary. The prospect of utilising acid halide based monomers was ruled out because of the high reactivity of acid halides towards hydroxyl groups making the synthesis of monomer challenging, if not impossible. Attention was, however, drawn towards the potential use of dehydrating agents such as carbodiimides in order to activate carboxylic acids towards ester formation. Whilst carbodiimide chemistry has been extensively studied in the area of peptide synthesis, it is only recently that this coupling chemistry has been investigated for the synthesis of polyesters.[39-40]

Moore *et al.* pioneered the early work in this area whereby they demonstrated that high molecular weight polyesters could be prepared from hydroxyl acids using a combination of diisopropylcarbodiimide (DIC) and 4-(dimethylamino)pyridinium 4-toluene-sulfonate (DPTS) (an adduct of dimenthylamino pyridine (DMAP) and *para*-tolune sulfonic acid (*p*TSA)) as the catalysts (**Figure 3.14**).[41] Preliminary experiments showed that a 1:1 molar ratio of DMAP and *p*TSA was optimal in minimising the

production of *N*-acylurea by-products allowing for higher degree of conversion in addition to the recycling of the *N*-acylpyridinium species which is required for subsequent catalytic cycles.[41]

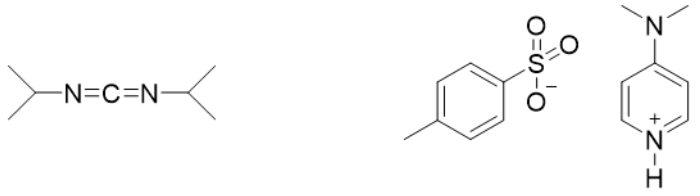

N,N'-diisopropylcarbodiimide (DIC)

4 -(dimethylamino)pyridinium 4-toluene-sulfonate (DPTS)

Figure 3.14. Chemical structures of the carbodiimide (*N*,*N*'diisopropylcarbodiimide) (DIC) and respective catalyst (4-(dimethylamino)pyridinium 4-toluene-sulfonate) (DPTS) used in the low temperature polymerisation of BnMa

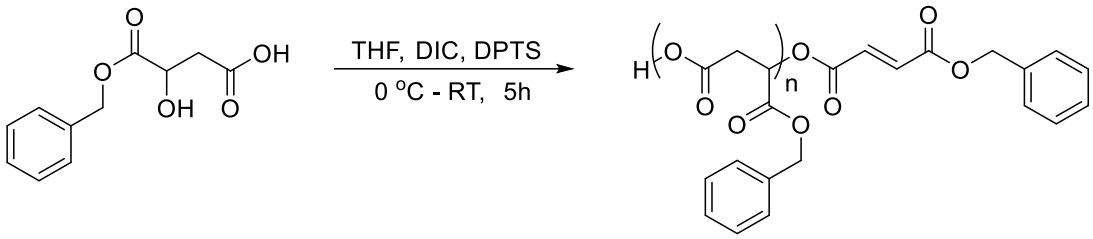

Scheme 3.12. Schematic depicting the low temperature step-growth polymerisation of BnMa and the reaction conditions used

Using a similar procedure to Moore *et al.* the step growth polymerisation of BnMa was carried out.[41] BnMa and DPTS were dissolved in dry THF and cooled to 0 °C before slow addition of DIC (**Scheme 3.12**). The P(BnMa) produced was characterised by SEC and ^{1}H NMR spectroscopy. SEC (**Figure 3.15**) revealed that the polymers prepared by low temperature carbodiimide coupling had a narrower dispersity ($Đ_m$ = 1.41) as compared with polymers prepared by elevated temperature methods that generally approached a dispersity of 2 at high conversions. Furthermore, the carbodiimide coupling chemistry also allowed for the production of polymers with a higher molecular weight (M_n = 2600 g mol^{-1}) in shorter timescales as compared with polymers prepared using high temperature polycondensation method (M_n = 2500 g mol^{-1}). For example, the low temperature polymerisation took less than 5 h, whilst the high temperature required more than 10 days stirring at 110 °C to reach a similar M_n.

It also led to the formation of polymers with lower extents of transesterification as is evident by the complete retention of benzyl functionality as demonstrated by the comparison of the integrals from chemical shifts corresponding to the benzylic protons at δ = 7.4 ppm to the integral from the main chain methylidine signal at δ = 5.6 ppm in the ^{1}H NMR spectrum (**Figure 3.16**).

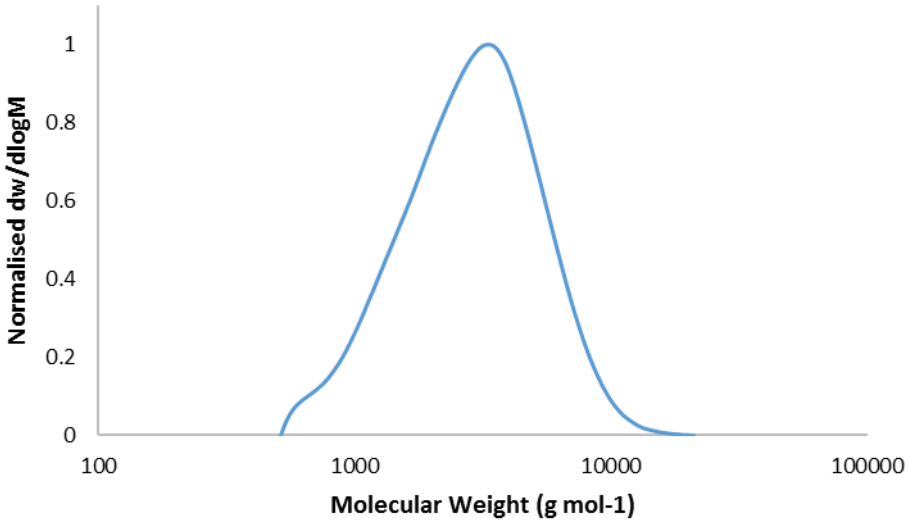

Figure 3.15. SEC chromatogram of P(BnMa) synthesised by low temperature methods with corresponding M_n, $M_w$and Đ$_m$ values of 2600 g mol^{-1}, 3700 g mol^{-1} and 1.41 respectively. Sample measured against PMMA standards using DMF as eluent

The carbodiimde coupling chemistry however results in polymer product with impurities which, after purification, leads to a low yield of the collected polymer product (< 10%). The ^{1}H NMR spectrum (**Figure 3.16**) demonstrates the presence of impurities from DIC (δ = 1.2 & 3.7 ppm) in addition to some fumarate by-product formation (δ = 6.9 ppm). Although the presence of such small amounts of fumarate formation were considered negligible, the extremely low yield makes this method not practical for production of polymeric materials in large quantity. The presence of potentially toxic DIC by-products is also undesirable, especially considering that the materials are anticipated to be exploited within biomedical applications. This method was therefore not chosen for future study. Despite some of the drawbacks associated with high temperature polymerisation (e.g. transesterification and long polymerisation

times), the condensation polymerisation is easier to transfer to large scale production, requires no purification, and produces less viscous materials. Thus, it is more industrially viable and more applicable to producing materials for the µSL process.

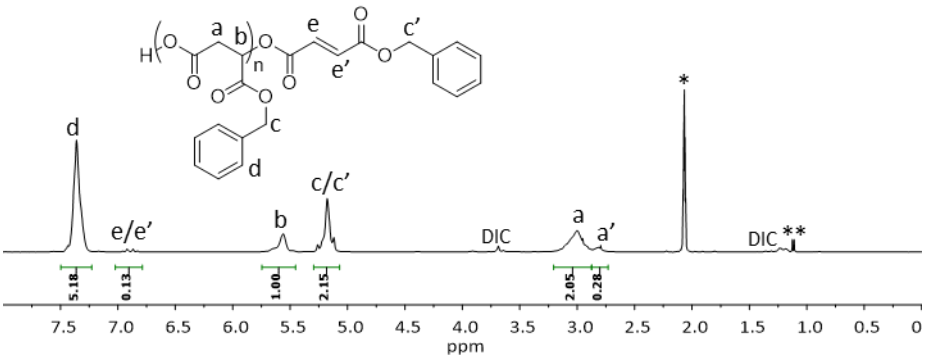

Figure 3.16. ^{1}H NMR spectrum of P(BnMa) made by low temperature polymerisation also illustrating the difficulty in removing impurities

3.2.3. Tuning and controlling hydrophobicity

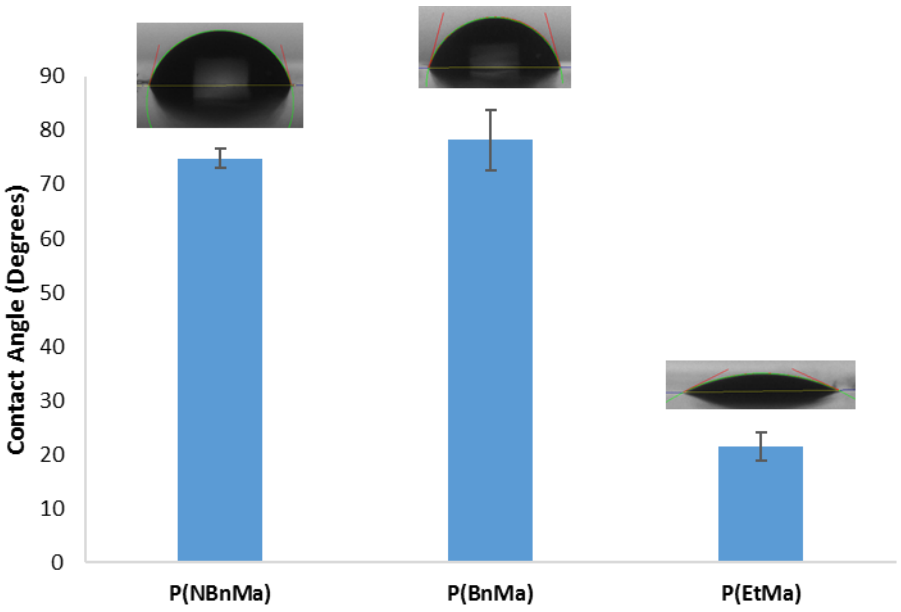

Figure 3.17. Drop shape analysis of distilled water on thin films of the NBnMa, BnMa & EtMa homopolymers demonstrating the difference in hydrophobicity.

Using the poly(malates) synthesised in section 3.2.2.1, thin films were produced by solvent casting each of the materials onto a glass slide from a 3 wt% solution in acetone. After drying, the thin films had their water contact angle (ɵ°) measured using drop shape analysis. Drop shape analysis (**Figure 3.17**) revealed that the contact angles for P(NBnMa) (ɵ = 74.8 ± 1.8 °) and P(BnMa) (ɵ = 78.2 ± 5.5 °) are nearly

four times greater than the contact angle for P(EtMa) ($\theta = 21.5 \pm 2.7$ °), indicating that the benzyl and nitrobenzyl functionalities induce more hydrophobicity of the resultant polymer film. This increase in hydrophobicity is a consequence of the lack of polarity of the aromatic rings. Despite the ethyl functionality being a relatively non-polar alkyl chain it still has more of a charge separation between the electro-positive alkyl part and the electro-negative ester moiety, making it easier to be solvated by polar solvents, as shown by smaller contact angle. Furthermore, the bulkier benzyl and nitrobenzyl functionalities will cause increase steric hindrance surrounding the hydrophilic polymer backbone which obstructs water ingress, whereas the ethyl functionality has much less steric bulk therefore allowing for more water ingress.

The variation in contact angles of the different homopolymers demonstrated the ability of poly(malates) to have their hydrophobicity tuned based on the nature of the ester moiety. With such a large difference in the contact angles displayed between P(BnMa) and P(EtMa), it was envisioned that the hydrophobicity could be tailored further by copolymerising the monomers in various ratios or utilising blends of the homopolymers during solvent casting. While this would have been an interesting study to investigate further, it was postulated that the same could be achieved utilising the photoresponsive P(NBnMa) homopolymer. More specifically, it was proposed that by subjecting a thin film of P(NBnMa) to a UV light source, partial photolysis of the nitrobenzyl functionality could be induced, thereby creating a gradient between nitrobenzyl functionalised polymer backbone and free carboxylic acid groups formed as a consequence of photolysis (**Scheme 3.13**) and ultimately decreasing the hydrophobicity.

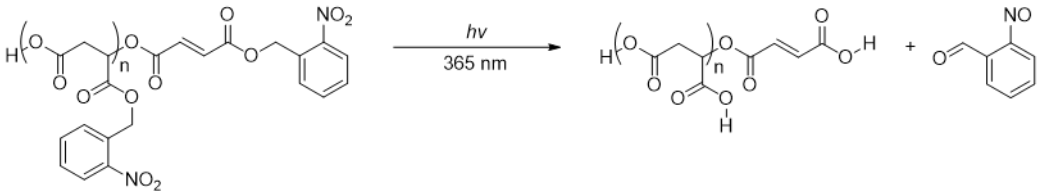

Scheme 3.13. Molecular structure of products formed as a consequence of photolysis of P(NBnMa)

The ability of P(NBnMa) to undergo photolysis was first tested in solution (THF) and followed by UV-Vis spectroscopy (**Figure 3.18**). After various exposure times to UV irradiation (365 nm) the decrease of the absorbance corresponding to the nitrobenzyl ester (261 nm) and the increase of absorbance corresponding to the nitrobenzyl aldehyde (302 nm) formed were monitored. **Figure 3.18** demonstrates that upon increasing exposure times to UV light (365 nm), photolysis of P(NBnMa) films does occur and results in the formation of the respective poly(malic acid) and nitrobenzaldehyde photodegradation products. Drop-shape analysis of the sample before and after UV exposure (**Figure 3.19**) revealed that after 30 min of UV light illumination, the contact angle of the P(NBnMa) thin film decreased from 67.2 ° to 51.9 ° indicating that the hydrophobicity of the polymer had decreased. This result confirmed that the surface wettability could be controlled by UV light.

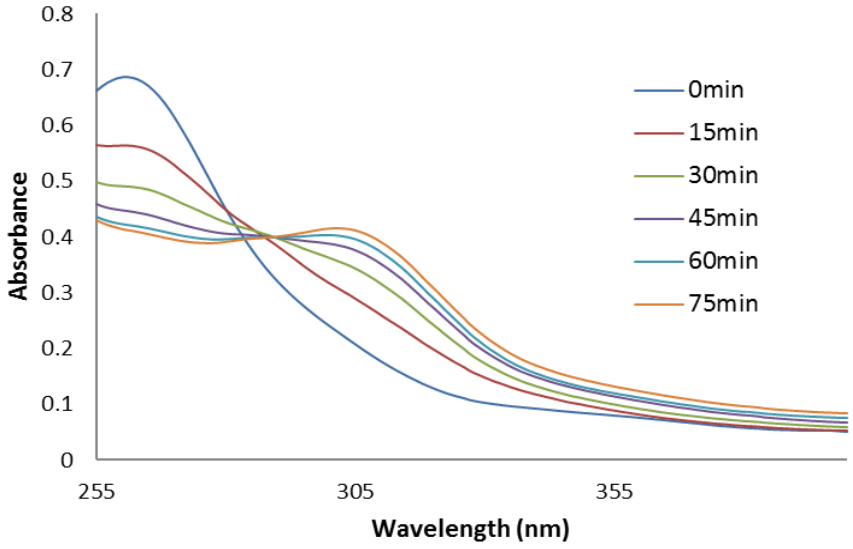

Figure 3.18. UV-Vis absorbance spectra of P(NBnMa) at different lengths of exposure to UV light demonstrating the loss of the absorbance corresponding to the nitrobenzyl ester and increase in the absorbance corresponding to the nitrobenzyl aldehyde photolysis product.

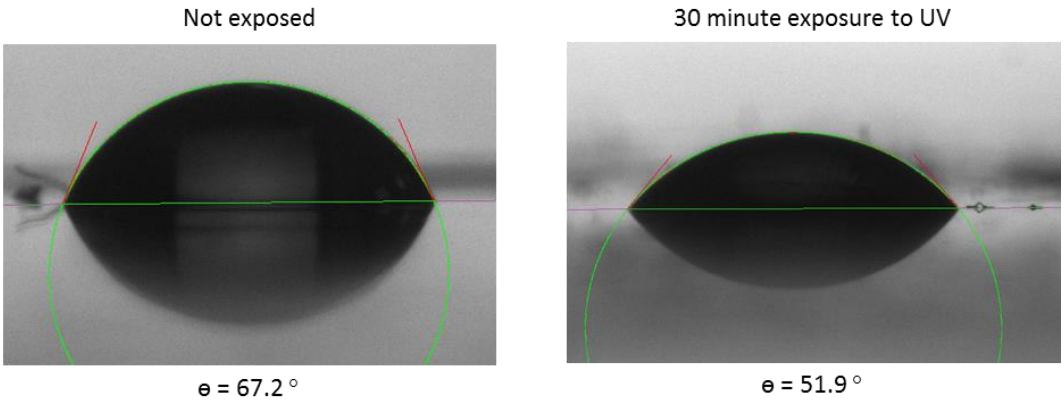

Figure 3.19. Drop shape analysis of P(NBnMa) thin films before and after a 30 minute exposure to UV light demonstrating the ability to alter the surface wettability upon exposure to an external stimulus

3.2.4. Copolymer synthesis

For the polymer to be used in µSL, a cross-linkable group in the polymer backbone is required in appropriate ratios. Thus, the amount of BuMa, which provides the crosslinkable alkene group, used in the copolymerisations with BnMa, NBnMa or EtMa is highly important. For example, in a copolymerisation between BuMa and EtMa, if the average degree of polymerisation (DP) is 10 then at least one fifth of the polymer chain is required to have alkene functionality so that step-growth propagation with the thiol functionalised cross-linker can occur. On the other hand, because the BuMa homopolymer tends to undergo intramolecular dehydration, the amount of BuMa used in copolymerisations should be kept to a minimum.

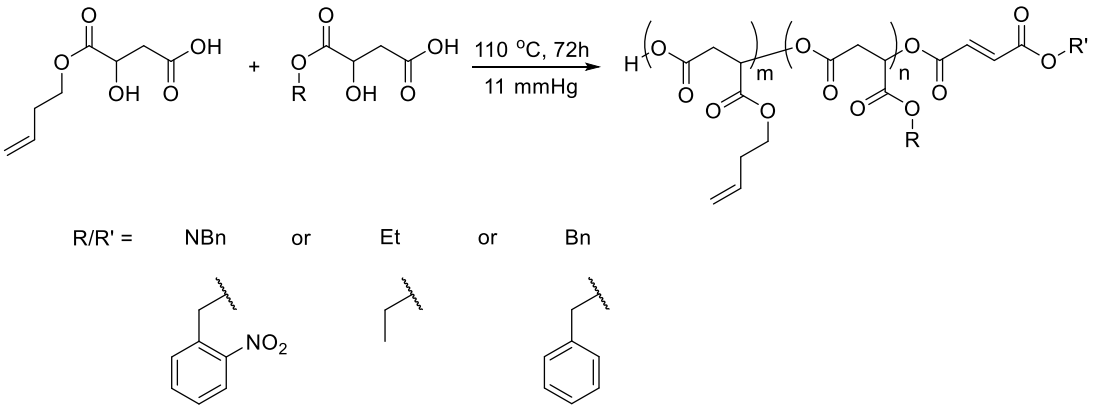

Scheme 3.14. Schematic representation of the copolymerisation of BuMa with either of NBnMa, EtMa or BnMa

Initially, 25% by molar mass of the alkene functional monomer (BuMa) was selected as a suitable starting point anticipating that an average degree of polymerisation of at least 8 could be achieved. Copolymerisations were carried out at 110 ˚C for 72 h (**Scheme 3.14**) and monitored by both SEC analysis and ^{1}H NMR spectroscopy. Because of the long period of the polymerisation and potential transesterification processes at high temperature, the rates of polymerisation of the various monomers were ignored in this study. The data from the SEC analysis (**Table 3.3**) shows that the three copolymers all proceeded to conversions greater than 80% over the course of 3 days with BnMa containing copolymers reaching M_n and M_w values of 1600 and 2300 g mol^{-1} respectively while EtMa containing copolymers reached similar M_n and M_w values of 1700 and 2300 g mol^{-1} respectively. NBnMa containing copolymers, however, reached a maximum M_n of 1600 g mol^{-1} after 2 days which then decreased to 1500 g mol^{-1} after 3 days. Once again, this decrease in molecular weight was attributed to intramolecular dehydration and other depolymerisation processes as a consequence of the monomers used in this polymerisation containing EWG. The SEC chromatograms (**Figure 3.20**) also provide evidence of this with the trace belonging to P(NBnMa-*co*-BuMa) displaying multiple lower molecular weight shoulders with a much broader dispersity ($Đ_m$ = 1.7) compared to the SEC analysis from P(BnMa-*co*-BuMa) ($Đ_m$ = 1.41) and P(EtMa-*co*-BuMa) ($Đ_m$ = 1.37) which both display a slight lower molecular weight shoulder.

Since SEC analysis only provides relative molecular weights from PMMA standards the exact molecular weight distributions of the copolymers produced here is still unknown therefore making determination of the degree of polymerisation (DP) and hence the number of alkene units per chain unviable. Thus, ^{1}H NMR spectroscopy was

utilised to define the average DP and to obtain a more accurate value of M_n. The number of alkene units per chain can also be deduced by working out the percentage incorporation of alkene functionality from the ^{1}H NMR spectrum.

Table 3.3. Extent of reaction and SEC data for the direct polycondensation of NBnMa, EtMa and BnMa with BuMa to form their respective copolymers carried out at 110 °C for 72h.

Copolymer	Time (hours)	Conversion (%)[a]	SEC M_w[b]	SEC M_n[b]	$Đ_m$[b]
P(BnMa-*co*-BuMa)	24	60	1400	1100	1.23
P(BnMa-*co*-BuMa)	48	77	1800	1400	1.34
P(BnMa-*co*-BuMa)	72	88	2300	1600	1.41
P(NBnMa-*co*-BuMa)	24	68	1600	1300	1.25
P(NBnMa-*co*-BuMa)	48	74	2200	1600	1.37
P(NBnMa-*co*-BuMa)	72	83	2500	1500	1.7
P(EtMa-*co*-BuMa)	24	56	1300	1000	1.23
P(EtMa-*co*-BuMa)	48	78	1800	1400	1.30
P(EtMa-*co*-BuMa)	72	89	2300	1700	1.37

[a] obtained by ^{1}H NMR spectroscopic analysis ($(CD3)_2CO$, 400 MHz) [b] obtained by SEC in DMF as eluent using PMMA standards

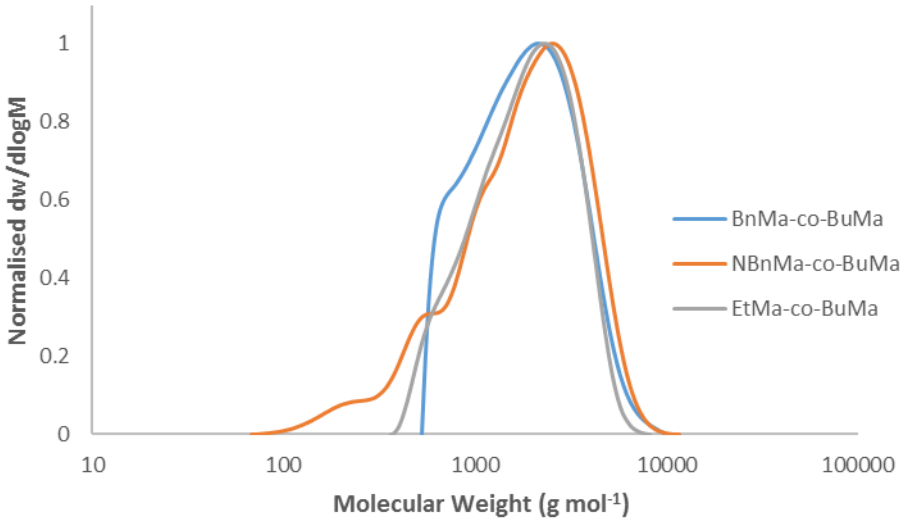

Figure 3.20. SEC chromatograms of copolymers of BnMa, NBnMa and EtMa with BuMa illustrating the lower moleculer weight species observed for the more EW P(NBnMa-*co*-BuMa) copolymer. Samples measured against PMMA standards using DMF as eluent.

The inability to determine DP (extent of reaction, $\overline{x}_n$) utilising the Carothers equation (1.1.) (as mentioned in section 3.2.2.) meant that alternative methods of deducing the DP were required. For a polymerisation whereby an initiator is used and remains attached to one end of the growing polymer chain, it is sometimes difficult to compare the integral of protons associated with the initiator compared to ones in the backbone of the polymer in order to determine DP. With the copolymers produced herein, no initiator was utilised and although there is a signal at δ = 4.7 ppm which can be assigned to the terminal hydrogen adjacent to terminal ester bond, they are convoluted with signals corresponding to the same hydrogen of the monomer species (**Figure 3.21**). Whilst the monomers could have been removed by precipitation in order to reveal the terminal hydroxylic hydrogen, this would have also removed lower molecular weight species thereby only providing a biased representation of the extent of polymerisation.

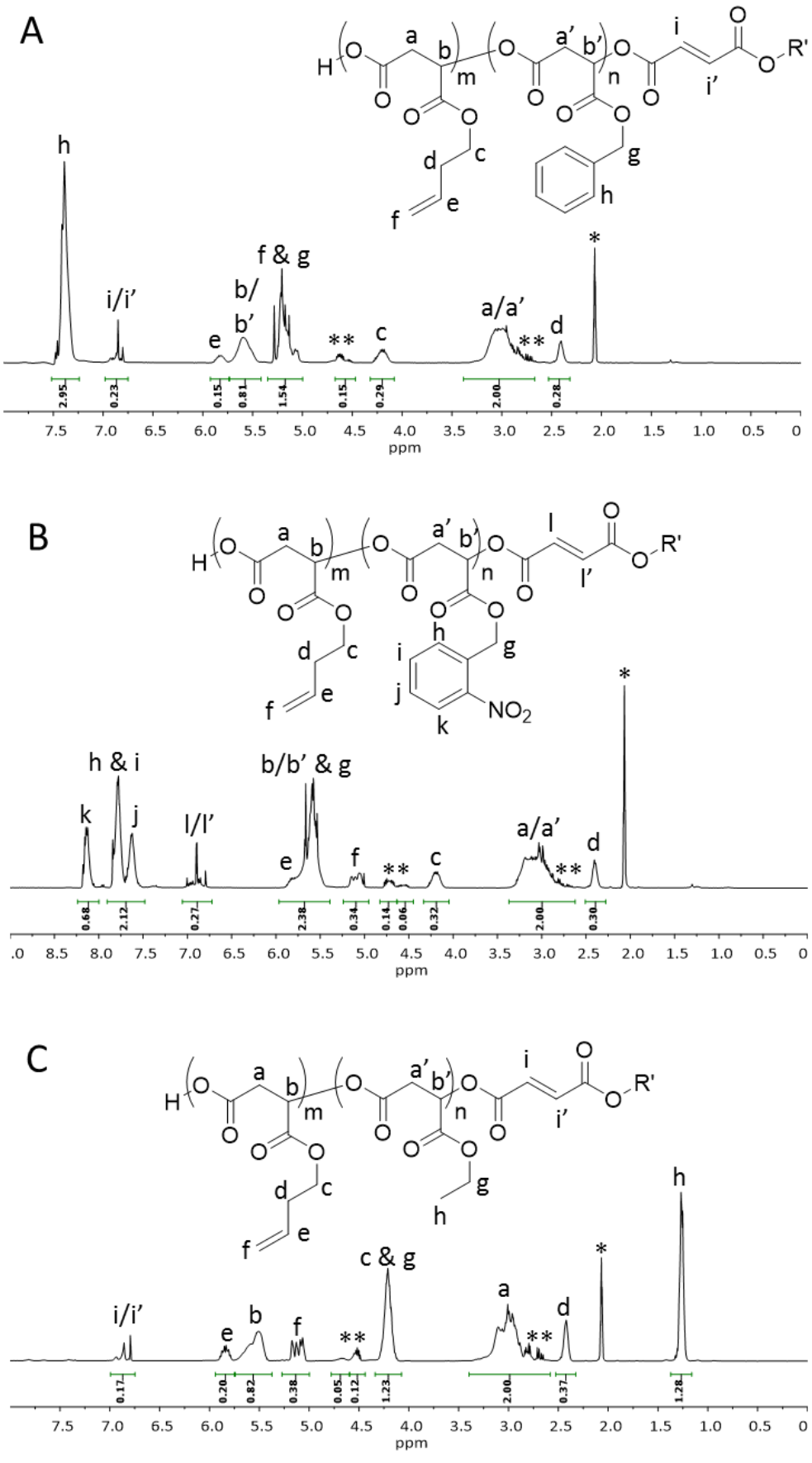

Figure 3.21. ^{1}H NMR spectra of copolymers of; A, P(BnMa-co-BuMa), B, P(NBnMa-co-BuMa) and C, P(EtMa-co-BuMa). (** = residual monomer * = acetone) (400MHz, $(CD_3)_2CO$) R' = Bn, NBn, Et or Bu.

As a consequence of this, it was decided that an approximate estimation of DP could be determined by making the assumption that all polymer chains are terminated by fumarate formation. It should be noted that this assumption is a 'worst-case scenario' and not all chains are actually terminated by fumarate formation, thus the actual value of DP determined would be higher than the calculated value based on this assumption. Using this assumption and the ^{1}H NMR spectra of the three copolymers (**Figure 3.21**), the integral corresponding to the olefinic protons (δ = 6.9 ppm) was compared to the integral corresponding to the main chain methylidine proton (δ = 5.6 ppm) to calculate an estimate of DP (**Figure 3.21**). The degree of alkene functionality was assessed by ^{1}H NMR by comparing integration of the chemical shifts corresponding to olefinic protons from both fumarate (δ = 6.9) and butenyl functionality (δ = 5.1 or δ = 5.8) with the main chain methylidine proton (δ = 5.6 ppm). This in turn allows for calculation of the average number of alkene units per chain.

Table 3.4. Conversion, degree of polymerisation (DP), Number avergae molecular weight (M_n), degree of alkene functionality as a percentage and average number of alkene units per polymer chain based on the assumption that all polymer chains are terminated by fumarate formation (all determined by ^{1}H NMR spectroscopy

Copolymer	Conversion (%)	DP ($\overline{x}_n$)	M_n (g mol^{-1})	Alkene Functionality (%)	Average no. of alkene units per chain
P(BnMa-*co*-BuMa)	88	8	1700	25	2
P(NBnMa-*co*-BuMa)	83	7.25	1800	31	2.25
P(EtMa-*co*-BuMa)	89	10.6	1800	32	3.4

Using the above assumption, it was estimated that there are at least 2 alkene units on average per chain for all three copolymers (**Table 3.4**), suggesting that all three prepared polymers are suitable for cross-linking in µSL by thiol-ene crosslinking. It is noted that the DP of copolymers containing more EDG esters were shown to be higher which is consistent with the data from SEC analysis (**Figure 3.20**). P(EtMa-*co*-BuMa)

was found to reach the highest DP (10.6), which is likely as a consequence of decreased steric hindrance of the ethyl pendant group compared to the bulky benzyl/nitrobenzyl groups. In addition, the electron donating nature of the ethyl group lowers the probability of fumarate formation.

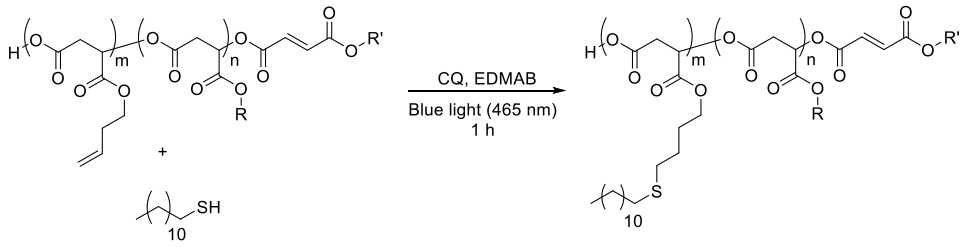

Scheme 3.15. Small molecule study used to determine the reactivity of the various copolymers (R = Bn, NBn or Et) towards dodecanethiol in the presence of camphorquinone and its coinitiator (EDMAB)

A model study at NMR scale was first undertaken to assess the reactivity of the alkene-containing polymer in the thiol-ene reaction. Thus, 2 equivalents of 1-dodecanethiol (DDT) was added to each of the copolymers in deuterated acetone followed by addition of camphorquinone (2 wt%) and its coinitiator ethyl 4-(dimethylamino)benzoate (EDMAB). The solution was then illuminated with blue light (465 nm) from the custom built blue light post exposure box (as described in chapter one) for one hour after which the solution was analysed by ^{1}H NMR spectroscopy (**Scheme 3.15**). ^{1}H NMR analysis indicated that only P(EtMa-co-BuMa) reacted with DDT (**Figure 3.22**). The ^{1}H NMR spectra demonstrate the significant reduction in intensity of peaks corresponding to thiol and alkenes in addition to the appearance of peaks corresponding to the methyl protons surrounding the thioether formed. By comparing the integrals of the alkene (δ = 5.1 and 5.8 ppm) and thiol (δ = 1.4 ppm) peaks with the main chain methylidine proton (δ = 5.6 ppm) the degree of functionalisation was found to be 67%.

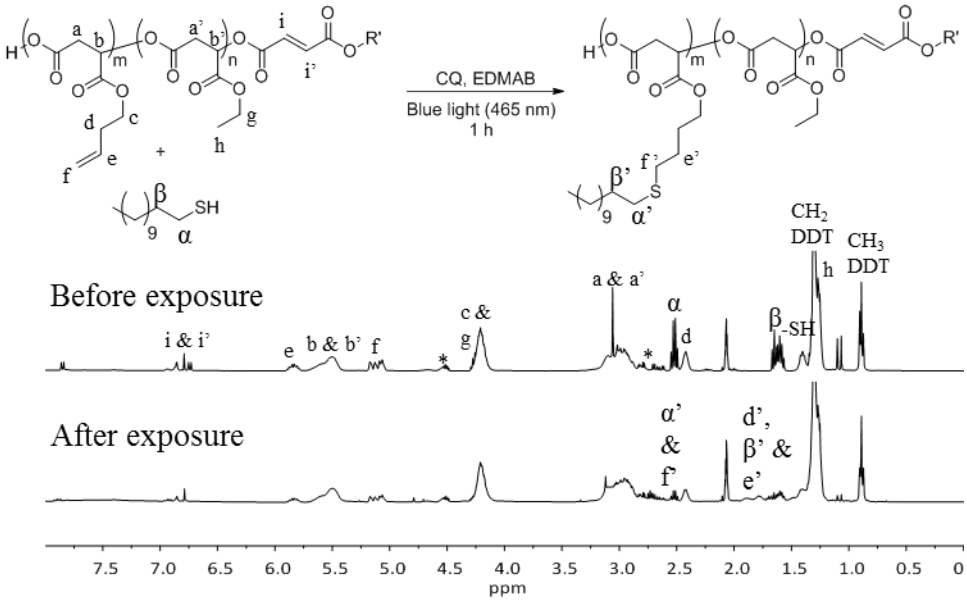

Figure 3.22. ^{1}H-NMR spectroscopy of the small molecule study carried out both before and after exposure to blue light (465 nm) for 1 h illustrating a 67 % reduction in the signals corresponding to the alkene functionality in addition to the appearance of peaks corresponding to the thioether functionality (*ca.* 1.8 ppm) ($(CD_3)_2CO$), 400 MHz)

The inert nature of NBnMa and BnMa containing copolymers toward DDT addition is attributed to the steric hindrance of the bulky benzyl moieties. To further evaluate the reactivity of the alkene group in the presence of either nitrobenyl or benzyl group, a small molecule study was undertaken using the monomers instead of the copolymers and the conditions were as described above. The ^{1}H NMR spectra shows that, in the presence of NBnMa, the alkene functionality of BuMa displays little to no reactivity towards DDT upon 1 h exposure to blue light using CQ as photoinitiator (**Figure 3.23**). On the other hand, BuMa undergoes nearly complete functionalisation with DDT in the presence of the Benzyl molecule, as seen from the disappearance of signals corresponding to the alkene protons in addition to the appearance of the proton marked as *d* (Figure 3.22) which has shifted from the original position of δ = 2.4 ppm to the position of δ = 1.8 ppm as a consequence of the alkene being converted to the corresponding thioether (**Figure 3.23** C and D).

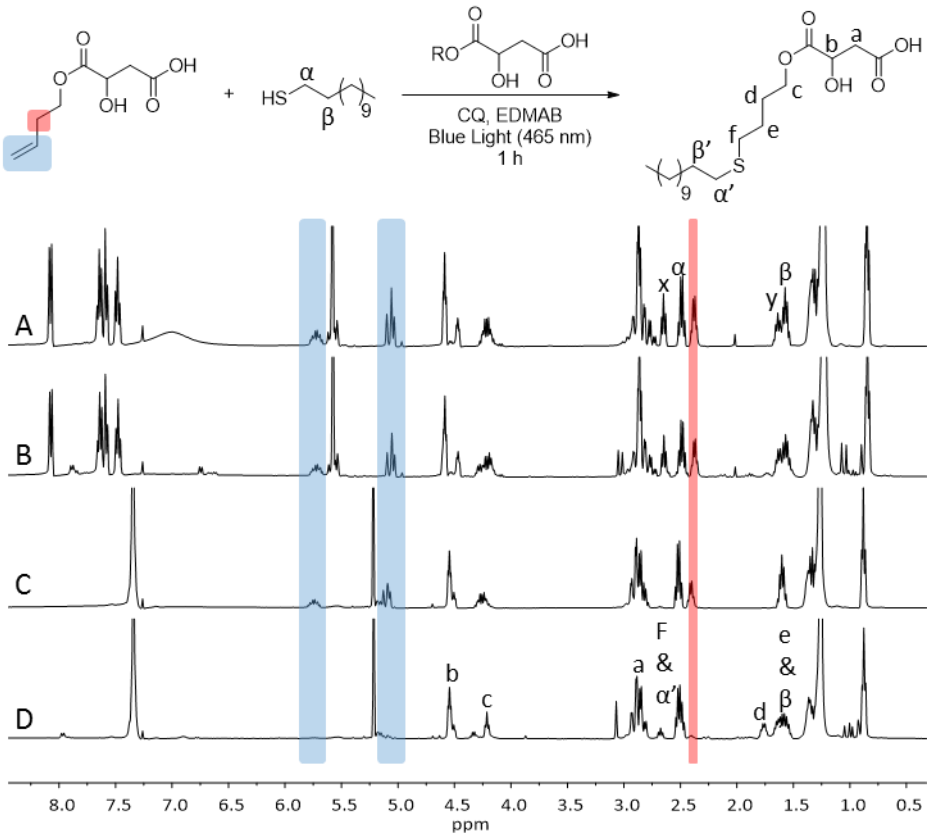

Figure 3.23. ^{1}H NMR spectra before (A & C) and after (B & D) exposure to blue light for 1 h illustrating the non-reactivity and reactivity of BuMa towards dodecanethiol in the presence of NBnMa (A & B) and BnMa (C & D), respectively ($(CD_3)_2CO$), 400 MHz)

These results suggest that, in the case of P(BnMa-*co*-BuMa) the increase in steric hinderance surrounding the alkene functionality is in fact inhibiting the thiol-ene reaction since BuMa displays reactivity toward DDT in solution in its unattached state. In the case of P(NBnMa-*co*-BuMa), the small molecule model result suggests that there may be additional factors affecting the reactivity of BuMa beyond the steric hindrance caused by the nitrobenzyl group. Upon closer inspection of the ^{1}H NMR spectra of **Figure 3.23** (A & B) additional signals are present in the case of NBnMa both before and after irradiation at δ = 2.6 and 1.6 ppm, which are assigned the protons from the interaction of DDT with the nitrate group of the NBnMa. Despite the presence of interacting DDT, there is still plenty of non-interacting DDT present and so reaction with the alkene of BuMa should still be possible.

In order to eliminate the possibility that the copolymers and in particular P(NBnMa-*co*-BuMa) was interfering or competing with the CQ photoinitiator for light absorption, UV-Vis spectroscopy was carried out on them to determine where they absorb in the UV or visible light spectrums (**Figure 3.24**). From the UV-Vis spectrum, it was determined that none of the copolymers synthesised absorbed in the same region as the camphorquinone based photoinitiator. Therefore, other factors than the light absorbance of the copolymer and DDT interaction with the nitro group of NBnMa were clearly inhibiting the thiol-ene reaction in the small molecule study. Indeed, it has been reported that the nitrobenzyl functionality is in fact a well-known radical scavenger and so it was postulated that the nitrobenzyl chromophores were in fact scavenging radicals generated by the photoinitiator before initiation of the thiol-ene reaction could take place.[42]

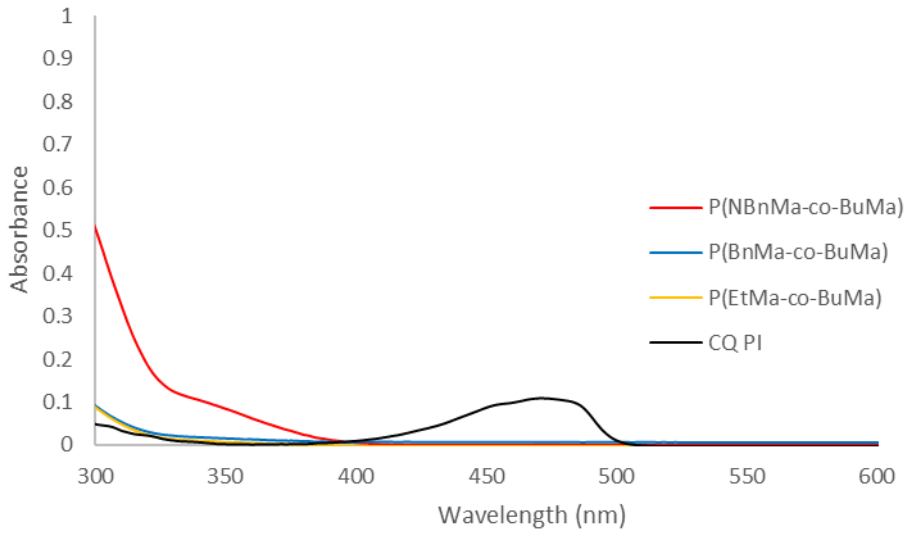

Figure 3.24. UV-Vis absorbance spectra of the various copolymers with respect to the camphorquinone photoinitiator used demonstrating that, at the same concentration, there should be no inhibition of the photoinitiator by the copolymers

3.3. Conclusions and future work

The successful synthesis of various malate monomers from mostly biomass derived resources and their subsequent polymerisation by polycondensation to form both homo- and copolymers have been described. The formation of a fumarate by-product has been studied for the different monomers used and has been shown to be beneficial providing it does not become the dominant dehydration process. The fumarate by-product formation was found to be more dominant at higher temperatures (>120 °C) as well as for monomers with more electron withdrawing esters and so an optimal temperature of 110 °C, that covers all of the monomers described herein, was realised. Other than the high temperatures utilised, the majority of green chemistry principles were adhered to and whilst an attempt was made at carrying out the polycondensation reaction at lower temperatures, it was found to deviate further away from green chemistry principles (*i.e.* use of solvents, low yields, stoichiometric amounts of catalyst, *etc.*) and was therefore abandoned. Drop shape analysis of thin films revealed that the hydrophobicity could be both tuned and controlled depending on the homopolymer used.

Whilst the homopolymerisation of BuMa showed an undesirable degree of fumarate formation and characteristics of cross-linking above 80 % conversion, the respective copolymerisations with the other 3 monomers was found to proceed with retention of the alkene functionality as required for cross-linking in the µSL process. Small molecule studies showed that BnMa and NBnMa containing copolymers were unsuitable for processing by µSL due to their lack of reactivity towards thiols whereas P(EtMa-*co*-BuMa) demonstrated the most promise and is shown to be compatible with the µSL process in the next chapter.

Although P(BnMa-*co*-BuMa) and P(NBnMa-*co*-BuMa) are unsuitable for use in µSL when utilising thiol-ene chemistry, there is potential for their functionality to be adapted in order to make them suitable for µSL utilising a different cross-linking chemistry. For example, the NBnMa containing polymer could be turned into an epoxy based resin by replacing the alkene functionality with epoxides. In the case of the BnMa containing polymers, it may simply be a case of moving the alkene functionality further away from the steric bulk of the polymer backbone and so further investigation in this area is required. Despite not having progressed NBnMa and BnMa containing polymers to the point of being 3D printed, they may find application in areas such as hydrophobic coatings for biomedical devices. The P(NBnMa) synthesised herein has already been exploited by Annette Christie (PhD student in the Department of Chemistry at the University of Warwick) to produce photoresponsive microparticles capable of releasing encapsulates upon exposure to UV for use in the agrochemical industry.

3.4. References

1. Tschan, M. J. L.; Brulé, E.; Haquette, P.; Thomas, C. M., Synthesis of biodegradable polymers from renewable resources. *Polym. Chem.* **2012,** *3* (4), 836-851.

2. Melchels, F. P.; Barradas, A. M.; van Blitterswijk, C. A.; de Boer, J.; Feijen, J.; Grijpma, D. W., Effects of the architecture of tissue engineering scaffolds on cell seeding and culturing. *Acta Biomater.* **2010,** *6* (11), 4208-4217.

3. Melchels, F. P.; Bertoldi, K.; Gabbrielli, R.; Velders, A. H.; Feijen, J.; Grijpma, D. W., Mathematically defined tissue engineering scaffold architectures prepared by stereolithography. *Biomaterials* **2010,** *31* (27), 6909-6916.

4. Melchels, F. P.; Feijen, J.; Grijpma, D. W., A poly(D,L-lactide) resin for the preparation of tissue engineering scaffolds by stereolithography. *Biomaterials* **2009,** *30* (23-24), 3801-3809.

5. King, S. L.; Truong, V. X.; Kirchhoefer, C.; Pitto-Barry, A.; Dove, A. P., Synthetic strategies, sustainability and biological applications of malic acid–based polymers. *Green Materials* **2014,** *2* (3), 107-122.

6. Lasprilla, A. J.; Martinez, G. A.; Lunelli, B. H.; Jardini, A. L.; Filho, R. M., Poly-lactic acid synthesis for application in biomedical devices - a review. *Biotechnol. Adv.* **2012,** *30* (1), 321-328.

7. Li, S.; McCarthy, S., Further investigations on the hydrolytic degradation of poly (DL-lactide). *Biomaterials* **1999,** *20* (1), 35-44.

8. Silva, M. M.; Cyster, L. A.; Barry, J. J.; Yang, X. B.; Oreffo, R. O.; Grant, D. M.; Scotchford, C. A.; Howdle, S. M.; Shakesheff, K. M.; Rose, F. R., The effect of anisotropic architecture on cell and tissue infiltration into tissue engineering scaffolds. *Biomaterials* **2006,** *27* (35), 5909-5917.

9. Hollister, S. J., Porous scaffold design for tissue engineering. *Nat. Mater.* **2005,** *4* (7), 518-524.

10. Braud, C.; Bunel, C.; Vert, M., Poly(β-malic acid) : a new polymeric drug-carrier. *Polym. Bull.* **1985,** *13* (4), 293-299.

11. Mauduit, J.; Boustta, M.; Vert, M., Hydrolytic degradation of benzylated poly(β-malic acid): Influence of sample size, sample shape, and polymer composition. *J Biomater Sci Polym Ed* **1996,** *7* (3), 207-220.

12. O'Brien, F. J., Biomaterials & scaffolds for tissue engineering. *Mater. Today* **2011,** *14* (3), 88-95.

13. Lee, J. W.; Lan, P. X.; Kim, B.; Lim, G.; Cho, D.-W., 3D scaffold fabrication with PPF/DEF using micro-stereolithography. *Microelectron. Eng.* **2007,** *84* (5-8), 1702-1705.

14. Elomaa, L.; Teixeira, S.; Hakala, R.; Korhonen, H.; Grijpma, D. W.; Seppala, J. V., Preparation of poly(epsilon-caprolactone)-based tissue engineering scaffolds by stereolithography. *Acta Biomater.* **2011,** *7* (11), 3850-3856.

15. Barker, I. A.; Ablett, M. P.; Gilbert, H. T. J.; Leigh, S. J.; Covington, J. A.; Hoyland, J. A.; Richardson, S. M.; Dove, A. P., A microstereolithography resin based on thiol-ene chemistry: towards biocompatible 3D extracellular constructs for tissue engineering. *Biomater. Sci.* **2014,** *2* (4), 472-475.

16. Grijpma, D. W.; Hou, Q.; Feijen, J., Preparation of biodegradable networks by photo-crosslinking lactide, ε-caprolactone and trimethylene carbonate-based oligomers functionalized with fumaric acid monoethyl ester. *Biomaterials* **2005,** *26* (16), 2795-2802.

17. Cook, W. D.; Chen, F.; Pattison, D. W.; Hopson, P.; Beaujon, M., Thermal polymerization of thiol–ene network-forming systems. *Polym. Int.* **2007,** *56* (12), 1572-1579.

18. Coulembier, O.; Degée, P.; Hedrick, J. L.; Dubois, P., From controlled ring-opening polymerization to biodegradable aliphatic polyester: Especially poly(β-malic acid) derivatives. *Prog. Polym. Sci.* **2006,** *31* (8), 723-747.

19. Becker, J. M.; Pounder, R. J.; Dove, A. P., Synthesis of Poly(lactide)s with Modified Thermal and Mechanical Properties. *Macromol. Rapid Commun.* **2010,** *31* (22), 1923-1937.

20. Guerin, P.; Vert, M.; Braud, C.; Lenz, R. W., Optically active poly (\-malic-acid). *Polym. Bull.* **1985,** *14* (2), 187-192.

21. Kimura, Y.; Shirotani, K.; Yamane, H.; Kitao, T., Ring-opening polymerization of 3(S)-[(benzyloxycarbonyl)methyl]-1,4-dioxane-2,5-dione: a new route to a poly(.alpha.-hydroxy acid) with pendant carboxyl groups. *Macromolecules* **1988,** *21* (11), 3338-3340.

22. Kimura, Y.; Shirotani, K.; Yamane, H.; Kitao, T., Copolymerization of 3-(S)-[(benzyloxycarbonyl)methyl]-1,4-dioxane-2,5-dione and l-lactide: a facile synthetic method for functionalized bioabsorbable polymer. *Polymer* **1993,** *34* (8), 1741-1748.

23. Johns, D. B.; Lenz, R. W.; Vert, M., Poly(Malic Acid) Part I— Preparation and Polymerization of Benzyl Malolactonate. *J. Bioact. Compat. Polym.* **1986,** *1* (1), 47-60.

24. Leboucher-Durand, M.-A.; Langlois, V.; Guérin, P., Poly(β -malic acid) derivatives with unsaturated lateral groups: epoxidation as model reaction of the double bonds reactivity. *React. Funct. Polym.* **1996,** *31* (1), 57-65.

25. Regaño, C.; Alla, A.; de Ilarduya, A. M.; Muñoz-Guerra, S., Linear polyamides from L-malic acid and alkanediamines. *J. Polym. Sci. A Polym. Chem.* **2004,** *42* (7), 1566-1575.

26. Regaño, C.; Alla, A.; Martínez de Ilarduya, A.; Muñoz-Guerra, S., Poly(ester amide)s Derived from l-Malic Acid. *Macromolecules* **2004,** *37* (6), 2067-2075.

27. Takasu, A.; Oishi, Y.; Iio, Y.; Inai, Y.; Hirabayashi, T., Synthesis of Aliphatic Polyesters by Direct Polyesterification of Dicarboxylic Acids with Diols under Mild Conditions Catalyzed by Reusable Rare-Earth Triflate. *Macromolecules* **2003,** *36* (6), 1772-1774.

28. Shibata, Y.; Takasu, A., Synthesis of polyester having pendent hydroxyl groups via regioselective dehydration polycondensations of dicarboxylic acids and diols by low temperature polycondensation. *J. Polym. Sci. A Polym. Chem.* **2009,** *47* (21), 5747-5759.

29. Hahn, C.; Wesselbaum, S.; Keul, H.; Möller, M., OH-functional polyesters based on malic acid: Influence of the OH-groups onto the thermal properties. *Eur. Polym. J.* **2013,** *49* (1), 217-227.

30. Yao, D.; Li, G.; Kuila, T.; Li, P.; Kim, N. H.; Kim, S.-I.; Lee, J. H., Lipase-catalyzed synthesis and characterization of biodegradable polyester containing l-malic acid unit in solvent system. *J. Appl. Polym. Sci.* **2011,** *120* (2), 1114-1120.

31. Li, G.; Yao, D.; Zong, M., Lipase-catalyzed synthesis of biodegradable copolymer containing malic acid units in solvent-free system. *Eur. Polym. J.* **2008,** *44* (4), 1123-1129.

32. Kajiyama, T.; Taguchi, T.; Kobayashi, H.; Kataoka, K.; Tanaka, J., Synthesis of high molecular weight poly(α,β-malic acid) for biomedical use by direct polycondensation. *Polym. Degrad. Stab.* **2003,** *81* (3), 525-530.

33. Kajiyama, T.; Kobayashi, H.; Taguchi, T.; Kataoka, K.; Tanaka, J., Improved Synthesis with High Yield and Increased Molecular Weight of Poly(α,β-malic acid) by Direct Polycondensation. *Biomacromolecules* **2004,** *5* (1), 169-174.

34. Ohtani, N.; Kimura, Y.; Kitao, T., Preparation of Poly (malic acid) and Its Ester Derivatives by Direct Polycondensation of Malic Acid and β-Ethyl Malate. *Kobunshi Ronbunshu* **1987,** *44* (9), 701-709.

35. He, B.; Wan, E.; Chan-Park, M. B., Synthesis and Degradation of Biodegradable Photo-Cross-Linked Poly(α,β-malic acid)-Based Hydrogel. *Chem. Mater.* **2006,** *18* (17), 3946-3955.

36. Hoyle, C. E.; Bowman, C. N., Thiol-ene click chemistry. *Angew. Chem. Int. Ed. Engl.* **2010,** *49* (9), 1540-1573.

37. Miller, M. J.; Bajwa, J. S.; Mattingly, P. G.; Peterson, K., Enantioselective syntheses of 3-substituted 4-(alkoxycarbonyl)-2-azetidinones from malic acid. *J. Org. Chem.* **1982,** *47* (25), 4928-4933.

38. Kajiyama, T.; Kobayashi, H.; Morisaku, K.; Taguchi, T.; Kataoka, K.; Tanaka, J., Determination of end-group structures and by-products of synthesis of poly(α,β-malic acid) by direct polycondensation. *Polym. Degrad. Stab.* **2004,** *84* (1), 151-157.

39. El-Faham, A.; Albericio, F., Peptide coupling reagents, more than a letter soup. *Chem. Rev.* **2011,** *111* (11), 6557-6602.

40. Han, S.-Y.; Kim, Y.-A., Recent development of peptide coupling reagents in organic synthesis. *Tetrahedron* **2004,** *60* (11), 2447-2467.

41. Moore, J. S.; Stupp, S. I., Room temperature polyesterification. *Macromolecules* **1990,** *23* (1), 65-70.

42. Hanson, J. E.; Reichmanis, E.; Houlihan, F. M.; Neenan, T. X., Synthesis and evaluation of copolymers of (tert-butoxycarbonyloxy)styrene and (2-

nitrobenzyl)styrene sulfonates: single-component chemically amplified deep-UV imaging materials. *Chem. Mater.* **1992,** *4* (4), 837-842.

4. Development of surface erodible materials for use in drug eluting implants made by μSL

4.1. Introduction

Whilst μSL has found a niche in the formation of tissue engineering constructs, there have only been a few examples of using the technology to create small molecule/drug containing implants that can subsequently be used as a method of delivery in the field of pharmaceutics.[1-3] The exploitation of AM technologies, and in particular μSL, in the production of drug delivery devices has the potential to progress medicine away from a 'one dose suits all' paradigm toward personalised medicines whereby devices with precise dosages and drug combinations can be specifically tailored to individual patients in addition to being manufactured *in situ*.[4]

Although there have been numerous examples of various AM techniques such as binder jetting and fused deposition modelling (FDM) to produce implantable, oral or patch devices for the delivery of drugs, they are all accompanied by significant drawbacks for pharmaceutical applications.[5-23] For instance, binder jetting is often limited in terms of the possible geometries of shapes that can be printed while FDM requires that the material being deposited is extruded at high temperatures thus degrading some of the model drugs.[24] Despite these limitations, the devices produced from these technologies have conferred a wide variety of release profiles including sustained, delayed, and rapid dispersion.[6] Pulsed and zero-order release profiles are more difficult to achieve and although there are a few examples in the literature, the devices produced remain more suited for use as oral tablets because of their relatively large size making them unsuitable for administration through a syringe.[10, 12, 25]

On the other hand, the μSL technology, is particularly suited for producing micro-sized implantable devices and to the best of our knowledge, there has only been a handful of reports using it in the production of drug administering devices.[3, 21, 26-28] Early work by Matsuda *et al.* investigated drug-coated microneedles made from

PTMC/PEG and PTMC/PCl based resins for the administration of the anti-inflammatory drugs, dexamethasone and indomethacin, respectively.[26-27] The microneedles had to be coated since attempts to print with the drug-containing resin only led to partially cured constructs as a consequence of the high optical absorbance of the drug inhibiting the curing process. More recently Wang *et al.* developed torus shaped oral dosage forms using 4-aminosalicylic acid and paracetamol as model drugs.[3] The tablet devices made, exhibited a sustained yet uncontrollable release profile because dissolution of the drug from the cross-linked network was dependent upon swelling of the PEG chains in the aqueous environment. Nevertheless, Goyanes *et al.* also utilised a PEG-based system for the fabrication of patch devices and demonstrated a far more linear (and therefore near zero-order) release profile, albeit for a very short amount of time.[21]

Another advantage of μSL is minimal heating of the sample caused by a light source because of the short exposure times required to cure the relatively thin layers. This allows for the incorporation of temperature sensitive drugs and/or other biologically active compounds such as proteins that would normally become denatured above biological temperatures. Kochhar *et al*. demonstrated the incorporation and subsequent release of bovine serum albumin (BSA) in another PEG-based microneedle device fabricated by μSL.[28] The release profile exhibited an initial burst of BSA followed by a steady sustained release with the majority of the encapsulated enzyme being released within the first hour or so. The use of PEG is ubiquitous because of its hydrophilic nature, allowing it to encapsulate hydrophilic drugs in addition to its ability to swell, thereby subsequently releasing encapsulated materials albeit in a relatively uncontrolled manner. The persistent use of PEG is a consequence of the lack of readily available, FDA-approved, resins that can both encapsulate and

release drugs. Thus, the continued development of other hydrolytically degradable polymeric resins with controlled release profiles is clearly warranted.

Hydrolytically biodegradable polymers have long been known to erode by either bulk or surface eroding mechanisms.[29] For bulk eroding polymers, the rate at which water ingresses into the material is greater than the degradation rate of the hydrolysable bonds along the polymer backbone. Consequently, material is lost from the entire volume of the polymer matrix and so the degradation rate is only dependent on the chemical composition of the polymer and not the size or shape of the material. Surface eroding polymers on the other hand, erode from the outside surface of the material because the rate of degradation is quicker than the rate at which water can diffuse into the polymer matrix (**Figure 4.1**). Thus, the rate of degradation in this instance is dependent not only on the chemical composition of the polymer matrix but the size and geometry of the material as well.

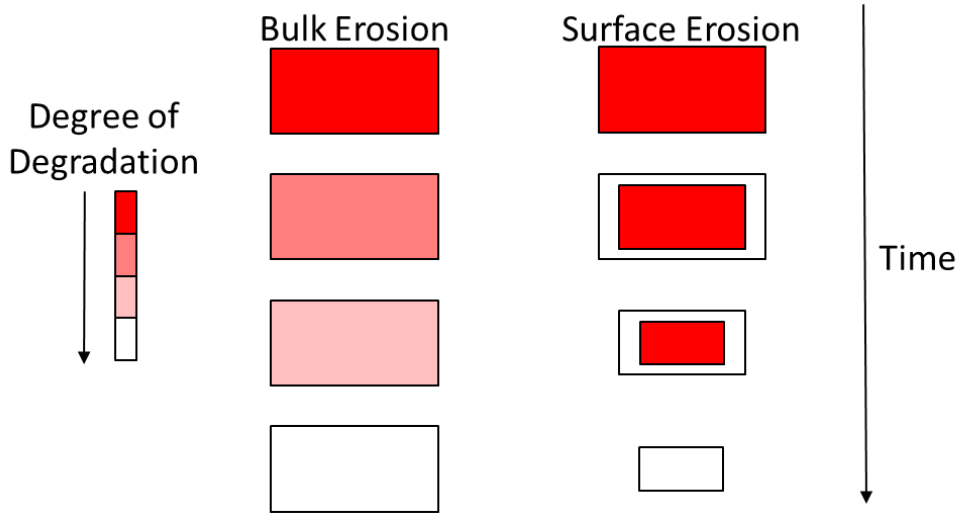

Figure 4.1. Schematic illustration of the surface and bulk eroding mechanisms undertaken by hydrolysable, biodegradable polymers[31]

Previously, the majority of biodegradable polymers were thought to erode solely *via* bulk erosion, however, more recently Burkersroda *et al*. were able to demonstrate that all biodegradable polymers were capable of undergoing either bulk or surface erosion depending on the critical device dimension ($L_{critical}$).[30] Using a theoretical model, they showed that press-formed devices with dimensions < $L_{critical}$ were only able to undergo bulk erosion whereas devices with dimensions > $L_{critical}$ degraded *via* surface erosion. By carefully tuning the dimensions of devices containing PLA and PLGA, two poly(α-hydroxy ester)s that were previously considered to only undergo bulk erosion, Burkersroda *et al*. demonstrated they were also able to undergo surface erosion.

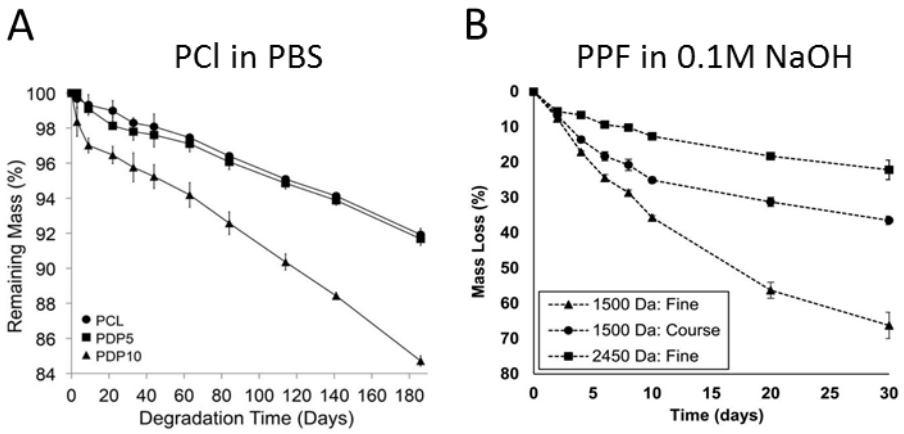

Figure 4.2. Gravimetric analysis of PCl-based (A) and PPF-based (B) materials printed from stereolithographic resins exemplifying their near linear surface eroding degradation profiles[28, 29]

Whilst bulk eroding materials suffice for some biomedical applications such as sutures or screws for fracture fixation, surface eroding materials are far more desirable for applications in tissue engineering and drug delivery. Not only do surface eroding materials maintain a level of their mechanical integrity throughout the degradation event, but they can also protect encapsulated drugs from body fluids that would ordinarily cause premature drug degradation in bulk eroding materials. Perhaps most importantly, surface erosion ensures a relatively constant and controllable rate of release of the payload from the material.

Recently, Elomaa *et al*. (**Figure 4.2**, A) showed that cross-linking PCL based resins in the µSL process, produced materials capable of undergoing surface erosion that would normally degrade *via* the bulk eroding mechanism for devices that are not cross-linked and of a smaller size than the $L_{critical}$ determined by Burkersroda *et al*.[30-31] In doing so, it was demonstrated that the $L_{critical}$ could be decreased for a classically bulk degrading material simply by cross-linking the polymer chains. Although Elomaa *et al.* eluded to the possibility of exploiting such a material for use in zero-order release applications, it was never expanded upon. Additionally, Becker *et al.* (**Figure 4.2**, B) have also demonstrated that materials made from PPF, another ordinarily bulk eroding material, are again capable of undergoing surface erosion after cross-linking in the µSL process.[32] Furthermore, cross-linked PPF tissue engineering scaffolds, with micron-scale resolution, underwent surface erosion again demonstrating the ability to decrease $L_{critical}$ by exploiting cross-linked materials. Thus, it was hypothesised that µSL could be leveraged in combination with a biodegradable material to produce drug/small molecule containing, micron-scale implants with zero-order release profiles. Furthermore, it was also postulated that using said materials in a multimaterial process could potentially allow for precise placement of encapsulated material within a complex 3D architecture. For more simple shapes, this allows for complex release profiles whereby there are periods of release and periods without release (**Figure 4.3**). Fine temporal control is possible by controlling the positioning of the layers within the part in addition to their respective thickness. For more complex

shapes, such as tissue engineering scaffolds, precise release can be accomplished by careful placement of small molecules within the matrix.

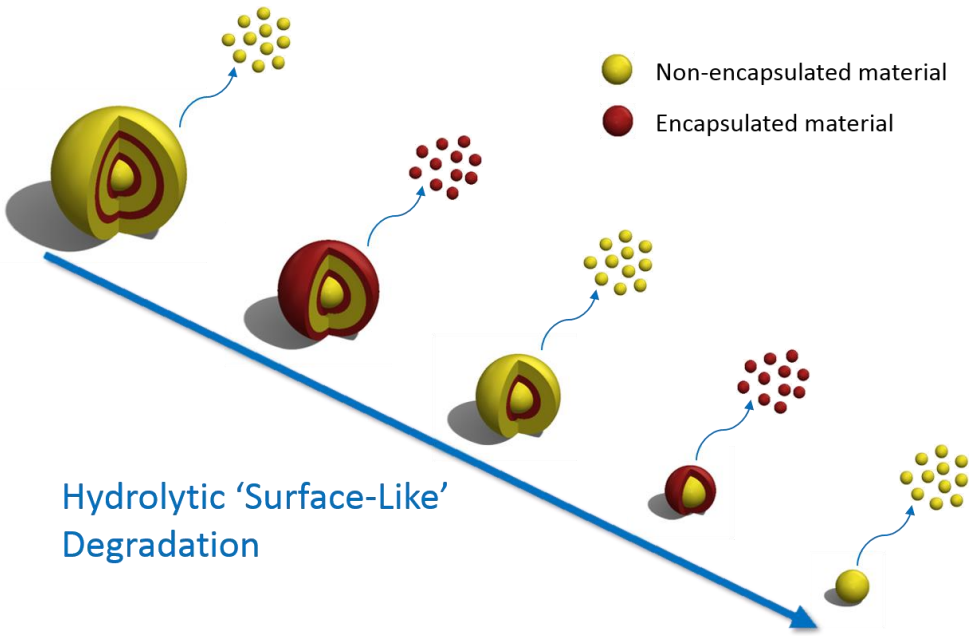

Figure 4.3. Schematic illustrating the potential temporal control over release from a multimaterial spherical device

In this work, P(EtMa-*co*-BuMa), as synthesised in the previous chapter, was optimised for processing by μSL and the printed devices were tested under various degradation conditions. It was confirmed that the printed material did undergo degradation *via* the surface eroding mechanism; subsequently a model drug/small molecule was encapsulated and the release kinetics monitored. From these studies it was determined that near zero-order release could be achieved. This chapter also describes a simple proof-of-concept as to how temporal release can be achieved by utilising both non-encapsulated and encapsulated material within the same device. Furthermore, the ability of the material to print complex 3D architectures, its mechanical properties and biocompatibility were also investigated.

4.2. Results and Discussion

4.2.1. Resin composition optimisation

The synthesis of P(EtMa-*co*-BuMa) was initially increased to a 50 g scale since larger volumes of material would be necessary for optimisation and ultimately printing. The monomers used (EtMa and BuMa) were both found to be readily scalable and capable of being produced in a one pot two-step process using similar procedures to those described in chapter 3. P(EtMa-*co*-BuMa) could be produced with M_n, and M_w values of 1700 g mol^{-1} and 2200 g mol^{-1} respectively, and a dispersity ($Đ_m$) of 1.29 as determined by SEC (**Figure 4.4**). This large-scale polymerisation was reproducible from the small-scale polymerisation (M_n = 1700 g mol^{-1}, M_w = 2300 g mol^{-1} and $Đ_m$ = 1.37) where enough alkene functionality was maintained for use in µSL. The resultant large-scale polymer was used without further purification or removal of monomer to maintain high yields whilst lowering the viscosity. The presence of acidic monomer was also considered advantageous since it would inhibit any premature nucleophilic/base catalysed thiol-ene michael addition of the more activated fumarate alkene.

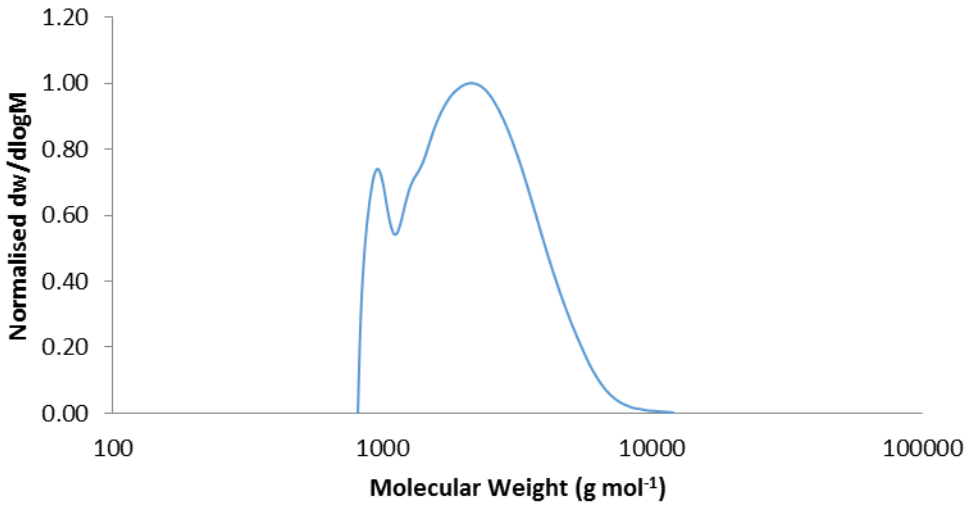

Figure 4.4. SEC chromatogram of P(EtMa-*co*-BuMa) produced on a large scale (> 50g). Samples measured against PMMA standards using DMF as eluent

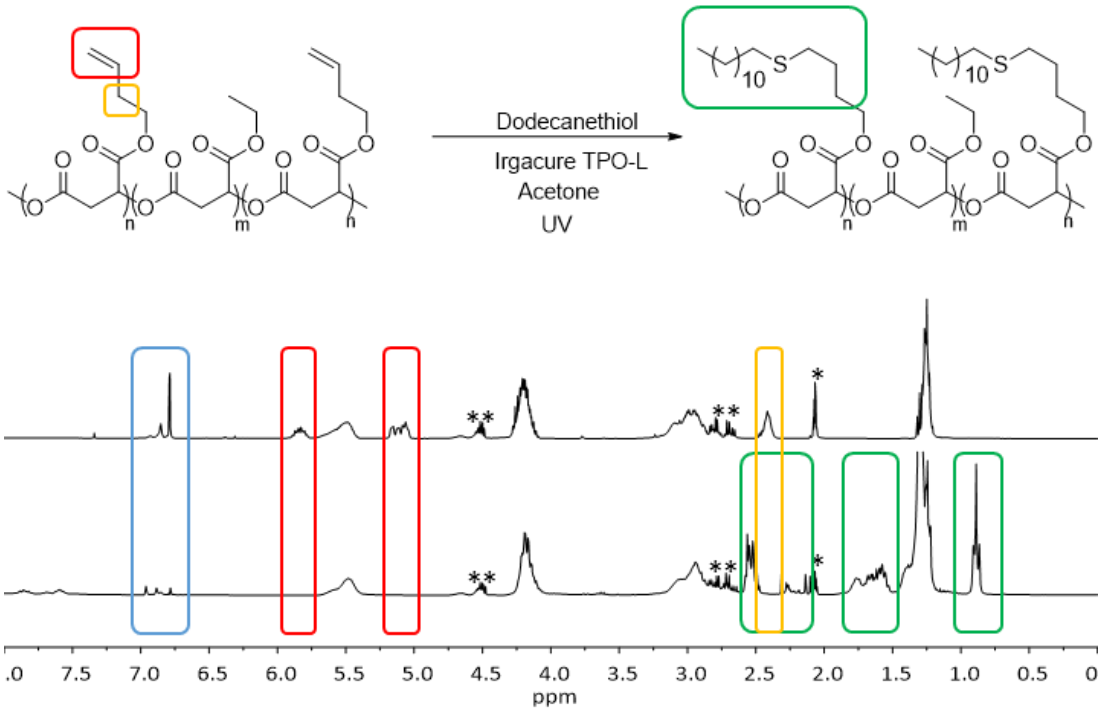

Figure 4.5. ^{1}H-NMR spectra of P(EtMa-*co*-BuMa) both before and after reaction with dodecanethiol illustrating the complete loss of signals corresponding to the olefinic protons after UV exposure (400MHz, * = acetone, ** = residual monomer)

Chapter 3 demonstrated that P(EtMa-*co*-BuMa) was the most efficient of the three copolymers produced in terms of thiol-ene reactivity towards dodecanethiol, however, it didn't undergo complete functionalisation. To confirm that P(EtMa-*co*-BuMa) was capable of complete functionalisation and therefore cement its applicability as a material for use in µSL, another small molecule study was carried out. According to ^{1}H NMR spectroscopy complete loss of the signals corresponding to olefinic protons was achieved suggesting complete functionalisation of the alkene by the small molecule thiol (**Figure 4.5**).

Despite aiming for low molecular weight polymers, in order to maintain a low viscosity, the material produced was considered far too viscous for the µSL process thus necessitating a search for suitable viscosity modifiers (see Introduction, section 1.2.6. Diluents). Initially, the possibility of utilising a non-reactive diluent was explored. As a consequence of its previous success in µSL resins based on thiol-ene

chemistry, propylene carbonate (PC) was initially screened.[33] However, PC was quickly ruled out since even modest amounts (10 wt%) at increased temperatures (65 °C) (utilised to decrease viscosity further) still failed to produce a viscosity within the working range for µSL (**Figure 4.6**). Furthermore, even at temperatures > 65 °C, the viscosity of P(EtMa-*co*-BuMa) was still outside of the working range (< 1000 mPa.s) considered suitable for producing high resolution parts in µSL. Whilst using greater amounts of PC was considered, it was deemed to be too detrimental to the end properties of the material. Although there is potential for using a heated resin vat to reduce viscosity, the tendency for the thiol-ene reaction to occur at raised temperatures would have led to premature cross-linking and ultimately failed prints.[34] Therefore, reactive diluents were explored as viscosity modifiers instead.

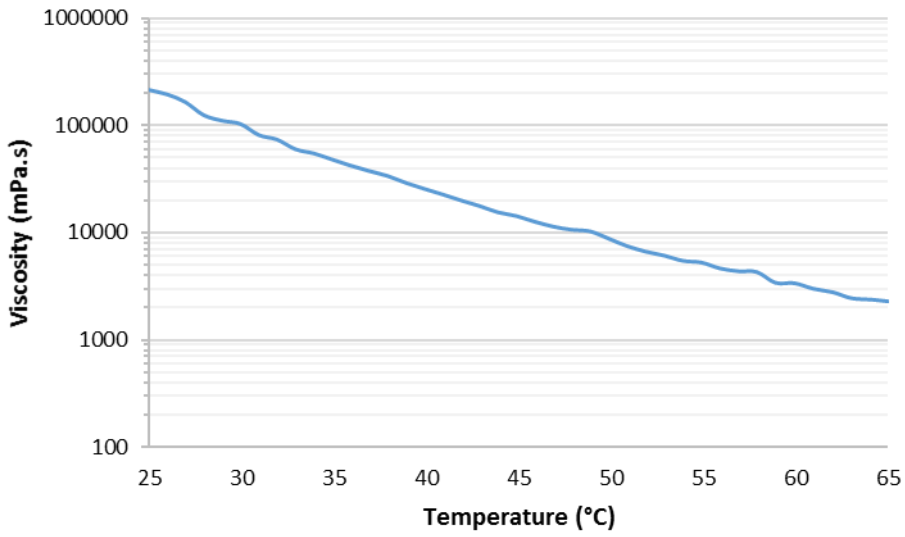

Figure 4.6. Viscosity vs. temperature graph illustrating the reduced viscosity of P(EtMa-*co*-BuMA) containing 10 wt% propylene carbonate as non-reactive diluent at higher temperatures

Whilst there are several reports of reactive diluents for acrylate based resins they are unexplored for use with thiol-ene based resins.[35-36] Diethyl fumarate (DEF) (a common reactive diluent for fumarate containing polymers) has been used alongside poly(propylene fumarate).[37] Despite DEF having similar reactivity to the fumarate end capped P(EtMa-*co*-BuMa) described here, it is not the main source of alkene

functionality and so the potential for synthesising an entirely new reactive diluent for use alongside P(EtMa-*co*-BuMa) was investigated. Considering that low incorporations of non-reactive diluent were not capable of reducing the viscosity enough it was postulated that relatively high incorporations (> 20 wt%) would probably be required. Thus, the reactive diluent was designed to embody as many of the traits of the utilised polymer as possible whilst also having a similar reactivity. Since DEF is a very low viscosity liquid at room temperature it was postulated that other similar diesters would also have low viscosity. As such, the ester, dibutenyl succinate (DBS), was selected as a candidate. The synthesis of DBS was a straightforward Fischer esterification of succinic acid, another biomass derived resource, with 3-buten-1-ol (the same alcohol used to make BuMa). After one distillation, the analytically pure product (**Figure 4.7**) displayed low viscosity (*c.a.* 4 mPa.s) liquid at room temperature. DBS also comprised of degradable ester bonds therefore maintaining the ability to undergo degradation via hydrolysis. It could also be produced on greater than a 30g scale in a two-step process thereby making it an industrially viable synthesis.

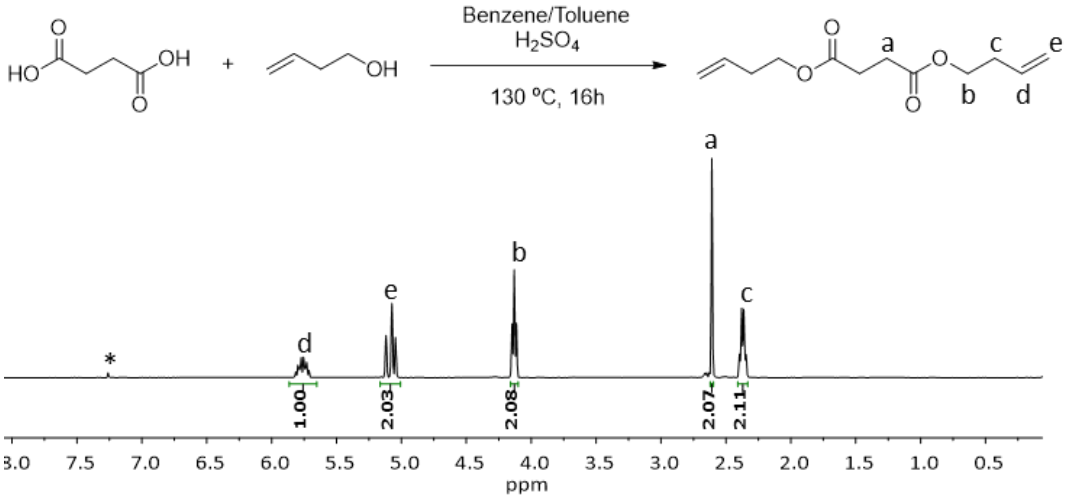

Figure 4.7. Synthesis scheme and assigned ^{1}H-NMR spectrum for Dibutenyl Succinate (DBS) (400MHz, * = $CHCl_3$)

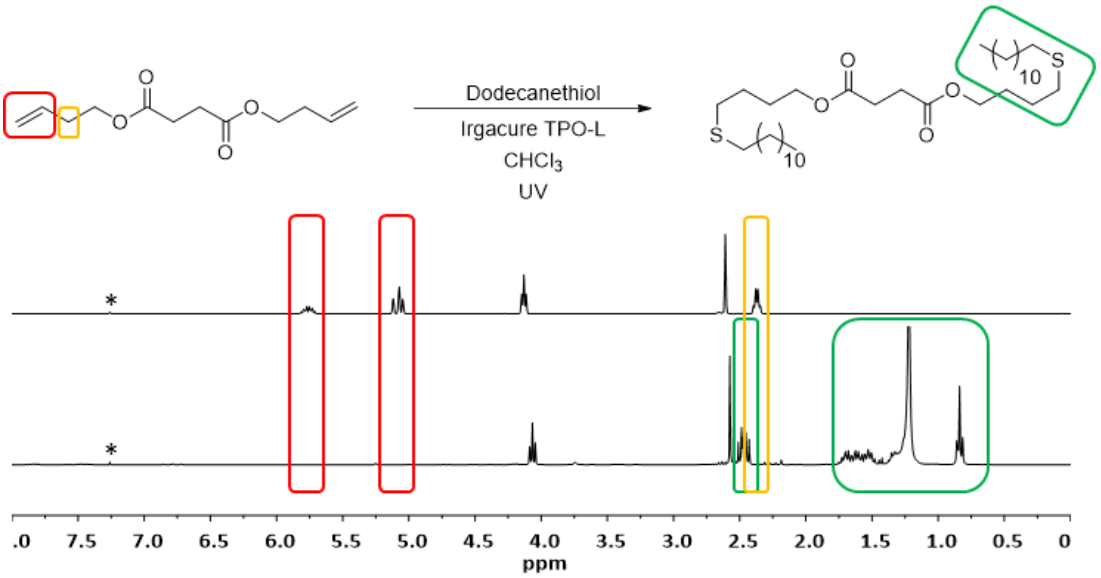

Figure 4.8. ^{1}H-NMR spectra of Dibutenyl Succinate (DBS) both before and after reaction with dodecanethiol illustrating the complete loss of signals corresponding to the olefinic protons after UV exposure (400MHz, * = Chloroform)

To confirm the thiol-ene reactivity of DBS, another small molecule study with dodecanethiol was carried out. According to ^{1}H NMR spectroscopy (**Figure 4.8**) complete loss of signals corresponding to the olefinic protons of DBS was observed after the addition of dodecanethiol thereby demonstrating its potential as a reactive diluent within the poly(EtMa-*co*-BuMa) resin composition.

To determine the quantity of DBS required to reduce the viscosity of P(EtMa-*co*-BuMa) to within a working range for µSL, rheological measurements were performed on various resin batches containing increasing amounts of DBS. Since the addition of the thiol cross-linker, pentaerythritol tetrakis(3-mercaptoproprionate) (PT3M), would decrease the overall viscosity of the resin further it was also taken into account when preparing the resin compositions such that a 1:1 ratio of thiol to alkene functionality was maintained. The resin composition chart (**Figure 4.9**, A) shows the amount of additional cross-linker required when increasing the amount of DBS with respect to P(EtMa-*co*-BuMa) in order to maintain this ratio whilst the graph below (**Figure 4.9**, B) demonstrates that a DBS content of 30 wt% or more (viscosity = 1010 ± 283 mPa.s)

with respect to oligomer is necessary since the 25 wt% (viscosity = 1983 ± 5 mPa.s) composition falls outside the workable range of µSL. Thus, the resin containing 30 wt% DBS was selected as a suitable starting point for printing.

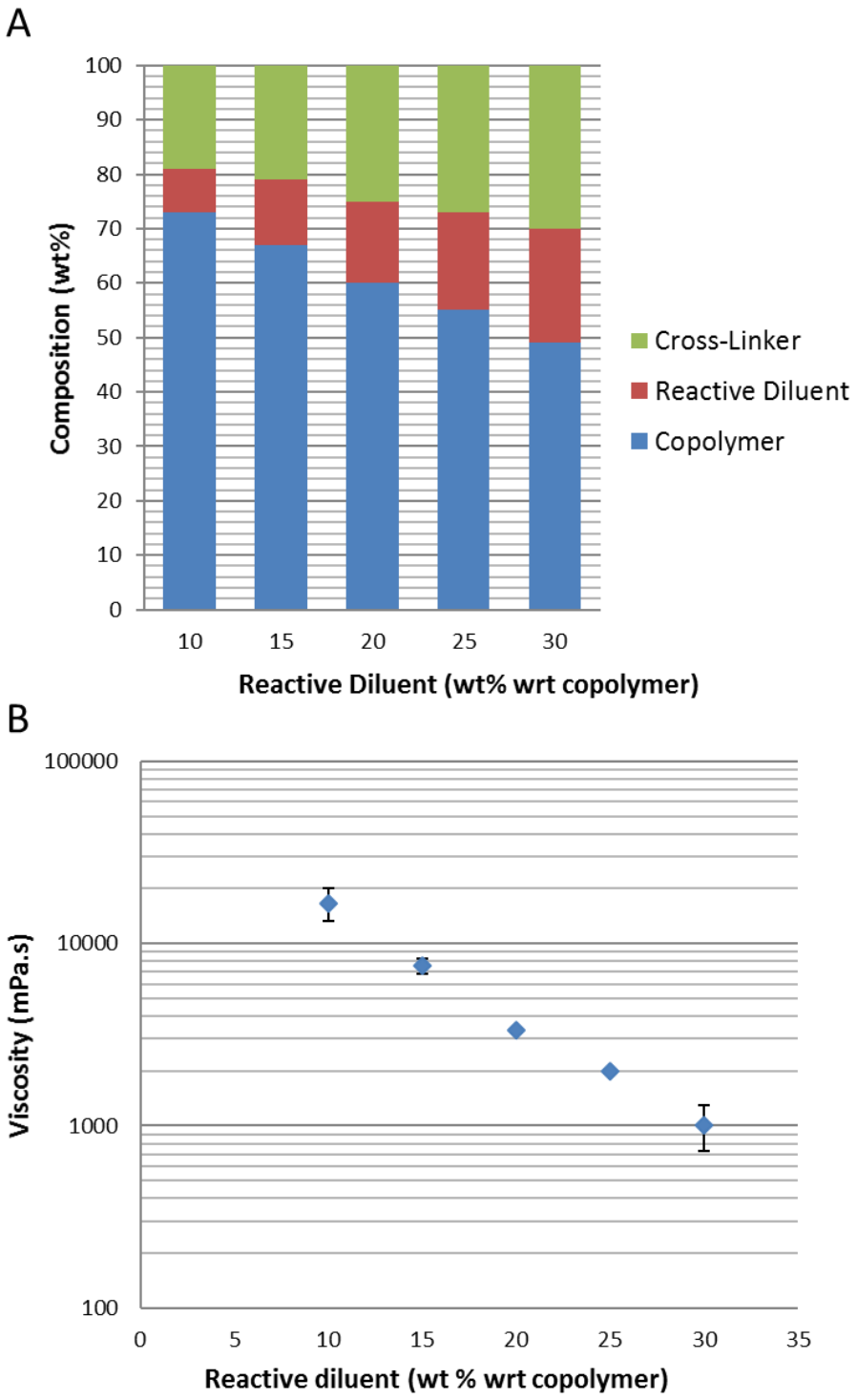

Figure 4.9. Resin composition comparison (A) for varying weight percentages of DBS with respect to Poly(EtMa-*co*-BuMa) and the respective viscosities (B) of these compositions as determined by rheology (sheer rate = 5 s^{-1})

4.2.2. Exposure time optimisation

To determine the minimum exposure time required to print 3D objects in the µSL process, a simple experiment was carried out whereby 5 layer high (layer thicknesses of 50 and 100 µm), 200 µm wide, walls were printed across a range of exposure times. To avoid extensive printing times associated with exposure time optimisation, a part (**Figure 4.10,** A) was designed to be capable of undergoing multiple exposures within the same layer so that walls could be exposed consecutively at increasing exposure times. This would then allow for the minimum exposure time required to build 5 layer-high walls to be determined. By designing the bars (representative of one layer in each wall) to be elevated above the surface of the rectangular base, whilst at different heights to one another, they are printed on, and then slicing them as one would slice a normal part (**Figure 4.10,** B), individual masks are generated for each of the bars (**Figure 4.10,** C). Each of these masks can then be projected onto the base for varying exposure times within the same layer by stopping motion on the z-axis. Upon completion of these projections, the z-axis was moved up by the desired layer height thickness and a subsequent set of bars was exposed. This process was repeated 5 times and upon completion, visual analysis of the walls was used to determine minimum exposure time.

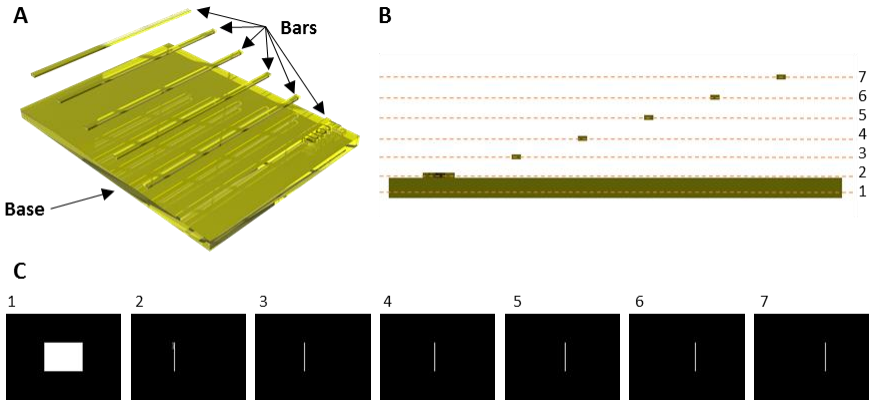

Figure 4.10. Rendered CAD drawing of curing time optimisation part (A) with side on view of the part illustrating the different height of the bars and the respective slice taken (dashed red line) (B) to produce the respective images masks (C).

Using Irgacure 784 as photoinitiator and paprika extract as the inhibitor, the resin containing 30 wt% reactive diluent (corresponding to the resin with a viscosity of 1010 ± 283 mPa.s) was used in the experiment outlined above in order to determine the minimum exposure time required to be able to build 3D parts for layer heights (resolution in the z-axis) of 50 and 100 µm (**Figure 4.11**).

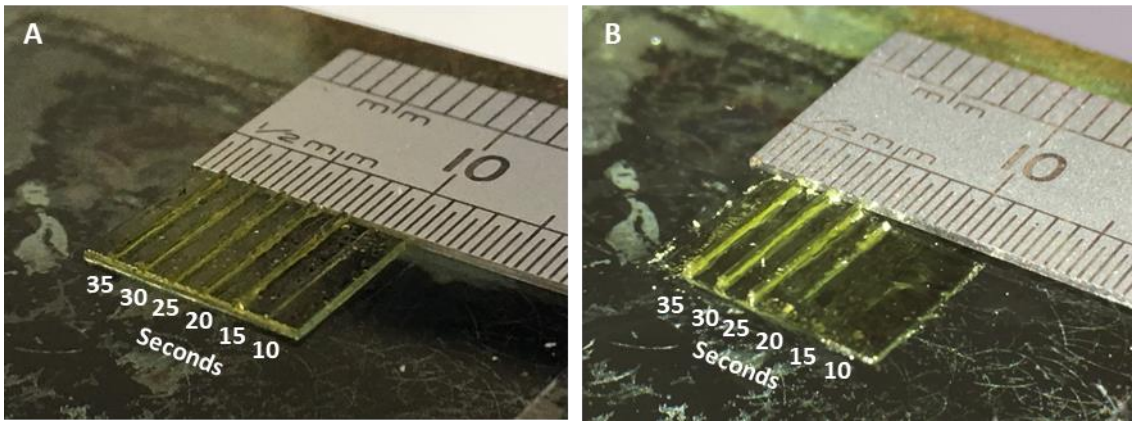

Figure 4.11. Images illustrating the ability of the material to print 5 layer walls at exposures greater than 15 seconds for a layer height of 50 µm (A) and greater than 25 seconds for a layer height of 100 µm (B).

For a layer height of 50 µm (**Figure 4.11,** A), the presence of a single layer was observed at an exposure time of 10 s demonstrating that although one of the layers was capable of adhering to the base at this exposure time, consecutive layers were not able to adhere to the layer above. However, upon increasing the exposure time to 15 s it was observed that all the layers of the 5 layer wall did print indicating that an exposure time of 15 s or more is a suitable starting point for printing micron-scale features at a 50 µm layer height. As expected, a layer height of 100 µm (**Figure 4.11,** B) required longer exposures of 25 s or more to produce walls.

4.2.3. Initial accelerated degradation study

To probe if the material underwent surface degradation rather than bulk degradation, an initial study was carried out under accelerated conditions. Firstly, a puck shaped part was designed and printed using the optimised resin composition containing 30 wt% DBS and optimised exposure time of 20 seconds. The initial mass of the printed

pucks were recorded and their subsequent mass loss after degradation in NaOH (1M) at physiological temperature (37 °C) was recorded at regular intervals and compared to that of pucks made from a non-degradable commercially available resin as a control since there are no commercially available degradable resins for comparison.

The data (**Figure 4.12**) shows that the pucks fabricated using the P(EtMa-*co*-BuMa) resin degraded in an almost linear manner and had essentially reached complete degradation after 140 minutes, whereas the pucks made using the commercially available resin displayed no signs of degradation on a similar timescale. This linear degradation behaviour is a hallmark of surface degradation and was further corroborated by monitoring the dimensions of the pucks during degradation. The pucks were intentionally designed to have a different base (top and bottom) and lateral (side) surface areas so that the dimension corresponding to the degradation of one of these would be dissimilar to the other providing they do in fact degrade as a function of the surface area (**Figure 4.13**).

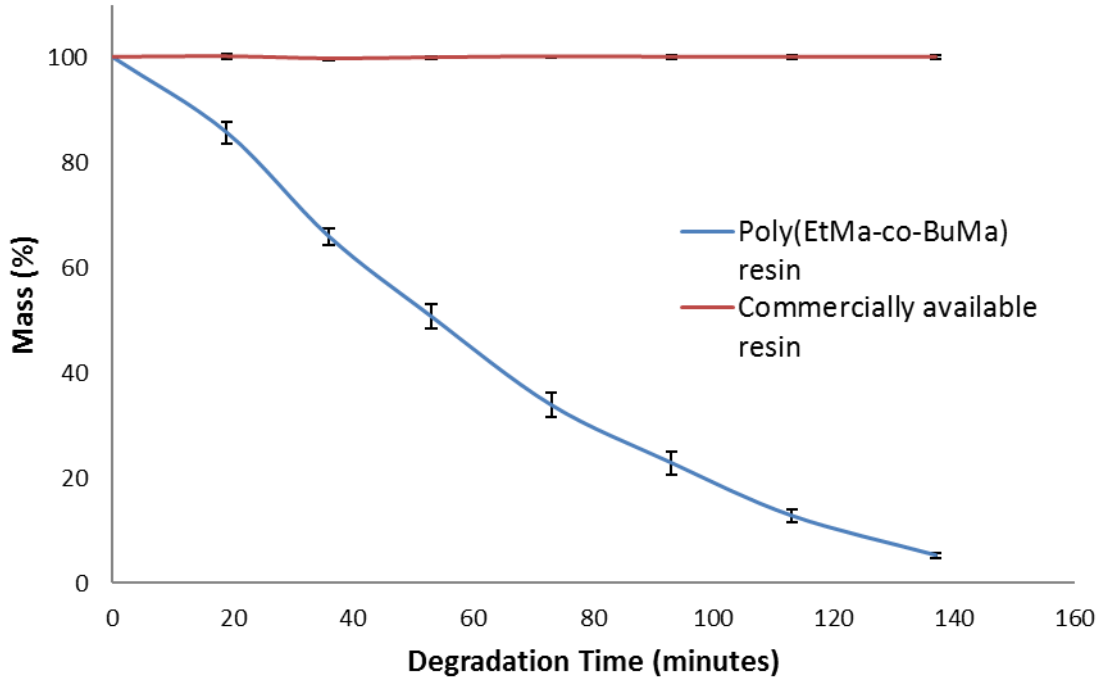

Figure 4.12. Gravimetric analysis of degradation pucks fabricated using the P(EtMa-*co*-BuMa) containing resin as compared with pucks fabricated using a commercially available resin (EnvisionTec R11) under accelerated conditions (1M NaOH) and physiological temperature (37 °C)

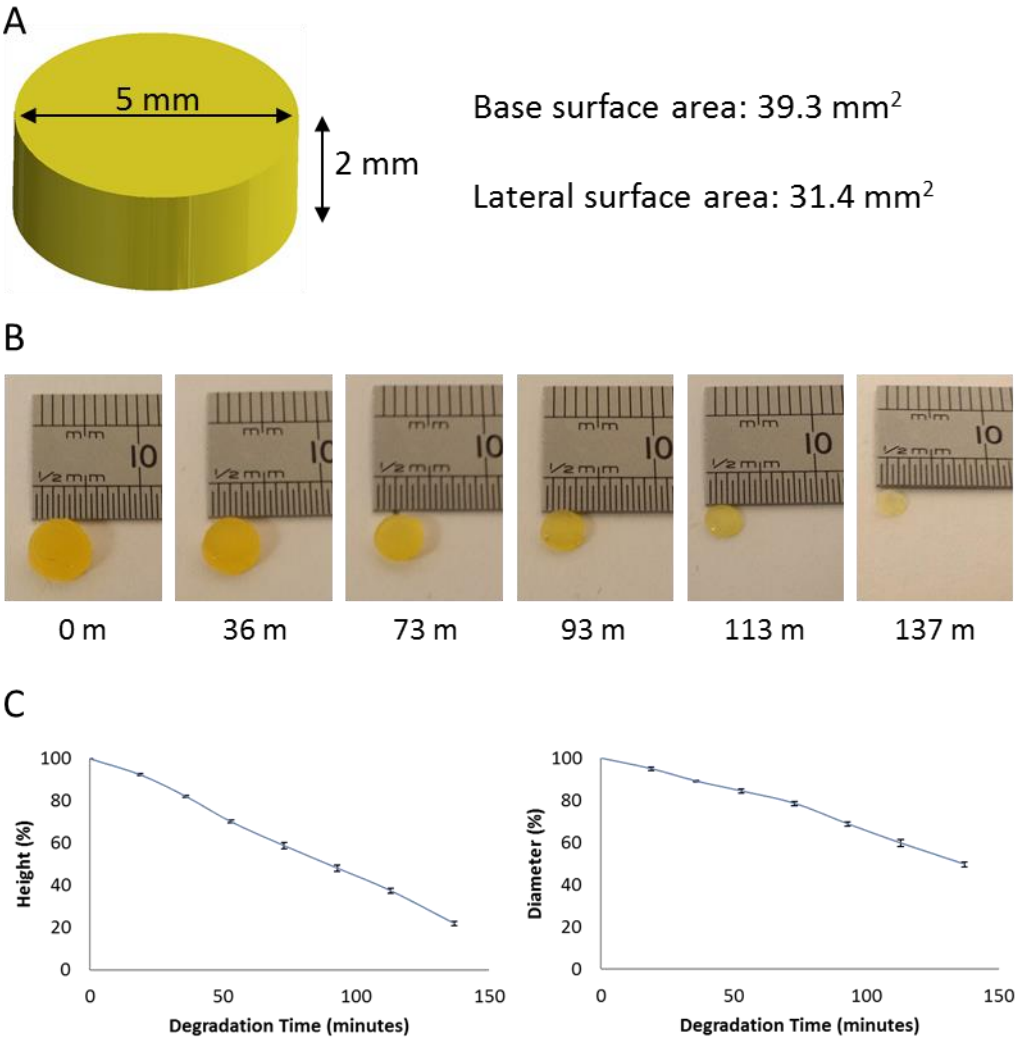

Figure 4.13. Dimensions and surface areas of the base and lateral surfaces of the designed puck (A). Images of an exemplar puck at various time points during degradation to illustrate the surface eroding nature of the material (B) and the data corresponding to the percentage decrease in both height and diameter during the course of degradation (C).

The dimensions of the puck and the respective base (39.3 mm^2) and lateral (31.4 mm^2) surface areas are depicted in **Figure 4.13,** A. Upon measurement of the pucks before degradation the actual dimensions were found to be 5.21±0.04 mm for the diameter and 1.97±0.01 mm for the height representative of a positive 4.2 % error in the XY axes and a negative 1.5% error in the Z axis thereby demonstrating the relatively high accuracy of the printed pucks as compared with the original CAD design. In addition to following the height and diameter dimensions during degradation, photos were taken of an exemplar puck at the same time points (**Figure 4.13,** B) that provide a

visual demonstration of the same puck becoming smaller and smaller thereby indicating a surface eroding nature. Similar to the mass loss profile (**Figure 4.12**), the loss in height and diameter profiles (**Figure 4.13,** C) also show a nearly linear decrease over the course of degradation again indicative of a surface eroding mechanism. More in depth analysis also shows that the height profile decreases to 22% of its original height whilst the diameter profile decreases to 50% of its original diameter which, considering the surface area affecting the degradation of the height is greater than the surface area affecting the degradation of the diameter, is to be expected and therefore it can be concluded that the material does undergo surface erosion under accelerated conditions.

4.2.4. Controlled small molecule release

Having confirmed that devices produced using the optimised resin composition underwent surface erosion upon degradation in basic media, it was postulated that loading the resin with a model drug/small molecule would allow for zero order release providing the device had an appropriate geometry. Whilst the puck geometry in the initial degradation study was previously chosen to demonstrate that degradation was a function of surface area it would be unsuitable for demonstrating zero order release since the rate of degradation occurs more rapidly from the base (top and bottom) faces as compared with the lateral face. The most suitable geometry for zero order release would be a spherical one, since this particular geometry has only one surface face. Spheres containing fluorescein (a fluorescent dye) were printed as hemispheres and bound together (**Figure 4.14**). The assembled fluorescein containing spheres were subjected to more mild conditions (0.1M NaOH compared to the previous 1M NaOH used) than the initial accelerated degradation of pucks to allow for greater time intervals between sampling.

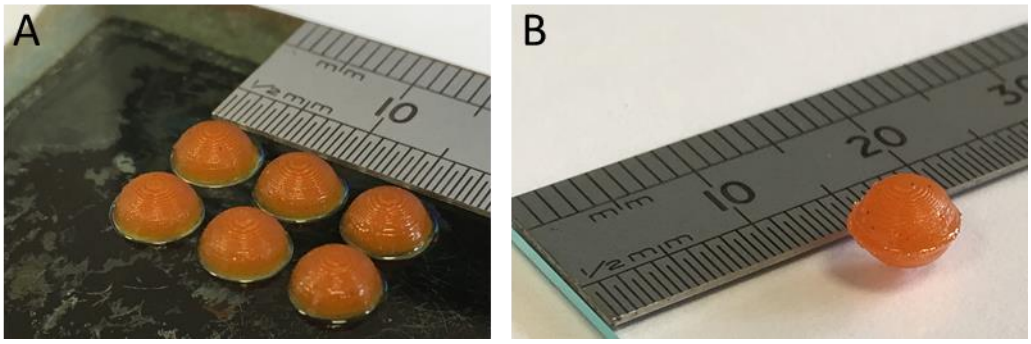

Figure 4.14. Pictures illustrating the printed hemispheres (A) and an assembled sphere (B).

The data (**Figure 4.15**, **A**) indicates that the spheres still degrade via a surface eroding mechanism since the mass loss profile is, again, almost linear after an initial swelling phase. This initial swelling may have occurred, but was perhaps not evident in the previous study (**Section 4.2.3**) because the degradation was accelerated and no data point was taken during this phase. After the initial swelling phase the mass loss profile for the sphere does adopt an almost linear decrease in mass over time thereby suggesting that after an initial ingress of degradation media into the bulk material that causes the swelling, the sphere does in fact undergo degradation *via* the surface eroding mechanism.

The release profile for the sphere (**Figure 4.15**, **B**) is in good agreement with the mass loss profile. For instance, there is an initial burst or increase in rate of release during the swelling phase as would be expected in a material that swells. After the swelling phase, the rate of release stabilises and is almost linear for the remainder of the degradation indicating near-zero order release. The near-zero order release rate for the P(EtMa-*co*-BuMa) containing sphere was considered a promising proof-of-concept. Such a result warranted further investigation and additional studies on whether or not the rate of degradation and release could be tuned by making small alterations to the resin composition.

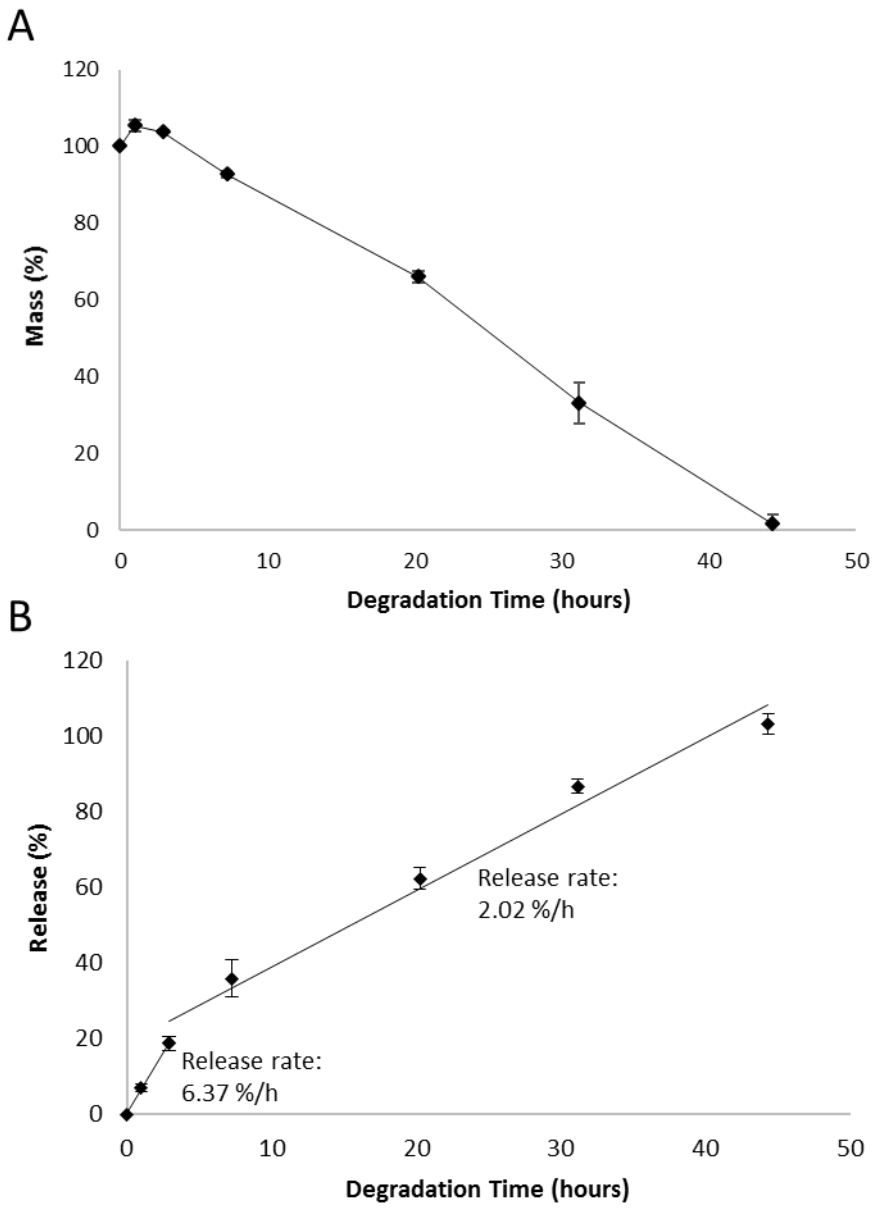

Figure 4.15. Gravimetric analysis of fluorescein loaded spheres fabricated using the P(EtMa-*co*-BuMa) containing resin (A) and the respective release profile (B) under accelerated degradation conditions (0.1M NaOH) and physiological temperatures (37 °C)

4.2.5. Resin composition alteration for tuning degradation and release

Initially, it was postulated that the degradability of the cured material could be altered by incorporating non-functionalised malic acid into the polymerisation of P(EtMa-*co*-BuMa). The incorporation of small quantities of malic acid could have decreased the hydrophobicity further thereby causing an increase in degradation rate. However, since the optimised resin (**Section 4.2.1**) degraded so quickly, the development of a slower degrading material was warranted. Additionally, studying the effects of malic

acid incorporation was regarded as time intensive and synthetically more complicated so it was abandoned. Instead, it was hypothesised that simply altering the amount of P(EtMa-*co*-BuMa) in the resin composition would vary the hydrophilicity and therefore the degradation rate of the cured materials produced.

In order to determine the effect that P(EtMa-*co*-BuMa) concentration had on the degradability of the sample, the quantities of other components- including the reactive diluent and thiol cross-linker- would have to be maintained as to only alter one variable at a time. Whilst it was necessary to keep the quantities of the other components the same, it was also considered undesirable for a system that relies on equal stoichiometry between alkene and thiol functionalities. This was because it could potentially lead to inefficient cross-linking which could also potentially affect the degradability of the material. Nevertheless, the study was carried out under the assumption that contributions to degradability by the cross-linking efficiency would be negligible. To make sure that resin compositions with varying amounts of P(EtMa-*co*-BuMa) were still within a workable range for µSL, the viscosity of resins containing between 20 and 60 wt% of the oligomer whilst maintaining a constant amount of both reactive diluent and cross-linker were determined (**Figure 4.16**).

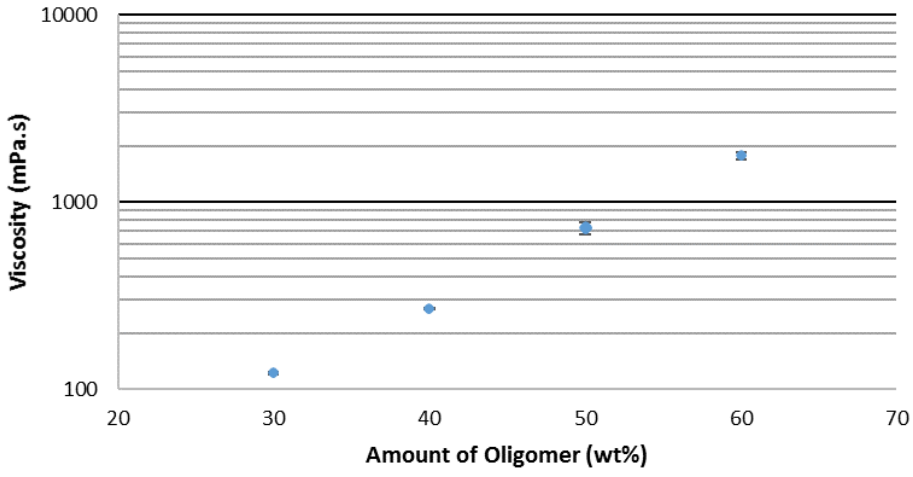

Figure 4.16. Graph illustrating the viscosity of resins containing between 30 and 60 wt% P(EtMa-*co*-BuMa) whilst maintaining constant quantities of reactive diluent and cross-linker.

The viscosity data (**Figure 4.16**) shows that all resin compositions below 50 wt% oligomer content fall within a workable range for µSL (< 1000 mPa.s). 30 wt% was found to be the lower limit for a resin containing P(EtMa-*co*-BuMa) since the 20 and 10 wt% compositions did not mix homogenously leading to phase separation that resulted in inconsistent viscosity data.

In addition to the resin containing 50 wt% P(EtMa-*co*-BuMa) (degradation study already carried out in **Section 4.2.3 & 4.2.4**), a resin containing 30 wt% and a resin free of any functional oligomer (0 wt%) were selected as a suitable starting point for decreasing the rates of degradation and release. The 0 wt% resin was also chosen as to demonstrate that parts not containing any P(EtMa-*co*-BuMa) are also capable of degradation albeit at a much slower rate. To confirm that decreasing the amount of P(EtMa-*co*-BuMa) in the resin composition decreases the hydrophilicity of the cured material, drop shape analysis was carried out on thin films made from resins containing 0, 30 and 50 wt% P(EtMa-*co*-BuMa) (**Figure 4.17**).

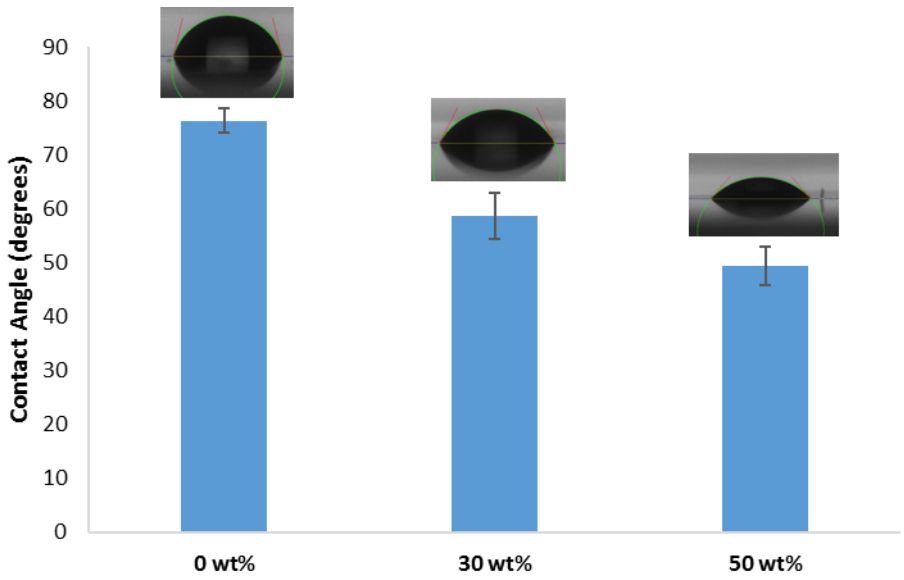

Figure 4.17. Drop shape analysis of distilled water on thin films of cured resin compositions containing 0, 30 and 50 wt% P(EtMa-*co*-BuMa), respectively.

Drop shape analysis (**Figure 4.17**) indicated that hydrophilicity was positively correlated to the amount of P(EtMa-*co*-BuMa) in the resin composition, with 0, 30 and 50 wt % compositions demonstrating contact angles of 76.3 ± 2.2 °, 58.6 ± 4.3 ° and 49.4 ± 3.5 °, respectively. If the degradability of the cured material is correlated to the hydrophilicity of the material, in addition to the degree of cross-linking, the cured materials with greater contact angles (higher hydrophobicity) should degrade more slowly. Before degradation and release studies were carried out on the new materials their mechanical properties and ability to print were examined.

4.2.6. Mechanical properties of the cured materials

To test the mechanical properties of the cured materials (containing 0, 30 or 50 wt% (P(EtMa-*co*-BuMa)), dog-bone shaped samples were prepared by pipetting the respective resin formulation into a stainless-steel plate (1.5 mm thick) containing dog-bone shaped templates and solidifying the resin into uniform dog-bone shapes by UV-post-curing. The mechanical strength of the moulded dog-bones was assessed by tensile testing (**Figure 4.18**). The 50 wt% material was found to have the lowest ultimate tensile strength (UTS) of 0.5 ± 0.1 MPa, however it also demonstrated the highest strain at break of 33.2 ± 5.2% with a Young's modulus of 1.2 ± 0.2 MPa,. The 30 and 0 wt% materials were found to have lower strain at breaks of 26.6 ± 3.8% and 23.4 ± 6.4%, respectively but with higher Young's moduli of 3.2 ± 0.2 MPa and 7.5 ± 0.4 MPa, respectively. The UTS of the 0 wt% material was found to be double (1.7 ± 0.4 MPa) the UTS observed for the 30 wt% material (0.9 ± 0.1 MPa) which was nearly double the UTS for the 50 wt% material.

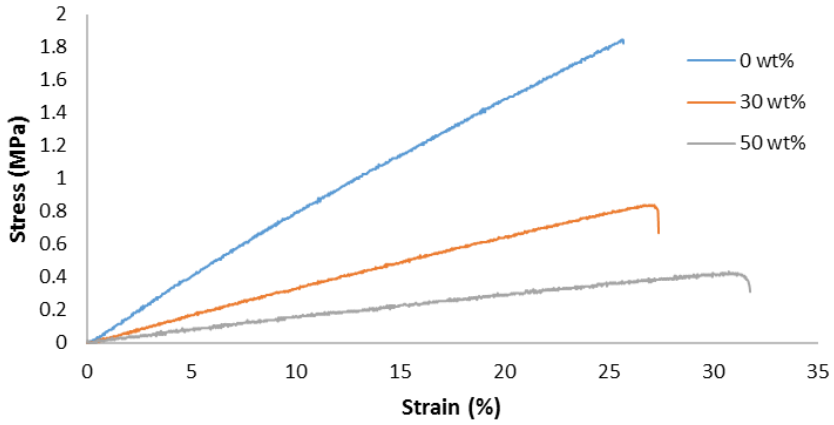

Figure 4.18. Plot of stress (MPa) vs. strain (%) for photocured resins containing 0, 30 and 50 wt% P(EtMa-co-BuMa) respectively

Thus, increasing the P(EtMa-*co*-BuMa) content decreased the ultimate strength of the cured material in addition to decreasing the amount of force required to stretch the material. Whilst the cured materials presented poor mechanical properties in terms of tensile strength, the ability to be put under relatively high amounts of strain were considered a desirable quality for subcutaneous drug delivery implants. The greater elongation observed with materials containing more P(EtMa-*co*-BuMa) was attributed to a decrease in cross-linking density. Additionally, the ratio of alkene to thiol functionalities could have been altered after changing the resin composition thereby also hampering the cross-linking efficiency. To investigate the cross-linking efficiency further, Raman spectroscopy was utilised to monitor the decrease in amounts of thiol and alkene functionality present in the cured material as compared with the uncured resin (**Figure 4.19**).

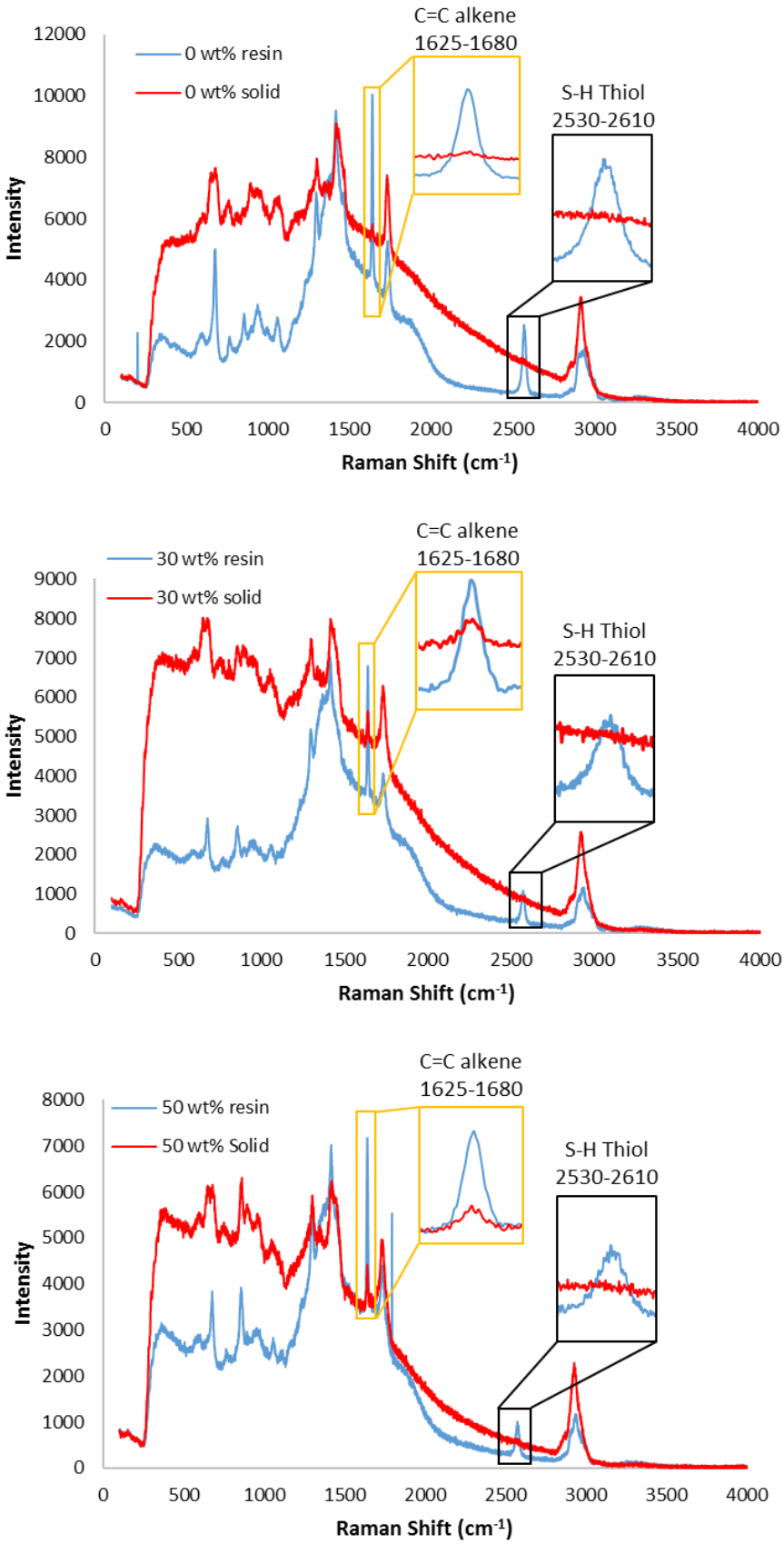

Figure 4.19. Raman spectra of the three resin compositions (0,30 and 50 wt% P(EtMa-*co*-BuMa) both in the liquid resin and the solidified material after the curing process

Using Raman spectroscopy, the diagnostic vibrations corresponding to the alkene and thiol functionalities can be found at 1625-1680 cm^{-1} and 2530-2610 cm^{-1}, respectively. According to Raman spectroscopy, for all three resin compositions, there is almost quantitative consumption of the thiol functionality after solidification of the resin (**Figure 4.19**). However, in the case of the alkene functionality, complete conversion was only observed for the 0 wt% resin formulation while 30 and 50 wt% materials retained unreacted alkene moieties. Although the presence of alkenes after the curing process suggest that there is incomplete cross-linking, the fact that the thiol functionality is still consumed in its entirety indicates that whilst cross-linking efficiency is not affected by a non-stoichiometric equivalence of alkene to thiol functionalities, the extent of cross-linking can be influenced. This supports the postulation made in section 4.2.5. since in a 'click' reaction where there are substoichiometric quantities of components, the cross-linking density will be influenced. Thus, further investigations into varying ratios of alkene to thiol functionality should be carried out to improve on this further.

4.2.7. 3D printing

To test the ability of optimised resin compositions to print complex 3D architectures using the µSL process, a highly intricate gyroid structure was chosen as a test print. More specifically, the gyroid-like '*(10, 3)-a'* crystal structure generated using mathematical algorithms by George Hart (hereafter referred to as a hartcube) was selected because of the difficulties associated with printing such an intricate structure (**Figure 4.20**). When scaled down, not only does the hartcube contain only micron-scale features, it also contains complexities such as overhangs and internal porosities that can be difficult to print.

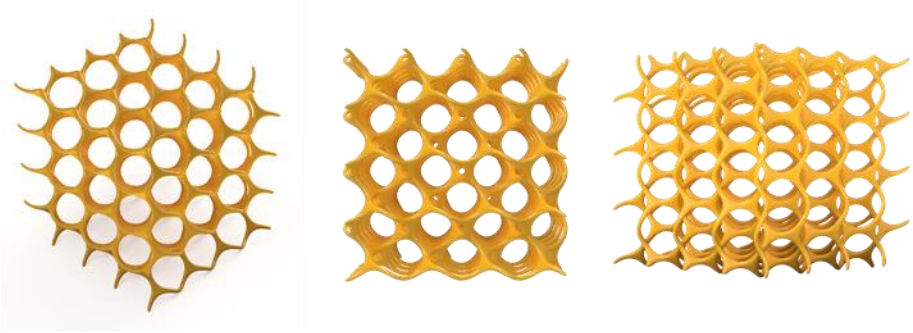

Figure 4.20. Varying views from a CAD render of the '(10, 3)-a' crystal structure generated by George Hart exemplifying the intricacy and complex nature of the design

All three resin compositions were all found to be capable of printing the hartcube at 50-micron layer heights albeit with varying levels of success (**Figure 4.21**). Each composition required specific exposure times per layer to achieve a successful print with a successful print being defined as the ability to print every layer within the job file whilst preserving the majority of features depicted in the original CAD design. The 0 wt% P(EtMa-*co*-BuMa) containing resin was found to require the shortest exposure time of 15 seconds per layer while the 30 and 50 wt% resins were found to require 18 and 25 seconds per layer, respectively. This was attributed to the higher viscosity of resins containing more P(EtMa-co-BuMa) thereby decreasing the mobility of reactive chain ends. Furthermore, the decrease in extent of cross-linking, as outlined in the previous section, may have also contributed to the higher exposure times required since for resin compositions containing 50 wt% P(EtMa-*co*-BuMa) it was found that decreasing the exposure time caused insufficient adhesion between layers and ultimately print failure. The variation in colour between the three hartcubes is a consequence of incomplete consumption of the photoinitiator which gradually fades overtime. For example, the 30 wt% hartcube has been printed most recently and is thus, the most vibrant.

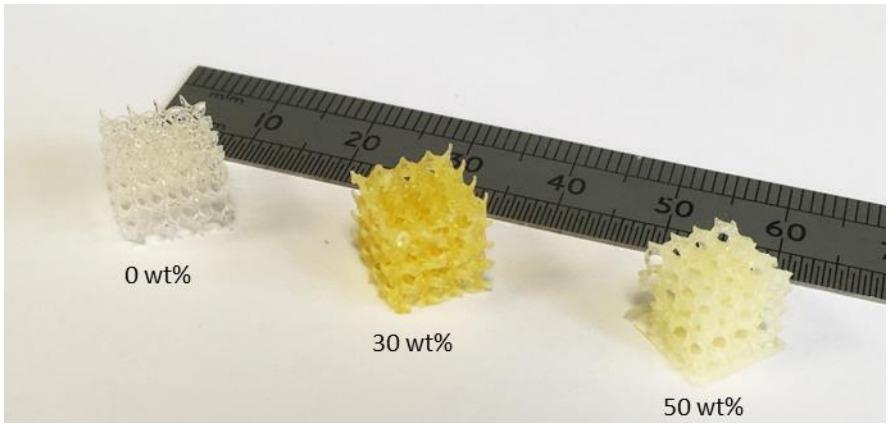

Figure 4.21. Photograph taken of the *(10, 3)-a* gyroid structures printed using the 0, 30 and 50 wt% P(EtMa-co-BuMa) containing resins

The dimensions of the hartcubes in all three axes (x, y and z) were measured using verniers so that a comparison between them and the initial design of the hartcube could be made. The dimensions of the original design were 9.18 mm for the x-axis and 9.17 mm for both the y and z-axis. For the 0 wt% hartcube, the x, y and z dimensions were found to be 107.1, 106.6 and 97.5 % of their targeted dimension, respectively. This indicated that the resin was in fact overcuring in the x and y directions whilst the discrepancy in the z direction was considered negligible. The hartcube made from the 30 wt% resin was found to be more accurate with x, y and z dimensions of 100.5, 99.9 and 96.7 %, respectively whilst the 50 wt% resin produced a hartcube with dimensions lower than those targeted at 95.8, 93.6, and 89.7 %. This trend of producing smaller structures with increasing P(EtMa-*co*-BuMa) contents was originally thought to be a consequence of shrinkage as is common in other resins that use acrylate cross-linking chemistry rather than thiol-ene, however, upon further inspection it soon became apparent that the hartcubes made from 30 and 50 wt% resins had deficiencies in the edge overhanging features likely because of the increased viscosity and decrease in

extent of cross-linking.[38] To investigate this phenomenon further, microCT analysis was employed (**Figure 4.22**).

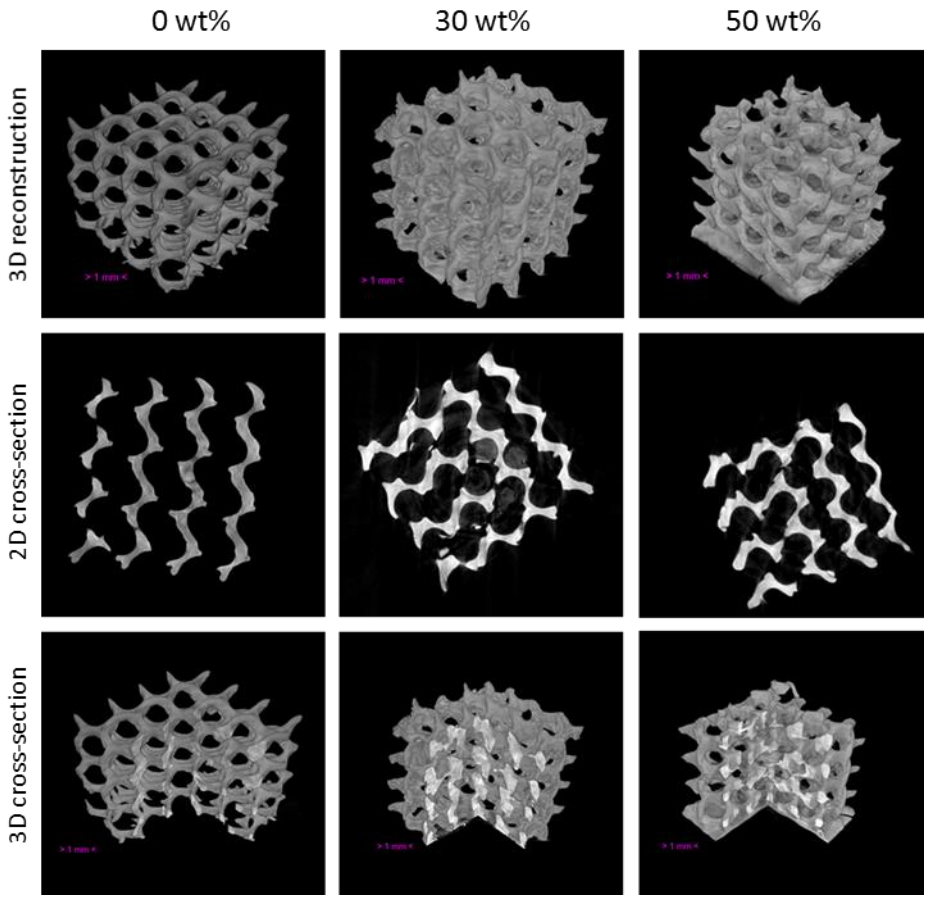

Figure 4.22. Images produced from microCT reconstructions illustrating the ability of 0, 30 and 50 wt% P(EtMa-*co*-BuMa) containing resins to print complex 3D structures in addition to representing the internal features and porous architectures of the printed hartcubes

Upon analysis of the hartcube microCT reconstructions, the nature of the resins containing more P(EtMa-co-BuMa) to be less capable of printing overhanging features was more apparent (**Figure 4.22**). These features are more obvious in the 0 wt% hartcube and far less pronounced in the hartcubes made from the 30 and 50wt % resins. In addition to corroborating that the higher P(EtMa-*co*-BuMa) content caused a decrease in printing resolution, the reconstructions from microCT scanning also revealed the internal features and thus the porosity within them. Initial examination showed that the 0 wt % resin produced a structure with the highest porosity whilst the 30 and 50 wt % resins produced hartcubes with thicker struts and therefore decreased

porosity. Indeed, when calculating the porosity of the structures produced it is found that the 0, 30 and 50 wt % structures have porosities of ϕ = 0.88, 0.65 and 0.64 respectively. This decrease in porosity was attributed to several factors including; the increased likelihood of resins with higher viscosities trapping themselves in pores above, the increased exposure time required for layer-to-layer adherence causing more overcure in the x and y directions and the potential for the paprika based photoinhibitor to undergo photocatalysed oxidation.[39] The microCT analysis also confirms that the resin compositions herein should not exceed P(EtMa-*co*-BuMa) contents of 50 wt% for the production of complex 3D parts. This also suggests that resin viscosity should not exceed 1000 mPa.s.

Despite the decreased porosity of P(EtMa-*co*-BuMa) containing hartcubes, the structures produced are still sufficiently porous demonstrating that these resins are suitable for printing complex 3D architectures in the µSL process. Additionally, it should be noted that any discrepancies between initial design and final product can, in most cases, be accounted for in the initial design and scaling of the model that is to be printed.

4.2.8. Tuneable degradation and release

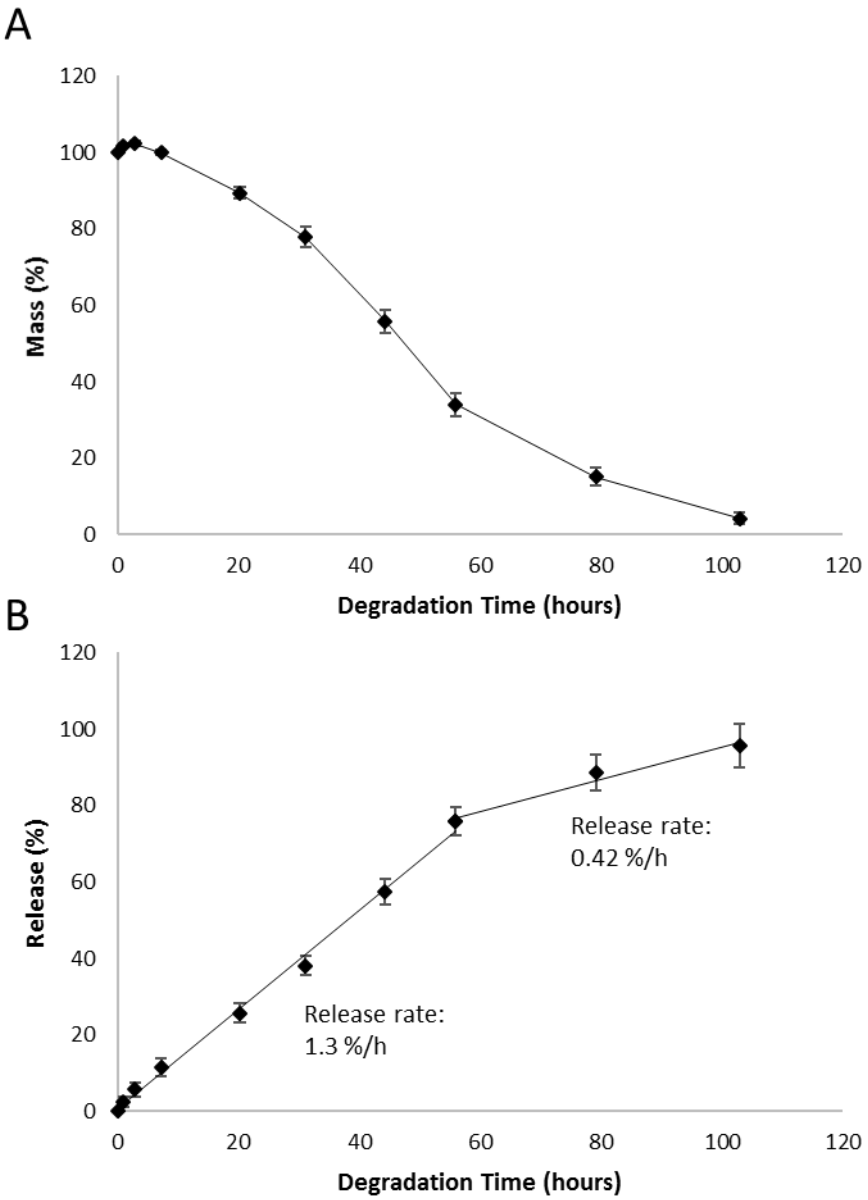

Figure 4.23. Gravimetric analysis of fluorescein loaded spheres fabricated using 30 wt% P(EtMa-*co*-BuMa) containing resin (A) and the respective release profile (B) under accelerated degradation conditions (0.1M NaOH) and physiological temperatures (37 °C)

Degradation spheres for the 30 and 0 wt% resin compositions were printed and assembled analogously to the 50 wt% resin (Section 4.2.4). Additionally, the degradation and release was monitored in a similar manner (**Figure 4.23**). The degradation profile of the sphere made from the 30 wt% sphere (**Figure 4.23, A**) also displays an almost linear trend thereby indicating the surface eroding nature of the material holds true for resin compositions containing lesser amounts of P(EtMa-*co*-

BuMa). Whilst the 30 wt% sphere still demonstrates a swelling phase, it is less significant than in the case of the 50 wt% sphere likely as a consequence of the decreased hydrophilicity. The 30 wt% sphere reaches a maximum swelling of 102.4% by mass whereas the 50 wt% sphere swells to 105.4% of its original mass. After the swelling phase the rate of mass loss thereafter starts off steadily increasing in rate until after 40 h whereby the degradation rate decreases. This decrease in degradation rate was attributed to the decrease in surface area as the size of the sphere decreases and so whilst the degradation profile is not perfectly linear, the data still suggests that the rate of degradation is a function of surface area.

The 30 wt% sphere displayed little to no signs of an initial burst release as would be expected considering the initial swelling phase was less prominent (**Figure 4.23**, **B**). Instead, the 30 wt% containing sphere underwent an initial, almost constant release rate up until after 40 h of degradation where the rate of release (and degradation rate) decreased. The excellent agreement between the release and degradation profiles suggests that the rate of release is dependent on the degree of degradation and not the concentration of fluorescein in the sample. Furthermore, although the rate of release is not constant throughout it can be said that there are periods within the degradation timeframe whereby the release is constant thereby displaying the ability to undergo zero-order release. In addition, there is a clear difference in rates between the 50 and 30 wt% P(EtMa-*co*-BuMa) containing spheres since the former took just over 2 days to degrade to 1.6% of its original mass while the latter took over 4 days to degrade to 4.3% of its original mass. This highlights the tunability of the degradation and release rates by simply altering the amount of P(EtMa-*co*-BuMa) in the initial resin composition.

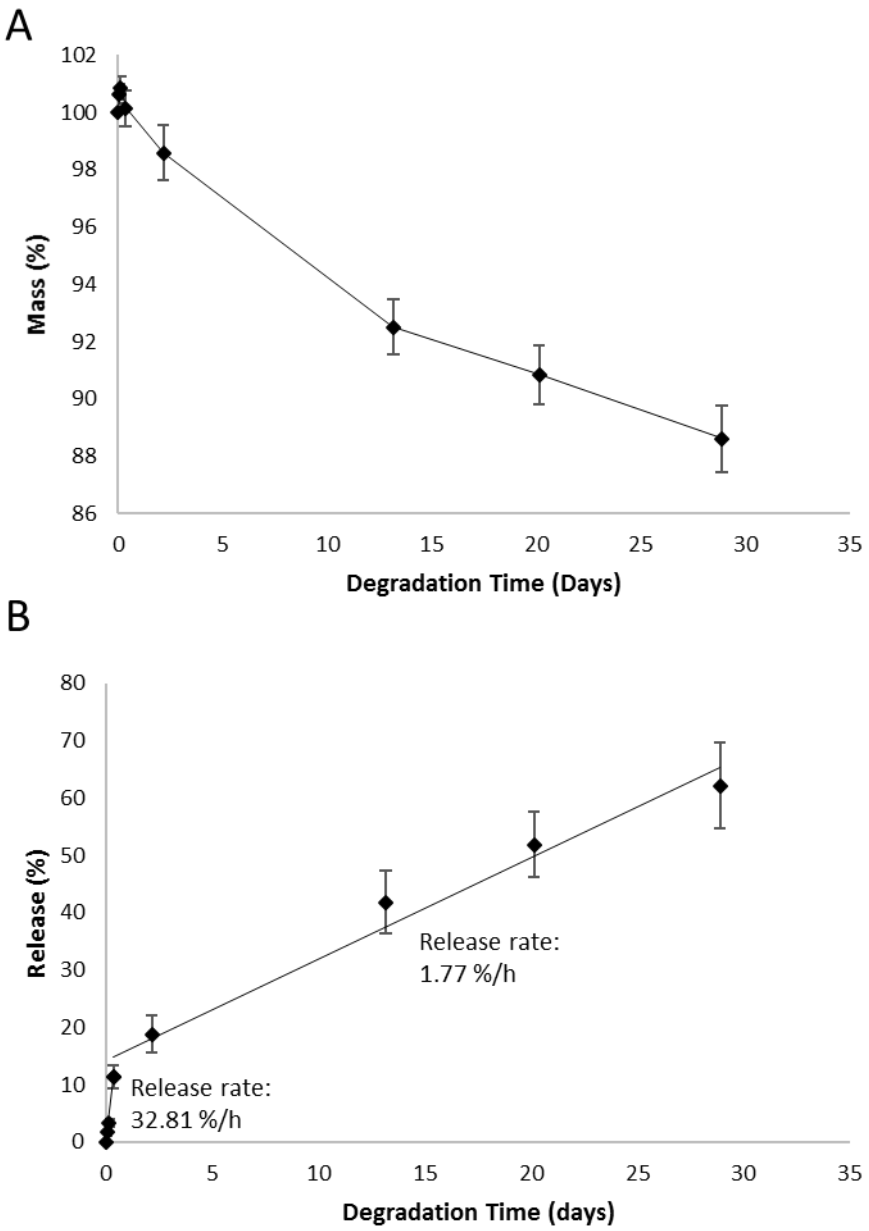

Figure 4.24. Gravimetric analysis of fluorescein loaded spheres fabricated using 0 wt% P(EtMa-*co*-BuMa) containing resin (A) and the respective release profile (B) under accelerated degradation conditions (0.1M NaOH) and physiological temperatures (37 °C)

As expected, the most hydrophobic resin containing 0 wt% poly(EtMa-*co*-BuMa), demonstrated a much slower degradation rate (**Figure 4.24,** A) and after 4 weeks of degradation only demonstrated a mass loss of 11%. The degree to which the sphere swelled was also less only swelling to 100.85% of its original mass again as a consequence of its increased hydrophobicity. In a similar manner to the other two resin compositions the 0 wt% material also exhibited an almost linear mass loss profile once

again suggesting surface erosion. Analysis of the release profile (**Figure 4.24,** B) revealed that within the same 4 weeks 62.2% of the encapsulated fluorescein was released. This was unexpected since the sphere had only lost 11% of its original mass, however, the release profile still remained almost linear indicative of near zero-order release. The large extent of release and increased release rate was attributed to the decreased solubility of the hydrophilic fluorescein in a more hydrophobic material matrix.

4.2.9. Non-accelerated *in vitro* degradation study

To gain a better understanding of how the materials developed herein might degrade *in vivo*, degradation pucks, similar to those used in **section 4.2.3**, were produced and their degradation was monitored over the course of 6 months in minimum essential medium (MEM) solution at 37 °C (**Figure 4.25**). MEM solution is a slightly basic buffer solution containing several amino acids that is normally utilised as a cell growth medium and was chosen as to attempt to mimic the extracellular matrix found in the human body.

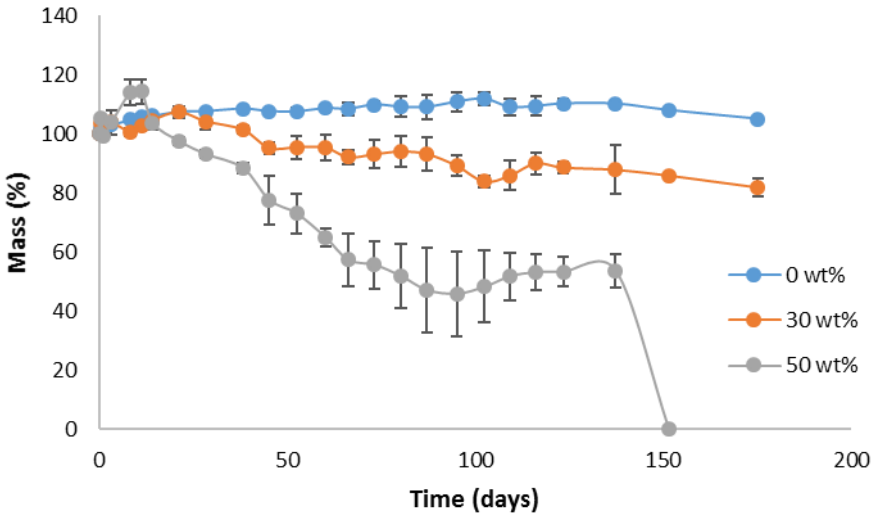

Figure 4.25. Gravimetric analysis of 0, 30 and 50 wt% P(EtMa-*co*-BuMa) containing degradation pucks under non-accelerated conditions (MEM) and physiological temperature (37 °C)

The data shows that there is a significant difference in degradation rates among materials with various amounts of P(EtMa-*co*-BuMa). As the amount of polymer increased, so did the degradation rates, although not in a linear manner. The degradation profiles for the three resin compositions all demonstrate an initial swelling phase with those containing more P(EtMa-*co*-BuMa) undergoing a greater degree of swelling. After the initial swelling phase the 30 and 50 wt% P(EtMa-*co*-BuMa) containing resins begin to degrade in an almost linear fashion whilst the 0 wt% material continues to swell up until roughly 100 days where its mass begins to slowly decrease in an almost linear manner. After 95 days in MEM and having lost 64% of its original mass, the 50 wt% material begins to swell again indicating that the rate of water ingress becomes greater than the rate of degradation and thus, the material stops undergoing surface-like degradation and subsequently bulk degrades losing its structural integrity and falling apart after 151 days. This bulk degrading behaviour was attributed to the device reaching its $L_{critical}$ dimension and so could potentially be improved further by increasing the cross-linking density.[30] The 30 wt% P(EtMa-*co*-BuMa) containing material lost 18% of its original mass whilst the 0 wt% still remained in a swelling phase at 105% of its original mass after 6 months.

Although the 50 wt% material was found to eventually succumb to bulk degradation it should be noted that the degradation up until this point is *via* the surface-like eroding mechanism and so release of small molecules could potentially still be controlled up until the device reaches the $L_{critical}$. Despite the dormant bulk eroding behaviour, the fact that the materials still underwent initial surface-like erosion was promising since the MEM solution was absent of the degradative enzymes that would normally be present *in vivo*. Furthermore, there would be other factors that affect the nature of degradation such as the continuous replenishment of medium within the body, auto-

catalysed acidolysis by the production of acidic degradation products in addition to mechanical forces being applied from surrounding tissue.[40-43] Thus, *in vivo* degradation studies are required to further probe the degredation mechanism of these materials.

4.2.10. Biocompatibility

To gain an insight into the materials' biocompatibility, an *in vitro* cell viability assay was performed using cover slips spin coated with the 0, 30 and 50 wt % P(EtMa-*co*-BuMa) resins in addition to a non-coated cover slip as a control. The slips were post-cured analogously to the printed parts and a cell viability assay using a mouse osteoblast cell line was performed. The cell viability was measured after 1, 3 and 7 days (**Figure 4.26**).

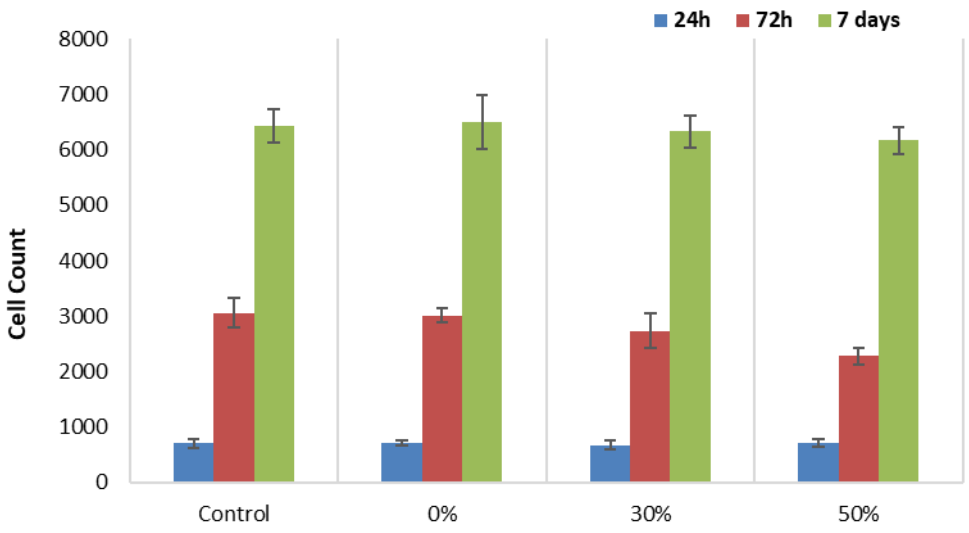

Figure 4.26. Cell counts from a cell viability assay carried out on cured 0, 30 and 50 wt% P(EtMa-*co*-BuMa) containing resins as compared with one carried out on a PLLA control sample

Overall, all three resin compositions did not inhibit cell proliferation as there was minimal difference between slides covered with P(EtMa-*co*-BuMa) materials and the non-coated controls over the course of the study. This suggests that the cured materials presented here do allow for mouse osteoblast cell proliferation *in vitro* and are non-cytotoxic.

4.2.11. Towards temporal release

To achieve temporal release, at least two distinct materials are required during the printing process. One material that contains no small molecules/model drugs (non-encapsulated) is utilised for time periods where no release is desired and another material containing a small molecule/model drug (encapsulated) is utilised for periods where a release is desired. Such a multi-material process adds many more difficulties to an already complex process including the requirement for being able to print multiple materials within the same layer. To achieve multimaterial printing in µSL separate vats/resin trays are required for each material and to minimise or remove contamination between materials a method of removing residual resin from the part when exchanging between the two resin vats is necessary. Furthermore, the slicing software used also needs to be adapted as to communicate with the printer to project two images within the same layer.

In the absence of a fully automated multi-material µSL system and slicing software capable of generating the code required to drive such a system, a manual process had to be developed. To temper the level of complexity, the simplest of devices required to achieve an on-off-on or off-on-off release profile was designed (**Figure 4.27**, A). The device was designed to be cubic and contain three shells with the shells being made from either the encapsulated (A) or non-encapsulated (B) resin in an ABA or BAB fashion. The dimension of the cube was 1 mm^2 to keep the number of layers for the print as low as possible since each layer added in terms of height doubles the number of layers exposed. To generate the dynamic masks required to build a multi-material part, the device had to be split into two separate bodies (**Figure 4.27**, B & C) that were sliced separately in normal slicing software. The images were then

recombined manually into one job file in a manner that would reduce the total number of material switches during the print (**Figure 4.27**, D).

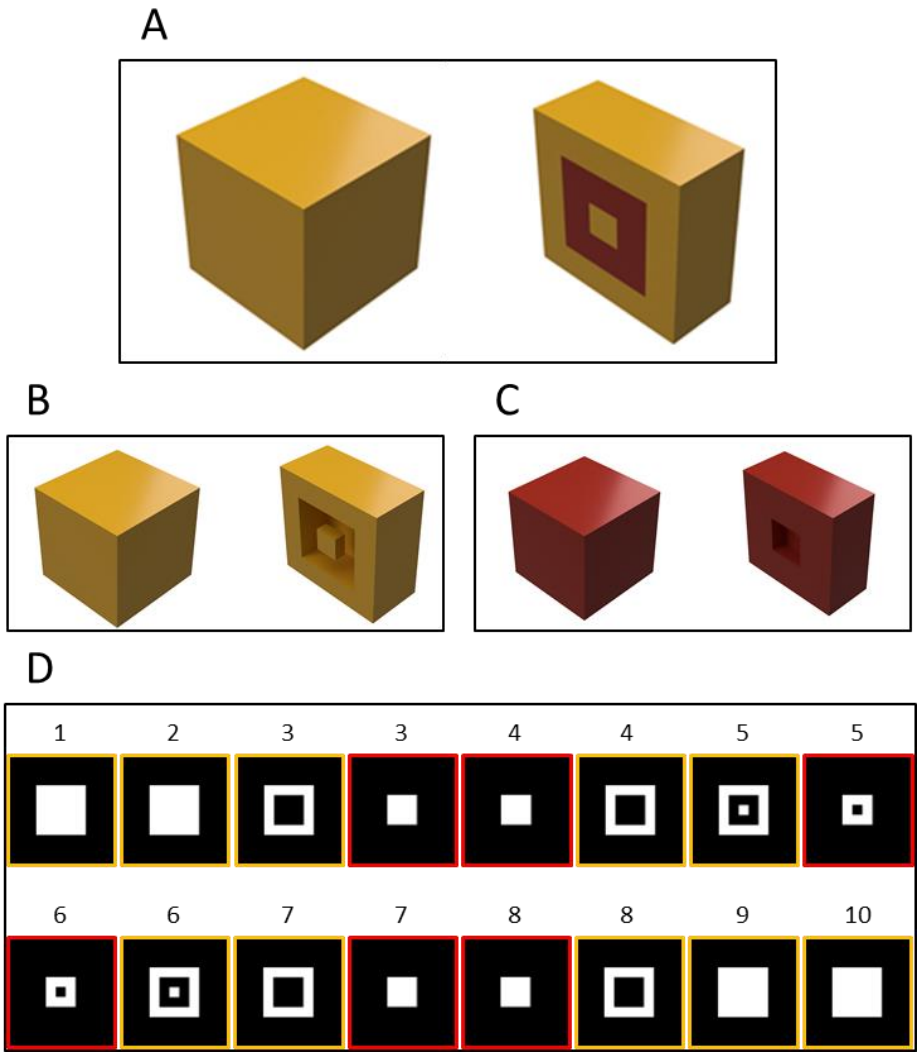

Figure 4.27. CAD design of 1 mm^2 multimaterial cube and its cross-sectional view (A), separate CAD designs and their cross sectional views for non-encapsulated (B) and encapsulated (C) parts and the respective masks generated, placed in order and colour coded to distinguish between the different layers and whether encapsulated (red) or non-encapsulated resin should be used (D)

An array of 16 multi-material cubes were partially printed to determine if there was any distinction between the encapsulated and non-encapsulated materials used (**Figure 4.28**). Despite manual efforts to remove residual resin from the devices between material switches, there was little to no distinction between material containing and not containing fluorescein. This contamination between materials was attributed to the intricacy and miniature features of the part causing resin to remain trapped between material exchanges. Whilst the design of a larger part with larger

features may have overcome this, the time required to print such a part in a manual process was considered too high. Thus, before attempting to automate the multi-material process, an alternative approach to achieving a proof-of-concept for demonstrating temporal release was investigated.

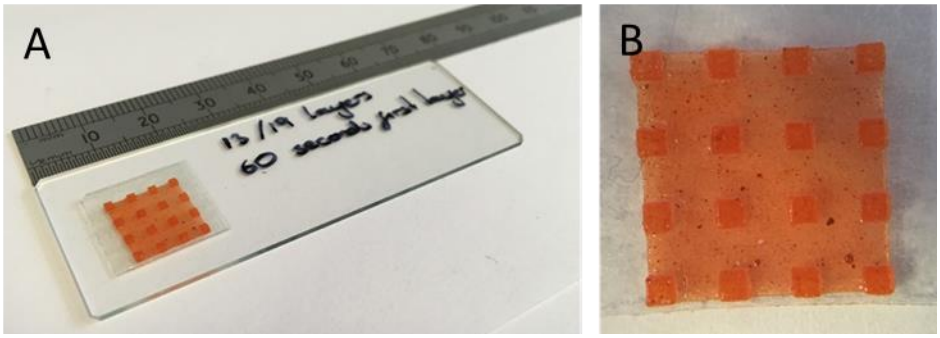

Figure 4.28. Images of the partially printed array next to a rule for scale (A) and a close up (B) to exhibit the lack of distinction between encapsulated and non-encapsulated material.

In a similar manner to the printing and assembly of spheres in **Sections 4.2.4 & 4.2.5**, an approach was taken whereby hollow hemispheres would be printed out of a non-encapsulated material, filled with an encapsulated material and later joined using a non-encapsulated binder as to remove unwanted contamination between materials (**Figure 4.29**). Such a device should provide the simplest of demonstrations of temporal release with there being an initial period of no release during degradation up until the inner encapsulated material is reached. After which, the encapsulated material should begin to release at a constant rate as determined by the choice of the resin composition (i.e. amount of P(EtMa-*co*-BuMa) used).

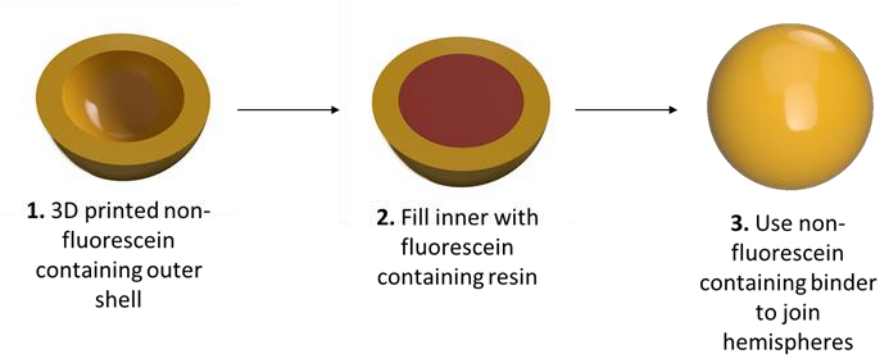

Figure 4.29. Process for fabrication of multimaterial spheres

Printing hollow hemispheres in a similar manner to the previously fabricated solid hemispheres was unachievable since resin trapped in the void upon closure and curing of subsequent layers of the hemisphere also cured. This undesirable curing of the resin within the void was likely due to an increase in the optical transparency of the thiol-ene based resins. Whilst increasing the loading of a photoinhibitor may have circumvented this problem, it would also lead to inconsistencies in the resin composition leading to inconsistencies in the amount of exposure time required.[44] Thus, the orientation of the hemispheres was changed so that curved surface was presented to the build plate thereby positioning the hollow inner sphere away from the build plate. The curved surface was also flattened slightly as to provide a preferential surface area for adhesion to the build plate during printing. **Figure 4.30,** A shows the three fabrication steps undertaken to successfully produce the multi-material devices whilst **Figure 4.30**, B and C exemplify the distinction between encapsulated material and non-encapsulated material in both an aerial shot of the filled hemisphere from step 2 and a photo of the completed device in solution, respectively. MicroCT scanning was utilised to confirm that no voids were formed across the seam during the fabrication process (**Figure 4.30**, D). The fabricated multi-material devices were composed of 50 wt% P(EtMa-*co*-BuMa) containing resin and were subjected to the same accelerated *in vitro* degradation conditions as the spheres produced in **Section 4.2.4**.

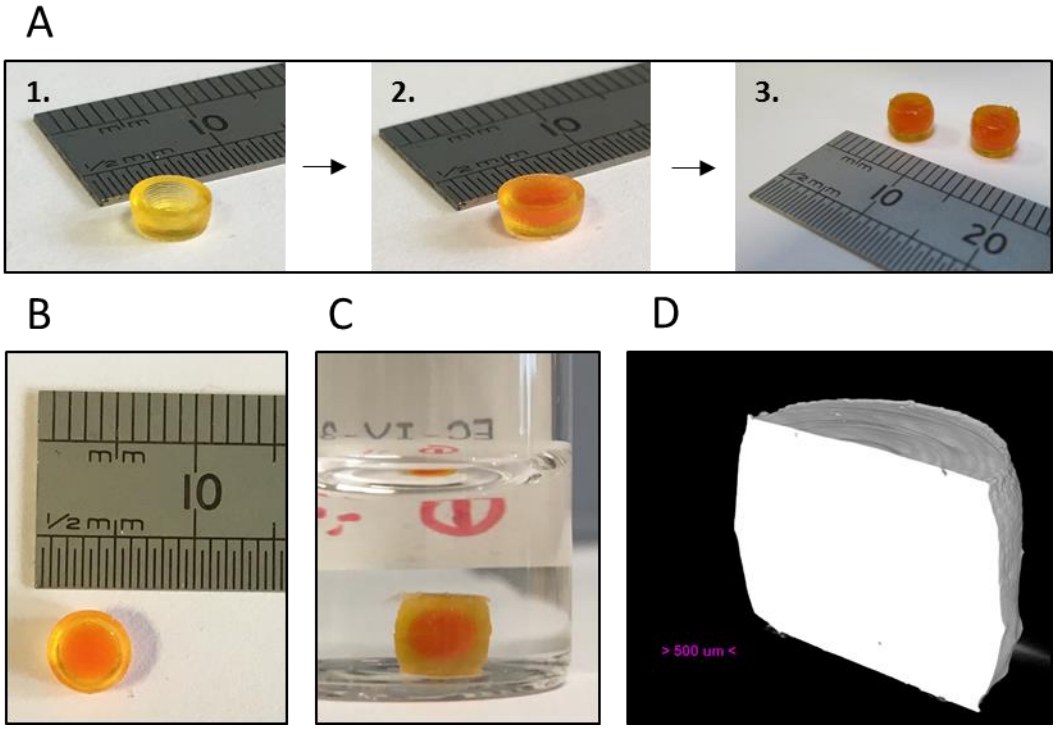

Figure 4.30. Photographs of exemplar parts made during the fabrication process (A), an aerial view of the filled hemisphere (B), two bound hemispheres in solution (C) and a microCT image of a cross-section of the fabricated part (D).

The degradation profile is essentially linear, similar to other materials composed of 50 wt% P(EtMa-*co*-BuMa), with nearly complete mass loss being achieved after just over two days in 0.1 M NaOH (**Figure 4.31,** A). Again, there is an initial swelling phase (106.2 ± 1% of its original mass) after which a steady decrease in mass is observed until the 23 h mark where there is a slight increase in the rate of degradation. The slight increase in degradation rate was attributed to the degradation reaching the interface between encapsulated and non-encapsulated materials whereby the resin may not be fully cured. After 28 h the steady decrease in mass loss resumes in an almost linear fashion indicative of a surface eroding mechanism.

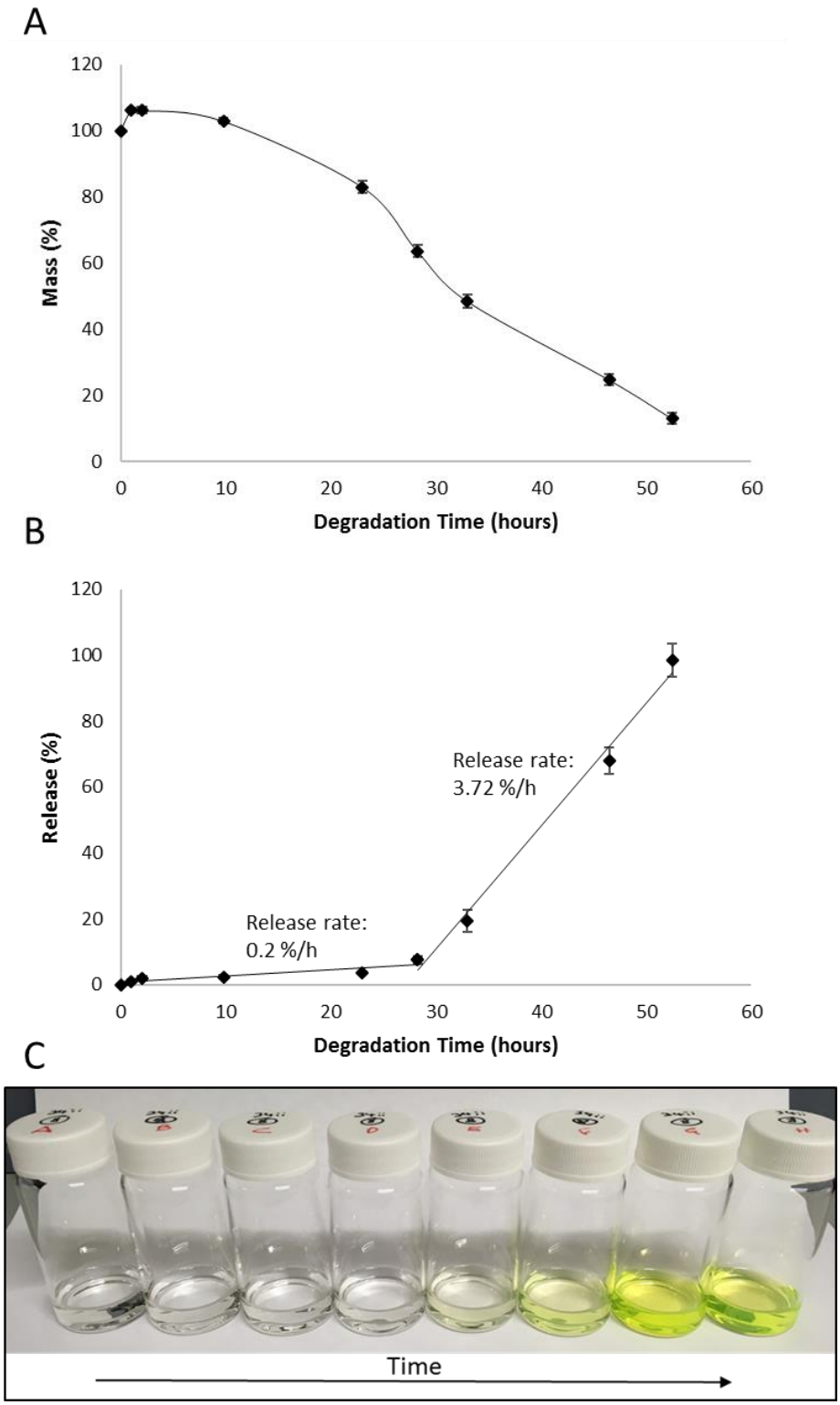

Figure 4.31. Gravimetric analysis of multimaterial almost spherical devices fabricated using 50 wt% P(EtMa-*co*-BuMa) containing resin (A), the respective release profile (B) under accelerated degradation conditions (0.1M NaOH) and physiological temperatures (37 °C), and photos of the degradation medium taken at each time point illustrating the 'off-on' release profile visually (C)

As expected, the release profile (**Figure 4.31,** B) in this instance exhibited negligible amounts of release during the first 23 h on account of the outer sphere containing no

fluorescein. The small amount (< 2.5%) of release observed during the first 23 h was likely because of errors in the fabrication process causing small amounts of seepage between the seams of the two joined hemispheres. After this initial 'off' period, there is initially a slow increase in release up to 7.52 ± 1.1% at the 28 h time point indicating that surface erosion of the device had reached the interface between the non-encapsulated outer sphere and the encapsulated inner sphere. Then, the release rate after 28 h accelerates before becoming steady illustrating a near zero-order release profile during the 'on' period. This initial data indicates that temporal release is possible from multi-material devices. A visual representation of this temporal release is shown in **Figure 4.31,** C where each vial contains the degradation medium sampled at various time points. The first four vials from the left in the image are indicative of the first 23 h of degradation whereby little to no release is observed and is exemplified by the clarity of the solution. The vials after this time point steadily become more green/fluorescent because of the release of fluorescein from the encapsulated inner sphere of the device.

4.3. Conclusions and Future work

The development of novel, biodegradable and biocompatible resins for use within the µSL technology in order to produce highly complex 3D architectures was accomplished. Bulk materials from these resins were found to undergo surface erosion under accelerated conditions with corresponding near zero-order release kinetics thereby showing promising potential for use as drug delivery devices. Furthermore, control of surface erosion rates was accomplished by simply altering the ratio of the main P(EtMa-*co*-BuMa) component within the resin formulation This highlights the controlled and tuneable nature of the degradation and release profiles. The use of both fluorescein encapsulated and non-encapsulated resins within a multi-material device

showed a simple proof-of-concept for temporal release. This warrants future investigation into the development of an automated multi-material µSL printer.

Upon development of an entirely automated µSL printer, it is envisioned that the large scale production of micro-scale drug delivery devices–with complete control over rate of release, timing of release and dosage–will be realised. Whilst there are currently examples of such multi-material printers, none have been made commercially available nor have their designs been open-sourced therefore making reproducibility difficult. Although the number of readily available biodegradable materials has undoubtedly limited the advancement of the µSL technology, the absence of a commercially available multi-material printer should be addressed as well.

4.4. References

1. Melchels, F. P.; Feijen, J.; Grijpma, D. W., A review on stereolithography and its applications in biomedical engineering. *Biomaterials* **2010,** *31* (24), 6121-6130.

2. Skoog, S. A.; Goering, P. L.; Narayan, R. J., Stereolithography in tissue engineering. *J. Mater. Sci. Mater. Med.* **2014,** *25* (3), 845-856.

3. Wang, J.; Goyanes, A.; Gaisford, S.; Basit, A. W., Stereolithographic (SLA) 3D printing of oral modified-release dosage forms. *Int. J. Pharm.* **2016,** *503* (1-2), 207-212.

4. Alomari, M.; Mohamed, F. H.; Basit, A. W.; Gaisford, S., Personalised dosing: Printing a dose of one's own medicine. *Int J Pharm* **2015,** *494* (2), 568-577.

5. Wu, B. M.; Borland, S. W.; Giordano, R. A.; Cima, L. G.; Sachs, E. M.; Cima, M. J., Solid free-form fabrication of drug delivery devices. *J. Control. Release* **1996,** *40* (1), 77-87.

6. Goole, J.; Amighi, K., 3D printing in pharmaceutics: A new tool for designing customized drug delivery systems. *Int J Pharm* **2016,** *499* (1), 376-394.

7. Katstra, W. E.; Palazzolo, R. D.; Rowe, C. W.; Giritlioglu, B.; Teung, P.; Cima, M. J., Oral dosage forms fabricated by Three Dimensional Printing™. *J. Control. Release* **2000,** *66* (1), 1-9.

8. Lin, S.; Chao, P.-Y.; Chien, Y. W.; Sayani, A.; Kumar, S.; Mason, M.; West, T.; Yang, A.; Monkhouse, D., In vitro and in vivo evaluations of biodegradable implants for hormone replacement therapy: Effect of system design and PK-PD relationship. *AAPS PharmSciTech* **2001,** *2* (3), 55-65.

9. Lee, K. J.; Kang, A.; Delfino, J. J.; West, T. G.; Chetty, D.; Monkhouse, D. C.; Yoo, J., Evaluation of critical formulation factors in the development of a rapidly dispersing captopril oral dosage form. *Drug Dev. Ind. Pharm.* **2003,** *29* (9), 967-979.

10. Wang, C. C.; Tejwani Motwani, M. R.; Roach, W. J.; Kay, J. L.; Yoo, J.; Surprenant, H. L.; Monkhouse, D. C.; Pryor, T. J., Development of near zero-order release dosage forms using three-dimensional printing (3-DP) technology. *Drug Dev. Ind. Pharm.* **2006,** *32* (3), 367-376.

11. Huang, W.; Zheng, Q.; Sun, W.; Xu, H.; Yang, X., Levofloxacin implants with predefined microstructure fabricated by three-dimensional printing technique. *Int. J. Pharm.* **2007,** *339* (1-2), 33-38.

12. Yu, D. G.; Branford-White, C.; Ma, Z. H.; Zhu, L. M.; Li, X. Y.; Yang, X. L., Novel drug delivery devices for providing linear release profiles fabricated by 3DP. *Int. J. Pharm.* **2009,** *370* (1-2), 160-166.

13. Yu, D. G.; Shen, X. X.; Branford-White, C.; Zhu, L. M.; White, K.; Yang, X. L., Novel oral fast-disintegrating drug delivery devices with predefined inner structure fabricated by Three-Dimensional Printing. *J. Pharm. Pharmacol.* **2009,** *61* (3), 323-329.

14. Wu, G.; Wu, W.; Zheng, Q.; Li, J.; Zhou, J.; Hu, Z., Experimental study of PLLA/INH slow release implant fabricated by three dimensional printing technique and drug release characteristics in vitro. *BioMedical Engineering OnLine* **2014,** *13* (1), 1-11.

15. Khaled, S. A.; Burley, J. C.; Alexander, M. R.; Roberts, C. J., Desktop 3D printing of controlled release pharmaceutical bilayer tablets. *Int J Pharm* **2014,** *461* (1), 105-111.

16. Khaled, S. A.; Burley, J. C.; Alexander, M. R.; Yang, J.; Roberts, C. J., 3D printing of tablets containing multiple drugs with defined release profiles. *Int. J. Pharm.* **2015,** *494* (2), 643-650.

17. Khaled, S. A.; Burley, J. C.; Alexander, M. R.; Yang, J.; Roberts, C. J., 3D printing of five-in-one dose combination polypill with defined immediate and sustained release profiles. *J. Control. Release* **2015,** *217*, 308-314.

18. Skowyra, J.; Pietrzak, K.; Alhnan, M. A., Fabrication of extended-release patient-tailored prednisolone tablets via fused deposition modelling (FDM) 3D printing. *Eur. J. Pharm. Sci* **2015,** *68*, 11-17.

19. Pietrzak, K.; Isreb, A.; Alhnan, M. A., A flexible-dose dispenser for immediate and extended release 3D printed tablets. *Eur. J. Pharm. Biopharm.* **2015,** *96*, 380-387.

20. Goyanes, A.; Buanz, A. B.; Basit, A. W.; Gaisford, S., Fused-filament 3D printing (3DP) for fabrication of tablets. *Int. J. Pharm.* **2014,** *476* (1-2), 88-92.

21. Goyanes, A.; Det-Amornrat, U.; Wang, J.; Basit, A. W.; Gaisford, S., 3D scanning and 3D printing as innovative technologies for fabricating personalized topical drug delivery systems. *J. Control. Release* **2016,** *234*, 41-48.

22. Goyanes, A.; Robles Martinez, P.; Buanz, A.; Basit, A. W.; Gaisford, S., Effect of geometry on drug release from 3D printed tablets. *Int. J. Pharm.* **2015,** *494* (2), 657-663.

23. Goyanes, A.; Wang, J.; Buanz, A.; Martinez-Pacheco, R.; Telford, R.; Gaisford, S.; Basit, A. W., 3D Printing of Medicines: Engineering Novel Oral Devices with Unique Design and Drug Release Characteristics. *Mol. Pharm.* **2015,** *12* (11), 4077-4084.

24. Goyanes, A.; Buanz, A. B. M.; Hatton, G. B.; Gaisford, S.; Basit, A. W., 3D printing of modified-release aminosalicylate (4-ASA and 5-ASA) tablets. *Eur. J. Pharm. Biopharm.* **2015,** *89*, 157-162.

25. Yu, D. G.; Yang, X. L.; Huang, W. D.; Liu, J.; Wang, Y. G.; Xu, H., Tablets With Material Gradients Fabricated by Three-Dimensional Printing. *J. Pharm. Sci. 96* (9), 2446-2456.

26. Kwon, I. K.; Matsuda, T., Photo-polymerized microarchitectural constructs prepared by microstereolithography (muSL) using liquid acrylate-end-capped trimethylene carbonate-based prepolymers. *Biomaterials* **2005,** *26* (14), 1675-1684.

27. Matsuda, T.; Mizutani, M., Liquid acrylate-endcapped biodegradable poly(ϵ-caprolactone-co-trimethylene carbonate). II. Computer-aided stereolithographic microarchitectural surface photoconstructs. *Journal of Biomedical Materials Research* **2002,** *62* (3), 395-403.

28. Kochhar, J. S.; Zou, S.; Chan, S. Y.; Kang, L., Protein encapsulation in polymeric microneedles by photolithography. *Int J Nanomedicine* **2012,** *7*, 3143-3154.

29. Tamada, J. A.; Langer, R., Erosion kinetics of hydrolytically degradable polymers. *Proceedings of the National Academy of Sciences of the United States of America* **1993,** *90* (2), 552-556.

30. Burkersroda, F. v.; Schedl, L.; Göpferich, A., Why degradable polymers undergo surface erosion or bulk erosion. *Biomaterials* **2002,** *23* (21), 4221-4231.

31. Elomaa, L.; Kang, Y.; Seppälä, J. V.; Yang, Y., Biodegradable photocrosslinkable poly(depsipeptide-co-ε-caprolactone) for tissue engineering: Synthesis, characterization, andIn vitroevaluation. *J. Polym. Sci. A Polym. Chem.* **2014,** *52* (23), 3307-3315.

32. Walker, J. M.; Bodamer, E.; Krebs, O.; Luo, Y.; Kleinfehn, A.; Becker, M. L.; Dean, D., Effect of Chemical and Physical Properties on the In Vitro Degradation of 3D Printed High Resolution Poly(propylene fumarate) Scaffolds. *Biomacromolecules* **2017,** *18* (4), 1419-1425.

33. Barker, I. A.; Ablett, M. P.; Gilbert, H. T. J.; Leigh, S. J.; Covington, J. A.; Hoyland, J. A.; Richardson, S. M.; Dove, A. P., A microstereolithography resin based on thiol-ene chemistry: towards biocompatible 3D extracellular constructs for tissue engineering. *Biomater. Sci.* **2014,** *2* (4), 472-475.

34. Cook, W. D.; Chen, F.; Pattison, D. W.; Hopson, P.; Beaujon, M., Thermal polymerization of thiol–ene network-forming systems. *Polym. Int.* **2007,** *56* (12), 1572-1579.

35. Badev, A.; Abouliatim, Y.; Chartier, T.; Lecamp, L.; Lebaudy, P.; Chaput, C.; Delage, C., Photopolymerization kinetics of a polyether acrylate in the presence of ceramic fillers used in stereolithography. *J. Photochem. Photobiol. Chem. A* **2011,** *222* (1), 117-122.

36. Zhiwei, G.; Jianhua, M.; Shuhuai, H.; Hongquan, X., Development of a hybrid photopolymer for stereolithography. *J. Wuhan Univ. Technol. Mat. Sci. Ed.* **2006,** *21* (1), 99-101.

37. Lee, J. W.; Lan, P. X.; Kim, B.; Lim, G.; Cho, D.-W., 3D scaffold fabrication with PPF/DEF using micro-stereolithography. *Microelectron. Eng.* **2007,** *84* (5-8), 1702-1705.

38. Karalekas, D.; Aggelopoulos, A., Study of shrinkage strains in a stereolithography cured acrylic photopolymer resin. *J. Mater. Process. Technol.* **2003,** *136* (1), 146-150.

39. Carnevale, J.; Cole, E. R.; Crank, G., Photocatalyzed oxidation of paprika pigments. *J. Agric. Food. Chem.* **1980,** *28* (5), 953-956.

40. Agrawal, C. M.; McKinney, J. S.; Lanctot, D.; Athanasiou, K. A., Effects of fluid flow on the in vitro degradation kinetics of biodegradable scaffolds for tissue engineering. *Biomaterials* **2000,** *21* (23), 2443-2452.

41. Fu, Q.; Rahaman, M. N.; Bal, B. S.; Kuroki, K.; Brown, R. F., In vivo evaluation of 13-93 bioactive glass scaffolds with trabecular and oriented microstructures in a subcutaneous rat implantation model. *J. Biomed. Mater. Res.* **2010,** *95A* (1), 235-244.

42. Middleton, J. C.; Tipton, A. J., Synthetic biodegradable polymers as orthopedic devices. *Biomaterials* **2000,** *21* (23), 2335-2346.

43. Thompson, D. E.; Agrawal, C. M.; Athanasiou, K., The effects of dynamic compressive loading on biodegradable implants of 50–50% polylactic acid–polyglycolic acid. *Tissue Eng.* **1996,** *2* (1), 61-74.

44. Hoyle, C. E.; Bowman, C. N., Thiol-ene click chemistry. *Angew. Chem. Int. Ed. Engl.* **2010,** *49* (9), 1540-1573.

5. Conclusions & Future Work

Conclusions

The goal of this thesis was to develop novel and functional materials for use within the μSL process that are capable of undergoing degradation thereby making them more applicable in end-user applications. Initial emphasis was towards the development of a 4D material for '4D printing', a concept that, at the beginning of this PhD, had not yet been described previously. The latter stages of the PhD saw the development of entirely novel resins capable of producing drug delivery devices that demonstrated the highly sought after zero-order release kinetics at various stages during physiological degradation. Applying the same resin to a multimaterial device saw a definitive proof-of-concept that controlled temporal release could also be realised. Thus, the aim of the thesis has been achieved and current work is focussed on commercialisation of similar drug delivery devices to those produced in Chapter 4.

Initially, a low molecular weight photodegradable oligomer based on the photosensitive *o*NB molecule was synthesised. It was hoped that combining it with other resin components, would allow for the material to cure under one wavelength of light in the μSL process and then degrade under a second wavelength of light thereby providing it with a 4^{th} dimension. Whilst the optimised resin was found to be capable of being selectively cured using visible light with exposure times suitable for μSL, the long exposure doses required for minimal selective etching limited the materials applicability to gradual surface finish refinements and as a potential support material. Additionally it could also find potential use as a combined negative and positive photoresist with curing rates an order of magnitude faster than those previously described. Unfortunately, no 3D objects were produced because of the small quantities of the material produced and so future work should focus on increasing the scale of synthesis or utilising a less complex photodegradable moiety. Future research in this

area should focus on applying similar materials to the fabrication of hydrogels *via* µSL since this would lessen the requirement for large scale production of the photodegradable molecule in addition to making the material more suited to biomedically relevant applications.

Chapter 3 encompassed the successful synthesis of various biomass derived malic acid based monomers and their subsequent polycondensation *via* both high temperature and low temperature methods to produce low molecular weight, homo- and copolymers. A selection of monomers were polymerised in order to convey a variety of properties in the final material. They were found to convey varying levels of hydrophilicity depending on the functionality used. Thin films of the NBnMa containing polymer were shown to be photosensitive and could have their hydrophilicity tuned as a result of being exposed to UV light as an external stimulus. However, only poly(EtMa-*co*-BuMa) was found to be compatible with the µSL process. Despite this, the NBnMa containing polymer synthesised herein has already been shown to be capable of being used in microparticles for stimuli responsive release within the agrochemical industry. Furthermore, there is also the possibility of adapting the reactive functionalities on the NBnMa and BnMa containing polymers in order to render them more compatible with the µSL process. Thus, future work in this area should focus on trying to expand upon the possible functionalities capable of being utilised in µSL.

Poly(EtMa-co-BuMa) as synthesised in chapter 3 was later combined with a newly synthesised reactive diluent also partially derived from biomass derived resources in an optimised resin composition. By varying the amount of poly(EtMa-*co*-BuMa) in the resin composition not only could the mechanical properties of the bulk material be tailored, the hydrophilicity and therefore rate of degradation of could also be tuned.

All resin compositions were found to be compatible with the μSL process so much so that highly complex 3D architectures could be fabricated. Fluorescein was successfully encapsulated in the bulk materials and upon degradation of bulk material under *in vitro* conditions near zero-order release was realised with varying rates of release depending on the resin composition used. The combined use of fluorescein containing and non-fluorescein containing resins within a multi-material device demonstrated that control over temporal release could also be accomplished. Current research is looking into the development of a multi-material printer capable of printing similar materials to those outlined here to produce exemplar devices with more complicated release profiles. Such implantable devices are envisioned to find application in the pharmaceutical field as a means of delivering patient specific drug dosages in an entirely controlled manner.

Future Work

While the work in this thesis is original and has proved several concepts as outlined in the conclusions above, it has opened new avenues for research on several fronts. For instance, although the photodegradable materials in chapter 2 showed potential as a new type of combined positive/negative photoresist and demonstrated that it has potential for use within μSL as either a prototyping or support material, the degree of degradability was limited. Thus, if this research were to be continued it ought to be directed toward systems whereby the photodegradation can be enhanced such as aqueous systems whereby degradation products can be transported away from the bulk material in situ. Hydrogels would be ideal for achieving this and whilst photodegradable hydrogel systems do exist there have been no examples of hydrogels that can be cross-linked under one wavelength of light prior to photodegradation under another wavelength of light.

The research conducted in chapter 3 could be furthered in several ways. Firstly, the polymers that were found to be unsuitable for µSL could be adapted in order to make them more µSL processable. For instance, in the case of the polymer containing the nitrobenzyl functionality, the alkene reactivity could be changed to an epoxide thus enabling cross-linking through a non-radical based reaction. While the benzyl monomer could be polymerised with a monomer that has its alkene functionality further away from the backbone thereby overcoming issues associated with the steric bulk of the benzyl malate monomer. Secondly, the ability to tune the hydrophobicity of the material either by mixing homopolymers or copolymerising ethyl and benzyl malate could also be investigated. Finally, the materials produced should also be tested for their use in alternative applications further such as thin films, coating and the production of microparticles.

The production of drug delivery devices in chapter 4 should be improved upon by incorporating them into a multimaterial printer that allows for far more complex release profiles. Thus, the development of printers with multimaterial capabilities that are compatible with potentially viscous polymer resins is a worthy avenue of investigation. The scope of deliverables also needs expanding upon to include model bio-actives from a broad range of treatments encompassing the likes of anti-inflammatories, biologics, vaccines, contraceptives, anti-cancer and fertility treatments. Thus, further research into the degree of control over release that can be achieved and the types of treatment that would benefit most from being released in this manner would be necessary. Biologics are of particular interest since devices containing biologics are required to be made in a sterile environment because of their lack of stability under typical sterilisation procedures and so 3D printing them may be an ideal way of achieving this. Furthermore, the fact that the materials surface erode

may cause there to be less localised increase in acidic by-products thereby helping stabilise biologics upon release.

6. Experimental

6.1. Materials

3-Buten-1-ol and benzyl alcohol were purchased from Acros Chemicals. Acetovanillone, acryloyl chloride, butylated hydroxytoluene (BHT), camphorquinone, diisopropylcarbodiimide (DIC), 4-dimethylaminopyridine (DMAP), dodecanethiol (DDT), dipentaerythritol penta-/hexa-acrylate (DPPHA), ethyl 4-(dimethylamino)benzoate (EDMAB), ethyl 4-bromobutyrate, Nitrobenzyl alcohol (NBnOH, recrystallized and sublimed before use), poly(ethylene glycol) (PEG), pentaerythritol tetrakis(3-mercaptopropionate) (PT3M), propylene carbonate,*para*-toluenesulfonic acid, sodium borohydride and succinic acid were purchased from Sigma Aldrich. DL-Malic acid was purchased from VWR International. (3-Dimethylaminopropyl)-N′-ethylcarbodiimide hydrochloride (EDC.HCl) was purchased from Carbosynth. Acetic acid, acetic anhydride, benzene, chloroform ($CHCl_3$), dichloromethane (DCM), dimethylformamide (DMF), ethyl acetate (EtOAc), ethanol (EtOH), hydrochloric acid (HCl) (37%), hexane, methanol (MeOH), magnesium sulphate ($MgSO_4$), sodium bicarbonate ($NaHCO_3$), sodium carbonate (Na_2CO_3), nitric acid (HNO_3), potassium carbonate (K_2CO_3), triethylamine (NEt_3), tetrahydrofuran (THF), toluene and trifluoroacetic anhydride (TFAA) were purchased from Fisher Scientific. Irgacure 784 and Irgacure TPO-L were kindly provided free of charge by BASF whilst paprika oleoresin extract was kindly donated by Kalsec. Deuterated chloroform and deuterated acetone were purchased from Apollo Scientific. All Chemicals were used as received unless stated otherwise.

6.2. Instrumental Methods

6.2.1. NMR Spectroscopy and Size Exclusion Chromatography (SEC)

All proton (^{1}H NMR) and carbon (^{13}C NMR) spectroscopy was recorded on Bruker DPX-300, DPX-400 or DPX-500 (300, 400 and 500 MHz, respectively) spectrometers

at 293 K. Chemical shifts are reported as δ in parts per million (ppm) and referenced to the residual solvent signals ($CDCl_3$: ^1H, δ = 7.26 ppm; ^{13}C, δ = 77.16 ppm, $(CD_3)_2CO$: ^1H, δ = 2.05 ppm, ^{13}C, δ = 29.84 ppm). Size Exclusion Chromatography (SEC) was used to determine relative molecular weights (M_n) and dispersities ($Đ_m$) of the polymers produced. SEC was conducted on Varian PL-GPC 50 systems in either Chloroform ($CHCl_3$) with 0.5% triethylamine (NEt_3) or Dimethylformamide (DMF) with 5 mM ammonium tetrafluoroborate (NH_4BF_4) as eluent. Both SECs were fitted with PL Gel guard columns and either 2 × PL Gel Mixed-D ($CHCl_3$ SEC) or 2 × PL Gel Mixed- C (DMF SEC) type columns in series with Refractive Index (RI) detection. Molecular weights were determined using calibration curves calculated from either poly(styrene) ($CHCl_3$ SEC) or poly(methyl methacrylate) (DMF SEC) Varian Polymer Laboratories Easi-Vial standards at a flow rate of 1 mL/min. Data generated from the SECs was analysed using Cirrus v3.3 software.

6.2.2. UltraViolet-Visible Light (UV-Vis), InfraRed (IR) and Raman Spectroscopy

UV-Vis spectra were recorded on either a Perkin Elmer UV-Vis Spectrometer (Lambda 35) fitted with a temperature controller (Peltier) or a Jenway 6_7 series Spectrometer. IR spectra were recorded using a Perkin-Elmer Spectrum 100 FT-IR spectrometer whilst Raman spectra were recorded on a Renishaw inVia Raman Microscope fitted with a 514.5 nm Argon laser calibrated to silica.

6.2.3. Optical Microscopy and Scanning Electron Microscopy (SEM)

Optical imaging of photodegraded thin films (chapter 2) was performed using an ZeissAxio optical microscope with a MPLAPONLEXT50 lens. Images were captured and subsequently processed in Image Pro Plus Software. Scanning Electron

Microscopy (SEM) was carried out utilising a Zeiss Gemini 500 SEM equipped with a large area SDD EDX detector.

6.2.4. Interferometry

Surface profilometry data was obtained using a Bruker Contour GT-X Optical Profiler and subsequently analysed using the software package Vision 64. Vertical Scanning Interferometry (VSI) was employed utilising either green or white light, a 5x objective lens, a 1x multiplier, 3x scanning speed and a 1 % threshold value. Analysed data was reconstructed and visualized in the Gwyddion 2.47 software.

6.2.5. Atomic Force Microscopy (AFM)

AFM was performed on a Asylum Research MFP-3D-SA microscope enclosed by a customised sound-isolated chamber placed on a Halcyonics Micro 40 Isolation Platform. Scans were carried out using a MikroMasch HQ:NSC18/Al BS tip in tapping mode with the image size set to 90 μm^2, a resolution of 1024 × 1024 and a scan rate of 0.15 Hz. Data was reconstructed and visualized in the Gwyddion 2.47 software.

6.2.6. Thermal Analysis

Differential Scanning Calorimetry (DSC) and Thermal Gravimetric Analysis (TGA) data was acquired using a Mettler Toledo DSC1 star and a TGA/DSC star system. DSC heating and cooling cycles were carried out in triplicate under a nitrogen atmosphere in a 40 µL aluminium crucible at a heating rate of ±10 ˚C min^{-1}. TGA was also carried out in a 40 µL aluminium crucible at a heating rate of ±10 ˚C min^{-1} starting at 30 ˚C and finishing at 500 ˚C. Data collected was analysed using STARe V12.0 software.

6.2.7. Drop Shape Analysis

Drop shape analysis was carried out using a KRUSS DSA10 Drop Shape Analyser. Polymers or resin compositions analysed were dissolved in acetone (3 wt% solutions) before being solvent cast onto glass slides. Solvent was allowed to evaporate at room temperature for one week after which resin compositions were cured in a Metalight UV chamber for 15 minutes before being washed with isopropanol and left to dry overnight. A 100 µl droplet of deionised H_2O was deposited onto the thin films and the static contact angle measurement was taken immediately.

6.2.8. Rheology

All resin viscosity measurements were recorded using an Anton Paar Modular Compact Rheometer MCR302 equipped with a PP50 plate and a temperature controlled hood. A gap of 100 µm was utilised with the force normalised throughout measurements and a sheer rate set to 5 s^{-1}. Each resin composition was tested in triplicate across at least 2 batches of synthesised material with results being analysed in the software package Anton Paar RheoCompass. Resin compositions all had 1 wt% BHT added as inhibitor to prevent unwanted curing of the material during measurements.

6.2.9. Microstereolithography

Microstereolithography was performed using a custom-built set-up designed for material development that has been described previously.[1] Briefly, Aerotech motion stages were used for movement of the build plate in the z-axis and the projector used was a modified Compaq MP1800 equipped with an Enfis blue LED (465 nm) light engine as the light source. The software used to run the printer was custom developed by another member of the DMTL group. The software allows for complete control

over parameters such as exposure time, peel speed, light intensity and layer height thereby making it incredibly suitable for developing new resins.

6.2.10. Degradation and Release

Printed degradation pucks were either degraded in accelerated (0.1 M NaOH) or non-accelerated degradation (Minimum essential medium solution) conditions. Pucks were placed into individual vials containing 3 mL of the respective degrading solution depending on what conditions were being used and incubated at 37 ºC using a Biosan ES-20 Incubator Shaker. Pucks were blotted dry before having their weight measured using an analytical balance. Pucks used in release studies had their degrading media collected which was then analysed for fluorescence intensity using a BMG Labtech Fluorostar Optima plate reader. All studies were carried out in triplicate or greater and degradation media was replaced after each data point.

6.2.11. Tensile Analysis

Dog bones for tensile testing were fabricated by pouring the respective resin into stainless steel dog bone moulds (1.5 mm thick) and subsequently curing them into the desired shape by flood irradiation with an Enfis blue LED (465 nm) light source. Tensile data was obtained at room temperature by axially loading the cured dog-bones in a Tensiometric M100-1CT tensile tester equipped with a 1kN load cell and a crosshead speed of 1 mm min^{-1}. All data was acquired using winTest v4.3.2 software and values reported were from an average of 8-10 repeats.

6.2.12. Micro X-ray Computed Tomography (MicroCT)

Micro CT scans were performed on a Bruker Skyscan 1174 Compact X-ray Microtomography system. Scans were carried out using small camera pixels for a 180 ° scan with a step rotation of 0.3 ° and an averaging of 3 frames in the Skyscan1174v2

software. The X-ray source was set to a maximum voltage and current of 50kV and 800µA respectively with no filter applied in this instance. The 3D reconstruction was carried out using NRcon software taking advantage of smoothing, a misalignment compensation of 2.5, a ring artefact reduction set to 16 and beam hardening set to 65% before being analysed and imaged using the CTVox software.

6.3. Experimental procedures for Chapter 2

The synthesis of the photodegradable *ortho*-nitrobenzylester molecule, 4-[4-(1-(Acryloyloxy)ethyl)-2-methoxy-5-nitrophenoxy] butanoic acid, was carried out according to modified procedures from several authors.[2-4]

6.3.1. Procedure for the synthesis of ethyl 4-(4-acetyl-2-methoxyphenoxy) butanoate, 3:

Potassium carbonate (88.6 g, 640 mmol) and ethyl 4-bromobutyrate (83.3 g, 430 mmol) were added to a solution of acetovanillone (71 g, 430 mmol) in DMF (350 mL). The mixture was left stirring for 16 hours at room temperature and subsequently heated to 50 ˚C for 3 hours before being filtered to remove excess salts. The resulting green solution was partitioned between EtOAc and H_2O three times, the organic phase was collected and washed several times with H_2O to remove DMF before being dried using $MgSO_4$ filtered and removal of solvent *via* rotary evaporation to afford a white powder that was used without any further purification (Yield: 101 g, 85 %). Characterisation was in good agreement with previous reports.[2, 4] ^{1}H NMR (400 MHz, Chloroform-*d*) δ: 7.51 (d, $^3J_{HH}$= 8.3 Hz, 1H), 7.49 (d, $^3J_{HH}$ = 1.8 Hz, 1H), 6.86 (d, $^3J_{HH}$ = 8.2 Hz, 1H), 4.16 – 4.06 (m, 5H), 3.88 (s, 3H), 2.53 (s, 4H), 2.50 (t, $^3J_{HH}$ = 7.2 Hz, 2H), 2.16 (m, 2H), 1.22 (t, $^3J_{HH}$ = 7.1 Hz, 3H). ^{13}C NMR (101 MHz, Chloroform-*d*) δ: 196.83 (s, C=O), 173.01 (s, C=O), 152.59 (s, C-O), 149.21 (s, C-O), 130.43 (s, CC), 123.22 (s,

CH), 111.18 (s, CH), 110.35 (s, CH), 67.76 (s, CH_2), 60.5 (s, CH_2), 55.97 (s, CH_3), 30.56 (s, CH_2), 26.23 (s, CH_3), 24.26 (s, CH_2), 14.22 (s, CH_3).

6.3.2. Procedure for the synthesis of ethyl 4-(4-acetyl-2-methoxy-5-nitrophenoxy)butanoate, 4:

Ethyl 4-(4-acetyl-2-methoxyphenoxy) butanoate, **3** (20 g, 71.3mmol) was dissolved in acetic anhydride (40 mL) and added dropwise to an ice cold solution of HNO_3 (200 mL) and acetic anhydride (40 mL) in a 1000 mL RBF. The solution was left stirring and kept below 5 ˚C for 5 hours before being precipitated into ice cold H_2O (1000 mL). The solution containing the yellow precipitate was cooled further in the freezer for 1 hour before being filtered, dissolved in DCM (500 mL) and washed with water (500 mL) and brine (500 mL). The organic phase was then dried with $MgSO_4$ and finally solvent was removed *via* rotary evaporation to afford a pale yellow powder (Yield: 18.17 g, 78 %). Characterisation was in good agreement with previous reports.[2, 4] ^{1}H NMR (400 MHz, Chloroform-*d*) δ: 7.63 (s, 1H), 6.76 (s, 1H), 4.27 – 4.07 (m, 4H), 3.97 (s, 3H), 2.56 (t, $^3J_{HH}$ = 7.2 Hz, 2H), 2.51 (s, 3H), 2.22 (m, 2H), 1.29 (t, $^3J_{HH}$ = 7.2 Hz, 3H). ^{13}C NMR (101 MHz, Chloroform-*d*) δ: 200.19 (s, C=O), 172.93 (s, C=O), 154.29 (s, C-O), 148.84 (s, C-O), 138.32 (s, CNO_2), 132.86 (s, CC), 108.71 (s, CH), 107.66 (s, CH), 68.46 (s, CH_2), 60.64 (s, CH_2), 56.62 (s, CH_3), 30.52 (s, CH_2), 30.45 (s, CH_3), 24.17 (s, CH_2), 14.25 (s, CH_3).

6.3.3. Procedure for the synthesis of 4-[4-(1-hydroxyethyl)-2-methoxy-5-nitrophenoxy]butanoic acid, 5:

Ethyl 4-(4-acetyl-2-methoxy-5-nitrophenoxy)butanoate, **4** (15 g, 46.1 mmol) was added to a hot (85 ˚C) solution of acetic acid (30 mL) and water (90 mL). Concentrated HCl (9 mL) was then added before heating under reflux for 1 hour at 115 ˚C. Once the solution had turned completely transparent it was allowed to cool to RT before filtering

off the precipitate and washing extensively with H_2O (1.5 L) to yield a yellow powder. The powder was dispersed in water (500 mL) to which $NaHCO_3$ (8.4 g, 100 mmol) was added in portions using EtOH (30 mL) to remove foams. Sodium Borohydride (5.4 g, 143 mmol) was added slowly over the course of 1 hour maintaining a pH between 9-11. The solution was found to turn red during this time with the evolution of bubbles. The reduction was left stirring at room temperature for 9 hours before being acidifed with 2M HCl. The precipitate formed was filtered, washed with H_2O and dried in a desiccator overnight (Yield: 11.41 g, 82.7 %). Characterisation was in good agreement with previous reports.[2, 4] ^{1}H NMR (300 MHz, Acetone-d_6) δ: 7.58 (s, 1H), 7.48 (s, 1H), 5.47 (qd, $^3J_{HH}$ = 6.2, 0.5 Hz, 1H), 4.18 (t, $^3J_{HH}$ = 6.3 Hz, 2H), 3.98 (s, 3H), 2.56 (t, $^3J_{HH}$ = 7.3 Hz, 2H), 2.18 – 2.09 (m, 2H), 2.06 (p, $^3J_{HH}$ = 2.2 Hz, 2H), 1.46 (d, $^3J_{HH}$ = 6.2 Hz, 3H). ^{13}C NMR (75 MHz, Acetone-d_6) δ: 175.02 (s, C=O), 154.08 (s, C-O), 146.67 (s, C-O), 139.24 (s, CNO_2), 138.08 (s, CC), 119.99 (s, CH), 108.92 (s, CH), 68.27 (s, CH_2), 65.16 (s, CH), 56.30 (s, CH_3), 30.22 (s, CH_2), 24.77 (s, CH_3), 24.21 (s, CH_2).

6.3.4. Procedure for the synthesis of 4-[4-(1-(Acryloyloxy)ethyl)-2-methoxy-5-nitrophenoxy] butanoic acid, 7:

4-[4-(1-hydroxyethyl)-2-methoxy-5-nitrophenoxy]butanoic acid, **5** (4.53 g, 15.1 mmol) was dissolved in anhydrous THF (50 mL) and TEA (8.28 mL) in a two-port 250 mL RBF. The mixture was cooled over ice bath and placed under nitrogen before acryloyl chloride (2.82 mL) in THF (15 mL) was added dropwise using a pressure equalizing dropping funnel. Once all the acryloyl chloride was added the reaction was allowed to warm up to RT before being left to stir for 24 hours. The reaction mixture was then poured into H_2O (1250 mL) and stirred at room temperature for 8 hours before being extracted with $CHCl_3$ (5 x 200 mL), dried with $MgSO_4$ and solvent

removed *via* rotary evaporation to yield a viscous yellow orange liquid (Yield: 3.62 g, 68 %). Characterisation was in good agreement with previous reports.[2, 4] ^{1}H NMR (400 MHz, Chloroform-*d*) δ: 7.52 (s, 1H), 6.94 (s, 1H), 6.46 (q, $^{3}J_{HH}$ = 6.4 Hz, 1H), 6.36 (dd, $^{3}J_{HH}$ = 17.3, 1.4 Hz, 1H), 6.10 (dd, $^{3}J_{HH}$ = 17.3, 10.4 Hz, 1H), 5.80 (dd, $^{3}J_{HH}$ = 10.4, 1.4 Hz, 1H), 4.05 (t, $^{3}J_{HH}$ = 6.2 Hz, 2H), 3.85 (s, 3H), 2.54 (t, $^{3}J_{HH}$ = 7.1 Hz, 2H), 2.10 (q, $^{3}J_{HH}$ = 6.7 Hz, 2H), 1.59 (d, $^{3}J_{HH}$ = 6.4 Hz, 3H). ^{13}C NMR (101 MHz, Chloroform-*d*) δ: 178.70 (s, C=O), 164.93 (s, C=O), 154.03 (s, C-O), 147.14 (s, C-O), 139.76 (s, CN), 133.31 (s, CC), 131.4 (s, CH_2), 128.21 (s, CH), 109.06 (s, CH), 108.12 (s, CH), 68.62 (s, CH), 68.02 (s, CH_2), 56.26 (s, CH_3), 30.26 (s, CH_2), 23.95 (s, CH_2), 21.99 (s, CH_3).

6.3.5. Procedure for the synthesis of PEG-oNB, 8:

4-[4-(1-(Acryloyloxy)ethyl)-2-methoxy-5-nitrophenoxy] butanoic acid, 7 (3.62 g, 10.2 mmol), EDC.HCl (2.93 g, 15.3 mmol) and DMAP (125 mg, 1.02 mmol) were dissolved in anhydrous DCM (100 mL) before $PEG_{0.4k}$ (1.21 mL, 3.4 mmol) was added slowly via syringe. The reaction mixture was left stirring overnight under nitrogen at RT before being washed with H_2O (3 × 100 mL), Na_2HCO_3 (3 × 100 mL) and brine (3 × 100 mL). The organic phase was dried using $MgSO_4$, filtered and solvent removed *via* rotary evaporation to yield a yellow/orange viscous liquid (Yield: 2 g, Conv: 90 %). ^{1}H NMR (400 MHz, Chloroform-*d*) δ: 7.60 (s, 1H), 7.02 (s, 1H), 6.54 (q, $^{3}J_{HH}$ = 6.5 Hz, 1H), 6.45 (dd, , $^{3}J_{HH}$ = 17.3, 1.4 Hz, 1H), 6.18 (dd, , $^{3}J_{HH}$ = 17.3, 10.4 Hz, 1H), 5.89 (dd, , $^{3}J_{HH}$ = 10.5, 1.4 Hz, 1H), 4.29 – 4.24 (m, 2H), 4.12 (t, , $^{3}J_{HH}$ = 6.2 Hz, 2H), 3.94 (s, 3H), δ 3.71 (t, , $^{3}J_{HH}$ = 4.8 Hz, 2H), 3.66 (s, 15H), 2.59 (t, $^{3}J_{HH}$ = 7.2 Hz, 2H), 2.20 (q, , $^{3}J_{HH}$ = 6.7 Hz, 2H), 1.67 (d, , $^{3}J_{HH}$ = 6.4 Hz, 3H). SEC analysis M_n = 1400 g mol^{-1}, $Đ_m$ = 2.19. (RI detection, $CHCl_3$ GPC).

6.4. Experimental Procedures for Chapter 3

The four malate monomers were synthesised according to modified procedures from Miller *et al.* and whilst Benzyl and Ethyl malate have been reported previously, Nitrobenzyl and butenyl malate have not.[5-6] High temperature polymerisations of these monomers were carried out in a similar manner to those used by Kajiyama *et al.*[7-9] Low temperature polymerisation of Benzyl malate was carried out using an adapted procedure to that carried out by Moore *et al.*[10]

6.4.1. Procedure for the synthesis of Benzyl malate, BnMa:

DL-Malic acid (5 g, 37.3 mmol) was cooled over ice before triflluoroacetic anhydride (TFAA) (12.5 mL, 89.5 mmol) was added slowly. After stirring at 0 ˚C for 3h a clear solution formed and volatiles were removed under reduced pressure whilst the mixture was kept on ice. Benzyl alcohol (BnOH) (64.5 g, 596.8 mmol) was added to the residual solid before being allowed to warm up to room temperature and being left to stir overnight. The reaction mixture was diluted with EtOAc (150 mL) and extracted with Na_2CO_3 (10 %, 3 × 100 mL). The aqueous phase was acidified to pH 7 using 1M HCl (*c.a.* 200 mL) and excess BnOH was extracted using EtOAc (4 × 100 mL) before recollecting the aqueous phase, acidifying further to pH 2/3 and extracting the pure monoester with more EtOAc (5 × 100 mL). The solution was dried using $MgSO_4$ before having solvent removed *via* rotary evaporation to leave a clear viscous liquid (Yield: 5.57 g, 67 %). Characterisation was in good agreement with previous reports.[6] ^{1}H NMR (500 MHz, Chloroform-*d*) δ: 7.44 – 7.27 (m, 5H), 5.21 (s, 2H), 4.55 (dd, $^3J_{HH}$ = 6.4, 4.3 Hz, 1H), 2.98 – 2.75 (m, 2H). ^{13}C NMR (126 MHz, Chloroform-*d*) δ: 175.66 (s, C=O), 173.12 (s, C=O), 134.89 (s, $C(CH)_2(CH_2)$), 128.69 (s, CH_{Ar}), 128.66 (s, CH_{Ar}), 128.44 (s, CH_{Ar}), 67.86 (s, CH_2), 67.17 (s, CHOH), 38.4 (s, CH_2).

6.4.2. Procedure for the synthesis of NitroBenzyl Malate, NBnMa:

DL -Malic acid (5 g, 37.3 mmol) was cooled over ice before triflluoroacetic anhydride (TFAA) (12.5 mL, 89.5 mmol) was added slowly. After stirring at 0 ˚C for 3 h a clear solution formed and volatiles were removed under reduced pressure whilst the mixture was kept on ice. Nitrobenzyl alcohol (NBnOH) (17.14 g, 111.9 mmol) in DCM (40 mL) was added to the residual solid before being allowed to warm up to room temperature and being left to stir overnight. DCM was removed via rotary evaporation before the rest of the reaction mixture was dissolved in EtOAc (150 mL) and extracted with Na_2CO_3 (10 %, 3 x 100 mL). The aqueous phase was acidified to pH 7 using 1M HCl (*c.a.* 200 mL) and excess NBnOH was extracted using EtOAc (4 × 100 mL) before recollecting the aqueous phase, acidifying further to pH 2/3 and extracting the pure monoester with more EtOAc (5 × 100 mL). The solution was dried using $MgSO_4$ before having solvent removed *via* rotary evaporation to yield an off-white powder (Yield: 5.05 g, 50%). ^{1}H NMR (400 MHz, Acetone-d_6) *δ:* 8.18 – 8.10 (m, 1H), 7.84 – 7.73 (m, 2H), 7.64 (m, 1H), 5.57 (m, 2H), 4.67 (dd, $^3J_{HH}$, 4.8 Hz, 1H), 2.97 – 2.66 (m, 2H). ^{13}C NMR (101 MHz, Acetone-d_6) *δ*: 172.47 (s, C=O), 170.98 (s, C=O), 147.34 (s, CNO_2), 133.91 (s, CH_{Ar}), 129.25 (s, CH_{Ar}), 129.06 (s, CH_{Ar}), 124.77 (s, CH_{Ar}), 67.6 (s, CHOH), 63.06 (s, CH_2), 38.43 (s, CH_2). Elemental analysis: anal. calcd for $C_{11}H_{11}NO_7$: C 49.08; H 4.12; N 5.2 %. Found: C 49.15; H 4.05; N 5.12 %. MS (ESI +ve): m/z 292 $[M + Na]^+$.

6.4.3. Procedure for the synthesis of Ethyl Malate, EtMa:

DL -Malic acid (26.6 g, 194 mmol) was cooled over ice before triflluoroacetic anhydride (TFAA) (100 g, 476.1 mmol) was added slowly. After stirring at 0 ˚C for 3 h a clear solution formed and volatiles were removed under reduced pressure whilst the mixture was kept on ice. Ethanol (EtOH) (50 mL, 970 mmol) was added to the

residual solid before being allowed to warm up to room temperature and being left to stir overnight. The reaction mixture was diluted with EtOAc (300 mL) and extracted with Na_2CO_3 (10 %, 3 × 200 mL). The aqueous phase was acidified to pH 7 using 1M HCl and excess EtOH was extracted using EtOAc (4 × 200 mL) before recollecting the aqueous phase, acidifying further to pH 2/3 and extracting the pure monoester with more EtOAc (5 × 200 mL). The solution was dried using $MgSO_4$ before having solvent removed *via* rotary evaporation to leave a white solid (Yield: 18.9 g, 54 %). Characterisation was in good agreement with previous reports.[5] ^{1}H NMR (400 MHz, Acetone-d6) δ: 4.49 (t, $^3J_{HH}$ = 6.0 Hz, 1H), 4.17 (qd, $^3J_{HH}$ = 7.1, 2.9 Hz, 2H), 2.86 – 2.59 (m, 2H), 1.24 (t, $^3J_{HH}$ = 7.1 Hz, 3H). ^{13}C NMR (101 MHz, Acetone-d6) δ: 172.85 (s, C=O), 171.05 (s, C=O), 67.5 (s, CH), 60.68 (s, CH_2) 38.53 (s, CH_2), 13.52 (s, CH_3).

6.4.4. Procedure for the synthesis of Butenyl Malate, BuMa:

DL -Malic acid (26.6 g, 194 mmol) was cooled over ice before triflluoroacetic anhydride (TFAA) (100 g, 476.1 mmol) was added slowly. After stirring at 0 ˚C for 3 h a clear solution formed and volatiles were removed under reduced pressure whilst the mixture was kept on ice. 3-Buten-1-ol (48.5 g, 672 mmol) was added to the residual solid before being allowed to warm up to room temperature and being left to stir overnight. Unreacted 3-Buten-1-ol was removed by vacuum distillation at 35-40 ˚C to yield pure BuMa (Yield: 40g, 95%). ^{1}H NMR (500 MHz, Chloroform-*d*) δ: 5.77-5.69 (m, 1H), 5.16 – 4.99 (m, 2H), 4.50 (dd, $^3J_{HH}$ = 4.0, 1.8 Hz, 0H), 4.28-4.18 (m, 2H), 2.95 – 2.71 (m, 2H), 2.41-2.36 (m, 2H). ^{13}C NMR (126 MHz, Chloroform-*d*) δ: 175.44 (s, C=O), 173.27 (s, C=O), 133.14 (s, CH), 117.65 (s, CH_2), 67.04 (s, CH), 64.99 (s, CH_2), 38.45 (s, CH_2), 32.81 (s, CH_2), 32.81 (s, CH_2). Elemental analysis: anal. calcd for $C_8H_{12}O_5$: C 51.06; H 6.43; N 0 %. Found: C 49.38; H 6.52; N 0 %. MS (ESI +ve): m/z 211 $[M + Na]^+$.

6.4.5. General procedure for high temperature homopolymerisations of malate monomers:

All hompolymerisations were carried out in bulk on a 2 g scale. The monomer was placed in the bottom of a vial equipped with stirrer bar before being placed in a sand-filled, round bottom dessicator and heated to 110 ˚C under high vacuum (11 mmHg). During the step-growth, polycondensation reaction samples were taken from the vials at set intervals to monitor their conversion and molecular weight by ^{1}H-NMR spectroscopy SEC analysis, respectively. After 7 days the polymerisations were stopped

P(BnMa): ^{1}H NMR (400 MHz, Acetone-d_6) δ: 7.55 – 7.21 (m, 30H), 7.01 – 6.73 (m, 2H), 5.78 – 5.44 (m, 7H), 5.38 – 5.01 (m, 12H), 4.72 – 4.52 (m, 0.3H$_{monomer}$) 3.34 – 2.72 (m, 15H). SEC analysis M_n = 2100 g mol^{-1}, $Đ_m$ = 1.75. (RI detection, DMF GPC).

P(NBnMa): ^{1}H NMR (400 MHz, Acetone-d_6) δ: 8.17 – 8.07 (m, 6H), 7.87 – 7.70 (m, 13H), 7.70 – 7.51 (m, 17H), 7.03 – 6.77 (m, 2H), 5.85 – 5.41 (m, 18H), 4.83 – 4.64 (m, 1H$_{monomer}$), 3.35 – 2.79 (m, 11H). SEC analysis M_n = 1900 g mol^{-1}, $Đ_m$ = 1.46. (RI detection, DMF GPC).

P(EtMa): ^{1}H NMR (400 MHz, Acetone-d_6) δ: 7.00 – 6.73 (m, 2H), 5.80 – 5.32 (m, 15H), 4.60 – 4.44 (m, 1H), 4.28 – 4.15 (m, 20H), 3.37 – 2.58 (m, 33H), 1.27 (t, $^{3}J_{HH}$ = 7.3 Hz, 30H). SEC analysis M_n = 2100 g mol^{-1}, $Đ_m$ = 1.41. (RI detection, DMF GPC).

P(BuMa): ^{1}H NMR (400 MHz, Acetone-d_6) δ: 6.98 – 6.70 (m, 2H), 5.88 – 5.81 (m, 2H), 5.72 – 5.37 (m, 3H), 5.24 – 4.95 (m, 5H), 4.51 (dd, $^{3}J_{HH}$ = 7.1, 4.7 Hz, 0H$_{monomer}$), 4.34 – 4.06 (m, 5H), 3.23 – 2.73 (m, 6H), 2.55 – 2.28 (m, 5H). SEC analysis M_n = 1500 g mol^{-1}, $Đ_m$ = 1.39. (RI detection, DMF GPC).

6.4.6. Procedure for ambient temperature homopolymerisation of BnMa:

4-(dimethylamino)pyridinium 4-toluene-sulfonate (DPTS) was synthesised according to previous procedures.[10] BnMa (0.5 g, 2.28 mmol) and DPTS (0.132 g, 0.45 mmol) were combined in a vial and dissolved in THF (2.5 mL) before being transferred to a suba sealed ampoule. THF was removed under reduced pressure and subsequently replaced with anhydrous THF (2.5 mL) before being cooled to 0 ˚C. DIC (0.422 g, 3.34 mmol) was added in a dropwise manner over the course of 15 minutes before slowly allowing the reaction mixture to warm up to room temperature. After stirring for 5 h at room temperature the reaction mixture was precipitated into ice cold hexanes/methanol (10:1, v/v) several times before being passed through a silica plug. ^{1}H NMR (400 MHz, Acetone-d_6) δ: 7.46 – 7.32 (m, 78H), 7.06 – 6.72 (m, 2H), 5.77 – 5.40 (m, 15H), 5.34 – 5.03 (m, 32H), 3.26 – 2.69 (m, 31H). SEC analysis M_n = 2600 g mol^{-1}, $Đ_m$ = 1.41. (RI detection, DMF GPC).

6.4.7. General procedure for copolymerisations of BnMa, NBnMa and EtMa with BuMa:

All copolymerisations were carried out in bulk on a 2 g scale. In a typical copolymerisation, 3 equivalents of either BnMa, NBnMa or EtMa were combined with 1 equivalent of BuMa in a vial equipped with stirrer bar. The vials were placed in a sand-filled, round bottom dessicator and heated to 110 ˚C under high vacuum (11 mmHg). Samples were taken after 24, 48 and 72 h in order to follow conversion and molecular weight by ^{1}H-NMR spectroscopy and SEC analysis, respectively. All copolymerisations were stopped after 72 h.

P(BnMa-co-BuMa): ^{1}H NMR (400 MHz, Acetone-d_6) δ: 7.53 – 7.25 (m, 26H), 7.00 – 6.72 (m, 2H), 5.83 (m, 1H), 5.75 – 5.41 (m, 7H), 5.34 – 4.97 (m, 13H), 4.62 (m,

$1H_{monomer}$), 4.20 (m, 3H), 3.32 – 2.60 (m, 17H), 2.40 (m, 2H). SEC analysis M_n = 1600 g mol^{-1}, $Đ_m$ = 1.41. (RI detection, DMF GPC).

P(NBnMa-co-BuMa): ^{1}H NMR (400 MHz, Acetone-d_6) δ: 8.14 (m, 5H), 7.80 (m, 10H), 7.64 (m, 6H), 7.07 – 6.72 (m, 2H), 5.94 – 5.39 (m, 18H), 5.22 – 4.95 (m, 3H), 4.84 – 4.47 (m, $1H_{monomer}$), 4.21 (m, 2H), 3.40 – 2.66 (m, 15H), 2.41 (m, 2H). SEC analysis M_n = 1500 g mol^{-1}, $Đ_m$ = 1.7. (RI detection, DMF GPC).

P(EtMa-co-BuMa): ^{1}H NMR (400 MHz, Acetone-d_6) δ: 7.02 – 6.70 (m, 2H), 5.95 – 5.72 (m, 2H), 5.75 – 5.36 (m, 10H), 5.24 – 4.99 (m, 5H), 4.61 – 4.44 (m, 1H), 4.21 (m, 15H), 3.43 – 2.76 (m, 24H), 2.43 (m, 4H), 1.27 (m, 15H). SEC analysis M_n = 1700 g mol^{-1}, $Đ_m$ = 1.29. (RI detection, DMF GPC).

6.4.8. Typical procedure for NMR scale study assessing alkene reactivity of the copolymers towards dodecanethiol:

Each of the three copolymers (P(BnMa-*co*-BuMa), P(NBnMa-*co*-BuMa) & P(EtMa-*co*-BuMa)) (50 mmol), camphorquinone (2 wt%) and ethyl 4-(dimethylamino)benzoate (EDMAB) (1:1 equivalents with camphorquinone) were dissolved in deuterated acetone (1 mL) before dodecanethiol (DDT) (100 mmol) was added. The reaction mixtures were transferred to NMR tubes before being illuminated with blue light (465 nm) from the blue light post exposure box for 1 h. ^{1}H-NMR spectroscopy was used to analyse the copolymers both before and after reacting with dodecanethiol.

6.5. Experimental Procedures for Chapter 4:

6.5.1. General procedure for the large-scale synthesis of P(EtMa-co-BuMa):

EtMa (30 g, 185 mmol) and BuMa (11.6 g, 61.6 mmol) were combined in a 250 mL RBF and heated to 110 ˚C in the bulk before being stirred using an overhead stirrer at

100 rpm under a continuous flow of nitrogen. Polymerisations were halted once the polymerisations had reached a conversion of between 75 and 80 %. ^{1}H NMR (400 MHz, Acetone-d_6) δ: 6.83 (dd, $^{3}J_{HH}$ = 26.6, 2.1 Hz, 2H), 5.94 – 5.73 (m, 5H), 5.76 – 5.38 (m, 16H), 5.25 – 4.98 (m, 9H), 4.84 – 4.60 (m, 5H), 4.62 – 4.43 (m, 8H), 4.36 – 4.01 (m, 38H), 3.33 – 2.85 (m, 38H), 2.85 – 2.61 (m, 13H), 2.52 – 2.31 (m, 9H), 1.36 – 1.17 (m, 40H). SEC analysis M_n = 1700 g mol^{-1}, $Đ_m$ = 1.37. (RI detection, DMF GPC).

6.5.2. Procedure for the synthesis of Dibutenyl Succinate:

3-Buten-1-ol (36.6 g, 508 mmol) was added to a mixture of benzene (75 mL) and toluene (75 mL) before being heated to 80 ˚C. Several drops of conc. H_2SO_4 were added before addition of succinic acid (15 g, 127 mmol). The reaction mixture was heated to reflux under dean-stark conditions and left stirring overnight. Benzene/toluene and any unreacted 3-buten-1-ol were removed under reduced pressure and the remaining crude product was purified *via* vacuum distillation at 145 ˚C and 11 mmHg to afford a non-viscous clear liquid (Yield: 25 g, 94 %). ^{1}H NMR (400 MHz, Chloroform-*d*) δ: 5.88 – 5.62 (m, 1H), 5.19 – 4.97 (m, 2H), 4.13 (t, $^{3}J_{HH}$ = 6.8 Hz, 2H), 2.61 (s, 2H), 2.37 (q, $^{3}J_{HH}$ = 7.0 Hz, 2H). ^{13}C NMR (101 MHz, Chloroform-*d*) δ: 172.18 (s, C=O), 133.88 (s, CH), 117.23 (s, CH_2), 63.73 (s, CH_2), 32.99 (s, CH_2), 29.11 (s, CH_2). Elemental analysis: anal. calcd for $C_{12}H_{18}O_4$: C 63.7; H 8.02; N 0 %. Found: C 63.54; H 8.14; N 0 %. MS (ESI +ve): m/z 248.8 $[M + Na]^+$.

6.5.3. Procedure for biocompatibility assay:

MC3T3 cells were obtained from Public Health England. Cells were cultured in 175 cm^2 tissue culture flasks using MEM alpha medium (Gibco), as advised by supplier, with addition of 10% FBS and 1% pen/strep, at 37 °C, 5% CO_2. Cells were used three weeks after culture. For the experiments, the different resin compositions (0, 30 and

50 wt%) were dissolved in acetone (3 wt%) and subsequently spin coated onto cover slips (thickness <500 microns as determined by interferometry). Cells were then seeded onto the coated cover slips in addition to a non-coated cover slip as a control at 2000 cells/cm^2 after having been sterilised in 70% EtOH. The cells were assayed for cell proliferation after 24 h, 72 h and 7 days, respectively, using Presto Blue metabolic assay.PrestoBlue fluorescence was measured after 1-4 h incubation using a BioTek plate reader (Ex: 530 Em: 590). Experiments were performed in triplicate.

6.6. References

1. Leigh, S. J.; Gilbert, H. T.; Barker, I. A.; Becker, J. M.; Richardson, S. M.; Hoyland, J. A.; Covington, J. A.; Dove, A. P., Fabrication of 3-dimensional cellular constructs via microstereolithography using a simple, three-component, poly(ethylene glycol) acrylate-based system. *Biomacromolecules* **2013,** *14* (1), 186-192.

2. Holmes, C. P., Model Studies for New o-Nitrobenzyl Photolabile Linkers: Substituent Effects on the Rates of Photochemical Cleavage. *J. Org. Chem.* **1997,** *62*, 2370-2380.

3. Kloxin, A. M.; Kasko, A. M.; Salinas, C. N.; Anseth, K. S., Photodegradable hydrogels for dynamic tuning of physical and chemical properties. *Science* **2009,** *324* (5923), 59-63.

4. Kloxin, A. M.; Tibbitt, M. W.; Anseth, K. S., Synthesis of photodegradable hydrogels as dynamically tunable cell culture platforms. *Nat. Protoc.* **2010,** *5* (12), 1867-1887.

5. Miller, M. J.; Bajwa, J. S.; Mattingly, P. G.; Peterson, K., Enantioselective syntheses of 3-substituted 4-(alkoxycarbonyl)-2-azetidinones from malic acid. *J. Org. Chem.* **1982,** *47* (25), 4928-4933.

6. Harjani, J. R.; Yap, B. K.; Leung, E. W. W.; Lucke, A.; Nicholson, S. E.; Scanlon, M. J.; Chalmers, D. K.; Thompson, P. E.; Norton, R. S.; Baell, J. B., Design, Synthesis, and Characterization of Cyclic Peptidomimetics of the Inducible Nitric Oxide Synthase Binding Epitope That Disrupt the Protein–Protein Interaction Involving SPRY Domain-Containing Suppressor of Cytokine Signaling Box Protein (SPSB) 2 and Inducible Nitric Oxide Synthase. *J. Med. Chem.* **2016,** *59* (12), 5799-5809.

7. Kajiyama, T.; Kobayashi, H.; Morisaku, K.; Taguchi, T.; Kataoka, K.; Tanaka, J., Determination of end-group structures and by-products of synthesis of poly(α,β-malic acid) by direct polycondensation. *Polym. Degrad. Stab.* **2004,** *84* (1), 151-157.

8. Kajiyama, T.; Kobayashi, H.; Taguchi, T.; Kataoka, K.; Tanaka, J., Improved Synthesis with High Yield and Increased Molecular Weight of Poly(α,β-malic acid) by Direct Polycondensation. *Biomacromolecules* **2004,** *5* (1), 169-174.

9. Kajiyama, T.; Taguchi, T.; Kobayashi, H.; Kataoka, K.; Tanaka, J., Synthesis of high molecular weight poly(α,β-malic acid) for biomedical use by direct polycondensation. *Polym. Degrad. Stab.* **2003,** *81* (3), 525-530.

10. Moore, J. S.; Stupp, S. I., Room temperature polyesterification. *Macromolecules* **1990,** *23* (1), 65-70.